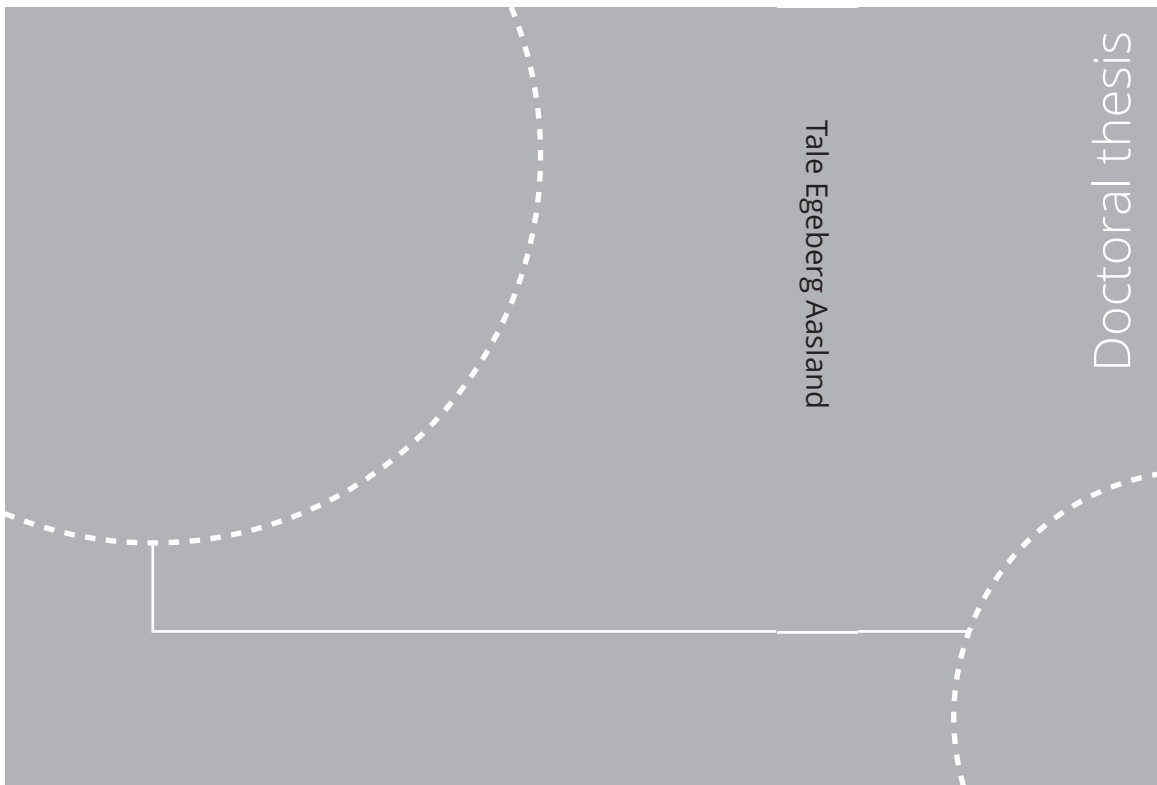


ISBN 978-82-326-7756-6 (printed ver.)  
ISBN 978-82-326-7755-9 (electronic ver.)  
ISSN 1503-8181 (printed ver.)  
ISSN 2703-8084 (electronic ver.)



Doctoral theses at NTNU, 2024:81

Tale Egeberg Aasland

# Numerical studies of viscous flow around straight and curved tandem cylinders

Doctoral theses at NTNU, 2024:81

**NTNU**  
Norwegian University of  
Science and Technology  
Thesis for the degree of  
Philosophiae Doctor  
Faculty of Engineering  
Department of Marine Technology



Tale Egeberg Aasland

# Numerical studies of viscous flow around straight and curved tandem cylinders

Thesis for the degree of Philosophiae Doctor

Trondheim, March 2024

Norwegian University of Science and Technology  
Faculty of Engineering  
Department of Marine Technology



Norwegian University of  
Science and Technology

**NTNU**

Norwegian University of Science and Technology

Thesis for the degree of Philosophiae Doctor

Faculty of Engineering  
Department of Marine Technology

© Tale Egeberg Aasland

ISBN 978-82-326-7756-6 (printed ver.)  
ISBN 978-82-326-7755-9 (electronic ver.)  
ISSN 1503-8181 (printed ver.)  
ISSN 2703-8084 (electronic ver.)

Doctoral theses at NTNU, 2024:81



Printed by Skipnes Kommunikasjon AS

For my father



# Contents

<b>Abstract</b>	<b>v</b>
<b>Preface</b>	<b>vii</b>
<b>Acknowledgment</b>	<b>ix</b>
<b>1 Introduction</b>	<b>1</b>
1.1 Viscous flow around bluff bodies . . . . .	2
1.2 Flow around tandem cylinders . . . . .	9
1.3 Cylinders with axial curvature . . . . .	13
1.4 Computational method . . . . .	16
1.5 Outline of the present study . . . . .	17
<b>2 Conclusions and outlook</b>	<b>19</b>
2.1 Summary of the results . . . . .	19
2.2 Recommendations for further work . . . . .	22
<b>References</b>	<b>25</b>
<b>3 Straight tandem cylinders in the reattachment regime</b>	<b>31</b>
3.1 Paper 1. Revisiting the reattachment regime: a closer look at tandem cylinder flow at $Re = 10\,000$ . . . . .	33
3.2 Paper 2. Asymmetric cellular bi-stability in the gap between tandem cylinders . . . . .	66
<b>4 Tandem cylinders with axial curvature</b>	<b>93</b>
4.1 Paper 3. Flow around curved tandem cylinders . . . . .	95
4.2 Paper 4. Flow topology in the gap and wake of convex curved tandem cylinders . . . . .	105
4.3 Paper 5. Turbulent flow around convex curved tandem cylinders . . . . .	142



# Abstract

The physics of flow around straight and curved cylinders in tandem is investigated by means of direct numerical simulations (DNS), for transitional and turbulent flow regimes.

For straight tandem cylinders in the reattachment regime, the effect on the gap and wake flow of transition to turbulence in the shear layers is scrutinized, along with the interaction between large-scale recirculating gap vortices and the development of the gap shear layers. The role of flow three-dimensionality in the gap and wake is studied. It is discovered that tandem cylinder flow regimes may be spanwise cellular and asymmetric in the gap region. The physical mechanism behind such cellular flow regime variations is discussed.

Tandem cylinders with axial curvature are studied for the first time. The convex configuration, where the incoming flow is directed towards the outside of the cylinder curvature, is chosen. The effect of axial flow on the forces on the cylinders and their characteristic frequencies is addressed, as well as spanwise variation of tandem cylinder flow regimes. Several flow regimes co-exist along the span, and some of these are unstable, which has a profound effect on the development of the wake. The flow topology of the gap and wake, vortex shedding modes and the complex interaction between the spanwise localized flow regimes are discussed in detail. The effect of transition to turbulence either in the wake or in the shear layers is addressed, as is the interaction between the primary instability and the shear layer instability, under influence of axial flow.





# Preface

This thesis is submitted to the Norwegian University of Science and Technology (NTNU) for partial fulfillment of the requirements for the degree of philosophiae doctor.

This doctoral work has been carried out at the Department of Marine Technology (DMT) at NTNU, Trondheim. Professor Bjørnar Pettersen from DMT is the main supervisor. Professor Helge Ingolf Andersson from DMT and Doctor Fengjian Jiang from Department of Ships and Ocean Structures, SINTEF Ocean, are the co-supervisors.

This work has been supported by the Norwegian Public Roads Administration, where the candidate has been employed throughout the PhD period, and the Research Council of Norway. Their support is greatly appreciated. The work was made possible by computational resources provided by UNINETT Sigma2, through project nn9191k.



# Acknowledgment

First of all, my most heartfelt thanks to my main supervisor, Bjørnar Pettersen. You have been an inspiration to me these many years; ever since 2010 when I, then an undergrad, knocked on the door of your office and asked for a job in research. Through our various projects together I have valued our discussions (on or off topic), your advice and support, not to mention your boundless enthusiasm for fluid mechanics. It's contagious and I caught it.

I have greatly enjoyed working with my co-supervisors, Helge I. Andersson and Fengjian Jiang. Thank you for sharing your knowledge and experience. Your perspective on these studies, in particular regarding the physics, has been invaluable. Helge, you keep me and Bjørnar in line; a momentous effort, no doubt.

Håkon Strandenes, former PhD student at IMT, now with KM Turbulenz, has been a great help throughout my PhD work. Thank you for answering all my questions with the patience of true Stoic.

Without the library, there would be no thesis. Even in this digital age, the actual, physical library is essential. I would like thank all librarians everywhere, but especially Ann-Johanne Bjørgen at the Marine Technology Library, who is nothing short of a bibliographical magician.

I owe a great debt to my friends, who have kept me sane by means of long phone calls, hikes, music, late-night shenanigans, rants about Tolstoy (Tolstoy?), completely unseasonable swimming and gallons upon gallons of coffee. You know who you are, and I love you all dearly. Christine Follo and Håkon Alseth deserve a special mention, though, for letting me stay at their house for weeks on end during my many trips to Trondheim in the past two years.

None of this would have been possible without the help and support of my family, who save the day on a weekly basis. You have my undying gratitude.

Last, but certainly not least: Erlend, my husband, my heart. Njord and Eir, my sun and moon, who ask "but, why?" until we've worked our way from celestial scale down to quarks. I love you. Thank you for the time and patience you have given me. I'll talk less about vortices from now on (possibly).

Tale Egeberg Aasland  
March 2024  
Trondheim, Norway



# Chapter 1

## Introduction

For centuries, wakes and vortices have fascinated laymen and scientists alike with their intricate beauty. The physics of wake flows are exceedingly complex, and remain an active topic of research to this day, not least owing to their importance for engineering purposes. Offshore pipelines for oil and gas, marine risers, chimneys, high-rise buildings, bridge decks and columns, or the towers of wind-turbines; these are just a few examples of bluff (non-streamlined) bodies that generate vortex-shedding wakes when subjected to water currents or wind. The oscillating drag and lift forces induced by vortex shedding is an essential part of structural design, as is the effect of the wake on nearby structures (or even pedestrians and cars).

Many engineering applications involve fluid flow around pairs or groups of bluff bodies. The present study is motivated by one of the more spectacular examples, namely submerged floating tunnels (SFT). No SFT has yet been built, but some proposed designs consist of two adjacent cylindrical tunnels (one for each traffic direction), with axial curvature (Aasland *et al.*, 2023), i.e. curved cylinders in tandem. One such design is the Bjørnafjord crossing (Eidem *et al.*, 2018), which sparked the idea for the work presented herein. Because there were no previous studies of flow around curved tandem cylinders, it was considered important to clarify the underlying flow physics, rather than to study one specific SFT. Therefore, the present study aims to characterize the fundamental fluid mechanic processes that govern the flow field around tandem cylinders with axial curvature. This also necessitates taking a closer look at some straight tandem cylinder cases. A guiding principle for our work has been that a thorough understanding of the physics is the ground on which more applications-oriented studies can be built, and crucial to the exploration of novel structure types, such as SFT's.

This chapter introduces some basic concepts of viscous fluid flow, and how these apply to cylinders, single or in tandem (section 1.1 and 1.2, respectively). Additionally, an overview of flow around single cylinders with axial curvature is given in section 1.3, since some of the features of such wakes are also found in the wakes of curved tandem cylinders. The present study is carried out by means of numerical simulations, and the computational aspects are outlined in section 1.4. Finally, an overview of the resulting papers is presented in section 1.5.

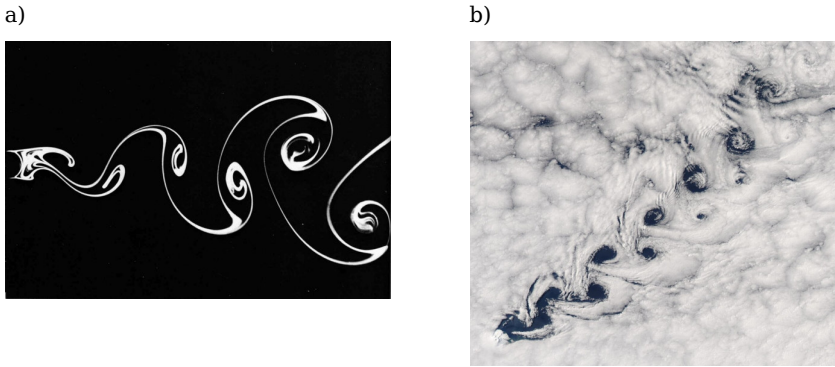


Figure 1.1: a) Cylinder wake in a water flume at  $Re = 140$ . Photo by S. Tandeda, reproduced from Zdravkovich (1997a). b) Wind-induced vortex shedding in the cloud layer behind Heard Island, captured by NASA's Aqua satellite on Nov 2, 2015 at 09:20 UTC (Schmaltz, 2015). Reynolds number estimated to be in the order of  $10^7$ .

## 1.1 Viscous flow around bluff bodies

Viscous flow around bluff bodies is normally discussed in terms of the Reynolds number, which describes the relative importance of inertial forces versus viscous (i.e. frictional) forces:

$$Re = \frac{\rho U_0 l}{\mu} = \frac{U_0 l}{\nu} \sim \frac{\text{inertial force}}{\text{viscous force}} \quad (1.1)$$

Here,  $U_0$  is the velocity of the incoming flow,  $\rho$  is the density of the fluid, and  $\mu$  its viscosity.  $l$  is a characteristic length scale, which might be the waterline length of a ship subjected to currents in the sea or the diameter  $D$  of a cylindrical column.

It is a peculiarity of bluff body flows that objects of vastly different size and geometry may produce wakes that are fundamentally similar. An example of this is shown in figure 1.1. Figure 1.1a depicts flow visualization of the wake behind a cylinder in a laboratory. Vortices form and are transported downstream by the flow to create what is known as the Kármán - Bénard (or, perhaps more commonly, simply von Kármán) vortex street, named after early descriptions by Bénard (1908) and von Kármán (1912). The same type of wake is shown in figure 1.1b, but on a much grander scale. These vortices form in the cloud layer downstream of Mawson Peak on Heard Island, captured for posterity by a NASA satellite. The cylinder has a length scale in the order of centimeters, while the characteristic length scale of Mawson Peak is in the order of kilometers. This implies that even for very low wind speeds, the Reynolds number of Mawson Peak will be in the order of  $10^7$ , compared to 140 for the cylinder.

The von Kármán vortex street arises when the boundary layer on a bluff body separates from the surface, which occurs when the pressure increases along the surface in the streamwise direction (although for bodies with sharp corners, separation will generally occur at the corner). The separated boundary layer, now called a shear layer, subsequently becomes unstable and forms vortices, as exemplified in figure 1.2.

In figure 1.3 the various stages of the development of the boundary layer and wake of a cylinder are shown, along with their respective Reynolds number ranges. For very

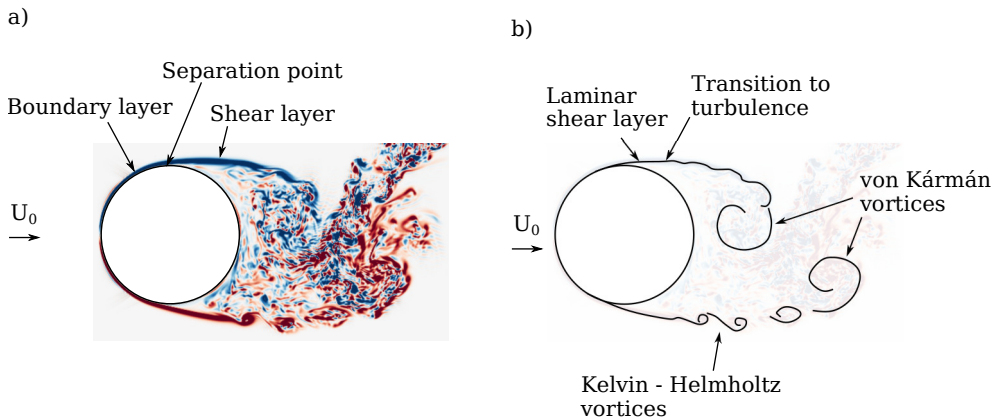


Figure 1.2: a) Viscous flow around a single cylinder at  $Re = 10^4$ , represented by spanwise vorticity,  $\omega_z$ . Red means positively signed vorticity and blue means negatively signed vorticity. b) schematic of the vortices in a). Data from the present study.

low Reynolds numbers, there is no separation, as shown in figure 1.3a. The flow field resembles the inviscid case. After separation, a pair of symmetric recirculating vortices form at the cylinder base. These vortices remain steady up to  $Re \approx 40$ . At this point, the viscosity can no longer stabilize the flow, and the so-called primary instability is triggered, resulting in a vortex street in the wake.

Initially, the vortex street is laminar and the flow is essentially two-dimensional. Around  $Re \approx 180 - 190$ , however, a three-dimensional instability is triggered in the wake, which leads to transition to turbulence. The transition is heralded by spanwise waves along the von Kármán vortices, and the occurrence of streamwise oriented vortices in the space between them (usually called the braid regions). The initial flow pattern, shown in figure 1.4a and 1.4c, is called mode A, and it is characterized by vortex loops with a typical spanwise wavelength of approximately  $4D$  (Williamson, 1996b). 'Spanwise wavelength' refers to the distance between the streamwise vortices.

Over the range  $Re \approx 230 - 260$ , there is a gradual transition from mode A to the instability called mode B (Williamson, 1996b; Jiang *et al.*, 2016), which results in a flow pattern like the one shown in figure 1.4b and 1.4d. Mode B is characterized by streamwise vortex pairs with a spanwise wavelength of approximately  $1D$ . Within the transition range, the flow switches intermittently between mode A and mode B, and two distinct vortex shedding frequencies can be observed, corresponding to each of the modes (Williamson, 1996a).

Within mode A, dislocations in the spanwise vortices occur frequently. Such vortex dislocations develop due to local frequency and/or phase differences along the span, and result in complex linking patterns between the vortex cores (Williamson, 1989). After transition to mode B, the dislocations largely disappear. Henderson (1997), however, showed that they may nonetheless develop spontaneously, provided that the spanwise length of the cylinder is sufficient. Dislocations may occur anywhere along the span, and the location varies with time. Forced and spontaneous vortex dislocations are shown in figure 1.5.

Further increasing the Reynolds number moves the transition point upstream in the



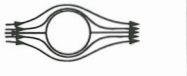


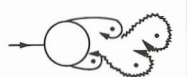
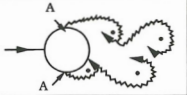
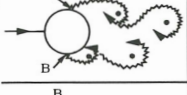
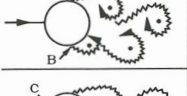
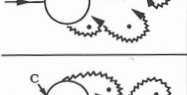
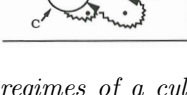
a)		No separation. Creeping flow	$Re < 5$
b)		A fixed pair of symmetric vortices	$5 < Re < 40$
c)		Laminar vortex street	$40 < Re < 200$
d)		Transition to turbulence in the wake	$200 < Re < 300$
e)		Wake completely turbulent. A: Laminar boundary layer separation	$300 < Re < 3 \times 10^5$ Subcritical
f)		A: Laminar boundary layer separation B: Turbulent boundary layer separation; but boundary layer laminar	$3 \times 10^5 < Re < 3.5 \times 10^5$ Critical (Lower transition)
g)		B: Turbulent boundary layer separation; the boundary layer partly laminar partly turbulent	$3.5 \times 10^5 < Re < 1.5 \times 10^6$ Supercritical
h)		C: Boundary layer comple- tely turbulent at one side	$1.5 \times 10^6 < Re < 4 \times 10^6$ Upper transition
i)		C: Boundary layer comple- tely turbulent at two sides	$4 \times 10^6 < Re$ Transcritical

Figure 1.3: Flow regimes of a cylinder with smooth inflow. Reproduced from Sumer & Fredsøe (2006).

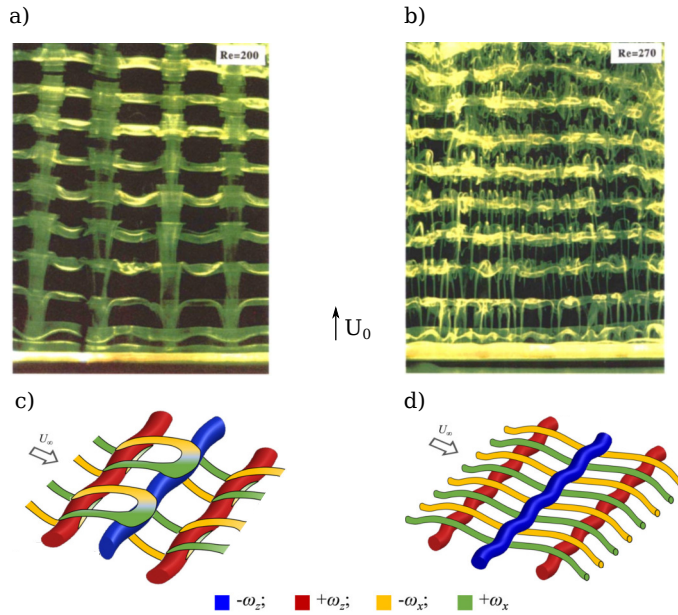


Figure 1.4: Three-dimensional wake modes of a single cylinder. Experimental flow visualizations of a) mode A and b) mode B, adapted from Williamson (1996a). Schematic of c) mode A and d) mode B, coloured by the sign of the streamwise and spanwise vorticity,  $\omega_x$  and  $\omega_z$ . Adapted from Rastan & Alam (2021)

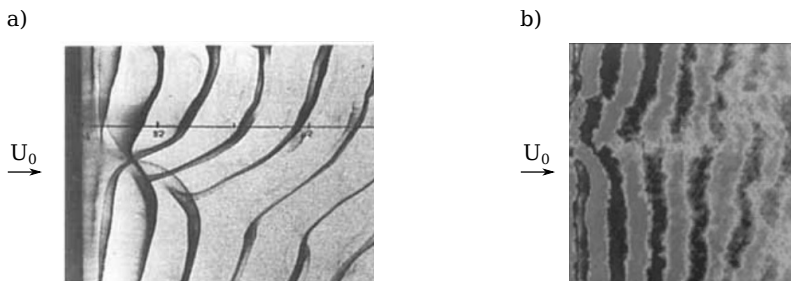


Figure 1.5: Vortex dislocations in a cylinder wake. a)  $Re = 100$  adapted from experimental flow visualizations by Williamson (1989). b)  $Re = 1000$ , adapted from numerical flow visualizations by Henderson (1997). Note that vortex dislocations do not occur naturally in laminar wakes. In a), the dislocations occur owing to the end conditions in the experimental setup.

wake, until the shear layers become unstable. The Reynolds number region where transition to turbulence occurs in the shear layers is commonly referred to as the subcritical regime. Transition in the shear layers causes the formation of small-scale eddies, the Kelvin-Helmholtz (K-H) vortices (named after the instability mechanism from which they arise). Such vortices are shown in figure 1.2b. The transition region moves upstream in the shear layer with increasing Reynolds number, but it is worth noting that this region also meanders randomly in the streamwise direction even when the Reynolds number remains constant (Prasad & Williamson, 1997). The meandering is caused by small eddies that are created during the formation of the von Kármán vortices (Rai, 2010). These eddies travel upstream in the recirculation region in the near wake. If they come into contact with the shear layers, the eddies may amplify the K-H instability and hasten transition to turbulence, provided that they are sufficiently strong.

For high Reynolds numbers, the transition points move into the boundary layer itself. Curiously, there is a narrow range of Reynolds numbers, called the critical regime, where the boundary layer is turbulent at separation on one side of the cylinder, and laminar at separation on the other side (Schewe, 1983). This regime is sketched in figure 1.3f. The asymmetric separation leads to loss of regular vortex shedding, accompanied by a significant drop in drag on the cylinder (the 'drag crisis'). Regular vortex shedding is re-established in the supercritical regime.

Beyond the critical regime, the transition point gradually moves upstream, until the entire boundary layer becomes turbulent. This does not occur simultaneously on both sides, however, as shown in figure 1.3h. Only beyond  $Re \approx 4 \times 10^6$  do both boundary layers become fully turbulent.

Turbulence in the boundary layer delays separation. Within the subcritical regime, where the boundary layer is fully laminar, the separation points are located near the top and bottom of the cylinder, as shown in figure 1.2. When transition to turbulence moves into the boundary layer, however, the separation points gradually move backwards (Sumer & Fredsøe, 2006).

The vortex shedding frequency  $f$  is normally given by the Strouhal number:

$$St = \frac{fD}{U_0} \quad (1.2)$$

The development of  $St$  as a function of the Reynolds number is shown in figure 1.6. There are two different modes of vortex shedding, called low-speed mode and high-speed mode (Zdravkovich, 1997b). In the low speed mode, which occurs within the laminar regime, the vortices grow gradually as they are convected downstream, as shown in figure 1.1a. In this mode,  $St$  increases with increasing  $Re$ .

In the high-speed mode, the vortices form and grow close to the cylinder base. A vortex is shed when the vortex on the opposite side becomes strong enough to pull the shear layer of the growing vortex across the wake, cutting off further supply of vorticity (Gerrard, 1966). This way, the vortex street is formed by alternating shedding of fully grown vortices.

In the high-speed mode,  $St$  is nearly constant with increasing  $Re$ , up to the critical regime. The backwards movement of the separation points beyond the critical regime leads to a jump in the Strouhal number, since the shear layers are now closer together and can interact faster. The final discontinuity in the  $St$  curve (near  $Re = 2 \times 10^6$  in figure 1.6) is caused by the asymmetrical boundary layer transition shown in figure 1.3h.

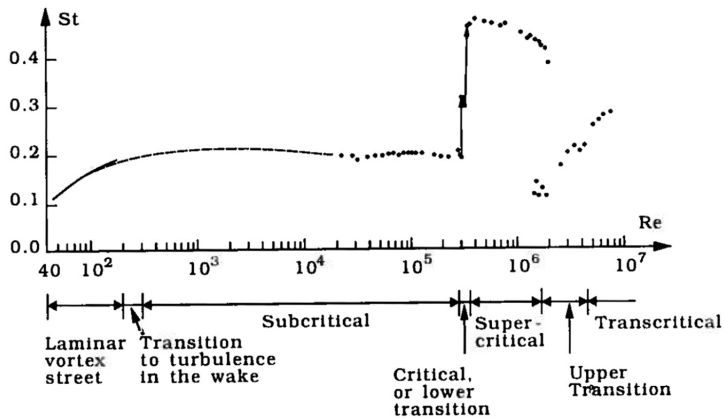


Figure 1.6: Strouhal number as a function of Reynolds number for a cylinder with smooth inflow. Reproduced from Sumer & Fredsøe (2006).

The constancy of the Strouhal number within the subcritical regime has received a lot of attention, especially since the vortex formation length  $L_f$  shrinks substantially with increasing Reynolds number within this regime.  $L_f$  is defined as the distance from the cylinder base to the point of maximum velocity fluctuations along the wake centerline. Gerrard (1966) explains the reduction of the vortex formation length as follows: The turbulent part of the shear layer entrains (i.e. absorbs or pulls in) significantly more fluid than the laminar part. This means that fluid entrainment into the shear layer increases with  $Re$ , since the transition region moves upstream. The length of the vortex formation region depends on the balance between fluid that is entrained into the shear layer from inside the near wake, and fluid that is entrained into the near wake by the forming vortex. Fluid entrained into the shear layer has oppositely signed vorticity from the shear layer itself, and that leads to weakening of the von Kármán vortices as  $Re$  grows. A weaker vortex cannot entrain as much fluid from outside the wake, which leads to a shortened formation region. A shorter vortex formation region should in turn cause a higher shedding frequency (Roshko, 1954), so there must be an opposing mechanism that ensures a near constant  $St$  in the subcritical regime.

According to Gerrard (1966), this mechanism is related to the thickness of the shear layers. Downstream of the transition point, the shear layer rolls up into Kelvin-Helmholtz vortices that diffuse and grow in diameter while being transported along the near wake. This causes the shear layer thickness to grow. It follows that an upstream movement of the transition region causes thicker, i.e. more diffused, shear layers. When the shear layers are more diffused, it takes longer to pull enough vorticity across the wake to initiate shedding. Moreover, greater diffusion of the vorticity results in less entrainment into the forming vortex, which in turn should result in higher vortex strength (since there is less fluid with oppositely signed vorticity). On this reasoning, increasing the Reynolds number and moving the transition region upstream should result in a decrease of the shedding frequency.

In short, the upstream movement of the shear layer transition region causes a shortening of the formation length, but the thickening of the shear layers counteracts the would-be

increase of the shedding frequency, so that  $St$  is kept nearly constant. To summarize, four main parameters influence the high-speed shedding mode (Gerrard, 1966): the width of the near wake (largely governed by the location of the separation points), the strength of the fully grown vortex, the thickness of the shear layers, and the entrainment into the near wake.

Several studies have found low-frequency variation of the vortex formation length in the wake behind cylinders (at a fixed  $Re$ ), as well as a number of other bluff bodies (Miau *et al.*, 1999; Lehmkuhl *et al.*, 2013; Cao & Tamura, 2020; Lorite-Díez & Jiménez-González, 2020). This variation is correlated with low-frequency variations in the base pressure. Miao *et al.* (1999) suggested that the balance between the free-stream pressure and the base pressure influences the curvature of the shear layers. An increase in base pressure (i.e. less suction) cause flatter shear layers, which leads to a lengthened formation region. This hypothesis is supported by the findings of Lehmkuhl *et al.* (2013), who found low-frequency variation between a high-energy and a low-energy vortex shedding mode. The high-energy mode had strong velocity fluctuations and a short formation length, whereas the low-energy mode had weaker fluctuations and a correspondingly longer formation length. Each mode had a distinct Strouhal number.

Because vortex shedding depends upon interaction between the shear layers on both sides of the wake, the shedding process can be inhibited or delayed by interfering with the shear layers' ability to interact. This can be accomplished by inserting an object, for instance a splitter plate, into the formation region. Depending on its length and its position relative to the cylinder base, a splitter plate may lengthen the formation region, reduce drag on the cylinder and delay the inception of the shear layer instability (Roshko, 1954; Apelt & Szewczyk, 1973; Cardell, 1993).

Finally, a short note should be made on the difference between the primary instability and the Kelvin-Helmholtz instability, since these are mentioned quite frequently herein. The crucial difference between these two instabilities does not lie in the size of the resulting vortices, though it may seem that way from figure 1.2<sup>1</sup>, but in the way the effect of the instability spreads in the fluid. The primary instability is absolute, while the Kelvin-Helmholtz instability is convective (Huerre & Monkewitz, 1985).

In the case of a convective instability, the disturbance the instability causes is transported downstream while growing in amplitude. In cylinder shear layers, the actual triggering of the instability occurs in the laminar part. This process is not visible to the naked eye, though the resulting fluctuations can be measured. As these fluctuations grow, the instability becomes visible as waves in the shear layer and, further downstream, Kelvin-Helmholtz vortices. These fluctuations downstream of the instability inception point do not, however, affect the shear layer upstream of this point.

For an absolute instability, the situation is the opposite. Pressure fluctuations resulting from an absolute instability are felt in the entire fluid domain, not just downstream of its inception point. This means that the pressure fluctuations from the von Kármán vortices are felt upstream even if the vortices do not come into direct contact with this part of the flow.

---

<sup>1</sup>In fact, the K-H instability may also occur on an atmospheric scale. The lucky observer might see clouds shaped much the same way as the K-H waves in cylinder shear layers.

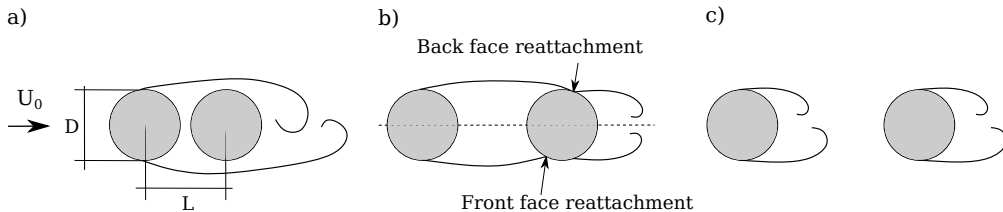


Figure 1.7: Basic tandem cylinder flow regimes a) Overshoot/extended-body  $1.0 \leq L/D \leq 1.2 - 1.8$  b) Reattachment  $1.2 - 1.8 \leq L/D \leq 3.4 - 3.8$  c) co-shedding  $3.4 - 3.8 \leq L/D$  (Zdravkovich, 1987).

## 1.2 Flow around tandem cylinders

When two cylinders are placed in tandem, so that the downstream cylinder lies along the centreline of the upstream cylinder wake, the cylinder flow fields interfere in two ways (Zdravkovich, 1987). Firstly, the proximity of the two cylinders modifies the pressure in the fluid, as well as on the surface of the cylinders themselves ('proximity interference'). Secondly, the downstream cylinder is located in the wake of the upstream cylinder ('wake interference'), which has consequences for vortex formation and shedding from both cylinders. The effect of the downstream cylinder is in some ways similar to that of a short splitter plate in the wake of a single cylinder (Zhou & Yiu, 2006). For instance, the experiments of Roshko (1954) give Strouhal number and base pressure results that are comparable to tandem cylinders at spacings equivalent to the spacing between the cylinder and splitter plate.

Flow around cylinders in tandem can be roughly grouped into three regimes, based on the behavior of the shear layers, as sketched in figure 1.7: overshoot, reattachment and co-shedding. These flow regimes depend on the Reynolds number and the streamwise distance between the cylinders, which is often called the gap ratio,  $L/D$ . Here,  $L$  is the center-to-center spacing between the cylinders, as shown in figure 1.7a.

Wake interference encompasses a class of vastly complex flows, resulting in something of a headache for those who wish to classify them. In fact, the regimes outlined in figure 1.7 include a proliferation of variations, some of which are sketched in figure 1.8. The reader will notice that the gap ratio range for each regime is not included in the figure. The omission is deliberate; due to the Reynolds number sensitivity (Xu & Zhou, 2004) several of these flows may be found at the same cylinder spacing. Furthermore, incoming disturbances in the flow, such as overall turbulence intensity (Ljungkrona *et al.*, 1991) or wind gust amplitude (Wang *et al.*, 2022), influence the flow regime. Even the spanwise length of the cylinders may play a role, due to the spanwise wavelength of the three-dimensional wake instability (Carmo *et al.*, 2010b). Nevertheless, several attempts have been made to classify the flow regimes according to the gap ratio, and the following classification by Zdravkovich (1987) is widely used: overshoot  $1.0 \leq L/D \leq 1.2 - 1.8$ , reattachment  $1.2 - 1.8 \leq L/D \leq 3.4 - 3.8$ , and co-shedding  $3.4 - 3.8 \leq L/D$ . Xu & Zhou (2004) later proposed a classification scheme based on maps of  $Re - L/D$  combinations, though this scheme never fully caught on.

In the following, a brief introduction to the main tandem cylinder flow regimes is given, although our focus is mainly on the reattachment regime. There are two reasons for this.

Firstly, this regime plays an important role in all the studies that comprise the present work. Secondly, the reattachment regimes is the most complex of the tandem cylinder flow regimes in terms of flow physics, and it includes a wide variety of sub-regimes (as figure 1.8 attempts to convey).

When the cylinders are very closely spaced the shear layers of the upstream cylinder completely envelop the downstream cylinder and roll up in its wake, so that vortex shedding essentially occurs from the upstream cylinder. There is little movement of the fluid in the gap, and two cylinders behave as a single bluff body. For that reason the overshoot regime is often called 'single-body' or 'extended-body'.

Increasing the spacing between the cylinders and/or the Reynolds number causes the upstream cylinder shear layers to reattach onto the surface of the downstream cylinder. Vortices are now shed exclusively from the downstream cylinder, but recirculating vortices may form in the gap. For low gap ratios, these are symmetrical (Lin *et al.*, 2002), as shown in figure 1.8c, but the vortices become alternating if the gap ratio increases (Carmo *et al.*, 2010a; Zhou *et al.*, 2019), as illustrated in figure 1.8d. In the literature, these recirculating gap vortices are often called 'quasi-steady' or 'quasi-stationary'. This is because their formation length is restricted by the width of the gap, and thus they remain at essentially the same streamwise location.

Initially, the reattachment points are located on the back face (i.e. downstream side) of the downstream cylinder, but with increasing gap ratio and/or Reynolds number, the points move upstream, as illustrated in figure 1.7b. The streamwise location of reattachment is important because it influences the strength of the vortices in the wake. Zhou & Yiu (2006) found that front face reattachment led to stronger vortices, compared to back face reattachment, since front face reattachment gives the boundary layer on the downstream cylinder more time to develop. Still, the vortices were weaker than in the overshoot regime, within which the strength was comparable to that of a single cylinder.

Provided that the Reynolds number is sufficiently high, there may be reattachment even for very low gap ratios. For instance, Tsutsui (2012) found reattachment at  $L/D = 1.2$  and  $Re = 10^5$ , which is in the upper subcritical Reynolds number range. For this flow regime, which is illustrated in figure 1.8bi, there was substantial fluid motion in the narrow gap between the cylinders.

For a wide range of gap ratio and Reynolds number combinations, reattachment is alternating (Zdravkovich, 1987). This means that one shear layer reattaches, while its opposite simultaneously overshoots the downstream cylinder. Different varieties of this regime are sketched in figures 1.8b - 1.8di. In the present study, alternating overshoot/reattachment occurred for both  $Re = 500$  and  $10^4$ , at the same gap ratio ( $L/D = 3$ ), as shown in figure 1.9. Towards the end of the reattachment regime, the reattachment becomes symmetrical (Zdravkovich, 1987), as shown in figures 1.8dii and 1.8e, and there is little movement of the reattachment points.

Transitions between tandem cylinder flow regimes are unstable and hysteretic (Carmo *et al.*, 2010b). Close to the limiting gap ratio (assuming  $Re$  is kept constant), the flow switches intermittently between regimes. Xu & Zhou (2004) observed such a switch between overshoot and reattachment, whereas Igarashi (1981) reported a switch between reattachment and co-shedding. Igarashi (1981) called this type of flow regime bi-stable, and the terms 'bi-stable' and 'bi-stability' have since come to be associated with the reattachment/co-shedding switch in the literature concerning tandem cylinder flow. The co-existence of two flow regimes results in dual dominant frequencies, each with a distinct

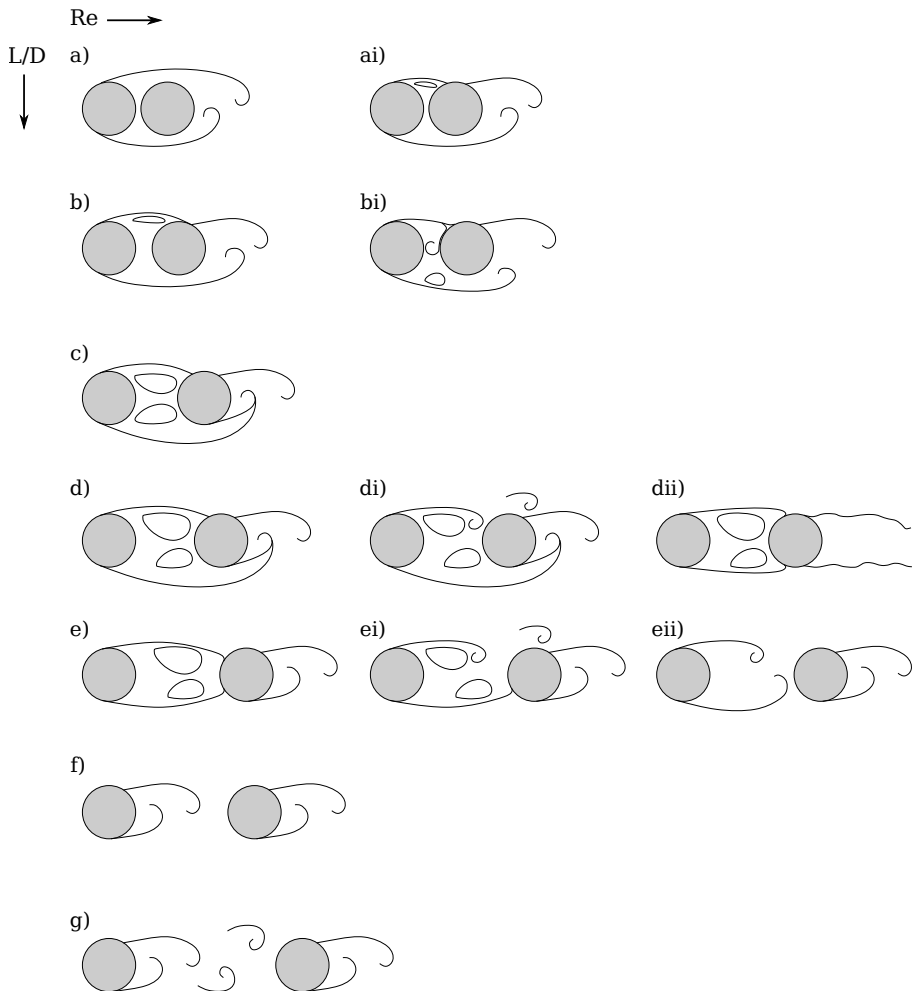


Figure 1.8: Some selected variations within the main tandem cylinder flow regimes. Due to sensitivity to Reynolds number and inflow conditions, as well as instability near transition between regimes, several types of flow regime may exist for the same gap ratio. For this reason specific  $L/D$  and  $Re$  ranges have been deliberately omitted from the figure.  $L/D$  grows from a) to g) and  $Re$  grows from left to right.



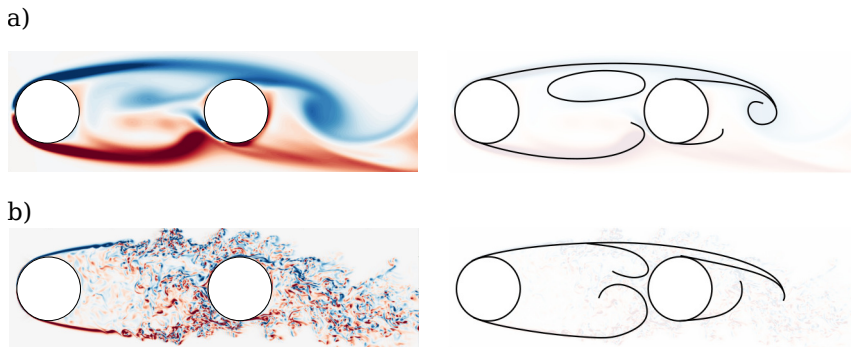


Figure 1.9: Alternating overshoot/reattachment for a)  $Re = 500$  and b)  $Re = 10^4$ . Flow field represented by spanwise vorticity,  $\omega_z$ , where red is positively signed and blue is negatively signed. Data from the present study.

peak in the velocity spectra.

The transition from reattachment to co-shedding is exceedingly intricate. Igarashi (1981) reports three different bi-stable regimes, called pattern D, E and E' in that study. Initially, the gap vortices become unstable, and shedding from the gap occurs intermittently (pattern D), similar to the illustration in figure 1.8di. Note that in a strict sense, this is not actual vortex shedding, because the opposite shear layer is not pulled across the gap centreline. It is more as though the vortex 'escapes' and is convected into the wake. True roll-up of the gap shear layers occurs in Igarashi (1981)'s regimes E and E'. The difference between these regimes is primarily the duration of the time intervals of co-shedding, which increases with increasing Reynolds number or gap ratio. The spacing between the spectral peaks that represent reattachment and vortex shedding from the gap increases with increasing Reynolds number. Kitagawa & Ohta (2008) found a different type of bi-stability. They reported a switch between symmetric reattachment, with a highly turbulent non-shedding wake, illustrated in figure 1.8dii, and a state where small vortices were shed from the gap shear layers, combined with a vortex street in the wake.

The spacing at which co-shedding starts is commonly called the 'critical spacing'  $L_c/D$ , and its value typically lies between 3.0 to 5.0 (Okajima, 1979; Igarashi, 1981; Xu & Zhou, 2004; Alam, 2014) From an engineering point of view, the transition from reattachment to co-shedding is important because it is accompanied by a discontinuous jump in the Strouhal number. Within the reattachment regime, the dominant frequency is comparably low, typically around 0.14-0.16 (Igarashi, 1981; Wu *et al.*, 1994; Lee & Basu, 1997; Kitagawa & Ohta, 2008), whereas within the co-shedding regime, the dominant frequency gradually approaches that of a single cylinder, as  $L/D$  increases. Moreover, the advent of co-shedding causes a jump in drag on the downstream cylinder. As long as there is reattachment, recirculation in the gap causes suction, which leads to a negative drag coefficient (i.e. thrust) for the downstream cylinder. When co-shedding starts, the drag on the downstream cylinder becomes positive. For that reason the critical spacing is sometimes referred to as the 'drag-inversion' spacing.

In every tandem cylinder flow regime, the Strouhal number of the two cylinders has been found to be practically identical (Xu & Zhou, 2004). Within the co-shedding regime, this is attributed to a 'lock-in' effect, i.e. that the vortices from the upstream cylinder

periodically impinge on the downstream cylinder, and this governs the frequency of the downstream cylinder vortex shedding (Alam & Zhou, 2007). It has been proposed that a similar mechanism is in play within the reattachment regime, so that the frequency of the alternating recirculating gap vortices impose their frequency on the downstream cylinder wake by forcing the boundary layer (Xu & Zhou, 2004). This is not agreed upon, however. It may also be the other way around; that the downstream cylinder vortices govern the frequency in the gap through pressure fluctuations.

The presence of the downstream cylinder affects the inception of the primary instability, as well as transition to turbulence in the wake. Mizushima & Suehiro (2005) found that the onset of the primary instability was delayed to  $Re = 100$  (compared to  $Re = 40$  for a single cylinder) for gap ratios  $L/d = 2$  and 4. A similar result was reported by Carmo *et al.* (2010b), where the critical Reynolds number for the primary instability was in the vicinity of 80 to 90 for gap ratios between  $L/D = 2$  and 5.

When it comes to transition to turbulence, the influence of the downstream cylinder depends on the gap ratio. Below the drag-inversion spacing, the downstream cylinder acts as a stabilizer, delaying the critical Reynolds number for transition. Within the co-shedding regime, however, it acts as a de-stabilizer, causing transition to occur at a lower Reynolds number than for a single cylinder (Papaioannou *et al.*, 2006).

The three-dimensional instability of the tandem cylinder wake was investigated by Carmo *et al.* (2010a,b), who found that below the drag-inversion spacing, the instability mechanisms differed somewhat from those of single cylinder wakes. Three different instabilities were discovered, called modes T1, T2 and T3. Keeping the mathematical details at an arms length, the main difference between the tandem and single cylinder instability modes, is the spanwise wavelength. T1 and T2, which were found for gap ratio ranges  $1.0 \leq L/D \leq 1.5$  and  $1.5 \leq L/D \leq 2.0$ , respectively, have a wavelength of approximately 3. T3, however, which exists from  $L/D \approx 2$  up to the drag-inversion spacing, has wavelengths between 4 and 10, depending on the Reynolds number. The practical consequence of this is that the minimum required spanwise length to capture the behavior of the tandem cylinder wake is different from a single cylinder wake (particularly important for numerical simulations). Except for laminar flow, the drag-inversion spacing cannot be correctly predicted by two-dimensional numerical simulations (Papaioannou *et al.*, 2006; Carmo *et al.*, 2010b). Conversely, the onset of turbulence is not correctly predicted unless the spanwise length is sufficient to encompass the wavelength of the three-dimensional instability.

### 1.3 Cylinders with axial curvature

When a cylinder is curved, the incoming flow is partially deflected along the cylinder axis, and this axial flow modifies the forces on the cylinder, as well as their characteristic frequencies. The inflow direction has a colossal impact on the wake of a curved cylinder. Directing the inflow to the inside of the curvature (concave configuration) or the outside of the curvature (convex configuration) produces completely different flows, as seen when comparing figures 1.10a and 1.10b. Of the two configurations, the convex wake is less intricate, and that is the primary reason for choosing this configuration for the study of curved tandem cylinders (because, as we shall see, a second cylinder certainly adds enough complexity to be getting on with). Apart from displaying it in all its considerable

splendor, concave curved cylinder flow will be left out from here on. For further reading on that subject, see Jiang *et al.* (2018, 2019), Shang *et al.* (2018) or Lee *et al.* (2020), where also oblique inflow directions are considered.

As shown in the flow sketch by Gallardo *et al.* (2014a), the incoming flow is deflected downwards along the front face of a convex curved cylinder, and there is significant axial flow in the near wake. There is a stagnation point on the back face of the cylinder. Above it, the flow is directed upwards (upwelling), and below it the flow is directed downwards (downdraft). The upwelling is considerably weaker than the downdraft, with a maximum velocity of about one fifth of the maximum downdraft velocity in the study of Gallardo *et al.* (2014a).

The wake of a convex curved cylinder appears similar to that of a straight cylinder. There is a von Kármán vortex street, as seen in figure 1.10b, and the Strouhal number is not very different from a straight cylinder at the same Reynolds number (Gallardo *et al.*, 2014a). However, the effect of the axial flow is significant, particularly in the lower wake. In this region, the downdraft is strong enough to interfere with the formation of the vortices. Communication between the shear layers is inhibited, similar to the effect of a near wake splitter plate (Roshko, 1954). In short, the downdraft blocks vortex shedding in the near wake. Instead, swirling vortices with a more streamwise orientation are formed and convected downstream, similar to a yawed straight cylinder with a free end (Ramberg, 1983). Actual vortex shedding is re-established further downstream in the wake (Gallardo *et al.*, 2014a), as shown in figure 1.10c.

The spanwise alignment of the vortices in the wake changes with the Reynolds number. Miliou *et al.* (2007) found that within the laminar regime, at  $Re = 100$ , the vortex cores were normal to the incoming flow, i.e. parallel with the upper part of the cylinder (parallel shedding mode). At  $Re = 500$ , the vortices had a slight angle in the plane of curvature (oblique shedding mode), similar to the vortices shown in figure 1.10b. Based on this finding, Miliou *et al.* (2007) suggested that the vortices would align increasingly with the axial curvature of the cylinder as the Reynolds number was increased. This hypothesis was confirmed by Gallardo *et al.* (2014a) for  $Re = 3900$ .

The swirling vortices in the lower wake are weaker than the vortices that form in the upper wake, where the cylinder axis is normal, or nearly normal, to the inflow direction. Because they are stronger, the upper wake vortices dominate the lower wake vortices, and govern their frequency. This causes the Strouhal number to be the same along the entire span. That finding is important because it disproves the so-called independence principle for the case of a curved cylinder. The independence principle is a useful simplification which allows one to ignore axial flow when computing the forces on an inclined straight cylinder or a cylinder with axial curvature. According to this principle, only the flow which is normal to the local cylinder cross section is significant, and this saves computing time and cost. The velocity vector is decomposed, and only the normal velocity is taken into consideration. It follows that there is a local Reynolds number for each cross section along the span, based on the local normal velocity. If this were the case in the real world, the local Reynolds number along a curved cylinder should gradually decrease along the span, as more of the flow is directed along the cylinder axis, and this should in turn lead to a *gradual change of the Strouhal number*. This is not the case for turbulent wakes behind convex curved cylinders, although Miliou *et al.* (2007) did see such behavior for laminar flow, at a Reynolds number of 100. However, to the comfort of engineers everywhere, Gallardo *et al.* (2014a) concluded that the independence principle is valid along the upper

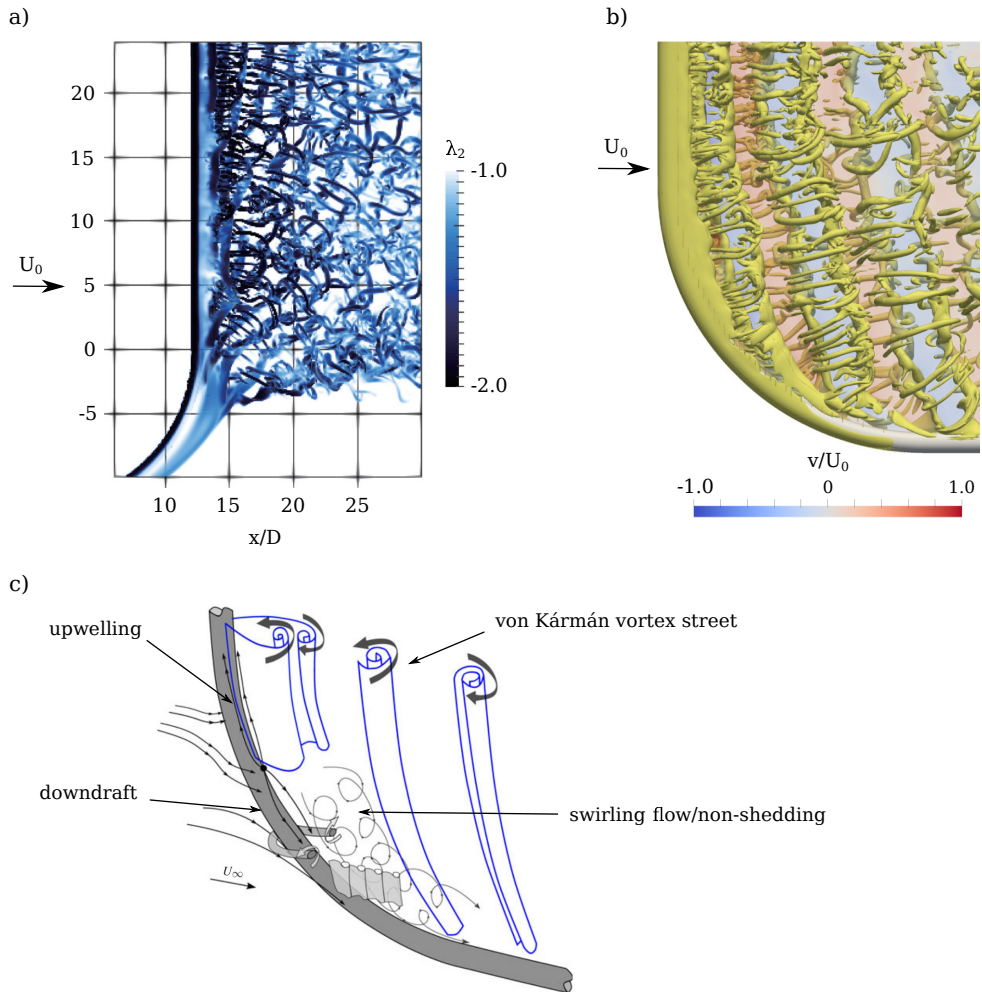


Figure 1.10: Flow around a single curved cylinder. a) Concave configuration at  $Re = 500$ , adapted from Jiang et al. (2018). b) Convex configuration at  $Re = 500$ , from a single curved cylinder validation study in the present work. c) Schematic of turbulent flow around a convex curved cylinder at  $Re = 3900$ , adapted from Gallardo et al. (2014a). All these cylinders consist of a quarter-ring with a radius of curvature of  $r_c = 12.5D$ . Moreover, straight extensions were added to both ends of the curved cylinder in all three studies, in order to lessen the influence from the computational domain boundaries.

half of the convex curved cylinder span where the axial velocity is comparably weak.

Because of the axial flow, the constraints at the cylinder ends exercise a strong influence on the flow field. Numerical studies of convex curved cylinders have often added a straight horizontal extension in order to avoid end effects, as well as aberrations caused by the computational boundary conditions (Miliou *et al.*, 2007; Gallardo *et al.*, 2014a; Lee *et al.*, 2020). Similarly, it was only when Gallardo *et al.* (2013) added a straight vertical extension to the top of their geometry that near wake upwelling was able to develop. Such a flow was not found in initial studies, such as that of Miliou *et al.* (2007), due to blockage from the top boundary. Restrictions such as blockage from tank walls or a free surface may significantly influence the flow in experimental studies (Shang *et al.*, 2018).

## 1.4 Computational method

The governing equations in the present study are the incompressible continuity equation and the Navier-Stokes equations:

$$\frac{\partial u_i}{\partial x_i} = 0, \quad (1.3)$$

$$\frac{\partial u_i}{\partial t} + u_j \frac{\partial u_i}{\partial x_j} = -\frac{1}{\rho} \frac{\partial P}{\partial x_i} + \frac{\partial}{\partial x_j} \left( \nu \left[ \frac{\partial u_i}{\partial x_j} + \frac{\partial u_j}{\partial x_i} \right] \right), i, j = 1, 2, 3 \quad (1.4)$$

The equations are solved by means of direct numerical simulations (DNS). In this context, 'direct' implies that there is no turbulence modeling or other simplifications, so that all length and time scales of the flow must be resolved. Provided that the grid resolution is sufficient, a DNS is the numerical equivalent of running a laboratory experiment, with the added benefit of not tripping over lab equipment (though, sadly, without the spiffing looking laser safety goggles).

All simulations herein have been carried out using the MGLET (Multi-Grid Large Eddy Turbulence) flow solver, a well-validated code which has been in use in the present research group for several years. Many studies have been carried out in close collaboration with Michael Manhart's group in Munich, Germany, where MGLET is developed. To mention just a few of these projects, the work over the past ten years has included investigations into the flow around convex curved cylinders and oscillatory flow around elliptic cylinders by Gallardo *et al.* (2013, 2014a,b, 2016), concave curved cylinders by Jiang *et al.* (2018, 2019), study of prolate spheroid wakes by Strandenes *et al.* (2019b,a), side-by-side and intersecting flat plates by Dadmarzi *et al.* (2016, 2017, 2018), and stepped cylinders and vortex dislocations by Tian *et al.* (2017, 2020, 2021, 2023b,a). Efforts to improve the grid generation methods, computational efficiency and scaling of MGLET were an integral part of the PhD work of Håkon Strandenes, and the reader is encouraged to peruse his thesis for details (Strandenes, 2019).

MGLET is based on a finite volume formulation of the incompressible Navier-Stokes equations. The equations are discretized on a three-dimensional staggered Cartesian grid, using linear interpolation of velocities, and a central-difference approximation of the velocity derivatives (Manhart, 2004). This method gives second-order accuracy in space. A third-order low-storage explicit Runge-Kutta time integration scheme is used for time stepping, and the Poisson equation is solved using an iterative, strongly implicit procedure (SIP) (Stone, 1968). Solid bodies are introduced through an immersed boundary method,

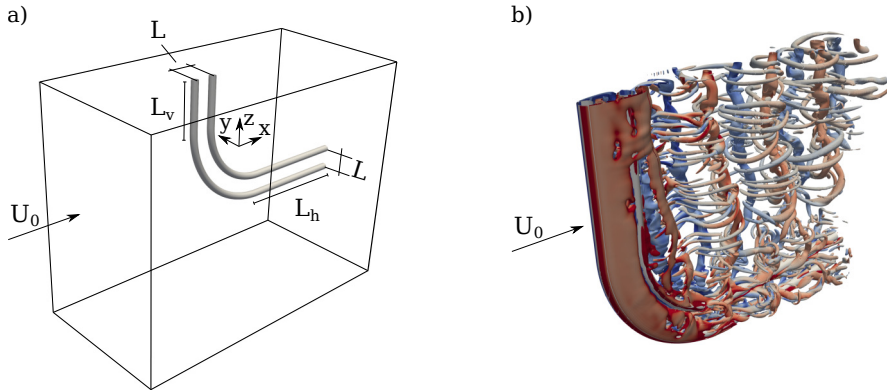


Figure 1.11: a) Curved convex tandem cylinders, computational geometry. b) Example of the resulting flow field at  $Re = 500$ .

where the boundary is discretized using either a ghost-cell approach (Peller *et al.*, 2006) or a cut-cell approach (Unglehrt *et al.*, 2022).

In order to compress a real-life SFT into a numerical model, a number of simplifications have been made. Firstly, the Reynolds number is considerably lower than for a full-size structure, in order to facilitate the use of DNS. The Bjørnafjord SFT, with an outer tunnel diameter of 15 meters would have had a Reynolds number in the order of  $10^6$  even for creeping current velocities. Secondly, the curvature of the cylinders is higher in order to compare with previous studies of single curved cylinders. Finally, all appendages (struts, support systems for pontoons, mooring lines etc.) have been removed, so that the cylinders are completely smooth. The gap ratio in the present study,  $L/D = 3$  is the same as it would have been for the Bjørnafjord SFT. The resulting geometry is illustrated in figure 1.11a, and figure 1.11b gives an example of what the instantaneous flow field might look like. Straight horizontal and vertical extensions were added to the curved cylinders, based on the experience of Gallardo *et al.* (2013). Details regarding computational aspects such as domain size, lengths of horizontal and vertical extensions ( $L_h$  and  $L_v$ ), boundary conditions, grid refinement, time-step etc. are given in each paper.

## 1.5 Outline of the present study

The present study is divided into two main parts: 1) straight tandem cylinders in the reattachment regime and 2) tandem cylinders with axial curvature. Part 1, which resulted in papers 1 and 2, delves into the fundamental physical processes that govern the reattachment regime. This forms a basis from which to explore the significantly more complex flow field of convex curved tandem cylinders, which is the topic of papers 3-5. In fact, paper 2 was motivated not only by our results from paper 1, but also by some of the new phenomena that arose in our work with curved tandem cylinders in the transitional Reynolds number range (i.e. papers 3 and 4). Thus, those investigations were carried out simultaneously; in tandem, if you will.

The papers that comprise this thesis are outlined in the following, and the results are summarized in section 2.1.

**Paper 1** Straight tandem cylinders within the reattachment regime are studied at a subcritical Reynolds number,  $Re = 10^4$  and a gap ratio of  $L/D = 3$ . The behavior of the gap shear layers and the interaction between the shear layers and the recirculating gap vortices are scrutinized, and the effect of transition to turbulence in the gap shear layers on the near wake is addressed. Comparison is made with a single cylinder at the same Reynolds number, and the results from that study are summarized in an appendix.

**Paper 2** The results from article 1 indicate that bi-stability may occur in cells along the cylinder span. This result is further investigated, though at a lower Reynolds number,  $Re = 500$ . The paper addresses the effect of three-dimensionality on the flow topology in the gap and wake, and discusses the mechanism behind cellular flow regime alterations.

**Paper 3** Curved convex tandem cylinders are investigated at  $Re = 500$ . The nominal gap ratio is  $L/D = 3$ , but the effective gap ratio varies along the span when the inflow is uniform. The primary object of the study is to determine the effect of curvature on the pressure, forces and Strouhal number. A first overview of the flow topology is given, and comparison is made with single convex curved cylinders.

**Paper 4** This paper builds on paper 3, continuing the investigation of curved convex tandem cylinders at  $Re = 500$ . The focus of the paper is the flow topology and the development of the vortices in the gap and wake; spanwise flow regime variations, vortex dislocations, parallel and oblique shedding modes and low-frequency variations are discussed. A parameter study on the required length of the straight vertical extension is presented in an appendix.

**Paper 5** The investigation of convex curved tandem cylinder is now extended to the subcritical Reynolds number regime, at  $Re = 3900$ . The main focus of the paper is the effect of transition to turbulence in the shear layer, and the interaction between the Kelvin-Helmholtz instability, the primary instability and the complex variation of tandem cylinder flow regimes along the span.

# Chapter 2

## Conclusions and outlook

### 2.1 Summary of the results

**Straight tandem cylinders in the reattachment regime:** Straight tandem cylinders at a gap ratio of  $L/D = 3.0$  were studied at Reynolds numbers 500 and  $10^4$ . The study at  $Re = 10^4$  is concerned primarily with the behavior of the shear layers and their interaction with the recirculating gap vortices and with the near-wake. Compared to a single cylinder, the influence of the downstream cylinder causes earlier separation on the upstream cylinder, and stabilizes the separation points as well as the gap shear layers. Transition to turbulence in the gap shear layer is delayed, because there are fewer eddies in the recirculation region that are strong enough to amplify the Kelvin-Helmholtz instability. On the other hand, the shear layers are given more time to develop after transition, so that shear layer vortex pairing is allowed to occur in the gap.

The above features are quite similar to flow around a circular cylinder with a splitter plate, but the flow differs from the splitter plate case because of the recirculating vortices. In the present case, these are alternating, with alternating overshoot/reattachment of the gap shear layers. We have seen that during the formation of the gap vortex, a jet-like flow will sometimes appear that traverses the gap and impacts the opposite shear layer. This amplifies the shear layer instability and enhances transition to turbulence. This phenomenon does not occur simultaneously along the span, but appears in distinct spanwise sections. Based on that observation, it is suggested that bi-stability may occur in spanwise cells. As the gap vortex grows, it eventually becomes big enough to directly interact with the opposite shear layer, which enhances the development of small-scale turbulence in the overshooting gap shear layer.

Transition to turbulence in the gap shear layers causes a highly turbulent inflow to the downstream cylinder. The downstream cylinder boundary layer and shear layers are continuously buffeted by small scale eddies from the upstream cylinder, which causes the separation points on the downstream cylinder to move backwards and the recirculation region to shorten. The overshooting gap shear layer lies outside of the shear layer of the downstream cylinder, and it is not necessarily completely entrained into the forming vortex. Some of the structures may pass over the vortex and continue into the wake.

The possibility of bi-stability occurring in spanwise cells was further investigated at  $Re = 500$ . Such cellular behavior is indeed found, along with the fascinating discovery



that the instability is asymmetric; vortices are repeatedly shed from a single gap shear layer for several periods, while the opposite gap shear layer reattaches. This asymmetry switches randomly between the gap shear layers.

The cellular behavior is closely related to the three-dimensional instability mode T3, which initiates in the gap. Mode T3 leads to a basic stable spanwise cell structure governed by the T3 wavelength. The spanwise length of the unstable cells varies approximately between  $0.3D$  and  $2.7D$ , but they seem to appear solely within the boundaries of the T3 basic cell structure. Moreover, the unstable cells may occur in the same spanwise location several vortex shedding cycles in a row, keeping approximately the same cell length. This is naturally intriguing because mode switches in tandem cylinder flow is assumed to be random processes. We believe that it is the entrainment of high-momentum fluid into the gap region during the first (random) occurrence of an unstable cell that leads to its recurrence in the subsequent cycles.

The long-term asymmetry in the gap intermittently becomes coherent for long spanwise sections, and this dramatically affects the amplitude of the drag on both cylinders. The lift is unaffected by this phenomenon. The mechanism behind the intermittent coherence is related to induced axial velocity when one or several unstable cells are triggered. The induced velocity may influence the velocity gradients at neighboring spanwise locations, and increase the spanwise vorticity at these locations through vortex stretching and tilting, which in turn triggers a new unstable cell.

**Convex curved tandem cylinders:** Convex curved tandem cylinders with a nominal gap ratio of  $L/D = 3.0$  were studied at  $Re = 500$  and  $3900$ . A defining feature of these flows is the spanwise variation of flow regimes, which occurs both owing to a spanwise variation of the effective gap ratio, and because of curvature-induced axial flow. At both Reynolds numbers, the vortex shedding switches intermittently between parallel and oblique shedding modes. Parallel shedding seems to be dominant for the transitional wake, while oblique shedding appears to be most common for the turbulent wake.

The oblique shedding mode is closely associated with spanwise vortex dislocations that occur by two main mechanisms: spanwise frequency and phase differences that arise from mode switches along the span, and shedding of gap vortices into (primarily) the lower wake. At  $Re = 500$ , the dislocations are almost exclusively restricted to the lower wake, whereas for  $Re = 3900$ , they occur along the entire height of the wake. This is likely because increasing the Reynolds number leads to transition between tandem cylinder regimes at lower gap ratios, i.e. higher up in the gap.

An important difference between  $Re = 500$  and  $3900$  is that for the transitional wake, the entire flow is dominated by a single Strouhal number, while in the turbulent case, three dominant frequencies are found. It appears that at  $Re = 500$ , the gap and wake flows are governed by the frequency of the upper wake vortices, in the same way as for single convex curved cylinders. The Strouhal number is almost exactly the same as that of the straight tandem cylinders at  $Re = 500$ , including the secondary frequencies that arise from bi-stability in the alternating overshoot/reattachment regime.

At  $Re = 3900$ , on the other hand, there is a gradual shift of the dominant frequency along the span. The three Strouhal numbers are associated with three different flow regimes: alternating overshoot/reattachment, symmetric reattachment and co-shedding. One of these flow modes is normally dominant along a given spanwise section, but a minimum of two modes co-exist along the majority of the span. In the region near the

transition from the curved cylinder part to the straight vertical extension, all three modes have equally high spectral energy, indicating multi-stability in this region. Only along the upper part of the straight vertical extension does alternating overshoot/reattachment dominate completely, but given that this is in itself a bi-stable regime at  $L/D = 3.0$ , there is no truly stable flow regime anywhere along the span.

For both  $Re = 500$  and  $3900$ , the velocity spectra in the gap and wake contain significant energy at low frequencies, which is associated with low-frequency variation of the vortex formation length in the lower gap. The low-frequency variation influences the drag and lift forces on the cylinders, for both Reynolds numbers. This may be of importance in some engineering applications. At  $Re = 500$ , an interesting effect of this variation is that higher up in the gap the asymmetric gap shedding mode, which is intermittent for straight tandem cylinders, becomes quasi-periodic with a period equivalent to some 14 vortex shedding cycles. Asymmetric gap shedding is found for  $Re = 3900$ , but owing to the co-existence of several modes at the same spanwise location, the distinct quasi-periodicity is lost.

The forces on the cylinders are affected by the axial velocity, as well as the Reynolds number. Drag on the upstream cylinder is largely comparable to straight tandem cylinders in the reattachment regime. For the downstream cylinder, the drag coefficient is negative at both Reynolds numbers, though its value is near zero at  $Re = 500$ . Drag on the downstream cylinder depends strongly on the spanwise extent of the reattachment region, since reattachment gives gap recirculation and hence a negative drag contribution. It should be noted that the length of the straight vertical extensions influence the spanwise size of the reattachment region. Lift on the downstream cylinder is, unsurprisingly, significantly stronger than on the upstream cylinder, albeit weaker than for straight tandem cylinders. Both cylinders are subjected to vertical forces. The vertical force on the upstream cylinder is positive, though lower than that on a single curved cylinder. On the downstream cylinder the vertical force is negative and of significantly smaller magnitude than that on the upstream cylinder. Moreover, the vertical force is weaker at  $Re = 3900$  than at  $Re = 500$ .

Being a subcritical Reynolds number, transition to turbulence occurs in the shear layers at  $Re = 3900$ . The shear layer transition region moves upstream in the gap with decreasing  $z/D$ , due to the gradual increase of the effective gap ratio, as well as the increase in axial velocity. There is also an upwards shift in the shear layer frequency  $f_{sl}$  in the upper curved gap, with a subsequent shift back to the original value of  $f_{sl}$  in the lower curved gap. The changes in the shear layer frequency occur approximately at the same spanwise locations as changes in the dominant shedding frequency. Moreover, the value of  $f_{sl}$  is always close to the value of the higher harmonics of the vortex shedding.

There is a complex system of interactions between the shear layer instability in both gap and wake, the primary instability and the axial flow, which is also connected to the low-frequency variation in the lower gap. The streamwise position of the transition region in the gap influences the vortex formation process in the wake through buffeting. Early transition to turbulence in the gap increases the effective turbulence intensity in the inflow to the downstream cylinder, which increases the fluid entrainment in the shear layers and may alter the vortex shedding frequency. The way  $f_{sl}$  seems to follow changes in  $St$ , as well as the fact it follows the higher harmonics of the vortex shedding frequency, seems to indicate that there may be direct feedback from the primary instability of the wake vortices to the shear layer instability in the gap. This means that small changes in  $St$

wrought by buffeting from the gap shear layers in turn influence the shear layer instability in the gap.

The position of the transition region is closely related to the downdraft region in the gap. When this region comes into contact with a shear layer, it may amplify the shear layer instability and hasten transition to turbulence. The strength and position of this downdraft region is governed by the vortex formation length in the lower gap, so that the low-frequency variation in this region actually indirectly influences transition to turbulence at locations rather far removed from the region itself.

Movement of the transition region in the gap shear layers is closely associated with flow mode switches, and we have seen that a mode switch at one spanwise location may trigger a switch at neighboring locations, since communication along the span may occur in both directions by means of the axial velocity.

## 2.2 Recommendations for further work

Our results for straight tandem cylinders show that although this field is considered to be well-explored, there are still phenomena that are not fully understood. The transitions between regimes are particularly challenging to characterize, as is the interaction between the gap and wake dynamics. This may be a fruitful field of research, although the sheer possible number of parameter combinations makes generalization challenging (and one runs the risk of plunging into Solaristics<sup>1</sup>).

It would be highly interesting, however, to explore the behavior of the three-dimensional instability in tandem cylinder flow at subcritical Reynolds numbers. While mode B has been observed in single cylinder wakes up to  $Re \approx 2.7 \times 10^5$  (Williamson, 1996*b*), there are no systematic studies, nor casual observations, of the three-dimensional instability of tandem cylinders beyond  $Re = 500$ . Stability analysis was not within the scope of the present study, but such methods might reveal if there are additional instabilities besides modes T1, T2 and T3. Results from well-resolved DNS and large-eddy simulations (LES) could also provide useful results, although the spanwise length requirements may make the simulations costly (the required spanwise length to capture a possible new three-dimensional instability is, naturally, unknown).

Something which has recently piqued the interest of the present author is the relationship between gap ratio, vortex formation length and shedding frequency for tandem cylinder below the drag-inversion spacing. For instance, is there a similar relation between formation length and vortex shedding frequency in tandem cylinder wakes as for single cylinders at subcritical Reynolds numbers? As of now, there is no study that systematically addresses this subject. Though there are an abundance of tandem cylinder studies within the subcritical regime (mostly experimental work), a quick review of the literature shows that formation length or recirculation length is rather seldom reported.

When it comes to curved tandem cylinders, it seems clear that the inflow direction will have a significant impact on the flow field. The present study was restricted to the convex configuration, but the concave configuration is likely to yield different and interesting results. Moreover, oblique flow in the crossflow plane would lead to a staggered, rather than tandem configuration. This type of flow has its own peculiarities (see Sumner (2010))

---

<sup>1</sup>The many-varied, random and non-repeatable variations of structures in the ocean on the planet Solaris was the source of an entire failed branch of research in Stanislaw Lem's famous novel (Lem, 1961).

that may be affected by axial curvature.

From an engineering perspective, the obvious way forward would be to increase the Reynolds number, first into the upper end of the subcritical regime, possibly using LES. Critical and supercritical Reynolds numbers would likely be more realistic for engineering purposes, and might be carried out experimentally or using different types of numerical methods with turbulence modeling. If the long-term gap asymmetry and the low-frequency variations we have found persist at higher Reynolds numbers, the resulting frequencies may be relevant for structure design purposes.

A parameter study of the effect of gap ratio, radius of curvature etc. could be fruitful. Moreover, the effect of oscillating inflow, stratification and shear currents, as well as free surface or wall proximity may be of interest. If we consider an SFT, all these parameters will be site-dependent, and there will surely be constraints that have not been mentioned herein.

Finally, the author feels compelled to note that the work herein was carried out under a lucky conjunction of events; within an engineering department, a research group was dedicated to the study of fundamental fluid mechanics, and given the time, resources and personnel to pursue complex long-term projects. One important prerequisite for these projects was the model for distributing computational resources, which, in short, awarded CPU hours based on scientific merit and publications. This allowed our group to carry out high-fidelity simulations, which might otherwise have been deemed too costly. For instance, the final study presented herein, convex curved tandem cylinders at  $Re = 3900$ , can boast a total of 3.9 billion grid cells, consuming nearly 10 million CPU hours.

The combined effort of the researchers and studies mentioned in section 1.4 has helped advance the field of bluff body fluid mechanics, as well as the computational techniques. The overwhelming majority of the studies within this research group have been carried out by means of DNS, which gives both an overview and a detailed insight into these complex fundamental flows that cannot be obtained by other methods (at least not by one single method). DNS data is also well-suited for validation of experimental results and numerical studies at higher Reynolds numbers, where modeling is required (see for example Strandenes *et al.* (2015), where DNS, LES and particle image velocimetry results are compared). Ultimately, while fundamental in nature, these cases provide insight that can improve our understanding of engineering applications. One can only hope that this valuable research will be allowed to continue in the future.



# References

- AASLAND, T. E., EIDEM, M. E., FAGGIANO, B., 'T HART, M., IOVANE, G., JACKSON, G., LEE, H. K., MINORETTI, A., PALUDAN-MÜLLER, C., SAFIER, E., SKORPA, L., VODOLAZKIN, M., XIANG, X., XIANG, Y. & ØSTLID, H. 2023 An owner's guide to submerged floating tunnels. *Tech. Rep.*. International Tunneling Association - ITA Working Group 11 for Immersed and Floating Tunnels.
- ALAM, M. M. 2014 The aerodynamics of a cylinder submerged in the wake of another. *J. Fluids Struct.* **51**, 393–400.
- ALAM, M. M. & ZHOU, Y. 2007 Phase-lag between vortex shedding from two tandem bluff bodies. *J. Fluids Struct.* **23**, 339–347.
- APELT, C. J. & SZEWCZYK, A. A 1973 The effects of wake splitter plates on flow past a circular cylinder in the range  $10^4 < R < 5 \times 10^4$ . *J. Fluid Mech.* **61** (1), 187–198.
- BÉNARD, H. 1908 Formation of centers of gyration in liquids at the back of an object in motion. *Comptes Rendus Hebdomadaires des Seances de l'Academie des Sciences* **147**, 839–842.
- CAO, Y. & TAMURA, T. 2020 Low-frequency unsteadiness in the flow around a square cylinder with critical angle of  $14^\circ$  at the Reynolds number of  $2.2 \times 10^4$ . *J. Fluids Struct.* **97**, 103087, 1–15.
- CARDELL, G. S. 1993 Flow past a circular cylinder with a permeable wake splitter plate. PhD thesis, California Institute of Technology.
- CARMO, B., MENEGHINI, J. & SHERWIN, S. 2010a Secondary instabilities in the flow around two circular cylinders. *J. Fluid Mech.* **644**, 395–431.
- CARMO, B. S., MENEGHINI, J. R. & SHERWIN, S. J. 2010b Possible states in the flow around two circular cylinders in tandem with separations in the vicinity of the drag inversion spacing. *Phys. Fluids* **22**, 054101, 1–7.
- DADMARZI, F. H., NARASIMHAMURTHY, V. D., ANDERSSON, H. I. & PETTERSEN, B. 2016 Turbulent wake behind two intersecting flat plates. *Int. J. Heat Fluid Flow* **62** (B), 482–498.
- DADMARZI, F. H., NARASIMHAMURTHY, V. D., ANDERSSON, H. I. & PETTERSEN, B. 2017 Turbulent wake behind a t-shaped plate: Comparison with a cross-shaped plate. *Int. J. Heat Fluid Flow* **65**, 127–140.

- DADMARZI, F. H., NARASIMHAMURTHY, V. D., ANDERSSON, H. I. & PETTERSEN, B. 2018 Turbulent wake behind side-by-side flat plates: computational study of interference effects. *J. Fluid Mech.* **855**, 1040–1073.
- EIDEM, M. E., MINORETTI, A., XIANG, XU. & AASLAND, T. E. 2018 The submerged floating tube bridge as an alternative for a crossing: pros and cons. In *IABSE Symposium: Tomorrow's Megastructures, Nantes, France, 19-21 September 2018*. International Association for Bridge and Structural Engineering (IABSE).
- GALLARDO, J.P., ANDERSSON, H. I. & PETTERSEN, B. 2014a Turbulent wake behind a curved circular cylinder. *J. Fluid Mech.* **742**, 192–229.
- GALLARDO, J.P., PETTERSEN, B. & ANDERSSON, H. I. 2013 Effect of free-slip boundary conditions on the flow around a curved circular cylinder. *Computers and Fluids* **86**, 389–394.
- GALLARDO, J.P., PETTERSEN, B. & ANDERSSON, H. I. 2014b Coherence and Reynolds stresses in turbulent wake behind a curved circular cylinder. *J. Turbulence* **15**, 883–904.
- GALLARDO, J. P., ANDERSSON, H. I. & PETTERSEN, B. 2016 Three-dimensional instabilities in oscillatory flow past elliptic cylinders. *J. Fluid Mech.* **798**, 371–397.
- GERRARD, J. H. 1966 The mechanics of the formation region of vortices behind bluff bodies. *J. Fluid Mech* **25** (2), 401–413.
- HENDERSON, R. D. 1997 Nonlinear dynamics and pattern formation in turbulent wake transition. *J. Fluid Mech.* **352**, 65–112.
- HUERRE, P. & MONKEWITZ, P. A. 1985 Absolute and convective instabilities in free shear layers. *J. Fluid Mech.* **159**, 151–168.
- IGARASHI, T. 1981 Characteristics of the flow around two circular cylinders arranged in tandem (1st report). *Bull. JSME* **24** (188), 323–330.
- JIANG, F., PETTERSEN, B. & ANDERSSON, H. I. 2019 Turbulent wake behind a concave curved cylinder. *J. Fluid Mech.* **878**, 663–699.
- JIANG, F., PETTERSEN, B., ANDERSSON, H. I., KIM, J. & KIM, S. 2018 Wake behind a concave curved cylinder. *Phys. Rev. Fluids* **3**, 094804.
- JIANG, H., CHENG, L., DRAPER, S., AN, H. & TONG, F. 2016 Three-dimensional direct numerical simulation of wake transitions of a circular cylinder. *J- Fluid Mech.* **801**, 353–391.
- KÁRMÁN, T. VON 1912 Resistance to motion of body in fluid. *Nachrichten von der Koniglicher Gesellschaft der Wissenschaften zu Gottingen, Mathematischen-Physikalische Klasse* **5**, 547–556.
- KITAGAWA, T. & OHTA, H. 2008 Numerical investigation on flow around circular cylinders in tandem arrangement at a subcritical Reynolds number. *J. Fluids Struct.* **24**, 680–699.

- LEE, S., PAIK, K.-J. & SRINIL, N. 2020 Wake dynamics of a 3D curved cylinder in oblique flows. *Int. J. Naval Arch. Ocean Eng.* **12**, 501–517.
- LEE, T. & BASU, S. 1997 Nonintrusive measurements of the boundary layer developing on a single and two cylinders. *Exp. Fluids* **23**, 187–192.
- LEHMKUHL, O., RODRIGUES, I., BORRELL, R. & OLIVA, A. 2013 Low-frequency unsteadiness in the vortex formation region of a circular cylinder. *Phys. Fluids* **25**, 085109.
- LEM, S. 1961 *Solaris*. Wydawnictwo Ministerstwa Obrony Narodowej.
- LIN, J.-C., YANG, Y. & ROCKWELL, D. 2002 Flow past two cylinders in tandem: Instantaneous and averaged flow structure. *J. Fluids Struct.* **16** (8), 1059–1071.
- LJUNGKRONA, L., NORBERG, CH. & SUNDEN, B. 1991 Free-stream turbulence and tube spacing effect on surface pressure fluctuations for two tubes in an in-line arrangement. *J. Fluid Struct.* **5**, 701–727.
- LORITE-DÍEZ, M. & JIMÉNEZ-GONZÁLES, J. I. 2020 Description of the transitional wake behind a strongly streamwise rotating sphere. *J. Fluid Mech.* **896**, A18.
- MANHART, M. 2004 A zonal grid algorithm for DNS of turbulent boundary layers. *Computers and Fluids* **33**, 435–461.
- MIAU, J. J., WANG, J. T., CHOU, J. H. & WEI, C. Y. 1999 Characteristics of low-frequency variations embedded in vortex-shedding process. *J. Fluids Struct.* **13**, 339–359.
- MILIOU, A., DE VECCHI, A., SHERWIN, S. J. & GRAHAM, J. M. R. 2007 Wake dynamics of external flow past a curved cylinder with free stream aligned with the plane of curvature. *J. Fluid Mech.* **592**, 89–115.
- MIZUSHIMA, J. & SUEHIRO, N. 2005 Instability and transition of flow past two tandem circular cylinders. *Phys. Fluids* **17**, 104107.
- OKAJIMA, A. 1979 Flows around two tandem circular cylinders at very high Reynolds numbers. *Bull. JSME* **22**, 504–511.
- PAPAIOANNOU, G., YUE, D. K. P., TRIANTAFYLLOU, M. & KARNIADAKIS, G. E. 2006 Three-dimensionality effects in flow around two tandem cylinders. *J. Fluid Mech.* **558**, 387–413.
- PELLER, N., LE DUC, A., TREMBLAY, T. & MANHART, M. 2006 High-order stable interpolations for immersed boundary methods. *Int. J. Num. Meth. Fluids* **53**, 1175–1193.
- PRASAD, A. & WILLIAMSON, C. H. K. 1997 The instability of the shear layer separating from a bluff body. *J. Fluid Mech.* **333**, 375–402.
- RAI, M. M. 2010 A computational investigation of the instability of the detached shear layers in the wake of a circular cylinder. *J. Fluid Mech.* **659**, 375–404.



- RAMBERG, S. E. 1983 The effects of yaw and finite length upon the vortex wakes of stationary and vibrating circular cylinders. *J. Fluid Mech.* **128**, 81–107.
- RASTAN, M. R. & ALAM, M. 2021 Transition of wake flows past two circular or square cylinders in tandem. *Phys. Fluids* **33**, 081705.
- ROSHKO, A. 1954 On the drag and shedding frequency of two-dimensional bluff bodies. Technical note 3169. NACA.
- SCHEWE, G. 1983 On the force fluctuations acting on a circular cylinder in crossflow from subcritical up to transcritical Reynolds numbers. *J. Fluids Mech.* **133**, 265–285.
- SCHMALTZ, J. 2015 NASA/GSFC/Jeff Schmaltz/MODIS land rapid response team: Cloud vortices over Heard Island. <https://www.flickr.com/photos/gsfcr/22531636120/>.
- SHANG, J. K., STONE, H. A. & SMITS, A. J. 2018 Flow past finite cylinders of constant curvature. *J. Fluid Mech.* **837**, 896–915.
- STONE, H. 1968 Iterative solution of implicit approximations of multidimensional partial differential equations. *SIAM J. Num. Anal.* **5** (3), 530–558.
- STRANDENES, H. 2019 Turbulent flow simulations at higher Reynolds numbers. PhD thesis, Department of Marine Technology, NTNU.
- STRANDENES, H., F., JIANG., PETERSEN, B. & ANDERSSON, H. 2019a Near-wake of an inclined 6:1 spheroid at Reynolds number 4000. *AAIA J.* **57** (4).
- STRANDENES, H., GALLARDO, J. P., VISSCHER, J., PETERSEN, B., ANDERSSON, H. I., LIE, H. & BAARHOLM 2015 A comparative study between DNS, LES and PIV for a marine riser with fairings. In *ASME 2015 34th International Conference on Ocean, Offshore and Arctic Engineering*, , vol. 2, p. V002T08A050. American Society of mechanical engineers ASME.
- STRANDENES, H., JIANG, F., PETERSEN, B. & ANDERSSON, H. I. 2019b Low-frequency oscillations in flow past an inclined prolate spheroid. *Int. J. Heat Fluid Flow* **78**, 108421.
- SUMER, B. M. & FREDSSØE, J. 2006 *Hydrodynamics Around Cylindrical Structures, Revised Edition*. World Scientific.
- SUMNER, D. 2010 Two circular cylinders in cross-flow: A review. *J. Fluids Struct.* **26**, 849–899.
- TIAN, C., F., JIANG, PETERSEN, B. & ANDERSSON, H. I. 2017 Antisymmetric vortex interactions in the wake behind a step cylinder. *Phys. Fluids* **29** (10), 101704.
- TIAN, C., JIANG, F., PETERSEN, B. & ANDERSSON, H. I. 2020 Vortex dislocation mechanisms in the near wake of a step cylinder. *J. Fluid Mech.* **891**, A24.
- TIAN, C., JIANG, F., PETERSEN, B. & ANDERSSON, H. I. 2021 Vortex system around a step cylinder in a turbulent flow field. *Phys. Fluids* **33** (4), 045112.

- TIAN, C., ZHU, J. & HOLMEDAL, L. E. 2023*a* Coexistence of natural and forced vortex dislocations in step cylinder flow. *Phys. Fluids* **35**, 094111.
- TIAN, C., ZHU, J., HOLMEDAL, L. E., ANDERSSON, H. I., JIANG, F. & PETTERSEN, B. 2023*b* How vortex dynamics affects the structural load in step cylinder flow. *J. Fluid Mech.* **972**, A10.
- TSUTSUI, T. 2012 Experimental study on the instantaneous fluid force acting on two circular cylinders closely arranged in tandem. *J. Wind Eng. Ind. Aerodyn.* **109**, 46–54.
- UNGLEHRT, L., JENSSEN, U., KURZ, F., SCHANDERL, W., KREUZINGER, J., SCHWERTFIRM, F. & MANHART, M. 2022 Large-eddy simulation of the flow inside a scour hole around a circular cylinder using a cut cell immersed boundary method. *Flow Turb. Comb.* **109**, 893–929.
- WANG, P., ZHOU, Q., ALAM, M. M., YANG, Y. & LI, M. 2022 Effects of streamwise gust amplitude on the flow around and forces on two tandem circular cylinders. *Ocean Eng.* **261**, 112040.
- WILLIAMSON, C. H. K. 1989 Oblique and parallel modes of vortex shedding in the wake of a circular cylinder at low Reynolds numbers. *J. Fluid Mech.* **206**, 579–627.
- WILLIAMSON, C. H. K. 1996*a* Three-dimensional wake transition. *J. Fluid Mech.* **328**, 345–407.
- WILLIAMSON, C. H. K. 1996*b* Vortex dynamics in the cylinder wake. *Annu. Rev. Fluid Mech.* **28**, 477–539.
- WU, J., WELSH, L. W., WELCH, M. C., SHERIDAN, J. & WALKER, G. J. 1994 Spanwise wake structure of a circular cylinder and two circular cylinders in tandem. *Exp. Thermal Fluid Sci.* **9**, 299–308.
- XU, G. & ZHOU, Y. 2004 Strouhal numbers in the wake of two inline cylinders. *Exp. Fluids* **37**, 248–256.
- ZDRAVKOVICH, M. M. 1987 The effect of interference between circular cylinders in cross flow. *J. Fluids Struct.* **1**, 239–261.
- ZDRAVKOVICH, M. M. 1997*a* *Flow Around Circular Cylinders Vol 1: Fundamentals*, chap. 4, pp. 79–93. Oxford Science Publications.
- ZDRAVKOVICH, M. M. 1997*b* *Flow around circular cylinders vol 1: Fundamentals*, chap. 5.3.7, pp. 120–123. Great Clarendon Street, Oxford: Oxford University Press.
- ZHOU, Q., ALAM, M. M., CAO, S., LIAO, H. & LI, M. 2019 Numerical study of wake and aerodynamic forces on two tandem circular cylinders at Re 1000. *Phys. Fluids* **31**, 045103.
- ZHOU, Y. & YIU, M. 2006 Flow structure, momentum and heat transport in a two-tandem-cylinder wake. *J. Fluid Mech.* **548**, 17–48.



## Chapter 3

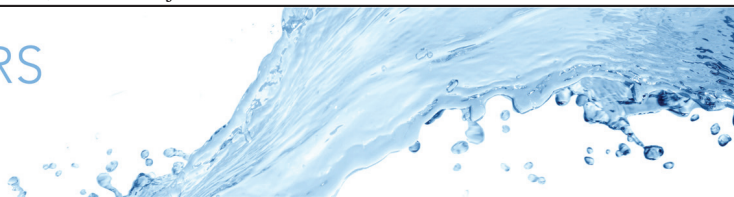
# Straight tandem cylinders in the reattachment regime



### 3.1 Paper 1. Revisiting the reattachment regime: a closer look at tandem cylinder flow at $Re = 10\,000$

Aasland, T. E., Pettersen, B., Andersson, H. I. & Jiang, F. 2022 Revisiting the reattachment regime: a closer look at tandem cylinder flow at  $Re = 10\,000$ . *Journal of Fluid Mechanics*; **953**, A18. <https://doi.org/10.1017/jfm.2022.960>





## Revisiting the reattachment regime: a closer look at tandem cylinder flow at $Re = 10\,000$

Tale E. Aasland<sup>1,†</sup>, Bjørnar Pettersen<sup>1</sup>, Helge I. Andersson<sup>2</sup> and Fengjian Jiang<sup>3</sup>

<sup>1</sup>Department of Marine Technology, Norwegian University of Science and Technology, NO-7491 Trondheim, Norway

<sup>2</sup>Department of Energy and Process Engineering, Norwegian University of Science and Technology, NO-7491 Trondheim, Norway

<sup>3</sup>SINTEF Ocean, NO-7052 Trondheim, Norway

(Received 30 March 2022; revised 6 September 2022; accepted 13 November 2022)

Tandem cylinder flow comprises several different flow regimes. Within the reattachment regime, the development of the gap shear layers is of utmost importance to the flow, but has received little attention so far. Through direct numerical simulations at  $Re = 10^4$ , for a gap ratio of 3.0, we have discovered that the shear layers are significantly altered with respect to a single cylinder. These differences include early onset of separation, crossflow stabilising, delayed transition to turbulence and little meandering of the transition region. Vortex pairing in the gap shear layers is reported for the first time. The interaction between the recirculating gap flow and the shear layers was investigated. Asymmetrical, large-scale gap vortices influence the position of transition to turbulence through direct contact and through secondary flows. The occurrence of transition in the gap shear layers has consequences for both the reattachment mechanism and the development of the downstream cylinder wake. The reattachment points are unsteady with large amplitude fluctuations on a fine time scale. Reattachment is seen to be a combination of impingement and modification of the upstream shear layers, which causes a double shear layer in the downstream cylinder near-wake. Buffeting by and interaction with the gap shear layers likely cause transition to turbulence in the downstream cylinder boundary layer. This leads to significant changes in the wake topology, compared with a single-cylinder wake.

**Key words:** shear layer turbulence, vortex dynamics, vortex shedding

† Email address for correspondence: [tale.e.aasland@ntnu.no](mailto:tale.e.aasland@ntnu.no)



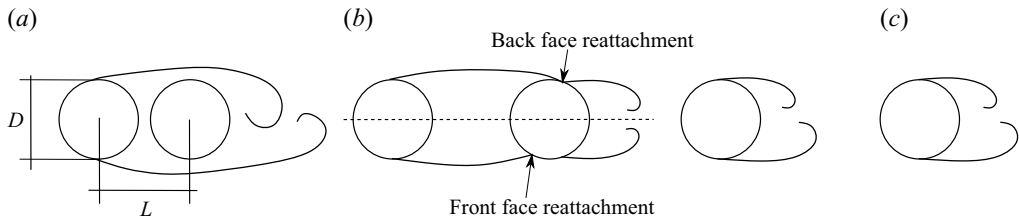


Figure 1. Schematic overview of the main tandem cylinder flow regimes. According to classification by Zdravkovich (1987) the regimes are found within the following gap ratio ranges: (a) overshoot/no reattachment  $1.0 \lesssim L/D \lesssim 1.2\text{--}1.8$ ; (b) reattachment  $1.2\text{--}1.8 \lesssim L/D \lesssim 3.4\text{--}3.8$ ; and (c) co-shedding  $3.4\text{--}3.8 \lesssim L/D$ . Reattachment of the upstream cylinder shear layers can occur either on the front face (upstream side) or on the back face (downstream side) of the downstream cylinder, depending on the gap ratio.

## 1. Introduction

Flow around tandem cylinders represents a basic configuration of flow interference and has been widely studied. Apart from its obvious engineering importance, it encompasses several aspects of fundamental flow physics, such as bluff body separation, shear layer reattachment and the interaction between multiple bodies and their shedding systems.

The flow is governed by the Reynolds number,  $Re = U_0 D / \nu$  and the separation between the cylinders, normally denoted the gap ratio  $L/D$ . Here,  $U_0$  is the inflow velocity,  $D$  is the cylinder diameter (for tandem cylinders of equal diameter),  $\nu$  the kinematic viscosity and  $L$  is defined as the centre-to-centre distance between the cylinders. Roughly, there are three fundamental flow regimes for tandem cylinders, as shown in figure 1: (a) no reattachment, commonly called overshoot, where the shear layers from the upstream cylinder bypass the downstream cylinder to roll up in the wake; (b) reattachment, where the shear layers from the upstream cylinder reattach onto the downstream cylinder and shedding of large-scale vortices takes place from the downstream cylinder; and (c) co-shedding, where large-scale vortices are shed from both cylinders.

In this study, we deal with tandem cylinders within the reattachment regime, and therefore a more detailed introduction is given of this particular regime, at the expense of the other two. However, thorough reviews of flow around two cylinders are given by Sumner (2010) and Zhou & Alam (2016), which include not only tandem cylinders, but also side-by-side and staggered configurations.

### 1.1. Tandem cylinders in the reattachment regime

Because the shear layers are very sensitive to the inflow conditions, the reattachment regime is found for a wide variety of combinations of  $Re$  and gap ratio. The nature of reattachment changes with the gap ratio, from alternating, through permanent to intermittent reattachment as the gap is increased (Zdravkovich 1987).

When there is stable alternating reattachment, one shear layer overshoots the downstream cylinder and rolls up, whereas the other reattaches. This regime is seen in the flow visualisations by Ishigai, Nishikawa & Cho (1972).

The gap ratio at which co-shedding commences is traditionally called the critical spacing,  $L_c/D$ . However, the change from one flow regime to the next is strongly  $Re$  dependent, so this spacing varies. Both an increase in  $Re$  (Xu & Zhou 2004) and the introduction of free-stream turbulence (FST) (Ljungkrona, Norberg & Sunden 1991) work to promote transition between regimes at lower gap ratios. The critical spacing typically lies between 3.0 and 5.0 (Okajima 1979; Igarashi 1981; Xu & Zhou 2004; Alam 2014),

which represents an upwards extension of Zdravkovich's (1987) initial classification of the reattachment regime. It is a testament to the  $Re$  sensitivity of tandem cylinders that Wang, Alam & Zhou (2018), did not see overshoot flow for  $Re = 4.27 \times 10^4$ , even for  $L/D = 0.5$ , when the cylinders touch.

Near the critical spacing, bi-stable flow is found. Here, the flow intermittently jumps between reattachment and co-shedding, and there are two distinct Strouhal numbers ( $St = f_v D/U_0$ , where  $f_v$  is the large-scale shedding frequency) (Igarashi 1981; Xu & Zhou 2004).

The reattachment point moves from the back face to the front face of the downstream cylinder as the gap ratio is increased, which results in a change of the flow interactions in the gap. Xu & Zhou (2004) proposed that the reattachment regime should be subdivided accordingly. In their proposed categories, the reattachment regime is divided into  $2 \leq L/D \leq 3$  where there is a gradual transition from stable overshoot to stable reattachment on the downstream cylinder back face, and  $3 \leq L/D \leq 5$  where there is transition from stable reattachment on the downstream cylinder front face to co-shedding.

The location of the reattachment point can significantly alter the wake structure. Zhou & Yiu (2006) found that reattachment on the back face corresponded with weak vortices with a slow decay rate and less vigorous interactions, compared with the overshoot regime. As the reattachment point moves towards the front face, the boundary layer on the downstream cylinder is given more time to develop, which enhances the vortex strength. Even so, the vortices remained weaker than in the overshoot regime, in which the strength was comparable to that of a single cylinder.

Though there is no vortex shedding from the upstream cylinder within the stable reattachment regime, there is recirculation in the gap. Igarashi (1981) describes non-shedding vortices (dubbed quasi-stationary by the author) in the gap for a  $Re$  range of  $8.7 \times 10^3 \leq Re \leq 5.2 \times 10^4$ , at gap ratios between 2 and 3.1. 'Quasi-stationary' and 'quasi-steady' are used interchangeably about the gap vortices in the literature, and taken to mean the same thing, namely that the vortices develop to somewhat in time, but remain essentially in the same location due to lack of shedding. The fact that they may have some degree of periodicity makes the term 'quasi-steady' counter-intuitive to some, and for this reason they will simply be referred to as gap vortices herein. Symmetrical and/or asymmetrical gap vortices were observed by, among others, Lin, Yang & Rockwell (2002), Wang *et al.* (2018) and Zhou *et al.* (2019).

Within the reattachment regime, the development of the shear layers is of utmost importance, but has received relatively little attention. Xu & Zhou (2004) reported a measurement of the shear layer frequency. However, the aim of their study was to characterise a broad range of tandem cylinder regimes, rather than conducting a detailed study of the shear layers. Lin *et al.* (2002) discussed the development of the gap shear layers, though primarily with respect to the onset of vortex shedding in the gap. They comment that increased entrainment demands with increasing  $Re$  should lead to a reduction of the critical spacing, and discuss the buffet loading from the gap shear layers as a function of the gap ratio.

## 1.2. Circular cylinder shear layers at subcritical Reynolds numbers

For circular cylinders in the approximate region  $1000 \leq Re \leq 200\,000$  (Williamson 1996), called the subcritical regime, transition to turbulence initiates in the shear layers. It is triggered by the Kelvin-Helmholtz (K-H) instability, starting out as oscillations of the shear layer which then roll up into discrete vortices when  $Re$  is increased. The shear layer

instability has its own distinct frequency,  $f_{sl}$ , which was first discovered by Bloor (1964), in range  $1300 \leq Re \leq 19\,000$ . Above this range, transition occurred directly after separation.

### 1.2.1. Intermittency

When measuring in a fixed point in the near-wake of a single cylinder, the shear layer instability appears intermittent, manifesting itself in the form of random so-called packets of velocity fluctuations. Prasad & Williamson (1997) found that intermittency occurs because the shear layer transition region exhibits random streamwise motion. Thus, the velocity fluctuations correspond to a shortening of the stable shear layer. This had already been observed visually, through particle image velocimetry (PIV), by Chyu & Rockwell (1996a). Prasad & Williamson (1997) suggested that the cause of the motion was temporal changes in the near-wake three-dimensional structures. An intermittency factor was defined, given as the frequency of occurrence of the velocity fluctuation packets in a fixed point.

The shear layer develops by a convective instability mechanism, meaning that disturbances are transported downstream and amplified. This implies that probes further downstream in the shear layer will experience more and higher-amplitude fluctuations than probes closer to the cylinder. Moreover, the transition region travels upstream towards the separation point as the  $Re$  increases, which also increases the fluctuations seen by a probe in the near-wake. Prasad & Williamson's (1997) findings correspond well with this, showing that the intermittency factor and the amplitude of the fluctuations increased with increasing  $Re$ , as well as when the measurement point was moved downstream. The meandering of the transition region was confirmed by flow visualisations.

Rai (2010) suggested that though intermittency in the measured time trace was indeed accompanied by a movement of the transition region, its cause was not sufficiently explained by Prasad & Williamson's (1997) hypothesis. The root cause was found to be strengthening of the shear layer vortices via vortex stretching, which, in turn, was caused by interaction between the shear layer and the vortices in the recirculation zone. These vortices hail from earlier breakdown events. When they are convected back upstream, some interact with the shear layer, essentially giving it a push or pull in the crossflow direction. The resulting crossflow dislocations serve to amplify the shear layer instability and hasten transition. Weaker recirculation vortices result in smaller amplitude intermittency, a finding which is pertinent to flow in the gap region of tandem cylinders.

### 1.2.2. Vortex pairing

Vortex pairing, a phenomenon where adjacent vortices interact by rolling around each other and finally combine into a single structure, is widely observed in mixing layers. Pairing was observed for ring vortices in a round jet by Becker & Massaro (1968), who noted that the frequency of the coalesced structure was half of that of the initial smaller structures. It follows that vortex pairing is detectable in the frequency spectrum as a peak around one half of the main peak.

The existence of shear layer vortex pairing in bluff body wakes was disputed for a long time. For the case of a circular cylinder, several early studies indicated that the von Kármán vortex shedding inhibits pairing (Unal & Rockwell 1988a), and that either external forcing (Peterka & Richardson 1969; Chyu & Rockwell 1996b) or von Kármán vortex suppression by a splitter plate (Unal & Rockwell 1988b) is needed to obtain it. However, pairing has since been observed in flow visualisations for the subcritical and transitional  $Re$  regimes (Law & Ko 2001; Lo & Ko 2001), without the use of forcing or large-scale vortex

suppression, and several studies have detected the presence of the subharmonic in the spectra (Cardell 1993; Ahmed & Wagner 2003; Rajagopalan & Antonia 2005; Khabbouchi *et al.* 2014).

Both Cardell (1993) and Rajagopalan & Antonia (2005) made observations that for uninhibited flow, the subharmonic was strengthened as  $Re$  was increased. Cardell (1993) argued that for low  $Re$  the shear layer instability does not develop sufficiently for the subharmonic to be detected before the shear layer vortices are swallowed by the von Kármán vortices. This could be part of the explanation as to why vortex pairing has not been observed in some studies. For instance, Unal & Rockwell's (1988a) highest  $Re$  was 5500, which is significantly lower than the threshold  $Re$  for the subharmonic found by Cardell (1993).

The intermittency phenomenon may shed some light onto why vortex pairing is hard to observe in the velocity spectra for low  $Re$ . In the cases where the recirculation vortices are strong enough to trigger early transition, with the corresponding shortening of the stable shear layer, the shear layer has more time to develop before it is entrained in the von Kármán vortex formation. This leads to enhanced pairing. Conversely, the pairing process is cut short by the primary vortices when early transition is not triggered. As the intermittency factor is lower at lower  $Re$ , capturing vortex pairing through measurement in a fixed point becomes correspondingly harder.

### 1.3. Motivation for the present investigation

Although tandem cylinders have been researched extensively, the main effort thus far has focused on the relation between gap ratio and  $Re$ , the effect on  $St$ , forces and the phase-lag between the forces on upstream and downstream cylinder, as well as the effect of vortex-induced vibrations. The interaction between the gap vortices and the shear layers, has not been addressed by previous studies, to the best of the authors' knowledge. Furthermore, although several studies have pointed to the recirculation in the gap and the change of the downstream cylinder wake, the mechanism of interaction between the gap and wake flow within the reattachment regime is not clarified. The aim of the present study is to characterise the development of the gap shear layers, and investigate the interaction between the recirculation in the gap, the gap shear layers and the near-wake of the downstream cylinder. This also includes the effect the inflow from the upstream cylinder has on downstream cylinder flow separation, shear layer development and vortex formation.

A secondary aim is to expand the  $Re$  range of detailed numerical investigations into tandem cylinder flow, as direct numerical simulations (DNS) in this field is thus far limited to  $Re \lesssim 1000$ . DNS can provide flow visualisations with a level of detail that cannot be achieved by any other method, save perhaps tomographic PIV (Hain, Kähler & Michaelis 2008) with a very high spatial and temporal resolution (correspondingly onerous in set-up and execution, and, unfortunately, with a limited field of view size). The usefulness of such data cannot be exaggerated as an aid in the effort to increase our understanding of bluff body flows.

## 2. Numerical method and set-up

The geometry used in the present study consist of tandem cylinders of equal diameter, with the cylinder axis normal to the inflow. The computational domain is shown in figure 2(a). The gap ratio was  $L/D = 3.0$ , which is in the middle of the reattachment regime, as defined by Xu & Zhou (2004), near the limiting gap ratio where reattachment moves from

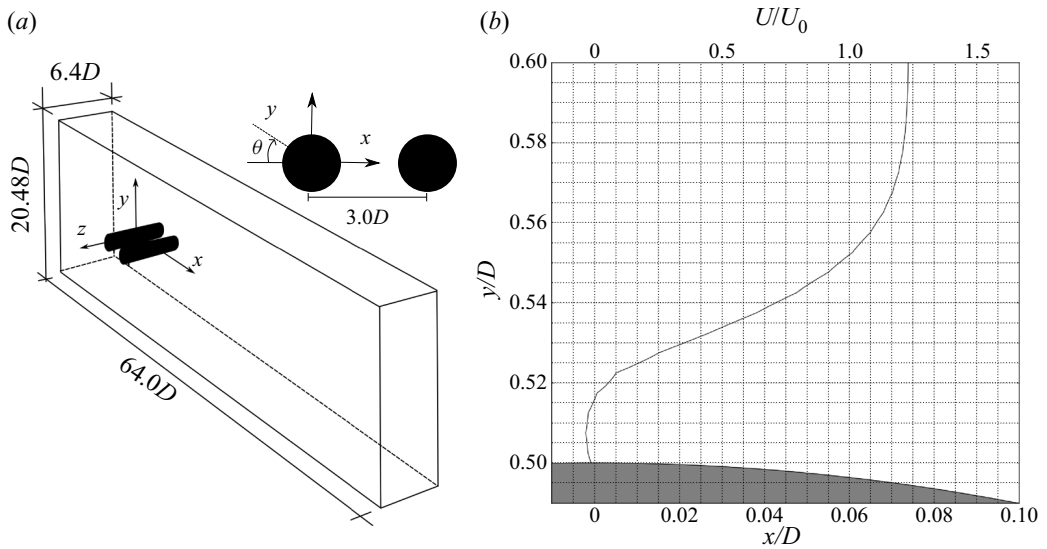


Figure 2. (a) Computational domain and (b) illustration of element size in the boundary layer.

the back face to the front face of the downstream cylinder. The  $Re$  was 10 000, which is high enough that stable reattachment on the front face is expected. A single-cylinder case at the same  $Re$  was computed, for comparison, and the results are provided in [Appendix A](#).

The governing equations are the three-dimensional, incompressible continuity equation and Navier–Stokes equations, which are solved through DNS:

$$\frac{\partial u_j}{\partial x_j} = 0, \quad (2.1)$$

$$\frac{\partial u_i}{\partial t} + u_j \frac{\partial u_i}{\partial x_j} = -\frac{1}{\rho} \frac{\partial P}{\partial x_i} + \frac{\partial}{\partial x_j} \left( \nu \left[ \frac{\partial u_i}{\partial x_j} + \frac{\partial u_j}{\partial x_i} \right] \right), \quad i, j = 1, 2, 3. \quad (2.2)$$

The simulations were carried out using the MGLET flow solver, which is based on a finite-volume formulation of the incompressible Navier–Stokes equations (Manhart 2004). MGLET uses a staggered Cartesian grid, and introduces solid bodies through an immersed boundary method (Peller *et al.* 2006). The immersed boundary is discretised using a ghost-cell method. A third-order low-storage explicit Runge–Kutta time integration scheme is used for time stepping, and the Poisson equation is solved using an iterative, strongly implicit procedure. MGLET has recently been used to explore complex wakes behind three-dimensional bluff bodies (e.g. Jiang, Pettersen & Andersson 2019; Dadmarzi *et al.* 2018).

Uniform inflow velocity  $U_0$  was imposed at the inlet  $x/D = -16$ . Periodic boundary conditions were implemented in the spanwise direction, and free-slip boundaries were used for the top and bottom of the domain. A Neumann condition was imposed on the velocity components at the outlet.

In this study, the grid resolution near the solid boundary is the same for single and tandem cylinders. Moreover, the resolution was the same for both upstream and downstream cylinders. Grid refinement was carried out by adding nested grid blocks, where each child block had half the element size of its parent. Within each block, the

grid is equidistant. The grid had six levels, and the smallest element size was  $\Delta x = \Delta y = \Delta z = 0.005D$ . The most refined grid block had a height of  $1.92D$  (symmetrical about the  $y$  axis) and a length of  $7.2D$ , starting at  $x/D = -0.5$ . It spanned the entire domain in the  $z$  direction. The grid size in the boundary layer of the upstream cylinder is illustrated in figure 2(b). The total number of elements was 682 and 987M for single and tandem cylinder studies, respectively. The same crossflow and spanwise domain size,  $20.48D$  and  $6.4D$ , was used for both cases, but the distance from the origin to the outflow was  $35.2D$  the single-cylinder case, as opposed to  $44.5D$  for the tandem case.

The spanwise length was chosen in consideration of the three-dimensional behaviour of the flow. In their DNS study of a single cylinder with the same  $Re$  as the present study, Dong *et al.* (2006) use a spanwise length of  $\pi D$ . However, Aljure *et al.* (2017) found that for a  $Re$  of 5000, a spanwise length of  $2\pi D$  was needed to correctly capture the three-dimensional phenomena of the flow field. An initial simulation was carried out for a single cylinder with a spanwise length of  $3.2D$ , and the pressure distribution and separation were somewhat affected. Compared with a spanwise length of  $6.4D$ , the shorter cylinder exhibits a slightly increased mean base pressure coefficient ( $\bar{C}_{pb} = (P - P_0)/(P_s - P_0)$ , where  $P$  is the pressure on the cylinder surface, and  $P_0$  and  $P_s$  are the free-stream and stagnation pressures, respectively) and shorter recirculation length  $L_r$  (defined as the distance from the cylinder base to the point where the mean streamwise velocity turns positive), and the primary separation angle  $\theta_1$  is delayed by approximately  $2^\circ$ . Based on that result a spanwise length of  $6.4D$  was chosen.

A grid refinement was carried out for the tandem cylinder case, where the smallest element was reduced to  $\Delta x = \Delta y = 0.0025D$ ,  $\Delta z = 0.005D$ , with a corresponding coarsening of the wake. The total number of elements was 2415 million. This resulted in a difference in the order of 4–5% in the spectral peaks,  $L_r$ , and  $\bar{C}_{pb}$  of the upstream cylinder, as well as a 16% decrease in the  $\bar{C}_{pb}$  of the downstream cylinder. However, the separation points were not affected, and the overall flow regime, with reattachment of the gap shear layers, remained unchanged. Therefore, in order to reduce computational cost while running a long-term simulation, the first grid was chosen.

In order to ensure ample data for statistics, the simulations were run for a long time. The sampling time for the single and tandem cases were  $tU_0/D \approx 1650$  and 2406, respectively, which corresponds to roughly 346 and 377 von Kármán vortex shedding cycles. The chosen timestep was  $dt = 0.002$ .

Power spectra of the velocity components have been calculated from the time traces taken at various locations in the wake of the single cylinder, and the gap and near-wake of the tandem cylinders. Fast Fourier transform (FFT) was used to calculate the spectra, and they were averaged in the spanwise direction.

At the time these simulations were carried out, MGLET did not support computing drag and lift separately on multiple geometries within the domain. Body forces were presented for the combined geometries. Therefore, the force coefficients are not presented for the tandem cylinders, only for the single-cylinder reference case. In order to compute the separation and reattachment points, the tangential velocity field near the cylinder and its radial derivative were calculated, which gave the approximate point of zero shear stress. The tangential velocity profiles near that location were then investigated to find the velocity turning point, and this was used to adjust the computed estimate.

Throughout this paper, coefficient subscripts  $U$  and  $D$  refer to the upstream and downstream cylinder, respectively.

	$L/D$	$Re$	$St$	$-\bar{C}_{pbU}$	$-\bar{C}_{pbD}$	$\theta_R$	Method
Present study	3.0	$10^4$	0.157	0.59	0.31	62.0	DNS
Present study, refined			0.162	0.62	0.26	62.0	
Hu, Zhang & You (2019)	3.0	$2.2 \times 10^4$	0.156	0.6	0.35	65.5	IDDES
Kitagawa & Ohta (2008)	3.0	$2.2 \times 10^4$	0.155	0.6	0.40	70	LES
Lee & Basu (1997)	3.2	$4.0 \times 10^4$	0.141		0.45	67.5	Exp.
Igarashi (1981)	3.09	$3.5 \times 10^4$	0.14/0.17	0.7	0.36	70	Exp.
		$8.7 \times 10^3$	0.16				
Wu <i>et al.</i> (1994)	3.0	$4.1 \times 10^4$	0.14				Exp.
Ljungkrona <i>et al.</i> (1991)	3.0	$2.0 \times 10^4$	0.15	0.6	0.45		Exp.
Alam (2014)	3.0	$9.7 \times 10^3$	0.143				Exp.

Table 1. Statistical flow parameters, tandem cylinders. Note that Igarashi (1981) found bi-stable flow at a gap ratio of 3.09, which is why two  $St$  values are included in the table.

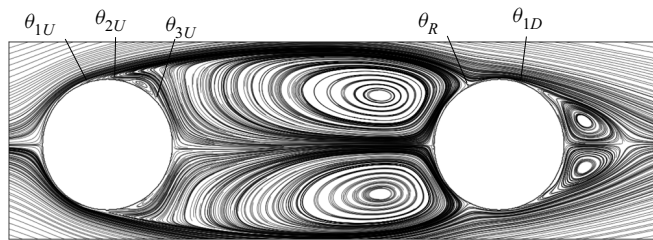


Figure 3. Time-averaged gap and near-wake streamlines for tandem cylinders with gap ratio  $L/D = 3.0$  and  $Re = 10000$ .

### 3. Results

#### 3.1. Time-averaged flow field

Main statistics are given in table 1. There is good agreement between our results and results from the literature within the reattachment regime, at comparable gap ratios and  $Re$ .

The mean gap flow, shown in figure 3, consist of an elongated, bounded recirculation region, with clear indication of large-scale vortex formation. These vortices are formed at the very end of the gap, and there is a rather long region of low velocities in the near-wake of the upstream cylinder. This is clearly shown in figure 4, which depicts the time-averaged contours of the streamwise and crossflow velocities. The base pressure coefficient of the upstream cylinder,  $\bar{C}_{pbU}$ , is very similar to the downstream cylinder pressure coefficient at  $\theta = 0$ , which has a value of  $-0.55$ . The same result was found by Igarashi (1981), who concluded that it indicated the presence of gap vortices. Another recirculation region is seen in the downstream cylinder wake. This is the result of von Kármán shedding, as we show in § 3.4.

For the upstream cylinder, the primary separation occurs at  $\theta_{1U} = 85.0^\circ$ , slightly further upstream compared with the single cylinder (see Appendix A). The recirculation in the gap results in a secondary separation bubble between  $\theta_{3U} = 137.9^\circ$  and  $\theta_{2U} = 108.1^\circ$ . It is smaller than for the single-cylinder case, and pushed further towards the primary separation point. This is because the velocity of the backflow is much lower than for a single cylinder, causing the flow to remain attached to the cylinder base longer.

There is clear reattachment of the upstream cylinder shear layers onto the front face of the downstream cylinder, and the reattachment point,  $\theta_R$ , compares well with the

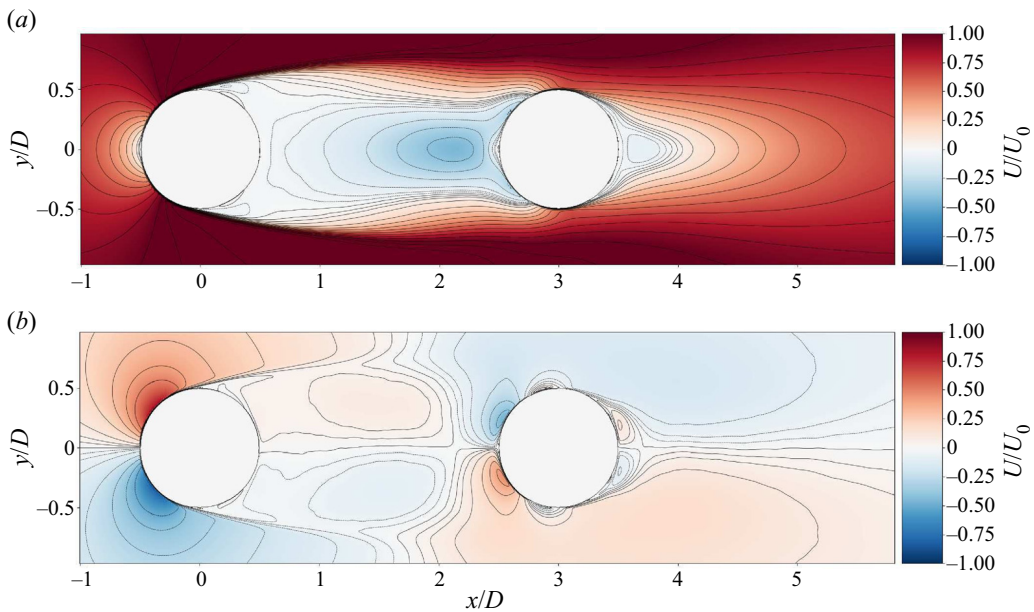


Figure 4. Time-averaged streamwise ( $U/U_0$ ) and crossflow ( $V/U_0$ ) velocity contours in the midplane. The gap region is characterised by recirculation, and there is an almost stagnant region in the immediate wake of the upstream cylinder. The recirculation bubble of the downstream cylinder is short and narrow. The maximum recirculation velocity is  $U/U_0 \approx -0.44$  in the gap, and  $U/U_0 \approx -0.19$  in the wake.

available literature. A noticeable feature of the downstream cylinder is that the subsequent separation occurs on the back face, at  $\theta_{1D} = 119^\circ$ , as opposed to a single cylinder in the subcritical regime. This is related to the turbulent inflow from the upstream cylinder, something discussed in detail in § 3.4.1. The delayed separation precludes the formation of a secondary separation bubble.

### 3.2. Instantaneous flow field in the gap region

The instantaneous flow field reveals the most important features of the gap flow, as shown in figure 5. These are the K-H instability and the associated shear layer vortices (A,B), their breakdown to turbulence (C), formation of large-scale gap vortices (D), a low-velocity stagnation region in the upstream cylinder near-wake (E) and a jet-like flow impinging on the upper shear layer (F). This last feature is important for the development of the shear layer instability and is discussed towards the end of this section.

The shear layers of the upstream cylinder are laminar upon separating, as expected in the subcritical  $Re$  range, and transition to turbulence starts approximately  $1-1.3D$  downstream of the separation point. Here, shear layer vortices start to form. At the end of the gap, these vortices are split up as they impinge on the downstream cylinder, so that part of the shear layer is entrained into the formation of large-scale gap vortices, and the remainder passes close by the downstream cylinder surface.

The shear layer vortices lose much of their coherence as they are convected downstream. Although the gap vortices are quite weak, the backflow in the gap exerts additional shear strain on the oncoming vortices, which increases dissipation and enhances the breakdown process after transition. Figure 6 shows how the shear layer vortices from the upstream cylinder break down while traversing the gap, forming smaller structures. There remains



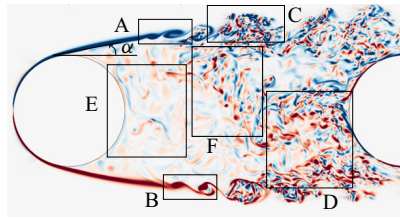


Figure 5. Snapshot of gap flow at  $tU_0/D = 2005.8$ , visualised by the normalised spanwise vorticity,  $\omega_z D/U_0$ . (A) K-H instability, (B) shear layer vortex shedding, (C) breakdown of shear layer vortices, (D) large-scale vortex formation, (E) low-velocity stagnation region and (F) jet-like flow impinging on the upper shear layer. The upstream cylinder shear layers are symmetrically displaced from the gap centreline by  $\alpha \approx 10^\circ$ .

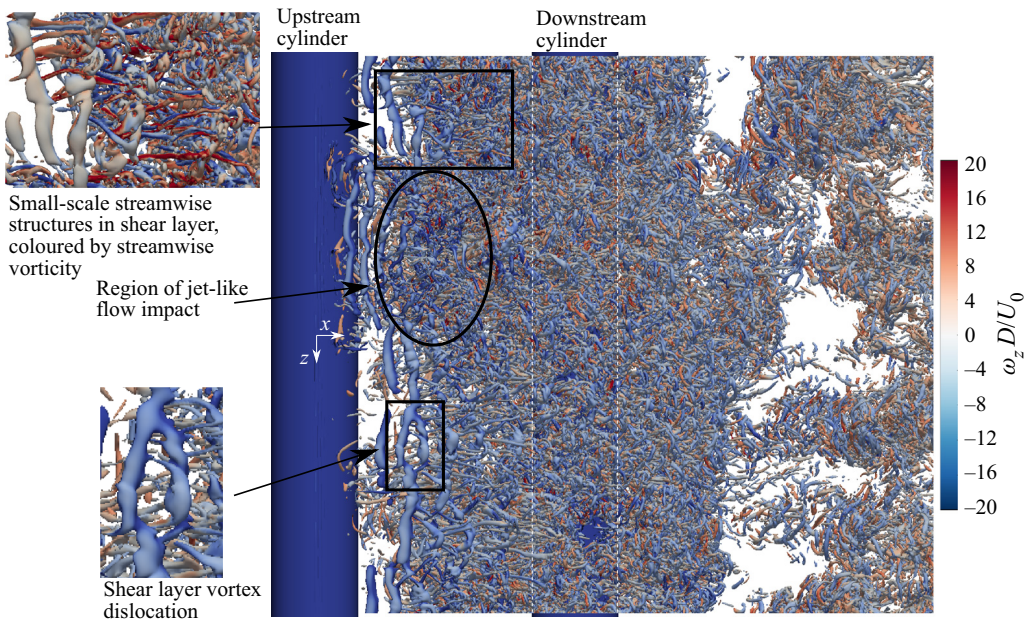


Figure 6. Development of shear layer vortices in the gap, visualised by isosurfaces of  $Q = 10$  coloured by the spanwise vorticity, at  $tU_0/D = 2406.15$ . For clarity, only the outermost part of the flow is included. The upper inset shows small-scale streamwise structures generated by stretching of the shear layer vortices. These have been coloured with the streamwise vorticity, to highlight their orientation. The lower inset shows an example of dislocations in the shear layer vortices.

a weak spanwise organisation of these structures until reattachment, that consists of originally well-defined shear layer vortices, now transformed into looser ensembles of small-scale eddies.

The K-H instability is two-dimensional, which means that the shear layer vortices are created with an essentially spanwise orientation. Three-dimensionality, however, quickly ensues. The shear layer vortices are organised streamwise in cells of several vortices with a short spanwise length. As a result, a number of dislocations are visible in the gap. One example of this is shown in an inset in [figure 6](#).

In this study, the transition to turbulence starts with the generation and shedding of shear layer vortices. Subsequently, vortex stretching and bending causes formation of streamwise structures in the shear layer, in a similar way to the mode B instability for single-cylinder wakes (Williamson 1996). This corresponds well with the finding of Williamson (1995),

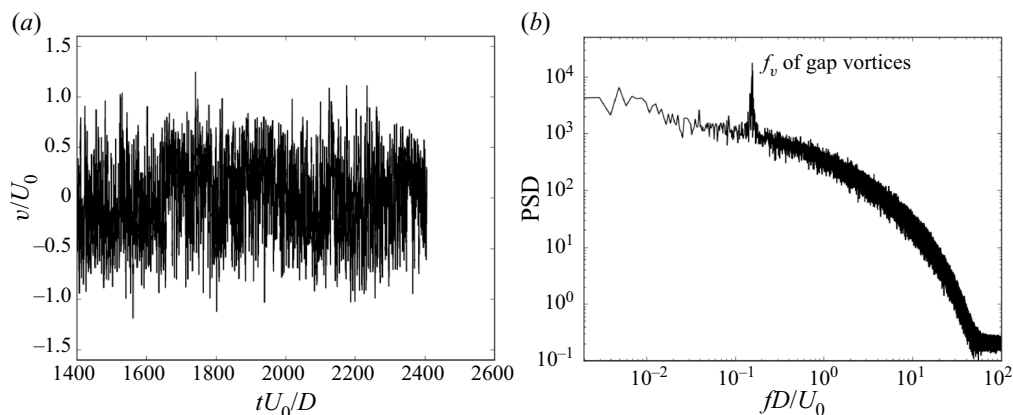


Figure 7. (a) Crossflow velocity signal at  $z/D = 0$  at a probe located directly upstream of the downstream cylinder, and (b) the corresponding spanwise-averaged spectrum. The spectral analysis clearly demonstrates the periodicity of the gap vortices. The exact position of the probe P4, is shown in [figure 8](#).

that there are two scales for streamwise vortices in the flow, one for the wake and one for the separated shear layers. Wei & Smith (1986) also observed streamwise counter-rotating vortices in the shear layers for  $1200 \leq Re \leq 11\,000$ . Early in the breakdown process, these streamwise vortices appear as loops reminiscent of the classical horseshoe vortices of plane mixing layers. An inset in [figure 6](#) shows these structures, coloured by the streamwise vorticity for clarity. A movie which highlights the development and breakdown of the shear layer vortices is available as supplementary movie 1 is available at <https://doi.org/10.1017/jfm.2022.960>.

The length of the stable part of the shear layer is significantly longer for the upstream tandem cylinder than for the single cylinder in [Appendix A](#). The gap shear layers are not parallel to each other as they separate, but appear to be pushed away from the gap centreline in opposite directions, as seen in [figure 5](#). The displacement is approximately  $10^\circ$ . Moreover, there is hardly any difference between the instantaneous and time-averaged position of the gap shear layers; their crossflow position is quite stationary. This becomes evident when comparing [figure 5](#) with [figures 3](#) and [4](#). Altogether, these features indicate that the presence of the downstream cylinder stabilises the shear layers and delays the development of the K-H instability.

Though the time-averaged field shows symmetrical recirculation in the gap, the large-scale gap vortices develop asymmetrically, reminiscent of wake vortices. They are not shed, however, but disintegrate after a cycle of growth, and symmetry reasserts itself temporarily. Analysis of the velocity time trace immediately upstream of the downstream cylinder, given in [figure 7](#), shows a clear spectral peak, demonstrating the periodicity of the gap vortices. Note that because the frequency of the gap vortices is the same as that of the wake vortices, it is marked  $f_v$  in the figure.

An important difference between the gap vortices and vortices developing in an unconstrained wake, is that the streamwise position of a gap vortex does not change appreciably during a cycle. The position is dictated by the gap length. From visual observation, the gap vortices develop in phase, or nearly in phase, with the von Kármán vortices in the wake. However, there is spanwise inhomogeneity, as illustrated in [figure 8\(a\)](#), which results in local phase lag.

One of the benefits of the present well-resolved numerical simulations is that we can follow the small-scale parts of the flow, such as the shear layer vortices, closely.

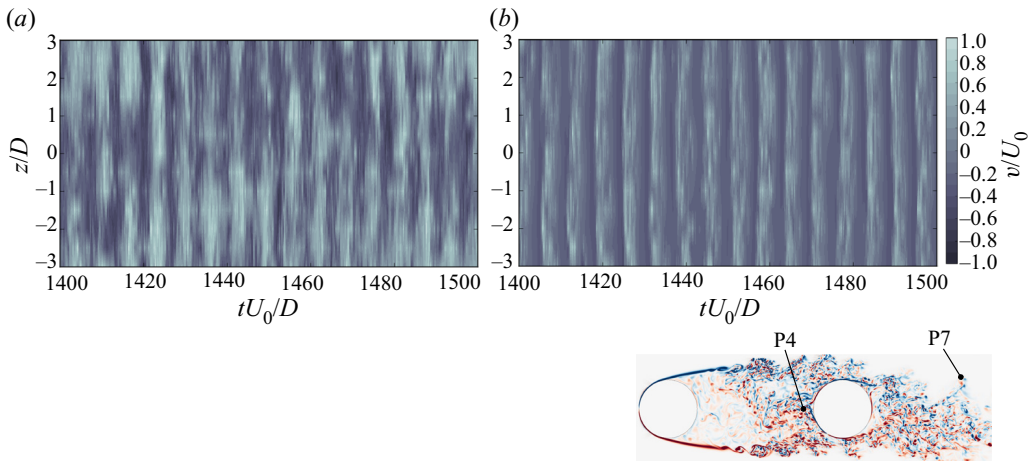


Figure 8. Spanwise inhomogeneity of the gap and wake vortices, illustrated by the temporal development of the crossflow velocity. The time signal is extracted at probe (a) P4 and (b) P7, located at  $(x/D, y/D) = (2.4, 0.0)$  and  $(x/D, y/D) = (0.65, 5.0)$ , respectively. The probe locations are illustrated in the inset. (a) shows that the gap vortices are inhomogeneous along the span, with patches of low crossflow velocities throughout the given time interval. The wake vortices in (b) are fairly homogeneous.

Snapshots of the evolution of some important flow features are provided in [figure 9](#). In the figure, the time between snapshots is approximately  $1/3$  of the shear layer vortex shedding period.

The snapshot series in [figure 9](#) begins just as the gap vortex from the upper shear layer has disintegrated and the lower shear layer has begun rolling up. Towards the end of the series, in [figure 9\(h\)](#), this vortex has grown distinctly. A sketch of its progression is superimposed. Before disintegration, its diameter will have increased so that it fills the entire height of the gap. This is shown in a supplementary movie 2, which covers the same time interval as Movie 1, and includes the series in [figure 9](#).

In [figure 9](#), we follow the development of two shear layer vortices, marked by arrows, one in the upper and one in the lower shear layer. The lower vortex is about to detach at the beginning of the series, in [figure 9\(a\)](#), and in [figure 9\(h\)](#) entrainment into the large-scale vortex has begun. Although the vortices in the lower shear layer deform significantly as they travel along the gap, it is apparent from these snapshots that they do not undergo full breakdown to turbulence before being entrained.

From a qualitative point of view, the disintegration of the vortices in the upper shear layer progresses faster than those on the opposite side of the gap, in the time period presented in [figure 9](#). The marked vortex in the upper shear layer has just started forming in [figure 9\(a\)](#), but by [figure 9\(h\)](#) it has undergone strong deformation and is well underway to disintegrate. The differences between the upper and lower shear layer are related to a high-velocity flow in the gap, the aforementioned jet-like flow, and discussed shortly.

A vortex pairing event unfolds after transition in the upper shear layer, marked by a small circle in [figure 9](#). The event is not very clear, due to the disordered state of the vortices, but we see that the two structures undergo pairing between [figures 9\(a\)](#) and [9\(g\)](#). In [figure 9\(h\)](#), it is evident that the pairing has resulted in a longer wavelength of the shear layer vortices.

All through the series in [figure 9](#), we see that there is very little activity in the region in the immediate wake of the upstream cylinder. The flow here is almost stagnant, compared with the evolution of the shear layers and the large-scale vortex. There seems to be little communication between the inner part of the shear layer, towards the separation point, and the gap vortex formation and shear layer impingement occurring at the end of the gap.

Revisiting the reattachment regime

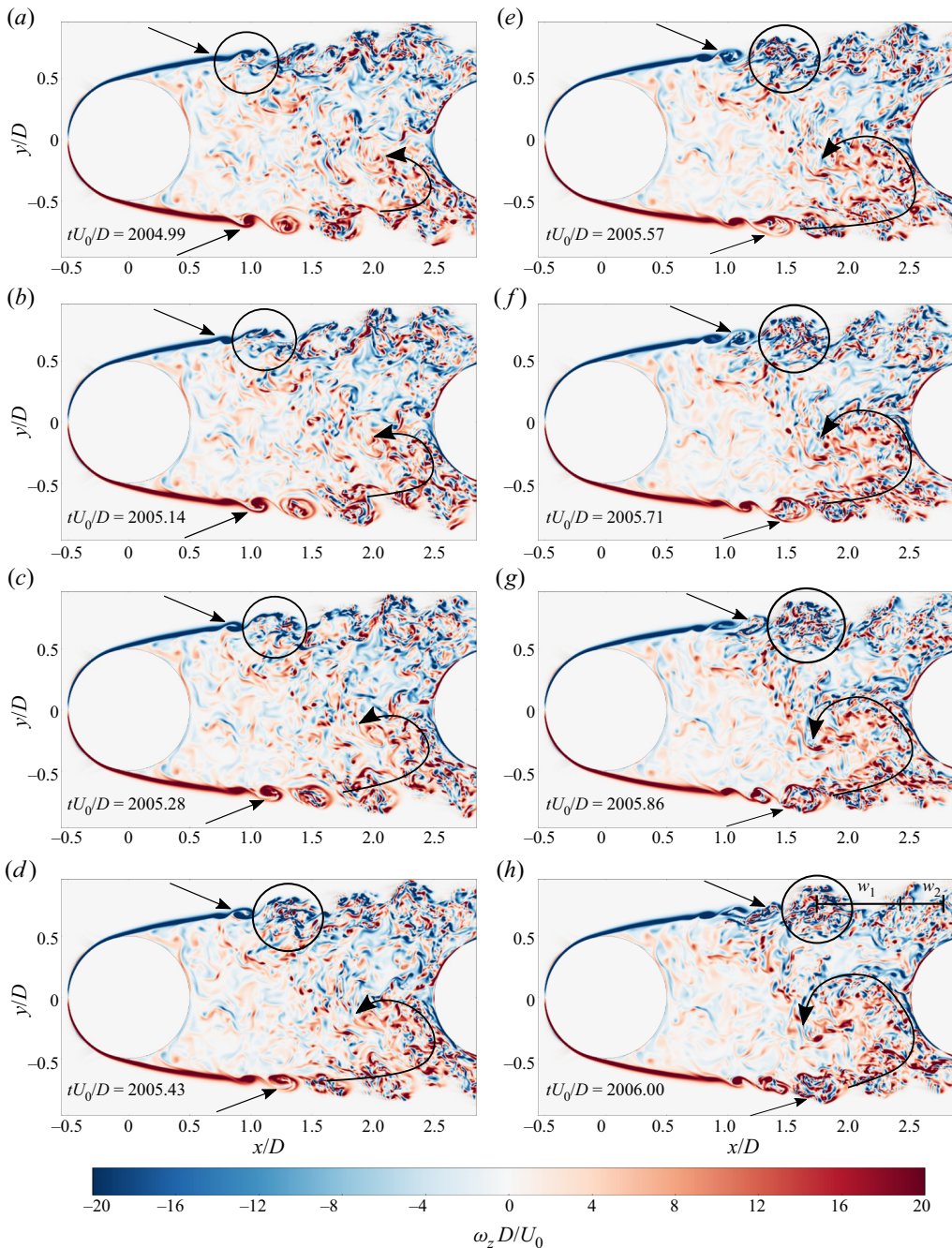


Figure 9. Development of structures in the gap, visualised by the spanwise vorticity. One part of the lower shear layer rolls up into a large-scale gap vortex, whereas the rest flows past the downstream cylinder. Shear layer vortices, marked by arrows, form in both shear layers and undergo breakdown towards turbulence while traversing the gap. They are still weakly coherent upon reattachment, seen as loose ensembles of smaller structures. The upper shear layer progresses faster towards turbulence than the lower. A pairing event takes place in the upper shear layer, marked by a small circle. The final wavelength,  $w_2$  is twice that of the preceding shear layer vortices,  $w_1$ .

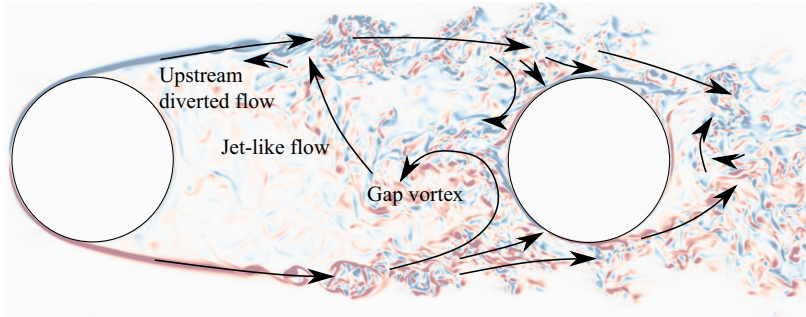


Figure 10. Flow directions in the gap and near-wake at  $tU_0/D = 2005.86$ , superimposed on the spanwise vorticity field. A jet-like flow crossing the gap impacts the opposite shear layer, increasing the turbulent activity. Part of the jet is diverted upstream, and if the vorticity in this fluid is strong enough it may trigger early transition to turbulence in the shear layer.

This has consequences for the development of the shear layer instability, which are discussed in § 3.3.

Figure 10, which shows the same time instant as figure 9(g), gives an indication of the mechanism behind the accelerated breakdown of the upper shear layer. Here, we draw the directions of different parts of the flow at a time instant when the gap vortex is approximately half way in its cycle of formation and disintegration. As the vortex forms, it entrains part of the lower shear layer from which it rolls up, as well as part of the recirculating fluid from the upper shear layer. This fluid is pushed down along the front face of the downstream cylinder and then pulled along the outer boundary of the vortex. Simultaneously a flow with higher velocities than the surrounding fluid is directed towards the upper shear layer. This flow is dubbed ‘jet-like’ because of its appearance in the visualisations, although it is a quasi-two-dimensional feature, not an actual axisymmetric jet. There is a small region of low-velocity fluid trapped between the upper shear layer, the recirculating part, the gap vortex and the jet. As the vortex grows, this region shrinks until the vortex comes in direct contact with the upper shear layer.

The jet-like flow is the main contributor to the enhanced breakdown of the shear layer opposite the gap vortex. Most of the jet fluid is entrained into the shear layer, but a small part is diverted towards the separation point. The jet-like flow may originate from the formation of the gap vortex, or it may be a remnant of the previous gap vortex. Most likely, perhaps, it is a result contributions from both vortices. It is strongest just after disintegration of the previous gap vortex, when the new one is beginning to form.

Interestingly, the jet-like flow phenomenon does not occur simultaneously along the whole cylinder span, which is related to the spanwise inhomogeneity of the gap vortices. An impact region is marked figure 6, where the jet-like flow visibly influences the development of the shear layer. In this case, the region is approximately  $1.5D$  long. The result of the spanwise variation in the gap vortex formation and the occurrence of the jet-like flow is enhanced three-dimensionality of the wake.

### 3.3. Development of the shear layers

Figure 11 shows the crossflow velocity time signal and spectrum taken from a probe in the shear layer of the upstream cylinder. Although the frequency of the large-scale vortex formation is detected in this region, it is significantly weaker than that of the shear layer vortices. Spectra computed from probes further downstream in the gap are also included

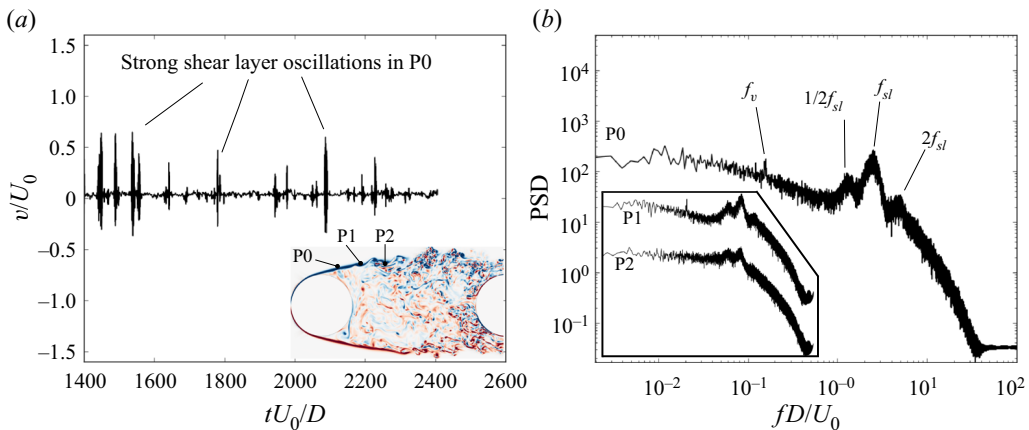


Figure 11. (a) Crossflow velocity signal in the plane  $z/D = 0$  and (b) spanwise-averaged power spectral density (PSD) for probe P0 in the upstream shear layer. The smaller graphs inset in (b) show the spectra from probes further into the gap (P1, P2). Here, turbulent activity is strengthened, which obscures the shear layer vortex peaks. Note that these spectra are shown for their shape only, and they are not scaled to the strength on the vertical plot axis. The inset in (a) illustrates the location of the probes. The coordinates of P0, P1 and P2 are  $(x/D, y/D) = (0.4, 0.6)$ ,  $(0.65, 0.65)$  and  $(1.0, 0.65)$ , respectively.

in figure 11(b), for comparison. The large-scale vortex frequency is gradually obscured by the increased turbulent activity when we move into the gap.

The tail of each spectrum in figure 11(b) is steep compared with velocity spectra for fully developed turbulence, which are expected approximately follow Kolmogorov's  $-5/3$  power law (Kraichnan 1974). This is because the flow at the locations of the probes in question is only intermittently turbulent. Similar spectra are found for velocity and turbulent kinetic energy in the outer region of free jets, where turbulence is also intermittent (Fellouah, Ball & Pollard 2009; Yaacob, Buchhave & Velte 2021). Probes placed further into the gap, where the flow is more turbulent, have less steep spectra, as seen when comparing P2 and P0.

Instead of one narrow peak, like that of the large-scale gap vortices, the shear layer covers a wide range of frequencies, seen as a broadband region with three distinctive peaks in figure 11(b). This is consistent with the single-cylinder studies of Khabbouchi *et al.* (2014) and Dong *et al.* (2006). The latter did not see separate shear layer peaks, rather a broadband plateau, similar to the single cylinder in the present study. The highest peak, with a main frequency of  $f_{sl} = 2.5U_0/D$ , is associated with the shedding of shear layer vortices, whereas the secondary peaks are its harmonic and subharmonic. Here  $2f_{sl}$  corresponds to shear layer vortex breakdown, whereas the subharmonic  $0.5f_{sl}$  is associated with vortex pairing in the shear layer. The value of the main peak frequency is very similar to that of the single-cylinder case, which is  $f_{sl} \approx 2.6U_0/D$ . The similarity indicates that, in addition to the delayed inception, the shear layer instability is not significantly affected by the presence of the downstream cylinder, as opposed to the primary instability. This is consistent with the observations of Kourta *et al.* (1987) for a single cylinder with a splitter plate in the wake. It is not an altogether surprising result, as K-H instability and the primary instability are two separate phenomena that may occur independently. For example, K-H vortices are found along the boundaries of free jets, or in the shear regions between atmospheric flows, as well as for single cylinders above a certain  $Re$ . When both instabilities are present in a flow, they may interact (Kourta *et al.* 1987), but one does not depend on the presence of the other in order to develop.

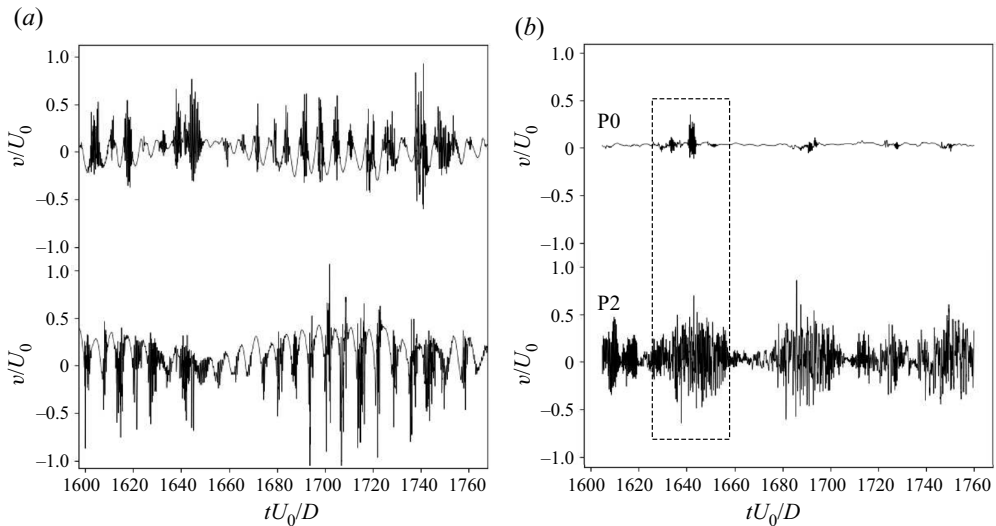


Figure 12. Crossflow velocity signal over 25 vortex shedding cycles for (a) single and (b) tandem cylinders at two probes in the shear layer, in the plane  $z/D = 0$ . Probe locations are shown in figure 11. For the tandem cylinders, early triggering of the shear layer instability leads to stronger oscillations downstream. One such event is marked by a dashed rectangle.

The transition region in the shear layers exhibits a degree of random meandering, manifested as intermittency in the velocity signal from probes in the gap, as exemplified in figure 11(a). Close to the upstream cylinder, the crossflow velocity signal shows distinct periods of strong fluctuations that occur at irregular intervals over a long period of time. When moving to a probe further downstream, strong oscillations become frequent. This is shown in figure 12, which compares the crossflow velocity signal sampled at two positions for single and tandem cylinders.

For the single-cylinder case in figure 12, there is very little difference in the number of shear layer fluctuations between the measurements taken in the near-wake and closer to the separation point. For the tandem cylinders, however, the difference is remarkable. Whereas only a few packets can be observed close to the upstream cylinder, the fluctuations are nearly continuous at  $x/D = 1.0$ . Recalling Prasad & Williamson's (1997) result, few packets at the upstream location implies that there is less meandering of the transition region in the tandem cylinder case. Furthermore, if we compare the influence of large-scale vortices on the shear layers, we see that the von Kármán shedding in the wake of the single cylinder clearly visible in the time traces in figure 12(a), but the gap vortices can barely be discerned in the time trace of the tandem cylinder gap probes in figure 12(b).

Being weaker than their single-cylinder counterparts, the gap vortices provide recirculated fluid with weaker vorticity. Further, the low-velocity region near the upstream cylinder back face is not directly touched by the gap vortices, as seen all through the snapshot series in figure 9. Little communication along the gap and weak vorticity means that there is a low supply of recirculated structures that are strong enough to amplify the shear layer instability and trigger transition close to the cylinder. This accounts for the low number of fluctuation 'packets' at probe P0, as shown in figure 12. P2, on the other hand, is almost always located in the transition region, and likewise receives an inflow of strong small-scale structures from the jet-like flow described in § 3.2. Conversely, it seems probable that early triggering of the shear layer instability (near probe P0) is caused by the

### Revisiting the reattachment regime

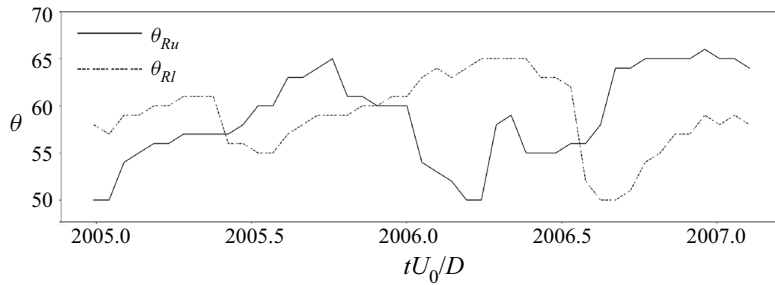


Figure 13. Instantaneous upper ( $Ru$ ) and lower ( $Rl$ ) reattachment points in the plane  $z/D = 0$ , during formation of a large-scale vortex in the lower shear layer. The points are gleaned by a simple method, visual observation of the instantaneous spanwise vorticity, but provide useful insight into the unsteadiness of the reattachment. The lower reattachment point is given by its absolute value, to facilitate comparison.

part of the jet-like flow that is diverted upstream. Although triggering events in the upper and lower shear layers may overlap in time, there is no evidence in the present study that they are generally in-phase. This is consistent with the results of previous investigations (Rai 2010).

Owing to transition to turbulence in the upstream shear layer, and the large-scale vortex formation in the gap, the reattachment points on the downstream cylinder are unsteady and asymmetrical with respect to the gap centreline. It is challenging to compute the instantaneous location of the reattachment points, but visual observation of the spanwise vorticity is a simple method that can give an indication of their whereabouts. The variation of the instantaneous reattachment in the plane  $z/D = 0$  has been recorded during part of the vortex formation in the lower shear layer. The results are shown in figure 13. During this short time interval, the absolute value fluctuates between  $50^\circ$  and  $65^\circ$ , for both reattachment points. Recalling from table 1 that the time-averaged reattachment location is  $62.0^\circ$ , it follows that the temporal variation must be significant. For a single cylinder, the shear layers move transversely due to large-scale vortex shedding, but, as we have seen, this is not the case for the tandem cylinders herein. Thus, the main contribution to the high-speed fluctuations in reattachment position comes from instantaneous changes in the thickness of the turbulent part of the shear layer.

In the present study, the results indicate that shear layer vortex pairing takes place both for single and tandem cylinders. For the single cylinder, the spectral peaks in figure 19(b) are less pronounced than for the tandem cylinders in figure 11(b), although the subharmonic and harmonic of  $f_{sl}$  can be discerned. This is consistent with the observations of Cardell (1993), who saw that for the unconstrained single-cylinder near-wake, the subharmonic had developed to approximately the same amplitude as the main shear layer peak at  $Re \approx 10\,000$ . For the tandem spectra the difference in energy between  $f_{sl}$  and  $0.5f_{sl}$  decreases into the wake, where pairing is more frequent. At P2, the peaks are almost of equal height, so that this part of the spectrum compares well with the single-cylinder spectrum in figure 19(b). In addition to the event from figure 9, two distinct shear layer vortex pairing events are seen in figure 14, one in each shear layer. These have been marked for clarity. To the best of the authors' knowledge, this is the first time vortex pairing in the gap shear layers of tandem cylinders has been reported.

#### 3.4. Instantaneous wake structure

The wakes of the single and tandem cylinders at the same Reynolds number are strikingly different. The inset in figure 15 clearly shows that the tandem wake is narrower, and the



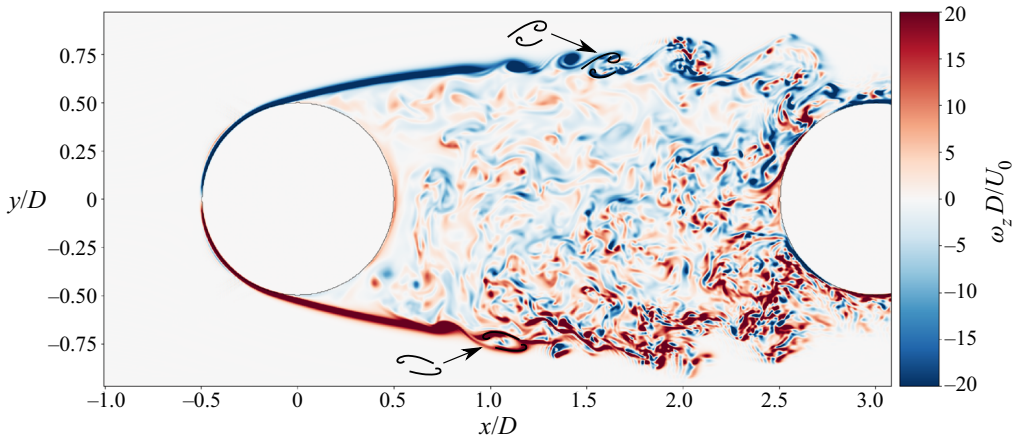


Figure 14. Vortex pairing events in the shear layers at  $z/D = 0.5$ ,  $tU_0/D = 2406.15$ , visualised by the spanwise vorticity.

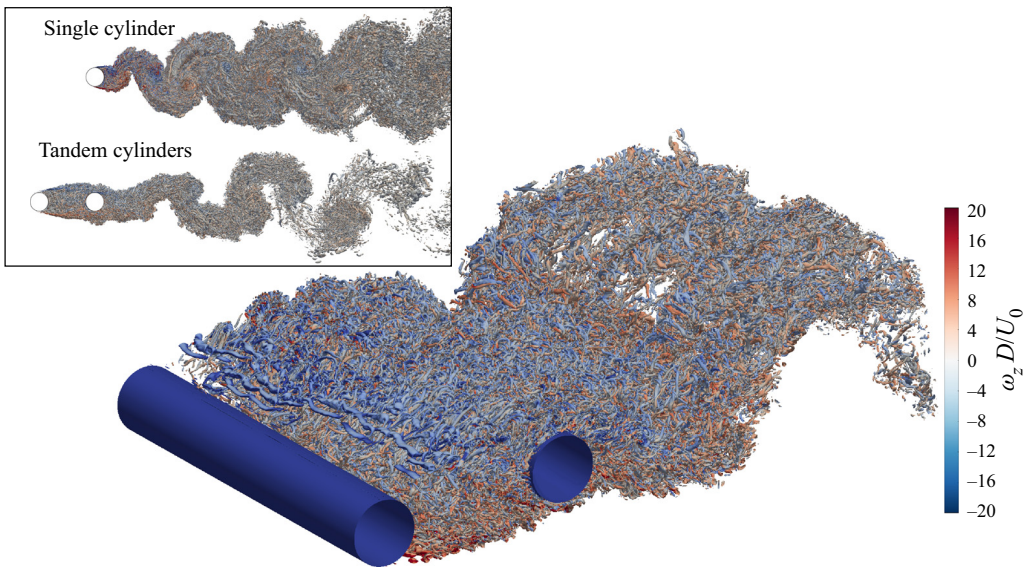


Figure 15. Isometric view of the gap and wake flow of the tandem cylinders at  $tU_0/D = 2406.15$ , represented by isosurfaces of  $Q(D/U_0)^2 = 5$  coloured by  $\omega_z D/U_0$ . The inset shows a side view of the single and tandem cylinder wakes. For the tandem cylinders, the wake is narrowed, and the vortices are elongated compared with the single-cylinder vortices. The streamwise structures from the single-cylinder wake are missing for tandem cylinders, due to turbulent activity from the upstream cylinder shear layers.

vortices appear elongated. Increased mixing and diffusion, due to turbulent inflow from the upstream cylinder, causes the small structures of the tandem cylinder wake to be more uniform in terms of scale, and also more three-dimensional, which is shown in figure 15. Unlike the single-cylinder wake (see figure 19c), the tandem wake does not display a clear spanwise versus streamwise organisation, apart from the large-scale shedding.

The disappearance of the streamwise vortical structures for the tandem cylinders must be seen in connection with the turbulent inflow, as well as the strength of the von Kármán vortices. The streamwise vortices formed in instability mode B originate when streamwise

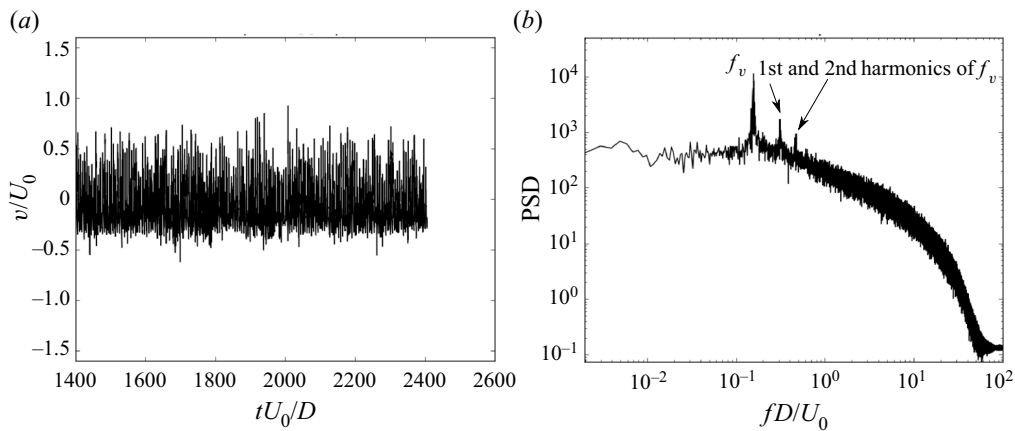


Figure 16. (a) Crossflow velocity signal at  $z/D = 0$  at probe P7 and (b) the corresponding spanwise averaged spectrum. The probe is situated in the downstream cylinder wake, and its exact location is given in figure 8.

vorticity is amplified through vortex stretching (Williamson 1996). However, this process is dampened by diffusion. The increased diffusion due to the turbulent inflow, coupled with the reduced strength of the primary vortices, giving a lower supply of vorticity to the braid regions, precludes the formation of sizable streamwise vortices. It must be noted that streamwise vortices have been observed in the wake of tandem cylinders at low  $Re$ , where transition to turbulence occurs in the wake rather than in the shear layers (Carmo, Meneghini & Sherwin 2010).

Lin *et al.* (2002) also pointed out the changed shape of the wake vortices. They claim that for gap ratios up to  $L/D = 2.0$ , the vortices have a tendency not to cut the opposing shear layer during the formation process. This cannot be the case because it is a prerequisite of shedding that the forming vortex cut the opposing shear layer. In our study, we see that this process is somewhat obscured by the incoming shear layer structures of the upstream cylinder, which may be a cause of the misunderstanding. Reattachment of the turbulent shear layers appears very neat and ordered in the time-averaged flow field (see figure 3), but in reality it is less straightforward. We have found that it is a combination of impinging structures, and structures that are drawn towards the downstream cylinder due to the increased velocity over the cylinder surface. The path and orientation of these outer structures are changed but they do not blend completely with the downstream shear layer. Rather they lie as an extra layer outside it until entrained in the von Kármán vortex. Moreover, the entire outer layer is not necessarily entrained during the wake vortex formation. Some of the structures pass over the forming vortices to merge with the wake a little further downstream. This can be seen in supplementary movie 2. The wake vortices do not necessarily cut through the outer layer of incoming shear layer structures as they form, just the shear layer originating from the downstream cylinder itself, which is likely what caused the erroneous conclusion of Lin *et al.* (2002) on that subject.

The von Kármán vortex shedding has a dominant frequency  $St = 0.157$ , which agrees well with previous studies (see table 1). Figure 16 shows the time signal and resulting spectrum of a probe in the wake. There are secondary peaks near  $f_v$ . A wider bandwidth of the vortex shedding frequency is typical of single-cylinder wakes above  $Re \approx 5000$ , resulting from spanwise frequency variations (Aljure *et al.* 2017).

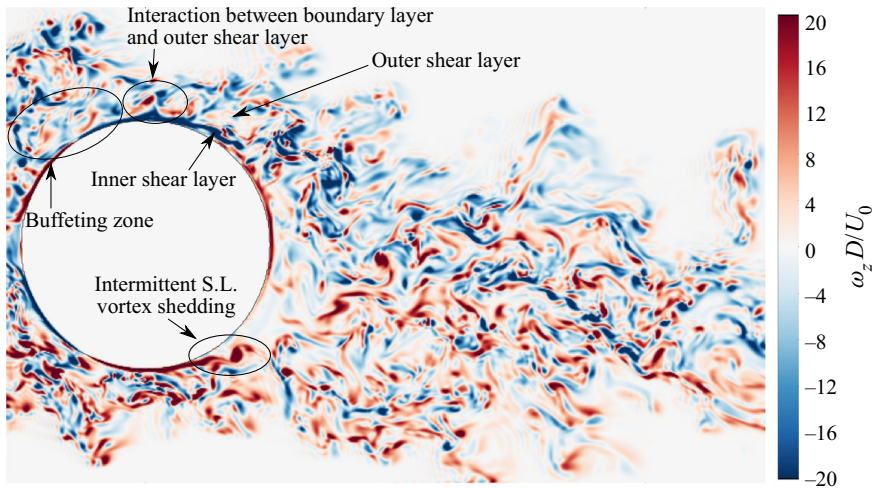


Figure 17. Snapshot of the downstream cylinder spanwise vorticity field, at  $tU_0/D = 2005.3$ . Interaction between the inner and outer parts of the shear layer leads to shortening and distortion of the inner layer, with only intermittent shedding of shear layer vortices. Buffeting of the boundary layer by the upstream cylinder shear layer and interaction with the outer part contributes to delayed separation.

### 3.4.1. The effect of turbulent inflow to the downstream cylinder

As already mentioned, the downstream cylinder is completely submerged in the turbulent wake of the upstream one. That perturbations in the incident flow affects the flow field around a single cylinder is well known, so we must expect alterations in the downstream cylinder flow field. It was established in the previous sections that the overall effect is relocation of the primary separation point to the back face, suppression of secondary separation and a narrowed wake. Surprisingly, the influence of the turbulent inflow to the downstream cylinder has not yet been examined in detail in the literature, although the effect of incident turbulence to both cylinders has been studied Ljungkrona *et al.* (1991), and the narrow wake as been remarked by several (Ljungkrona *et al.* 1991; Lin *et al.* 2002; Zhou *et al.* 2019). With good resolution of the flow near the solid bodies, we are in a unique position to study this phenomenon.

Figure 17 shows the effect of the incoming turbulence on the instantaneous flow features of the downstream cylinder. The boundary layer is subjected to continuous buffeting near the reattachment point, as well as additional strain from interaction with the outer shear layer. No shear layer frequency peak could be detected in this region, and only intermittently is elongation of a laminar inner shear layer seen, with the shedding of shear layer vortices.

Few tandem cylinder studies explicitly list the separation angle of the downstream cylinder, but the overall impression is that within the reattachment regime, separation occurs on the back face. Lee & Basu (1997) and Alam *et al.* (2003) found separation angles of  $120^\circ$  and  $113^\circ$ , respectively, for  $Re = 4.0 \times 10^4$  and  $6.5 \times 10^4$ . The result of Zhou *et al.* (2019) is interesting, in this respect. At a  $Re$  of  $10^3$ , they found that the separation on the downstream cylinder varied between  $122^\circ$  and  $128^\circ$  for gap ratios  $1.5 \leq L/D \leq 3.5$ . Although the  $Re$  is significantly lower than in the present study, the result is qualitatively similar. This indicates that, at least within the subcritical range, the flow around the downstream cylinder is independent of  $Re$ .

The recirculation bubble is shortened compared with the single-cylinder reference case, from  $L_r = 0.62$  to  $0.45$ . Ishigai *et al.* (1972) also saw a substantial shortening of the

recirculation region,  $L_r = 0.25$ , at a gap ratio of 3.0 and  $Re = 3900$ . Lin *et al.* (2002), on the other hand, found that although the wake was narrowed, the recirculation length was not affected to any significant degree for gap ratios 1.25 to 2.0 and  $Re = 10\,000$ .

When looking at the flow field of the downstream cylinder, it is instructive to consider the effect of incident FST on a single cylinder. Naturally, this is a simplified model. We must also keep in mind that the turbulence level of the flow impinging on the downstream cylinder is significantly higher than in the available studies, which typically have turbulence intensities of 1–10% (Zdravkovich 1997). Mechanisms associated with FST are accelerated transition to turbulence in the free shear layers and boundary layer, and enhanced mixing and entrainment (Bearman & Morel 1983). Khabbouchi *et al.* (2014) reported that increased FST promoted breakdown of shear layer vortices and corresponded with a decrease in recirculation length, which corresponds well with the present results. However, for a single cylinder in the subcritical regime, the influence of FST is expected to be limited to the shear layers, with the boundary layer remaining laminar.

In the present study, it is likely that transition to turbulence in the downstream cylinder boundary layer is triggered by the buffeting from, and interaction with, the upstream cylinder shear layers. This hypothesis is strengthened by the fact that the primary separation point is moved to the back face, which is a known feature of transition to turbulence in the boundary layer for single cylinders. That shedding of shear layer vortices (a feature of transition in the shear layers) does happen in the present study, albeit intermittently, indicates that the boundary layer transition is not stationary in time.

#### 4. Discussion

The gap flow shares many similarities with single cylinders with splitter plates, where large-scale vortex shedding is partially or completely suppressed in the near-wake region. This includes stabilisation of the separation point, delayed transition to turbulence in the separated shear layers, enhanced vortex pairing and reduced meandering of the transition region (Unal & Rockwell 1988*b*; Cardell 1993). Studies with a gap between the cylinder base and splitter plate underline the similarity (Roshko 1954; Ozono 1999). Qualitatively, the effect on the upstream cylinder is the same irrespective of whether the downstream interference element, to use Roshko's terminology, is a cylinder or a flat plate. From this, we may infer that the mechanism of stabilisation is the same, namely inhibited communication between the separated shear layers.

The nature of the recirculation in the gap changes with the gap ratio. Lin *et al.* (2002) reported intermittent alternations between symmetrical and asymmetrical recirculation patterns at  $L/D = 2.0$ , and a similar result was found by Zhou *et al.* (2019). In our case the recirculation is distinctly periodic and asymmetrical. By comparing our study with others at different gap ratios, a hypothesis is formed that there is a second critical gap spacing, preceding the transition co-shedding, at which the primary instability can start developing. This would explain why Lin *et al.* (2002) saw only symmetrical recirculation at low gap ratios, followed by intermittent symmetry/asymmetry when the gap ratio increased. Before this new critical spacing is reached, the recirculation in the gap is caused primarily by geometrical constraint. The downstream cylinder blocks the path of separated shear layer and forces its lower part to recirculate, whereas the upper part is reattached. Then, as the gap ratio is increased, true roll-up of the shear layer into large-scale eddies starts to happen. As we have only investigated a single gap ratio in this study, we cannot conclude firmly on this.

The interaction between the gap vortices depends on the type of recirculation. The mechanisms seen in the present study, direct interaction between a gap vortex and the

opposite shear layer, as well as the jet-like flow, are features of asymmetrical recirculation. Lin *et al.* (2002) found a different type of jet flow, acting horizontally, along the centreline of the gap, where interaction occurs primarily with the upstream cylinder base. It is conceivable that, should this jet be strong enough, it could influence the development of the shear layers when the jet fluid is diverted outwards after impinging on the upstream cylinder.

In Ishigai *et al.*'s (1972) study, the visualisations show that the transition region in the gap shear layer moves upstream with increasing gap ratio, at essentially the same  $Re$  (variation only within the range 3400–4000). The experimental technique (Schlieren method, where the cylinder is heated) makes estimation of the shear layer thickness from the photograph impossible. However, the trend regarding the transition region is still valid, and it can be coupled with Rai's (2010) result regarding the shear layer instability. In the present study, we have seen that the low strength of the gap vortices with respect to a single cylinder leads to less meandering of the transition region. If the gap ratio is increased, so is the strength of the gap vortices, accompanied by stronger small-scale recirculated structures, and a corresponding upstream movement of the shear layer transition region. Here, we must underline that instability of the shear layer occurs regardless of whether or not there is recirculation, but we believe that for tandem cylinders, its inception, and hence the position of the transition region, is influenced by the mechanism described previously.

The position of the transition region is important because it influences the near-wake of the downstream cylinder, and hence the structure of the large-scale shedding. Early transition allows the shear layer to develop further before reattachment, which results in an increase in the turbulence intensity in the inflow to the downstream cylinder. In § 3.4.1, it was suggested that this leads to transition to turbulence in the boundary layer, instead of in the shear layers. Zhou *et al.*'s (2019) results show that the downstream cylinder separation angle increases with increasing gap ratio within the reattachment regime. In addition to increasing the turbulence of the inflow, increasing the gap ratio also pushes the reattachment point upstream, allowing the downstream boundary layer to develop further before separating, as pointed out by Zhou & Yiu (2006). These two factors, increased turbulence and increased time for the boundary layer to develop, lead to delayed separation with increasing gap ratio.

The spanwise inhomogeneity of the gap vortices is interesting in itself, and because it gives rise to dynamics that influence the development of the shear layers. A possible explanation for the inhomogeneity is the mode B instability (Williamson 1996), which causes waviness of spanwise structures. This could potentially lead to spanwise crossflow velocity variations such as those observed in figure 8(a). Another possibility is that there is spanwise localised bi-stability, i.e. that the flow regime switches from reattachment to co-shedding intermittently, within a spanwise cell. For single cylinders, cellular vortex shedding is known to occur, caused by spanwise variations in phase and/or frequency. In experiments, a high aspect ratio is required to obtain this, due to blockage. In numerical simulations, the use of periodic boundary conditions in the spanwise direction allows for a lower aspect ratio. In the study of Aljure *et al.* (2017), spanwise von Kármán cells and dislocations are evident for  $z/D = 2\pi$  and  $3\pi$ . The velocity spectra in both figures 7 and 11 show signs of a secondary peaks near  $f_v$ . This is indicative of slight frequency differences in the von Kármán vortex shedding, and may include a mode of bi-stability with alternating reattachment, similar to the findings of Kitagawa & Ohta (2008). The spanwise behaviour of the large-scale vortices is not discussed in the literature, where the flow regime is normally presented on a two-dimensional cross section, implicitly implying homogeneity. Meanwhile, with the degree of three-dimensionality observed in

the present study, combined with the bandwidth of the crossflow velocity spectra, cell-like occurrences of bi-stability are not unlikely.

Considering the reduced recirculation length behind the downstream cylinder, it is seemingly a paradox that the Strouhal number is lower than for a single cylinder at the same  $Re$ . Xu & Zhou (2004) suggested that this was caused by a ‘lock-in’ effect similar to what has been reported within the co-shedding regime, where the shedding behind the downstream cylinder is governed by the wake shedding of the upstream cylinder (Wang *et al.* 2018). Overall, the gap and wake vortices develop in-phase, and gap vortices exert direct periodic forcing on the downstream cylinder boundary layer, which supports the lock-in hypothesis. Moreover, the low frequency is consistent with an elongated recirculation length, such as that of the gap vortices. Although the lock-in hypothesis seems most probable in the present case, it is possible that the mechanism of interaction between the gap and wake flow changes with the gap ratio. As long as the primary instability of the gap vortices is blocked, at low gap ratios, periodicity in the gap region may be driven by upstream influence from the wake vortices.

## 5. Concluding remarks

In this study, DNS of flow around tandem cylinders at  $Re = 10\,000$  have been carried out for the first time, at a gap ratio of  $L/D = 3.0$ . The obtained spatial and temporal resolution made it possible to study the gap shear layers and their development with unprecedented detail. This gives new insight into the dynamics of the tandem cylinder gap region and the interaction between large- and small-scale vortical structures, as well as the reattachment mechanism and the effect on the development of the downstream cylinder wake.

We have seen that the flow in the gap between tandem cylinders in the reattachment regime shares similarities with that of a single cylinder with a splitter plate in the wake, due to the lack of vortex shedding in the gap. This is manifested in enhanced stability of the separation points, as well as the shear layers. Little or no crossflow motion of the shear layers is seen, and the onset of the K-H instability is delayed. Shear layer vortex pairing is reported for the first time for tandem cylinders.

There is formation of vortices at the end of the gap, which are asymmetrical and distinctly periodic, with the same frequency as the downstream cylinder wake shedding. Surprisingly, however, the gap vortices are not homogeneous along the span, and the results suggest that there may be spanwise localised bi-stability, with intermittent shedding in spanwise cells.

The gap vortices and the gap shear layers interact by two main mechanisms. One is direct, as the cyclic growth of the gap vortex is large enough for it to come into contact with the opposite shear layer before it disintegrates. The other mechanism is indirect. In the early stages of gap vortex formation, when the previous gap vortex is nearly disintegrated, a jet-like flow is directed towards the opposite shear layer, which contributes to increased turbulent activity. Moreover, some of the fluid from this flow is directed upstream, where it amplifies the shear layer instability and contributes to early transition to turbulence in the shear layer. Because the gap vortices are spanwise inhomogeneous, the jet-like flow does not occur simultaneously across the span. This enhances the three-dimensionality in the gap and wake flow.

Reattachment itself is seen to be very complex, due to transition to turbulence in the gap shear layers. The instantaneous reattachment position exhibits random fluctuations over a range of some  $20^\circ$ , on a very fine time scale. Moreover, we have found that reattachment is not complete, in the sense that the upstream cylinder shear layer does not merge directly with that of the downstream cylinder. Rather, reattachment is a

combination of impingement and interaction between the upstream cylinder shear layer and the downstream cylinder boundary layer and shear layer. The upstream cylinder shear layer lies outside the downstream one, without merging with it, until they are both entrained in the wake. This type of a double shear layer has not been reported in previous tandem cylinder studies, to the best of the authors' knowledge.

The wake of tandem cylinders in the reattachment regime is significantly altered with respect to a single cylinder at the same  $Re$ , with delayed separation on the downstream cylinder, a shortened recirculation length and a significantly narrowed wake width. We believe that forcing of the downstream cylinder boundary layer from the impinging part of the upstream shear layer, as well as interaction downstream of the reattachment point, causes transition to turbulence in the boundary layer.

The turbulent inflow to the downstream cylinder changes the flow topology of the wake, causing the disappearance the streamwise vortical structures seen for the single cylinder. This is due to enhanced diffusion and weaker large-scale vortex strength, both of which weaken the mode B type instability in the wake.

Finally, it is interesting to note that between the few tandem cylinder studies that have reported separation angle for the downstream cylinder, there is relatively good agreement even over a wide range of  $Re$ . Therefore, it is not an unreasonable conjecture that within the subcritical regime, the inflow  $Re$  has little influence on the flow field of the downstream cylinder, and the flow tends to a one-parameter case determined only by the gap ratio. A more extensive survey is required to conclude firmly.

**Supplementary movies.** Supplementary movies are available at <https://doi.org/10.1017/jfm.2022.960>.

**Funding.** This work is supported by the Research Council of Norway through the Public Sector PhD Scheme, and the National Public Roads Administration, where the first author is an employee. Computational hours were granted by the Norwegian HPC project NN9191K.

**Declaration of interest.** The authors report no conflict of interest.

**Author ORCIDs.**

- ◆ Tale E. Aasland <https://orcid.org/0000-0002-8504-930X>;
- ◆ Fengjian Jiang <https://orcid.org/0000-0002-5321-3275>.

## Appendix A. Flow around a single circular cylinder at Reynolds number 10 000

As a reference case, the flow field around a single cylinder at  $Re = 10\,000$  was computed. Statistical flow parameters are given in [table 2](#), and compared with previous investigations. The present results agree with the literature, although the obtained  $L_r$  is somewhat shorter. It is difficult to pinpoint the exact reason for this, but one possibility is that there is a long-term variation of  $L_r$  that has been captured in our simulation. For example [Dong \*et al.\* \(2006\)](#) sampled statistics over approximately 50 vortex shedding cycles, whereas we have sampled over nearly 350 cycles. For a single cylinder at  $Re = 3900$ , [Parnaudeau \*et al.\* \(2008\)](#) investigated the sensitivity of the recirculation length with respect to time integration, and found that no convergence can be expected before approximately 250 shedding cycles.

The time-averaged streamwise and crossflow velocities, as well as the streamlines, are shown in [figure 18](#). Separation occurs at  $\theta_1 = 88.1^\circ$ . This compares well with [Jordan \(2002\)](#), [Wornom \*et al.\* \(2011\)](#) and [Prsic \*et al.\* \(2014\)](#) who found primary separation at  $87.8^\circ$ ,  $87^\circ$  and  $87.6^\circ$ , respectively. [Son & Hanratty \(1969\)](#) reported separation at  $84^\circ$  for  $Re = 10^4$ .

	$Re$	$St$	$f_{sl}/f_v$	$C_D$	$C_{Lrms}$	$-\bar{C}_{pb}$	$L_r$	Method
Present study	$10^4$	0.201	12.95	1.28	0.587	1.22	0.62	DNS
Dong <i>et al.</i> (2006)	$10^4$	0.200	11.83	1.208	0.547	1.201	0.82	DNS
Gopalkrishnan (1993)	$10^4$	0.1932		1.1856	0.3842			Exp.
Jordan (2002)	$8.0 \times 10^3$	0.204	9.4	1.06	0.115	1.08		LES
Lo & Ko (2001)	$10^4$		16					Exp.
Khabbouchi <i>et al.</i> (2014)	$9.6 \times 10^3$	0.2	12.0					Exp.
Nguyen & Nguyen (2016)	$10^4$	0.1961		1.1329	0.3629	1.1		DES
Norberg (1987)	$8.0 \times 10^3$	0.205	10.2			1.0		Exp.
Norberg (1993)	$10^4$	0.2						Exp.
Prsic <i>et al.</i> (2014)	$1.3 \times 10^4$	0.2038		1.3132	0.5454	1.26	0.722	LES
Wei & Smith (1986)	$9.5 \times 10^3$		11					Exp.
	$1.1 \times 10^4$		12.5					
Wornom <i>et al.</i> (2011)	$10^4$	0.20		1.22	0.476	1.15	0.87	LES

Table 2. Flow statistics for a single cylinder. Wei & Smith (1986) tested several cylinders of varying diameter. Here, only the  $d = 5.84$  cm case is included. The drag and lift coefficients,  $C_D$  and  $C_L$ , are defined as  $C = 2F/\rho U_0^2 D L_z$ , where  $F$  is the drag or lift force,  $\rho$  is the fluid density and  $L_z$  is the spanwise cylinder length. The r.m.s. of  $C_L$  is used.

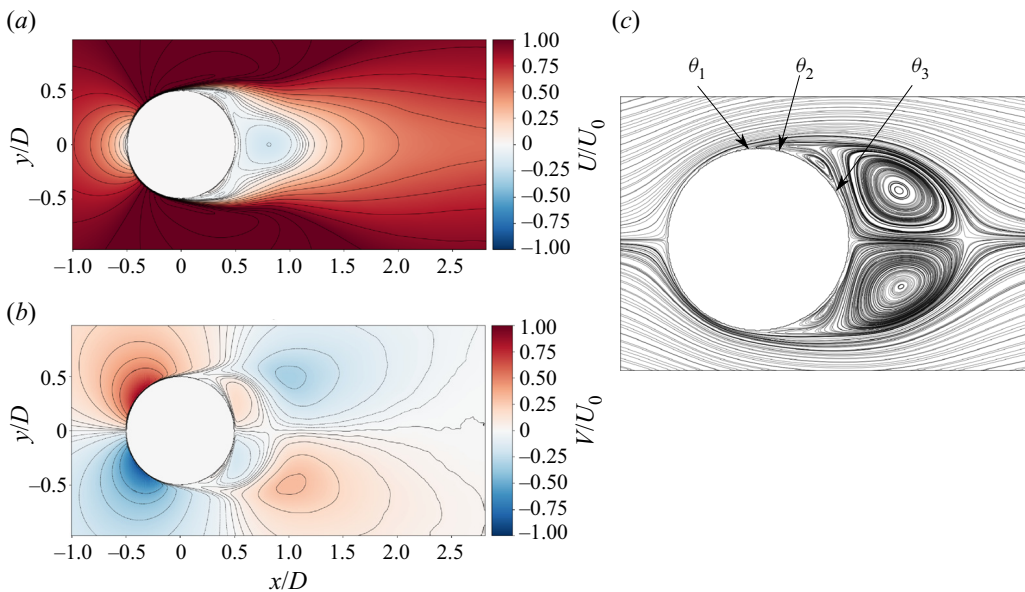


Figure 18. Time-averaged (a) streamwise and (b) crossflow velocities and (c) time-averaged streamlines for a single cylinder at  $Re = 10\,000$ . Primary separation occurs at  $\theta_1 = 88.1^\circ$ , and there is a secondary separation bubble.

There is secondary separation initiated by the recirculating flow at  $\theta_3 = 157.6^\circ$ , which reattaches at  $\theta_2 = 110.0^\circ$ . Both Prsic *et al.* (2014) and Son & Hanratty (1969) report secondary separation with  $\theta_2 = 106^\circ$ .

Figure 19(a) depicts the instantaneous flow, represented by the spanwise vorticity. The shear layers are almost parallel to each other, and roll up to form a von Kármán vortex street in the wake. Shear layer vortices form  $0.75D$ – $1.0D$  downstream of separation.



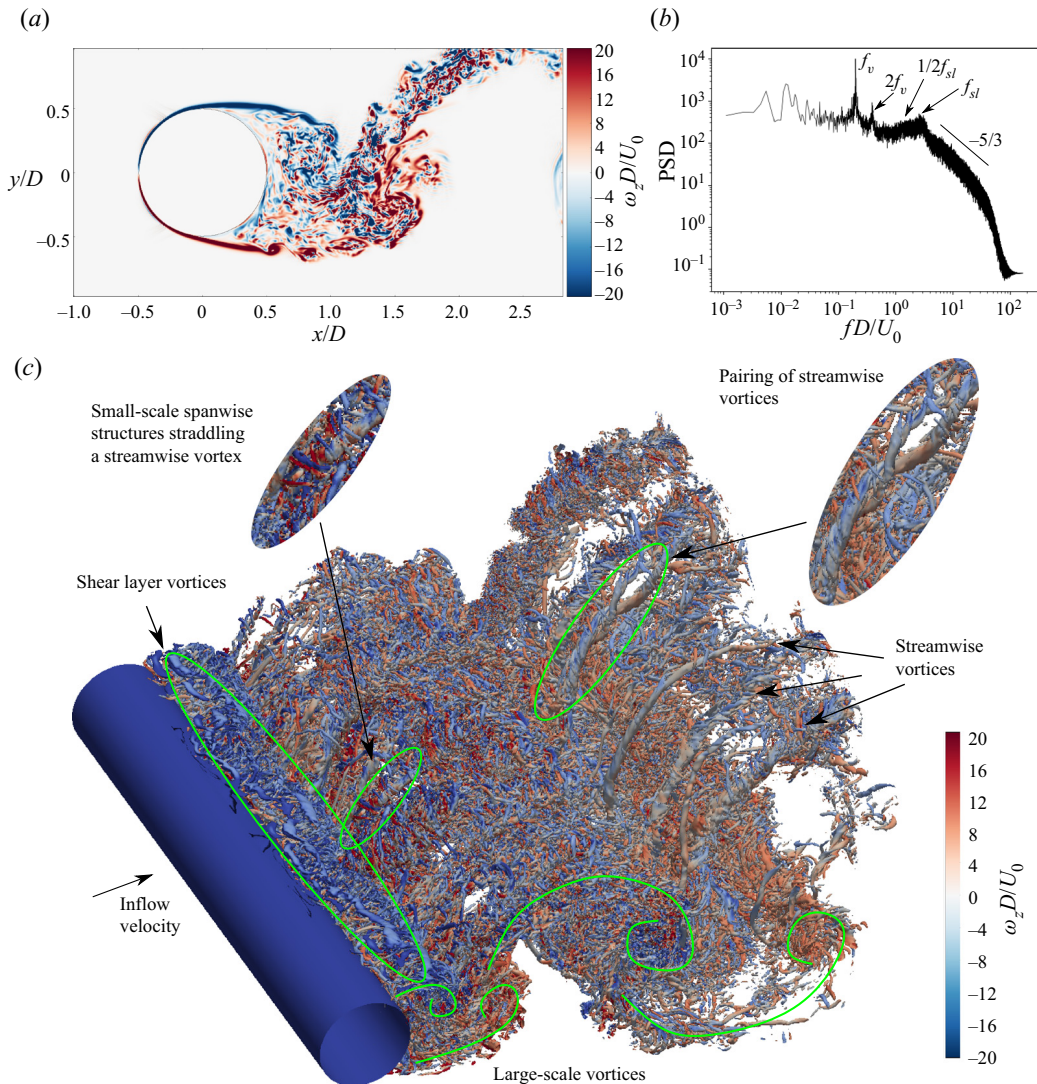


Figure 19. Instantaneous wake of a single cylinder at  $Re = 10\,000$ , at  $tU_0/D = 1050$ . (a) Spanwise vorticity in the plane  $z/D = 0$ . The shear layers are nearly parallel and shear layer vortices are formed  $0.75D-1D$  after separation. (b) Crossflow velocity spectrum at  $(x/D, y/D) = (0.4, 0.6)$ . (c) Isosurfaces of  $Q(D/U_0)^2 = 25$  coloured by  $\omega_z$ . Shear layer vortices organised in spanwise stacks are seen in the near-wake. Streamwise structures bridge the large-scale vortices in the wake, and the streamwise vortices are themselves straddled by small-scale spanwise vortices. Pairing of streamwise vortices is observed downstream.

In figure 19(c), the instantaneous wake structure is visualised by isosurfaces of non-dimensionalised  $Q$  (Hunt, Wray & Moin 1988). We see that the streamwise position of transition to turbulence in the shear layer is not coherent across the cylinder span. This spanwise non-uniformity of transition causes the shear layer vortices to appear in cells or stacks, which in turn causes dislocations in these small-scale structures, contributing to rapid development of three-dimensionality.

Owing to the high  $Re$ , the wake is turbulent and the large-scale vortices consist of a number of smaller structures with different orientations. The large-scale vortices are

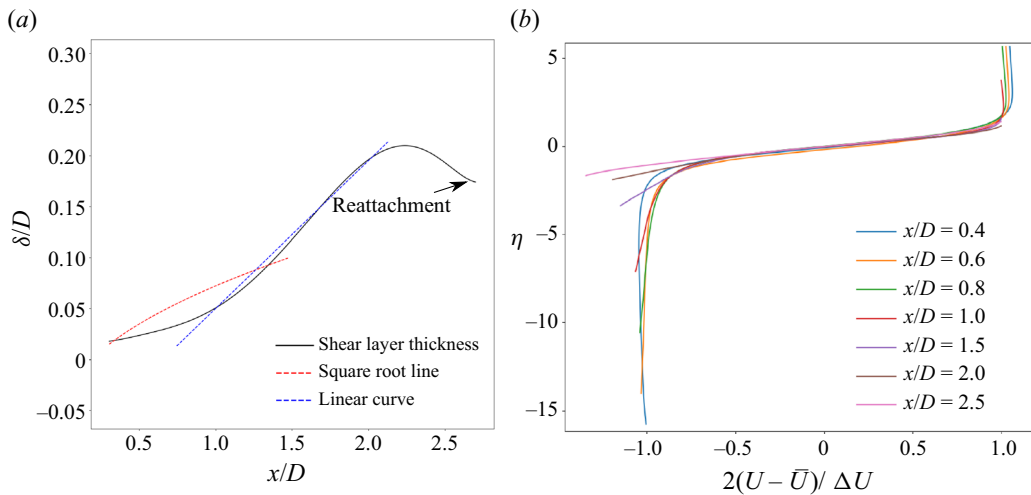


Figure 20. Shear layer thickness of the upstream cylinder, and velocity profiles in the gap plotted against similarity coordinates. To determine geometrical properties of the shear layer, the time-averaged free stream and gap velocities,  $U_f$  and  $U_g$ , were used. The shear layer thickness was defined as the distance between the points where the time-averaged streamwise velocity was equal to  $[\bar{U} + 0.5(U_f - \bar{U})]$  and  $[\bar{U} - 0.5(\bar{U} - U_g)]$ . Here,  $\bar{U} = 0.5(U_f + U_g)$ . The velocity profiles are normalised as  $U_n = 2(U - \bar{U})/\Delta U$ , where  $\Delta U = U_f - U_g$ . They have been plotted against the similarity variable  $\eta = (y - y_c)/\delta$ , where  $\delta$  is the shear layer thickness and  $y_c$  is the centreline of the shear layer.

connected by streamwise structures that form counter-rotating pairs. These are the result of a mode B three-dimensional wake instability (Williamson 1996).

In the near-wake, the streamwise vortical structures are straddled by several smaller vortices with spanwise orientation. The dynamics of the wake are complex, and pairing of streamwise vortices occurs. This is shown in an inset in figure 19(c), where two of these structure roll-around one another and combine. For mode B, the spanwise wavelength of the streamwise structures is expected to be around  $1D$ . Huang, Zhou & Zhou (2006) observed larger wavelengths than this at  $x/D = 5$ , for  $Re = 10\,000$ . The findings were attributed to spanwise vortex dislocations, but our visualisation indicates that vortex pairing is another possible explanation.

The crossflow velocity spectrum taken at a location in the shear layer is presented in figure 19(b). The large-scale shedding frequency and its first harmonic are seen, as well as the shear layer frequencies. The latter are seen as a broadband plateau centred around the shear layer vortex shedding frequency,  $f_{sl}$ . The plateau encompasses frequencies around the subharmonic  $0.5f_{sl}$ , which indicates that vortex pairing occurs in the shear layers.

## Appendix B. The similarity between tandem cylinder shear layers and plane mixing layers

It has been suggested that the time-averaged properties of shear layers in a cylinder near-wake where the von Kármán vortex shedding is suppressed develop similar to plane mixing layers (Unal & Rockwell 1988b; Cardell 1993). One study even makes this claim for cylinders with unimpeded vortex shedding (Khabbouchi *et al.* 2014). We have investigated this for the tandem cylinder case by looking at the shear layer thickness, and the behaviour of the streamwise velocity profiles in the gap, both shown in figure 20.

In the initial stages, the growth rate of the shear layer thickness is small, but it accelerates after  $0.8D$ . This is approximately where transition to turbulence starts, although there is a small variation in the location of the transition region, as we have seen. The growth of the gap shear layer is restricted by reattachment, and [figure 20\(a\)](#) shows how the shear layer thickness decreases after  $x/D \approx 2.25$ . This is the point where part of the shear layer starts diverting into the gap, and the remaining part goes on to reattach to the downstream cylinder. The approximate reattachment point is seen as a small kink at the end of the gap profile, around  $x/D = 2.7$ .

In a plane mixing layer, the width grows as the square root of the downstream distance within the laminar region, and linearly after transition (White 2006). This is distinctly not the case with the gap shear layer, as shown in [figure 20\(a\)](#). As the K-H instability is sometimes triggered as early as  $x/D = 0.4$ , the part of the shear layer which can strictly be called laminar is short. However, the square root curve is not a good fit in any part of the shear layer close to the upstream cylinder. With some goodwill, the growth post-transition can be called quasi-linear. Up to  $x/D \approx 2.0$ , the development of the shear layer thickness is qualitatively similar to a single circular cylinder (Gkiolas, Kapiris & Mathioulakis 2020), and, even more so, to side-by-side flat plates of gap width  $g/D = 1$  (Dadmarzi *et al.* 2018). These wake flows have large-scale vortex shedding in common. Clearly, the mixing layer analogy has its limits when there is formation of large-scale vortices.

The growth of the tandem cylinder shear layers between transition and reattachment does share some qualitative similarities with mixing layers. One is the transition through stretching of the shear layer vortices. Another is the growth of the structures that comprise the shear layer. Vortex pairing is known to be the primary mechanism of growth for plane mixing layers for low  $Re$  (Winant & Browand 1974). However, recent research has shown that in the transitional and turbulent states, the linear growth of the mixing layer thickness happens, not by vortex pairing, but by linear growth of the coherent spanwise vortices themselves. Although, vortex pairing certainly occurs after transition, it was found to be a consequence of the growth of the spanwise vortices, rather than the main cause for mixing layer growth (D'Ovidio & Coats 2013; McMullan, Gao & Coats 2015). This is reminiscent of the development of the tandem cylinder shear layer vortices after transition, recalling their transformation from compact vortex cores to larger, loosely coherent ensembles of small-scale structures. [Figure 9](#) also indicates that pairing events after transition do not increase the thickness of the shear layer, which corresponds with the findings of McMullan *et al.* (2015).

For both single and tandem circular cylinders, the shear layers do not reach a fully turbulent state before they roll up or reattach, respectively. Therefore, we cannot expect true self-similarity of the velocity profile across the shear layer. In this study, we do see a degree of self-similarity in the early part of the shear layer ( $x/D < 0.6$ ), as shown in [figure 20\(b\)](#). This part of the shear layer is predominantly laminar, with intermittent triggering of the K-H instability. Deviation from similarity develops as the transition region approaches, and is strongest in the lower part of the shear layer, due to the recirculation. The same discovery was made by Cardell (1993), who found two different similarity profiles in the shear layer: self-similarity in the initial growth stage, and the expected self-similarity for turbulent mixing layers, which could develop downstream when large-scale vortex formation was suppressed. The author suggested that it was possible that the boundary layer developed a self-similar profile prior to transition, and that this profile persisted in the laminar part of the shear layer.

This discussion serves to clarify a few points: the tandem cylinder shear layers are indeed mixing layer-like in that they have a quasi-linear growth after transition, and that vortex pairing occurs. However, the growth of the shear layer in the laminar region is

nothing like a mixing layer. This means that the near self-similarity in the laminar part of the shear layer cannot be used as an argument towards likeness with mixing layers. In extension, this also applies to single cylinders, because the mechanism of shear layer instability is the same for both cases.

REFERENCES

- AHMED, N.A. & WAGNER, D.J. 2003 Vortex shedding and transition frequencies associated with flow around a circular cylinder. *AIAA J.* **41** (3), 542–544.
- ALAM, M.M. 2014 The aerodynamics of a cylinder submerged in the wake of another. *J. Fluids Struct.* **51**, 393–400.
- ALAM, M.M., MORIYA, M., TAKAI, K. & SAKAMOTO, H. 2003 Fluctuating fluid forces acting on two circular cylinders in a tandem arrangement at a subcritical Reynolds number. *J. Wind Engng Ind. Aerodyn.* **91**, 139–154.
- ALJURE, D.E., LEHMKUHL, O., RODRIGUES, I. & OLIVA, A. 2017 Three dimensionality in the wake of the flow around a circular cylinder at Reynolds number 5000. *Comput. Fluids* **147**, 102–118.
- BEARMAN, P.W. & MOREL, T. 1983 Effect of free stream turbulence on the flow around bluff bodies. *Prog. Aerosp. Sci.* **20**, 98–123.
- BECKER, H.A. & MASSARO, T.A. 1968 Vortex evolution in a round jet. *J. Fluid Mech.* **31** (3), 435–448.
- BLOOR, S. 1964 The transition to turbulence in the wake of a circular cylinder. *J. Fluid Mech.* **19**, 290–301.
- CARDELL, G.S. 1993 Flow past a circular cylinder with a permeable wake splitter plate. PhD thesis, California Institute of Technology.
- CARMO, B., MENEGHINI, J. & SHERWIN, S. 2010 Secondary instabilities in the flow around two circular cylinders. *J. Fluid Mech.* **644**, 395–431.
- CHYU, C. & ROCKWELL, D. 1996a Evolution patterns of streamwise vorticity in the turbulent near wake of a circular cylinder. *J. Fluid Mech.* **320**, 117–137.
- CHYU, C. & ROCKWELL, D. 1996b Near wake structure of an oscillating cylinder: effect of controlled shear layer vortices. *J. Fluid Mech.* **322**, 21–49.
- DADMARZI, F.H., NARASIMHAMURTHY, V.D., ANDERSSON, H.I. & PETERSEN, B. 2018 Turbulent wake behind side-by-side flat plates: computational study of interference effects. *J. Fluid Mech.* **855**, 1040–1073.
- DONG, S., KARNIADAKIS, G.E., EKMEKCI, A. & ROCKWELL, D. 2006 A combined direct numerical simulation - particle image velocimetry study of the turbulent near wake. *J. Fluid Mech.* **569**, 185–207.
- D’OVIDIO, A. & COATS, C.M. 2013 Organised large structure in the post-transition mixing layer. Part 1. Experimental evidence. *J. Fluid Mech.* **737**, 466–498.
- FELLOUAH, H., BALL, C.G. & POLLARD, A. 2009 Reynolds number effects within the development region of a turbulent round free jet. *Intl J. Heat Mass Transfer* **52**, 3943–3954.
- GKIOLAS, D., KAPIRIS, P. & MATHIOULAKIS, D. 2020 Experimental study of the near wake of a circular cylinder and its detached shear layers. *Exp. Therm. Fluid Sci.* **113**, 110040.
- GOPALKRISHNAN, R. 1993 Vortex-induced forces on oscillating bluff cylinders. PhD thesis, Department of Ocean Engineering, MIT, Cambridge, MA.
- HAIN, R., KÄHLER, C.J. & MICHAELIS, D. 2008 Tomographic and time resolved PIV measurements on a finite cylinder mounted on a flat plate. *Exp. Fluids* **45**, 715–724.
- HU, X., ZHANG, X. & YOU, Y. 2019 On the flow around two circular cylinders in tandem arrangement at high Reynolds numbers. *Ocean Engng* **189**, 106301.
- HUANG, J.F., ZHOU, Y. & ZHOU, T. 2006 Three-dimensional wake structure measurement using a modified PIV technique. *Exp. Fluids* **40**, 884–896.
- HUNT, J.C.R., WRAY, A.A. & MOIN, P. 1988 Eddies, stream and convergence zones in turbulent flows. In *Center for Turbulence Research Report CTR-S88*, pp. 193–208.
- IGARASHI, T. 1981 Characteristics of the flow around two circular cylinders arranged in tandem (1st report). *Bull. JSME* **24** (188), 323–330.
- ISHIGAI, S., NISHIKAWA, E. & CHO, K. 1972 Experimental study of gas flow in tube banks with tube axes normal to flow (part 1, Kármán vortex flow around two tubes at various spacings). *Bull. JSME* **5** (86), 949–956.
- JIANG, F., PETERSEN, B. & ANDERSSON, H.I. 2019 Turbulent wake behind a concave curved cylinder. *J. Fluid Mech.* **878**, 663–699.

- JORDAN, S.A. 2002 Investigation of the cylinder separated shear-layer physics by large-eddy simulation. *Intl J. Heat Fluid Flow* **23**, 1–12.
- KHABBOUCHI, I., FELLOUAH, H., FERCHICHI, M. & GUELLOUZ, M.S. 2014 Effects of free-stream turbulence and Reynolds number on the separated shear layer from a circular cylinder. *J. Wind Engng Ind. Aerodyn.* **135**, 46–56.
- KITAGAWA, T. & OHTA, H. 2008 Numerical investigation on flow around circular cylinders in tandem arrangem at a subcritical Reynolds number. *J. Fluids Struct.* **24**, 680–699.
- KOURTA, A., BOISSIN, H.C., CHASSING, P. & HA MINH, H. 1987 Nonlinear interaction and the transition to turbulence in the wake of a circular cylinder. *J. Fluid Mech.* **181**, 141–161.
- KRAICHNAN, R.H. 1974 On Kolmogorov's inertial-range theories. *J. Fluid Mech.* **62** (2), 305–330.
- LAW, C.W. & KO, N.W.M. 2001 Bistable flow in lower transition regime of circular cylinder. *Fluid Dyn. Res.* **29**, 313–344.
- LEE, T. & BASU, S. 1997 Nonintrusive measurements of the boundary layer developing on a single and two cylinders. *Exp. Fluids* **23**, 187–192.
- LIN, J.-C., YANG, Y. & ROCKWELL, D. 2002 Flow past two cylinders in tandem: instantaneous and averaged flow structure. *J. Fluids Struct.* **16** (8), 1059–1071.
- LJUNGKRONA, L., NORBERG, C.H. & SUNDEN, B. 1991 Free-stream turbulence and tube spacing effect on surface pressure fluctuations for two tubes in an in-line arrangement. *J. Fluids Struct.* **5**, 701–727.
- LO, K.W. & KO, N.M.W. 2001 At the upper transition of subcritical regime of a circular cylinder. *Trans. ASME J. Fluids Engng* **123**, 422–434.
- MANHART, M. 2004 A zonal grid algorithm for DNS of turbulent boundary layers. *Comput. Fluids* **33**, 435–461.
- MCMULLAN, W.A., GAO, S. & COATS, C.M. 2015 Organised large structure in the post-transition mixing layer. Part 2. Large-eddy simulation. *J. Fluid Mech.* **762**, 302–343.
- NGUYEN, V.-T. & NGUYEN, H.H. 2016 Detached eddy simulations of flow induced vibrations of circular cylinders at high Reynolds numbers. *J. Fluids Struct.* **63**, 103–119.
- NORBERG, C. 1987 Effects of Reynolds number and low-intensity freestream turbulence on the flow around a circular cylinder. PhD thesis, Chalmers Tekniska Hogskola.
- NORBERG, C. 1993 Pressure forces on a circular cylinder in cross flow. In *Bluff-Body Wakes and Instabilities* (ed. H. Eckelmann, J.M.R. Graham & P.A. Monkewitz), pp. 275–278. Springer-Verlag.
- OKAJIMA, A. 1979 Flows around two tandem circular cylinders at very high Reynolds numbers. *Bull. JSME* **22**, 504–511.
- OZONO, S. 1999 Flow control of vortex shedding by a short splitter plate asymmetrically arranged downstream of a cylinder. *Phys. Fluids* **11**, 2928–2934.
- PARNAUDEAU, P., CARLIER, J., HEITZ, D. & LAMBALLAIS, E. 2008 Experimental and numerical studies of the flow over a circular cylinder at Reynolds number 3900. *Phys. Fluids* **20**, 085101.
- PELLER, N., LE DUC, A., TREMBLAY, T. & MANHART, M. 2006 High-order stable interpolations for immersed boundary methods. *Intl J. Numer. Meth. Fluids* **53**, 1175–1193.
- PETERKA, J.A. & RICHARDSON, P.D. 1969 Effect of sound on separated flows. *J. Fluid Mech.* **37**, 265–287.
- PRASAD, A. & WILLIAMSON, C.H.K. 1997 The instability of the shear layer separating from a bluff body. *J. Fluid Mech.* **333**, 375–402.
- PRASIC, M., ONG, M.C., PETTERSEN, B. & MYRHAUG, D. 2014 Large eddy simulations of flow around a smooth circular cylinder in uniform current in the subcritical flow regime. *Ocean Engng* **77**, 61–73.
- RAI, M.M. 2010 A computational investigation of the instability of the detached shear layers in the wake of a circular cylinder. *J. Fluid Mech.* **659**, 375–404.
- RAJAGOPALAN, S. & ANTONIA, R.A. 2005 Flow around a circular cylinder - structure of near wake shear layer. *Exp. Fluids* **38**, 393–402.
- ROSHKO, A. 1954 On the drag and shedding frequency of two-dimensional bluff bodies. NACA Tech. Note 3169.
- SON, J.S. & HANRATTY, T. 1969 Velocity gradients at the wall for flow around a cylinder at Reynolds numbers from 5k to 100k. *J. Fluid Mech.* **35**, 353–368.
- SUMNER, D. 2010 Two circular cylinders in cross-flow: a review. *J. Fluids Struct.* **26**, 849–899.
- UNAL, M.F. & ROCKWELL, D. 1988a On the vortex formation from a cylinder, part 1. The initial instability. *J. Fluid Mech.* **190**, 491–512.
- UNAL, M.F. & ROCKWELL, D. 1988b On the vortex formation from a cylinder, part 2. Control by splitter plate interference. *J. Fluid Mech.* **190**, 513–529.
- WANG, L., ALAM, M. & ZHOU, Y. 2018 Two tandem cylinders of different diameters in cross-flow: effect of an upstream cylinder on wake dynamics. *J. Fluid Mech.* **836**, 5–42.

## Revisiting the reattachment regime

- WEI, T. & SMITH, C.R. 1986 Secondary vortices in the wake of circular cylinders. *J. Fluid Mech.* **169**, 513–533.
- WHITE, F.M. 2006 *Viscous Fluid Flow*, 3rd edn, Table 6.3. McGraw Hill.
- WILLIAMSON, C.H.K. 1995 Scaling of streamwise structures in wakes. *Phys. Fluids* **7**, 2307–2309.
- WILLIAMSON, C.H.K. 1996 Vortex dynamics in the cylinder wake. *Annu. Rev. Fluid Mech.* **28**, 477–539.
- WINANT, C.D. & BROWAND, F.K. 1974 Vortex pairing: the mechanism of turbulent mixing-layer growth at moderate Reynolds number. *J. Fluid Mech.* **63** (2), 237–255.
- WORNOM, S., OUVRARD, H., SALVETTI, M.V., KOOBUS, B. & DERVIEUX, A. 2011 Variational multiscale large-eddy simulations of the flow past a circular cylinder: Reynolds number effects. *Comput. Fluids* **47**, 44–50.
- WU, J., WELSH, L.W., WELCH, M.C., SHERIDAN, J. & WALKER, G.J. 1994 Spanwise wake structure of a circular cylinder and two circular cylinders in tandem. *Exp. Therm. Fluid Sci.* **9**, 299–308.
- XU, G. & ZHOU, Y. 2004 Strouhal numbers in the wake of two inline cylinders. *Exp. Fluids* **37**, 248–256.
- YAACOB, M.R., BUCHHAVE, P. & VELTE, C.M. 2021 Mapping of energy cascade in the developing region of a turbulent round jet. *Evergreen Joint J. Novel Carbon Resource Sci. Green Asia Strat.* **8** (2), 379–396.
- ZDRAVKOVICH, M.M. 1987 The effect of interference between circular cylinders in cross flow. *J. Fluids Struct.* **1**, 239–261.
- ZDRAVKOVICH, M.M. 1997 *Flow Around Circular Cylinders Vol 1: Fundamentals*, chap. 14, pp. 432–442. Oxford University Press.
- ZHOU, Y. & ALAM, M.M. 2016 Wake of two interacting circular cylinders: a review. *Intl J. Heat Fluid Flow* **62**, 510–537.
- ZHOU, Q., ALAM, M.M., CAO, S., LIAO, H. & LI, M. 2019 Numerical study of wake and aerodynamic forces on two tandem circular cylinders at  $Re$  1000. *Phys. Fluids* **31**, 045103.
- ZHOU, Y. & YIU, M. 2006 Flow structure, momentum and heat transport in a two-tandem-cylinder wake. *J. Fluid Mech.* **548**, 17–48.

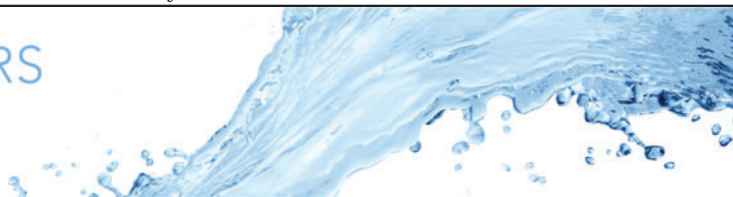


### **3.2 Paper 2. Asymmetric cellular bi-stability in the gap between tandem cylinders**

Aasland, T. E., Pettersen, B., Andersson, H. I. & Jiang, F. 2023 Asymmetric cellular bi-stability in the gap between tandem cylinders. *Journal of Fluid Mechanics*, **966**, A39. <https://doi.org/10.1017/jfm.2023.468>







# Asymmetric cellular bi-stability in the gap between tandem cylinders

Tale E. Aasland<sup>1,†</sup>, Bjørnar Pettersen<sup>1</sup>, Helge I. Andersson<sup>1</sup> and Fengjian Jiang<sup>2</sup>

<sup>1</sup>Department of Marine Technology, Norwegian University of Science and Technology, NO-7491 Trondheim, Norway

<sup>2</sup>SINTEF Ocean, NO-7052 Trondheim, Norway

(Received 13 February 2023; revised 11 May 2023; accepted 6 June 2023)

In the gap region of tandem cylinders, within the reattachment regime, bi-stability is seen to be cellular. Direct numerical simulations at a Reynolds number of 500, and a gap ratio of 3.0, show that shedding of gap vortices occurs in spanwise cells, with lengths between 0.3 and 2.7 cylinder diameters. These unstable vortex cells tend to be asymmetric with respect to the gap centreline, so that vortices are repeatedly shed from just one gap shear layer for several periods. The unstable cells appear within the basic spanwise cell structure dictated by the three-dimensional instability, and their cell lengths do not exceed those of the basic cells. Unstable cells intermittently become spanwise coherent, and this leads to a significant increase in drag amplitude. The mode change in the gap is associated with low-frequency variation of the reattachment and separation points on the downstream cylinder, causing low-frequency modulation of the vortex formation length.

**Key words:** vortex shedding, vortex dynamics, separated flows

## 1. Introduction

Flow around tandem cylinders has attracted considerable research interest both from an engineering point of view and among those who study the fundamentals of fluid mechanics. While there are now quite a number of investigations into this topic, its complex form of wake interference is still not fully understood. This is particularly true for the transition between tandem cylinder flow regimes, where the flow may be unstable and hysteretic (Carmo *et al.* 2010*b*).

† Email address for correspondence: [tale.e.aasland@ntnu.no](mailto:tale.e.aasland@ntnu.no)

Generally, there are three different regimes of tandem cylinder flow: overshoot, reattachment and co-shedding. These depend on the spacing between the cylinders and on the Reynolds number,  $Re = U_0 D/\nu$  (here,  $U_0$  is the inflow velocity,  $D$  is the cylinder diameter and  $\nu$  is the kinematic viscosity of the fluid). When the cylinders are very close, the shear layers from the upstream cylinder envelop the downstream cylinder and roll up in the wake, so that vortex shedding occurs solely from the upstream cylinder. Increasing the spacing between the cylinders leads to reattachment of the upstream shear layers onto the downstream cylinder. Vortex shedding now occurs from the downstream cylinder. Reattachment may be alternating, quasi-steady/symmetrical or intermittent, from smaller to larger spacing (Zdravkovich 1987). Further increase of the spacing will finally result in vortex shedding from both cylinders, so that there is a wake in the gap between them, i.e. co-shedding.

Due to Reynolds number dependency (Xu & Zhou 2004), it is challenging to give a consistent classification of tandem cylinder flow regimes based on the cylinder spacing alone. Still, the classification of Zdravkovich (1987) is commonly used: (a) overshoot/no reattachment  $1.0 \leq L/D \leq 1.2 - 1.8$ , (b) reattachment  $1.2 - 1.8 \leq L/D \leq 3.4 - 3.8$  and (c) co-shedding  $3.4 - 3.8 \leq L/D$ . Here,  $L/D$  is the centre-to-centre cylinder spacing, normally called the gap ratio, a term that will be used throughout the present paper from here on.

Reattachment may occur on the downstream or upstream side of the downstream cylinder. Based on this, Xu & Zhou (2004) suggested that the reattachment regime should be subdivided (as well as extended with respect to the findings of Zdravkovich (1987)): in the range  $2 \leq L/D \leq 3$  there is a transition from overshoot to reattachment and in the range  $3 \leq L/D \leq 5$  the flow transitions from reattachment to co-shedding.

The gap ratio at which co-shedding first occurs is traditionally called the critical spacing, or drag-inversion spacing. The latter term hails from the fact that, as long as there is shear layer reattachment, recirculation in the gap causes suction and results in a negative drag coefficient for the downstream cylinder. When co-shedding commences, the sign of the downstream cylinder drag coefficient is reversed, and becomes positive. Drag inversion typically occurs between  $L/D = 3.0$  and  $5.0$  (Okajima 1979; Igarashi 1981; Xu & Zhou 2004; Alam 2014), depending on the Reynolds number, but also on factors such as free-stream turbulence (Ljungkrona, Norberg & Sunden 1991) or inflow gust amplitude (Wang *et al.* 2022), as well as the aspect ratio (Carmo, Meneghini & Sherwin 2010a). Higher  $Re$  and increased non-uniformity of the inflow conditions favour transition at lower gap ratios. The effect of aspect ratio is related to the development of three-dimensionalities in the wake at moderate Reynolds numbers, which will be elaborated shortly. For further details regarding the co-shedding regime, the reader is referred to the reviews of Sumner (2010) and Zhou & Alam (2016).

Within the reattachment regime, there are recirculating vortices in the gap. For lower gap ratios, these tend to be symmetrical (Lin, Yang & Rockwell 2002), but become alternating as the gap ratio increases (Carmo, Meneghini & Sherwin 2010b; Zhou *et al.* 2019). Such vortices are often called quasi-stationary or quasi-steady in the literature, because their formation length is limited by the gap length, and thus they remain at essentially the same streamwise location. Herein, we call them ‘gap vortices’ or ‘recirculating vortices’ for simplicity. Igarashi (1981) discovered that close to the drag-inversion spacing, the gap vortices became unstable and shedding was detected intermittently (called regime D in that study). This is the beginning of a regime where the flow may switch intermittently between reattachment and co-shedding. The term ‘bi-stability’ was first used by Igarashi (1981) to describe this behaviour, and has been widely adopted since.

Bi-stability manifests as dual peaks in the velocity spectra. In the study of Igarashi (1981), for a given gap ratio, the peaks start out at similar frequencies, but move further apart as the Reynolds number increases. Based on the measured data, as well as flow visualisations, it was concluded that the flow exhibited two stable states (although it may perhaps be more accurate to call them conditionally stable), with one of them (reattachment) being ‘more stable than the other’. The number of occurrences of intermittent co-shedding and their duration increased with increasing Reynolds number and/or gap ratio.

Xu & Zhou (2004) reported another type of bi-stable flow, namely a switch between stable overshoot and stable reattachment. For gap ratios 2.0, 2.5 and 3.0, this occurred within the Reynolds number ranges  $Re = 5 \times 10^3 - 7 \times 10^3$ ,  $Re = 4 \times 10^3 - 7 \times 10^3$  and  $Re = 3 \times 10^3 - 6 \times 10^3$ , respectively.

At first, the relationship between gap ratio, Reynolds number and tandem flow regimes received more interest than the three-dimensional characteristics of the flow field (Zdravkovich 1972, 1987; Lee & Basu 1997; Xu & Zhou 2004; Zhou & Yiu 2006; Alam *et al.* 2003). This changed with three studies published nearly at the same time, independently of each other: Deng *et al.* (2006), Papaioannou *et al.* (2006) and Carmo & Meneghini (2006). Wake transition was the main interest of Deng *et al.* (2006) and Carmo & Meneghini (2006), whereas Papaioannou *et al.* (2006) also quantified three-dimensional effects and spanwise variations. A common conclusion of all three investigations was that two-dimensional numerical simulations fail to predict the correct drag-inversion spacing for a three-dimensional wake. Moreover, both Deng *et al.* (2006) and Papaioannou *et al.* (2006) note that the downstream cylinder may partially or completely suppress three-dimensionality when placed within the drag-inversion spacing. This corresponds well to previous observations that transition to turbulence in the wake occurred later, in terms of Reynolds number, for tandem cylinders within the reattachment regime, than for a single cylinder (Zdravkovich 1972).

The work of Carmo & Meneghini (2006) was later expanded to include a classification of secondary instabilities in tandem cylinder wakes (Carmo *et al.* 2010*b*) and the relation between the onset of these instabilities and transition between tandem cylinder flow regimes (Carmo *et al.* 2010*a*). Three different secondary instability mechanisms for tandem cylinders were identified, T1–T3. The third type is most pertinent to the present study, as we shall soon see, because, among the different three-dimensional instabilities, only T3 originates in the gap. Carmo *et al.* (2010*b*) argue that this mode is kindred to the mode A (Williamson 1996) of single cylinders (albeit with oppositely signed streamwise vorticity). Their reasoning is that the underlying physical mechanism, namely a cooperative elliptical instability, is the same. The cooperative nature of the instability, meaning that it depends on interaction between the shear layers, was verified by placing a splitter plate in the far end of the gap. This was seen to obliterate three-dimensionality altogether for  $L/D = 2.3$ ,  $Re = 300$ .

Regarding drag inversion and wake transition predictions, it is the characteristic perturbation wavelength of the three-dimensional instabilities that causes the discrepancy between two-dimensional and three-dimensional simulations, as well as between studies with low and high aspect ratios. For instance, Carmo *et al.* (2010*a*) report that, for  $L/D = 3.5$ , the onset of T3 occurs at  $Re = 217$ , with a wavelength of  $9.97D$ . In comparison, Deng *et al.* (2006) report onset of three-dimensionality at  $Re = 250$ , with a mode A structure. Carmo *et al.* (2010*a*) argue that Deng *et al.* (2006) could not capture mode T3 because of insufficient spanwise domain length.

The three-dimensional wake instability causes waviness of the spanwise vortex cores, and this waviness gives rise to phase differences in the flow field, as observed by

Papaioannou *et al.* (2006). In their case with  $L/D = 2$  and  $Re = 500$ , both gap and wake show clear evidence of periodic spanwise structures. A similar result was recently reported by Wang *et al.* (2021) for channel-confined tandem cylinders.

The existence of spanwise phase differences implies the possibility of variation between different tandem flow regimes along the cylinder span, near the drag-inversion spacing. This idea was put forth by Aasland *et al.* (2022), who suggested that bi-stability may occur in spanwise cells, based on the observation of spanwise inhomogeneity at  $L/D = 3$  and  $Re = 10\,000$ . In the present study, we have investigated this hypothesis. A Reynolds number of 500 was chosen, in order to ascertain that the flow regime was far away from transition between different three-dimensional instabilities. The gap ratio was kept at  $L/D = 3$ . According to Carmo *et al.* (2010a), the present study should be well within the region of T3. Moreover, using a lower Reynolds number allowed for a long spanwise length while keeping the computational cost manageable. Tandem cylinders near the drag-inversion spacing bring together several fundamental phenomena of bluff-body fluid mechanics, and the outcome of the computation will enable an in-depth exploration of the surprisingly complex vortex dynamics in this particular flow regime.

## 2. Problem formulation and computational approach

### 2.1. Governing equations and numerical method

In the present study, the incompressible continuity and Navier–Stokes equations are solved by means of direct numerical simulations (DNS). The governing equations are

$$\frac{\partial u_i}{\partial x_i} = 0, \quad (2.1)$$

$$\frac{\partial u_i}{\partial t} + u_j \frac{\partial u_i}{\partial x_j} = -\frac{1}{\rho} \frac{\partial P}{\partial x_i} + \frac{\partial}{\partial x_j} \left( \nu \left[ \frac{\partial u_i}{\partial x_j} + \frac{\partial u_j}{\partial x_i} \right] \right), \quad i, j = 1, 2, 3, \quad (2.2)$$

where  $u$  is velocity,  $P$  is pressure and  $\rho$  is fluid density. The simulation was carried out using the MGLET (Multi Grid Large Eddy Turbulence) flow solver. MGLET is based on a finite volume formulation of the incompressible Navier–Stokes equations, and uses a staggered Cartesian grid (Manhart 2004). Solid bodies are introduced through an immersed boundary method (Peller *et al.* 2006), where the boundary is discretised using a cut-cell approach. A third-order low-storage explicit Runge–Kutta time integration scheme is used for time stepping, and the Poisson equation is solved using an iterative, strongly implicit procedure.

Periodic boundary conditions were used in the spanwise direction, and a free-slip condition was used on the top and bottom boundaries ( $y$ -direction, see figure 1a). Uniform inflow was imposed at the inlet, and a Neumann condition was imposed on the velocity components at the outlet.

In order to accelerate the development of the flow field, a turbulence intensity of 0.2% was imposed in the domain for a short time, at the very beginning of the simulation. Sampling of statistics started after 100 convective time units ( $U_0/D$ ). Before sampling commenced, the time step was gradually adjusted to obtain a target Courant number of 0.5. The final non-dimensional time step was  $dt = 2.0562 \times 10^{-3}$ . Statistics were sampled for 800 time units, which amounts to around 114 vortex shedding cycles.

### 2.2. Computational domain and grid

The computational domain and a schematic view of the grid are displayed in figure 1. The inflow boundary is located at  $x/D = -15$ . The grid is refined in nested boxes, as shown

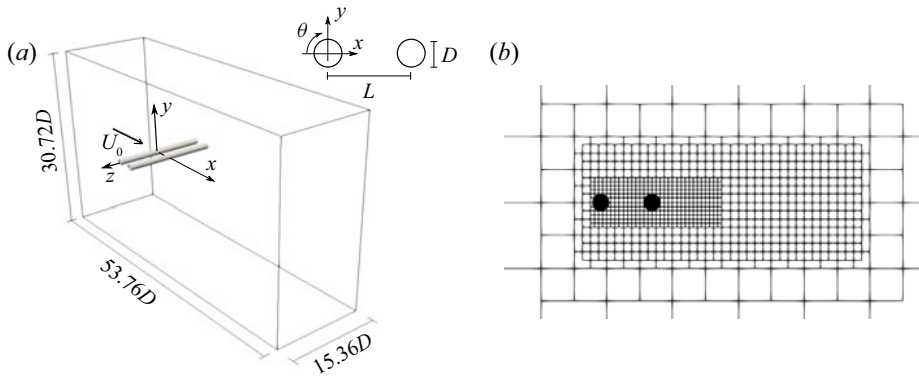


Figure 1. Computational domain and (b) grid schematic.

in figure 1(b), where each child box has half the cell size of its parent. The nested grid structure is the reason for the seemingly arbitrary domain size, since each dimension must be an integer multiple of the largest grid cell size. There were six grid levels in total, and the smallest grid cell size was  $dx = dy = dz = 0.0075D$ . This gives a total number of grid cells of nearly  $1.4 \times 10^9$ . The innermost grid refinement box is  $2.5D$  long in the  $y$ -direction (symmetrical about  $y/D = 0$ ), and stretches from  $x/D = -0.63$  to  $x/D = 7.0$ . The finest grid spans the entire domain in  $z$ -direction.

A grid convergence study has not been carried out specifically for the purpose of this investigation. However, in our previous study with a Reynolds number of 10 000, a grid cell size of  $0.005D$  gave good results (Aasland *et al.* 2022). Therefore, we are confident that a similar cell size will be sufficient also at the present Reynolds number, which is nearly two orders of magnitude lower.

The effect of spanwise length and spanwise boundary conditions on the flow field was assessed, without any change of the grid cell size and distribution. A pair of simulations were carried out initially, using a spanwise domain size of  $L_z = 7.68D$ . One case used periodic spanwise boundary conditions, and the other used free-slip spanwise boundary conditions. Statistical sampling time was 700 and 600 time units, respectively. The results are listed in table 1, and it is clear that the main statistical quantities are quite robust, with differences of the order of 1% or 2%. The use of free-slip walls more than doubles the value of the spanwise force fluctuations, however. For the periodic  $L_z = 7.68D$  case, the values are  $C_{zrms} = 3.1 \times 10^{-4}$  and  $6.7 \times 10^{-4}$ , for the upstream and downstream cylinders, respectively, whereas for the free-slip case, the corresponding values are  $C_{zrms} = 7.9 \times 10^{-4}$  and  $17.2 \times 10^{-4}$ . This increase of spanwise force fluctuations is reflected in the spanwise velocity fluctuations, and gives rise to more frequent occurrences of the second gap vortex mode described in § 3.2.

In the case of periodic spanwise boundary conditions, there is virtually no difference in the main statistics between  $L_z = 7.68D$  and  $15.36D$ . Thus,  $L_z = 7.68D$  is possibly sufficient in order to capture the physics of the present case. It was the wholly unexpected observation of the long-term gap asymmetry, detailed in § 3.2, that precipitated the doubling of the spanwise domain size. The asymmetry was initially believed to be an effect of numerical perturbations related to the spanwise length, but was found to be a real physical phenomenon. Despite the increased computational cost, we decided to continue with  $L_z = 15.36D$  in order to get a better overview of the complex spanwise variations of the flow field.

	$Re$	$L/D$	Upstream cylinder			Downstream cylinder			$St$	
			$\bar{C}_{Du}$	$C_{Lrmsu}$	$-\bar{C}_{pbu}$	$\bar{C}_{Dd}$	$C_{Lrmsd}$	$-\bar{C}_{pbd}$		$\theta_r$ (deg.)
Present study										
$L_z = 7.68D$ , slip boundary condition	500	3.0	0.917	0.023	0.60	-0.145	0.312	0.40	69.5	0.140/0.159
$L_z = 7.68D$ , periodic boundary condition	500	3.0	0.917	0.024	0.60	-0.142	0.320	0.40	69.6	0.141/0.156
$L_z = 15.36D$ , periodic boundary condition	500	3.0	0.917	0.023	0.60	-0.146	0.313	0.39	66.6	0.143/0.155
Papaioannou <i>et al.</i> (2006)	500	2.5	0.958	—	—	-0.142	—	—	—	0.150
Papaioannou <i>et al.</i> (2006)	500	3.5	0.894	—	—	-0.126	—	—	—	0.144
Song & Zhu (2017)	500	3.0	1.12	—	—	-0.25	—	—	—	—
Zhou <i>et al.</i> (2019)	1000	3.0	0.88	0.03	0.63	-0.15	0.34	0.42	67	0.149
Kitagawa & Ohia (2008)	22 000	3.0	0.80	0.02	0.6	-0.20	0.3	0.4	70	0.155/0.165
Lee & Basu (1997)	40 000	3.2	—	—	—	—	—	0.45	67.2	0.144

Table 1. Main statistics compared with results in the literature. Here,  $\theta_r$  denotes the reattachment angle (see figure 2).

## Asymmetric cellular bi-stability in tandem cylinder flow

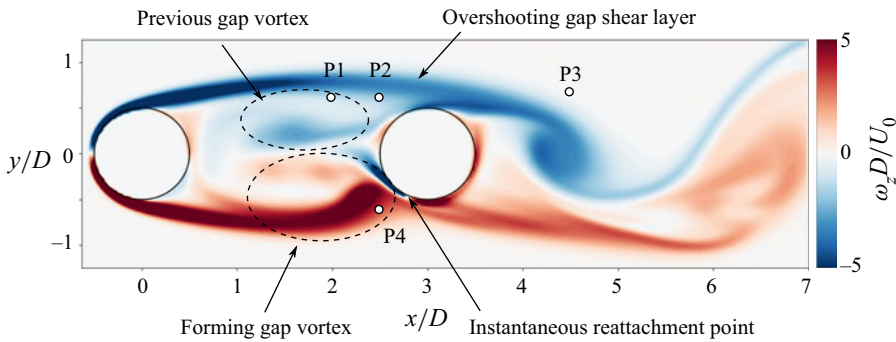


Figure 2. Basic flow regime, i.e. alternating reattachment/overshoot, illustrated by a snapshot at  $tU_0/D = 126.23$ ,  $z/D = 1$ . Recirculating vortices alternate in the gap. The gap shear layer which is not rolling up overshoots the downstream cylinder, merging with its shear layer. The instantaneous location of shear layer reattachment is marked in the figure. The time-averaged position of this point is denoted  $\theta_r$ . The small circles mark probe lines used for sampling velocity data for spectral analysis; P1 and P2 are located at  $(x/D, y/D) = (1.98, 0.60)$  and  $(x/D, y/D) = (2.49, 0.60)$ , respectively, P3 is located at  $(x/D, y/D) = (4.50, 0.65)$  and P4 at  $(x/D, y/D) = (2.49, -0.60)$ .

Finally, the spanwise coherence described in § 3.3 occurred once during the  $L_z = 7.68D$  periodic simulation, but not for the free-slip simulation. This may be due to the duration of the simulation, and we cannot conclude on whether it is an effect of the boundary conditions.

### 2.3. Definitions

The time-averaged base pressure coefficient is given as  $\bar{C}_{pb} = (\bar{P} - \bar{P}_0)/(\bar{P}_s - \bar{P}_0)$ . Here,  $\bar{P}_0$  is the pressure at the inlet and  $\bar{P}_s$  is the stagnation pressure. Force coefficients are defined as  $C_F = 2F/\rho U_0^2 A$ , where  $F$  is the force component in question,  $\rho$  is the fluid density and  $A$  is the projected frontal area. The lift coefficient is given by its root mean square (r.m.s.) value. Subscripts  $D$  and  $L$  denote drag and lift, respectively. To separate the upstream and downstream cylinder coefficients, lower case  $u$  and  $d$  subscripts are used. The Strouhal number is defined as  $St = f_v U_0/D$ , where  $f_v$  is the von Kármán vortex shedding frequency.

Herein, spectral analysis has been carried out by means of fast Fourier transform (FFT) of velocity time traces from a set of probes in the wake and gap. These probes have an internal spacing of  $0.03D$ , which corresponds to the grid resolution on the third finest grid level. The frequency resolution was approximately  $0.0012U_0/D$ .

## 3. Results

### 3.1. Overview of the flow topology

In the present study, with  $L/D = 3.0$  and  $Re = 500$ , the basic tandem cylinder flow regime is alternating overshoot/reattachment, where the reattachment points are located on the upstream side of the downstream cylinder, as illustrated in figure 2. Recirculating vortices form alternately in the gap. The gap shear layer which is not undergoing roll-up overshoots the downstream cylinder and merges with its shear layer in the near wake. The shear layers are laminar and transition to turbulence occurs in the wake. Figure 3 gives an instantaneous view of the flow topology. In both the gap and wake, the flow exhibits strong three-dimensional features. Streamwise vortical structures bridge the von Kármán



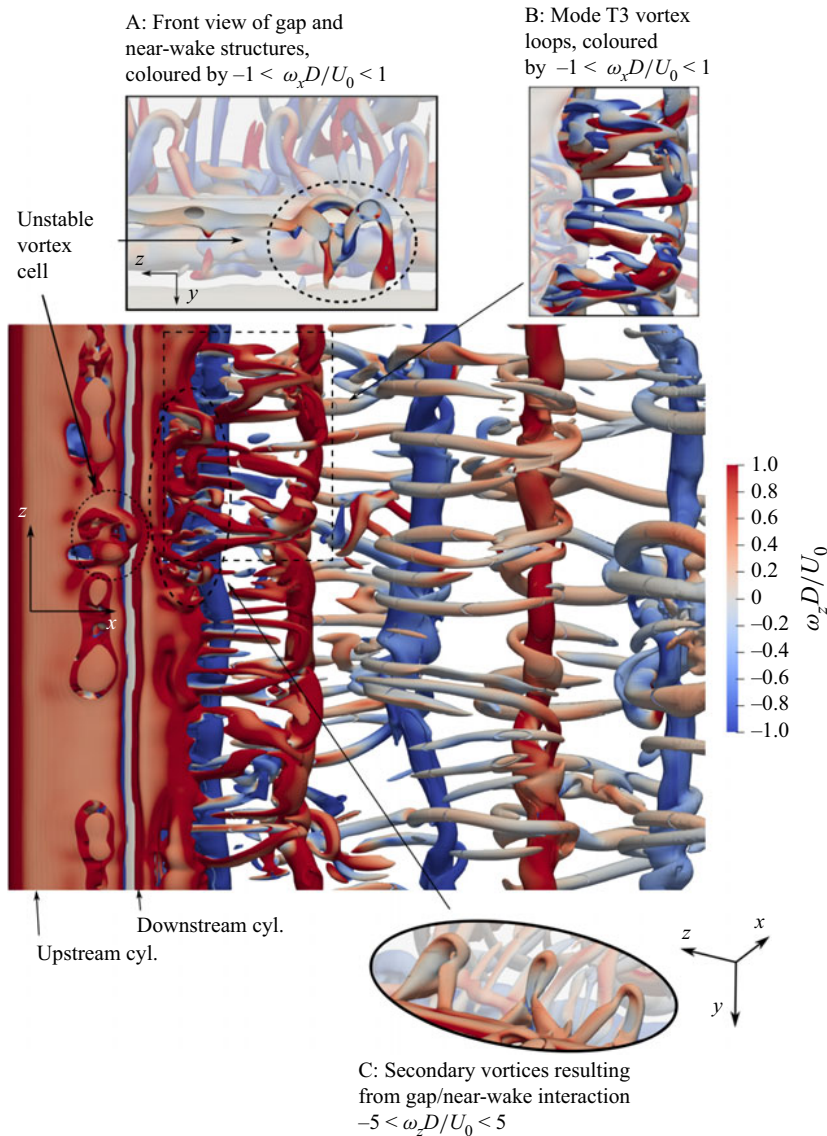


Figure 3. Instantaneous view of the lower shear layer at  $tU_0/D = 800.77$ . The flow field is visualised by isosurfaces of  $Q(D/U_0)^2 = 0.05$ , coloured by the spanwise vorticity. Inset A shows an unstable vortex cell coloured by the streamwise vorticity. Here,  $Q(D/U_0)^2 = 1$  is used. Mode T3 type vortical structures are shown in inset B. Inset C shows secondary vortices in the near wake. The formation process of such vortices is illustrated in [figure 7](#).

vortices, forming loops: this is the three-dimensional instability T3, as described by Carmo *et al.* (2010b) (see [figure 3](#), inset B).

The main statistics are listed in [table 1](#), and there is good agreement between the present study and results from the literature.

The flow is clearly bi-stable, with two modes that have distinct Strouhal numbers. This is seen from the velocity spectra in the gap and wake, shown in [figure 4](#). The Strouhal number is  $St \approx 0.14$  (0.140 from probe lines P1 and P2 in the gap and 0.143 from probe line P3 in the wake), whereas the secondary mode has a slightly higher frequency, with

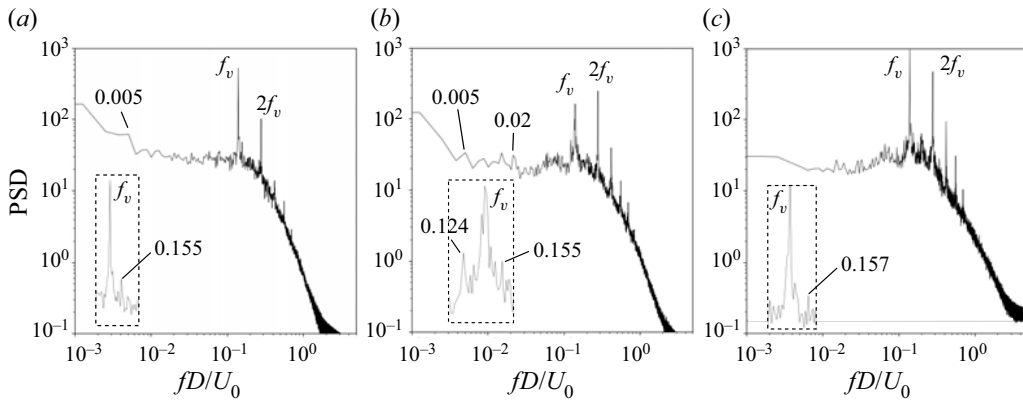


Figure 4. Spanwise-averaged cross-flow velocity spectra in the gap at (a) P1 and (b) P2, and in the wake at (c) P3 (see figure 2 for exact probe locations). The insets show a close up of the main peak, so that the secondary peaks can be distinguished. Flow bi-stability manifests as a secondary spectral peak at approximately  $fD/U_0 = 0.155$ .

a peak near 0.155. The existence of a second mode has been verified by spectral analysis of the forces, although these plots are not shown herein. The second mode is associated with a stronger dynamics in the gap and intermittent shedding of gap vortices, as well as overshoot of the gap shear layers further into the near wake, and wider gap and wake widths. This is shown in the supplementary movie 1 available at <https://doi.org/10.1017/jfm.2023.468> (the second mode starts around  $tU_0/D = 379$ ). This flow regime is very similar to observations of Igarashi (1981) and Kitagawa & Ohta (2008) for  $L/D \approx 3.0$ , although these have significantly higher Reynolds numbers.

Similar to the findings of Papaioannou *et al.* (2006) and Wang *et al.* (2021), the gap is organised into spanwise cells with a length of approximately  $2.5D$  to  $3.8D$ . This is clearly seen in the time-averaged streamwise and spanwise velocity fields, shown in figures 5(a) and 5(b), respectively. The largest observed cell length is comparable to that of the previous studies, which is approximately  $4D$  for Reynolds numbers 500 and 400 (Papaioannou *et al.* 2006; Wang *et al.* 2021). Note that the cell length value was gleaned from instantaneous plots in those studies, and we do not possess information regarding variation or time-averaged values. The spanwise cells of the present study and their locations are quite persistent in time in both gap and near wake, as shown in figure 6. The horizontal stripes of similar magnitude  $C_{pb}$  show the cells, their centres being the regions of lowest magnitude. The time-averaged cell boundaries are marked by dashed lines. We see that there is some meandering and merging of the instantaneous cells, perceived as ‘dislocations’ or blurred areas. Some of these are highlighted by dashed ovals in figure 6(a).

The differences in phase and structure caused by the basic spanwise organisation are significant. Figure 7 shows a series of flow snapshots taken over one vortex shedding period, in the planes  $z/D = 0$  and  $z/D = 1$ . Considering that these spanwise locations are separated only by one diameter, the variation is striking. Most obvious to the eye, is that at  $z/D = 0$  (left-hand panels of figure 7) there is a strong roll-up of the upper shear layer during this interval, while at  $z/D = 1$  (right-hand panels of figure 7) the same occurs, but in the opposite (lower) shear layer. There are also differences in phase and strength of the wake vortex shedding, but these are less profound than those of the gap. In the inset of figure 7, the spanwise velocity has been averaged over  $351.54 \leq tU_0/D \leq 358.51$ .

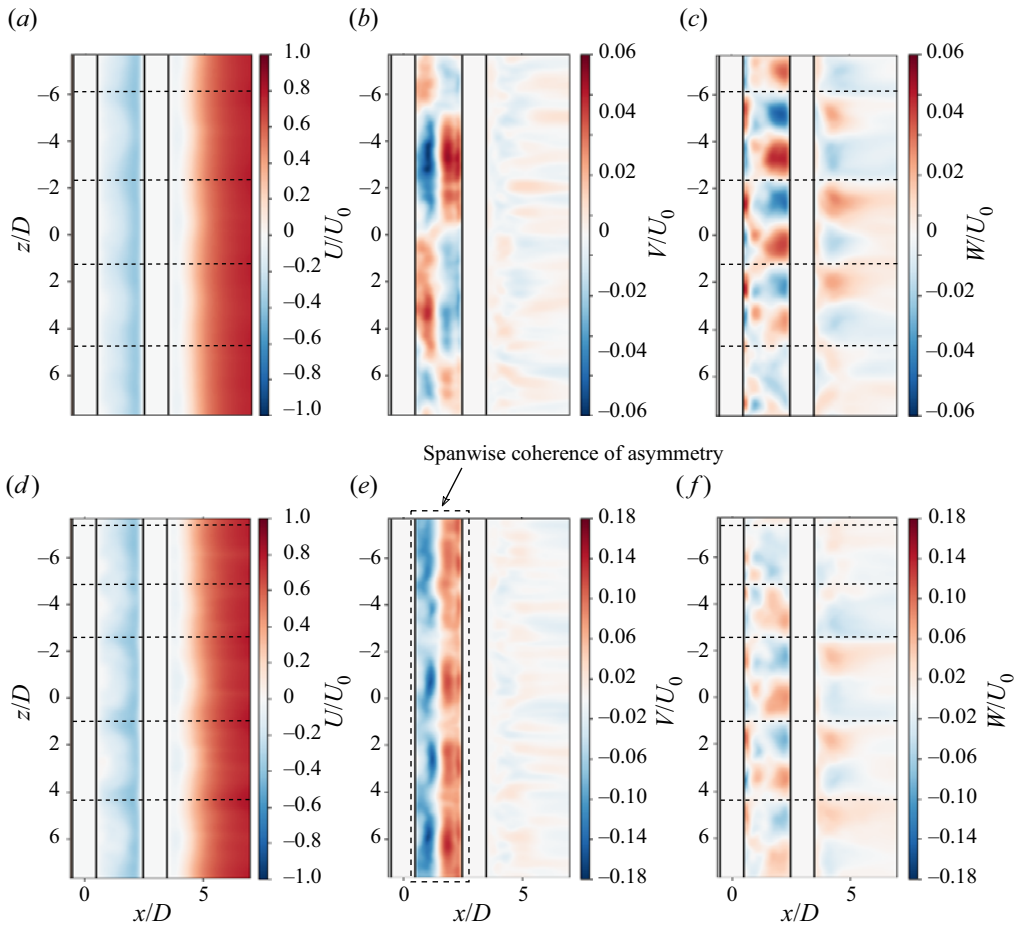


Figure 5. Time-averaged velocity field in the gap and near wake, in the plane  $y/D = 0$ . Panels (a–c) are averaged over the entire duration of the simulation, whereas (d–f) are averaged over  $378 \leq tU_0/D \leq 493$ , which corresponds to approximately 16.4 vortex shedding cycles. The spanwise cell structure is marked by dashed lines. The cell boundaries are defined by sign switch of  $W/U_0$  in the gap. The averaged cross-flow velocity is non-zero in the gap, due to persistent asymmetry of the gap vortices, as described in § 3.2. In (e), this asymmetry is coherent along the span, which is connected with increased drag amplitude, as shown in figure 10(b).

The plot indicates that  $z/D = 0$  and  $z/D = 1$  are located in different spanwise cells during this interval, with  $z/D = 1$  being very close to the boundary of its cell. This is one of the main reasons for the observed differences. Another important factor is the existence of unstable gap shedding cells, which will be elaborated in § 3.2.

Inset C in figure 3 shows the existence of secondary gap vortices, which are created through interaction between the overshooting gap shear layer and near wake. The formation process is highlighted in figure 7(a ii–h ii). A video of this time interval is available in supplementary movie 2. In the first snapshot, figure 7(a ii), the lower gap shear layer has begun to roll up after previously overshooting into the near wake. The roll-up starts with a concentration of vorticity forming well upstream of the downstream cylinder. This causes the downstream part of the gap shear layer (marked by a dashed oval), which extends beyond the gap, to be pinched off. The process is amplified, in this case, by a remnant of the previous gap vortex, marked by a black arrow. In figure 7(c ii), the pinched-off

## Asymmetric cellular bi-stability in tandem cylinder flow

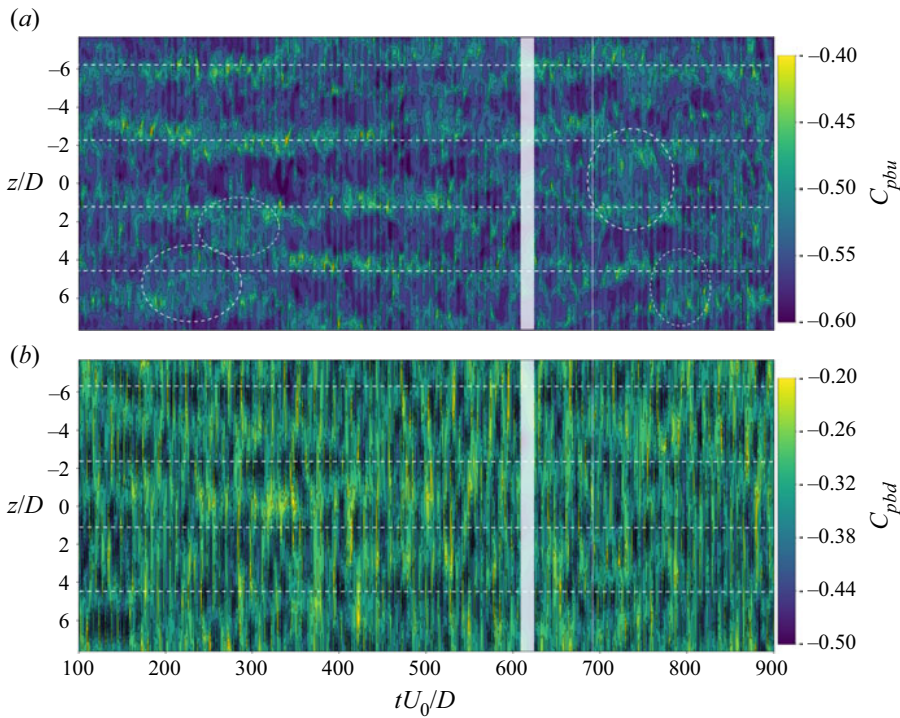


Figure 6. Instantaneous base pressure coefficient of the (a) upstream and (b) downstream cylinders, calculated from probe data along the line  $(x/D, y/D) = (0.51, 0)$ . The spanwise distribution clearly shows cells that are persistent in time, and remain in nearly the same spanwise location for long periods. The dashed lines mark the boundaries of the time-averaged cell structure, given in figure 5(a). The dashed ovals mark intervals of cell ‘dislocations’. Note that (a,b) use different scales, in order to enhance the cell structures. (Due to an output writing error, data are missing in the time interval  $611 \leq tU_0/D \leq 625$ .)

gap shear layer has been completely cut loose, and continues to roll up into a secondary vortex as it is convected downstream. This makes it appear as though the period of the von Kármán vortex street is doubled on just one side of the wake, as seen in figure 7(g ii, h ii). In inset C of figure 3, however, we see that this type of vortex has a very short spanwise length (the spacing between the legs of these horseshoe vortices is around  $1D$ ), and their primary effect is to increase the overall three-dimensionality in the wake. To our knowledge, this is the first time such vortices are described in the literature.

### 3.2. Unstable children: shedding in short spanwise cells

We have discovered that bi-stability may indeed be cellular, as suggested by Aasland *et al.* (2022). Local manifestations of the mode switch emerge clearly from the velocity time traces in figure 8. It is evident that the second mode does not as a rule occur simultaneously at different spanwise locations. Moreover, the mode appears to be asymmetric with respect to the midplane  $y/D = 0$ , which is seen when comparing the time traces from two probes on opposite sides of the gap, shown in figure 8(a iii, b). It must be mentioned that occurrences of the second mode can be quite brief, typically one or two periods, but occur often during a given time interval. In figure 8, the vertical dashed lines mark the boundaries between time intervals where the time traces predominantly display the first or second mode.

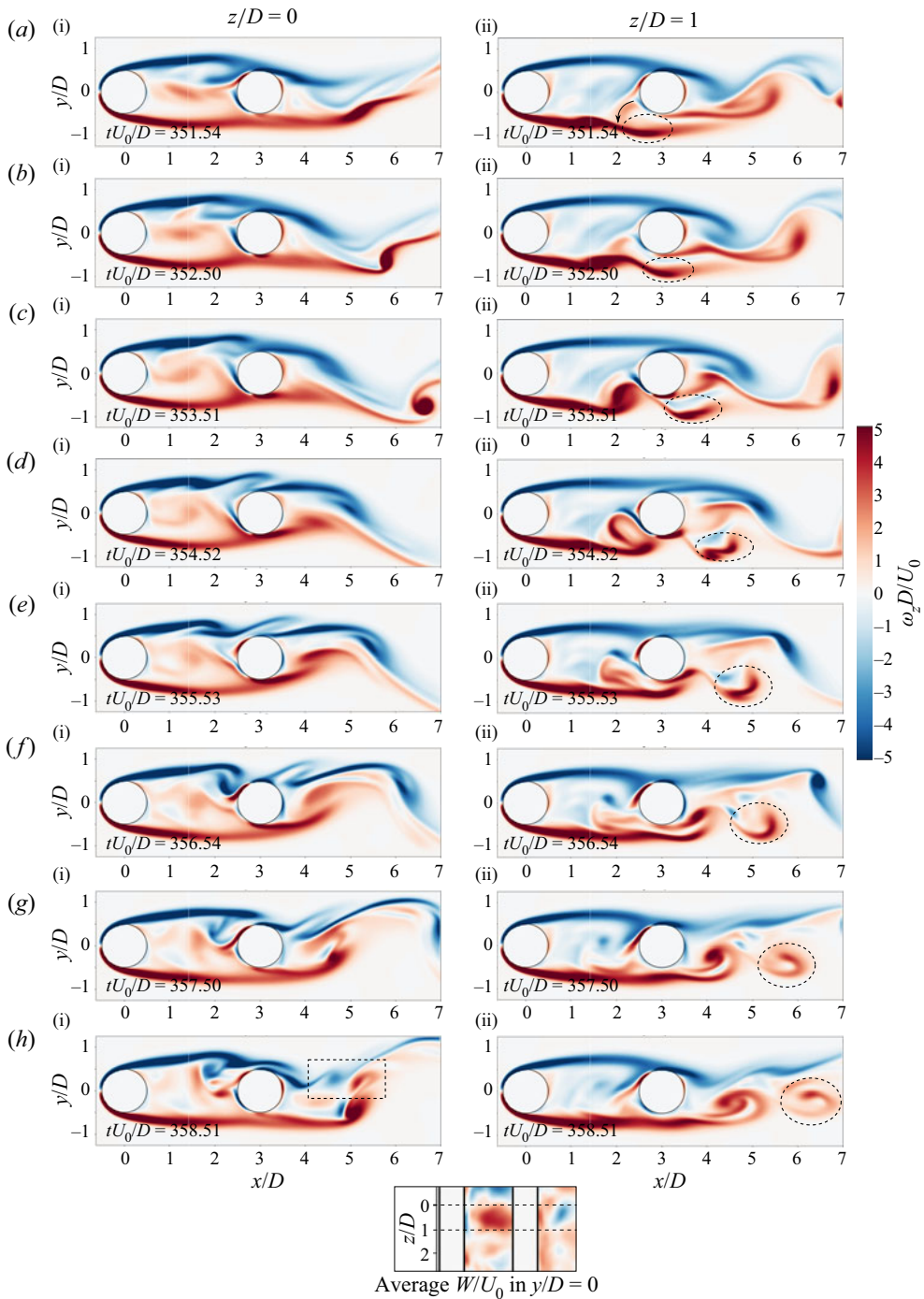


Figure 7. Instantaneous flow during one vortex shedding period, represented by  $\omega_z D/U_0$ , in the planes  $z/D = 0$  and  $z/D = 1$ . A secondary vortex is marked by the dashed oval, and interaction between secondary vortices is shown in (h*i*), marked with a dashed rectangle. There are significant differences in the vortical structures of the two planes, even if they are a mere diameter apart. This is likely because the planes are located in different spanwise mother cells, as indicated in the inset, which shows the time-averaged spanwise velocity during this vortex shedding period.

### Asymmetric cellular bi-stability in tandem cylinder flow

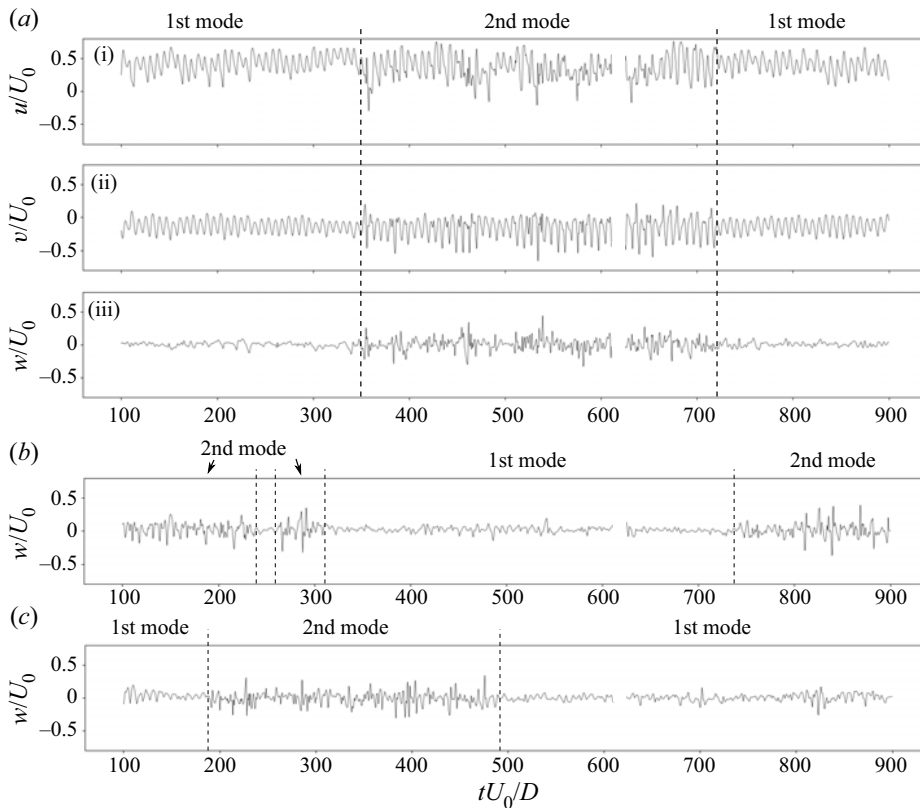


Figure 8. Velocity time history at the end of the gap, at (a) P2 and (b) P4 for  $z/D = 0$ , and (c) P2 for  $z/D = -6$ . For brevity, only  $w/U_0$  is shown in (b,c). The mode switch manifests asymmetrically and locally, so that different spanwise locations do not always exhibit the same mode. Even at a given spanwise location there can be large differences between the upper and lower gap shear layers, as seen when comparing (a iii,b).

In the gap, vortex shedding occurs in relatively short spanwise cells. Such a cell is shown in inset A of figure 3. This particular cell consists of three small horseshoe vortices, and has a spanwise length of approximately  $0.75D$ . Our observations indicate that the unstable cells appear within the boundaries of the basic spanwise cell structure, and their length does not exceed the basic cell length. For this reason the basic cells and the unstable cells can be considered as ‘mother’ and ‘child’ structures, respectively.

A simplified method was used for estimating the length of unstable children, taking velocity data from probe line P2 (see figure 2). For each time a gap vortex formed on this side of the gap, the point of minimum cross-flow velocity ( $v_{min}$ ) was found. If  $v_{min}$  was less than  $-0.5$ , this was assumed to be an unstable child. The cell length was then taken to be the spanwise extent around the location of  $v_{min}$  where the condition  $v/U_0 \leq 0.9v_{min}$  was satisfied. Both the location of the probe line and the velocity constraint were chosen empirically. This method has some obvious drawbacks, one of them being that only one cell is estimated during each period, although cells may appear at several spanwise locations. With the long sampling time, however, there were still ample events on which to base an estimate. The cell length varies considerably, going from  $0.3D$  to  $2.7D$ . However, an overall average of  $0.78D$  implies that most cells are quite short.

Intriguingly, unstable children may manifest themselves in the same location, with reasonably similar cell length for several consecutive periods. An example of this is shown

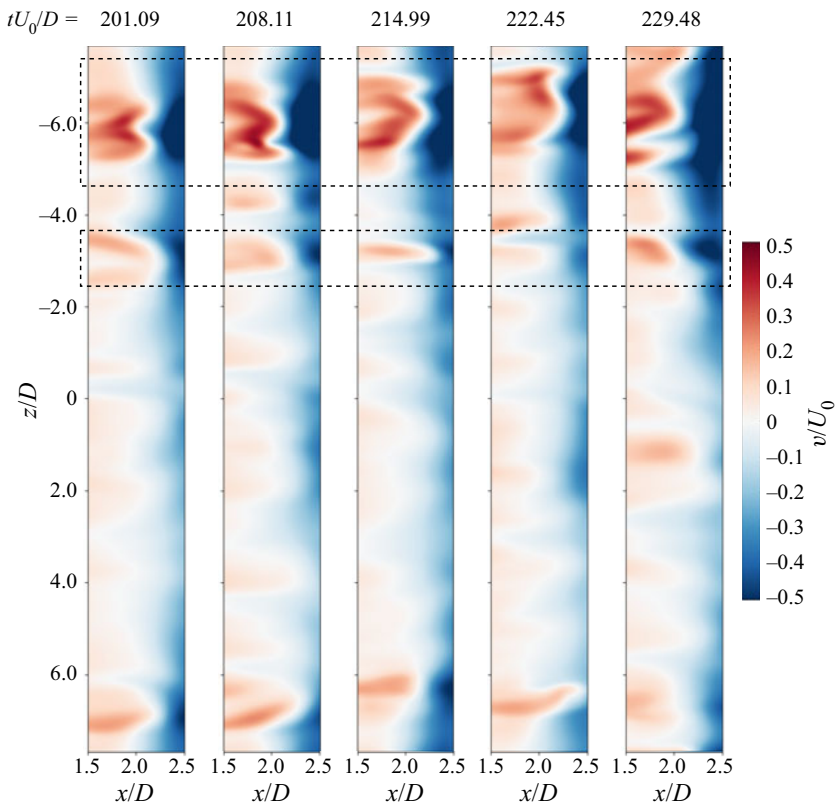


Figure 9. Cross-flow velocity in a plane in the gap, at  $y/D = 0.6$ . During the time interval shown, vortex cells of similar cell length recur at the same spanwise location over five vortex shedding periods. These events are marked by a big dashed rectangle. A smaller rectangle marks a weaker recurring structure. Gap shedding occurs within the boundaries of the mother cell, which is likely the reason for the consistent location. When roll-up occurs in the gap, high-momentum fluid is pulled into the recirculation region and this contributes to maintaining the gap shedding mode over several periods.

in figure 9, where the cells are visualised by means of the cross-flow velocity. Here, an unstable child appears in the same spanwise location for five successive periods. The child maintains approximately the same cell length throughout, except at  $tU_0/D = 229.48$ , where it has grown somewhat. This cell is centred around  $z/D = 6$ , whereas another significantly smaller and weaker structure is centred near  $z/D = 3$ .

The recurrence of unstable children leads to asymmetry with respect to the  $y$  axis in the gap, as shown in the time traces in figure 8, so that strong vortices are formed repeatedly on one side of the gap for long intervals. This inevitably skews the velocity field, and has the practical consequence that the time-averaged cross-flow in the gap centreplane takes a long time to reach zero, as one would expect from experience with single cylinder vortex shedding. In fact, it may theoretically never do so, seeing as the asymmetry manifests randomly. This is illustrated in figure 5(b), where the cross-flow velocity in the gap is seen to have a cellular structure which is different from the mother cells.

Given that the switch between reattachment and shedding is assumed to be a random process, it is indeed curious, and seemingly a paradox, that an unstable child should reappear in the manner that we have observed. However, we believe the explanation is a simple one: the first occurrence in a series of gap vortex shedding events is truly

random, the result of triggering the instability in the gap. Meanwhile, when the gap vortex rolls up early, i.e. away from the surface of the downstream cylinder, this opens the gap recirculation region so that high-momentum fluid from the outside can first be entrained and subsequently recirculated. In turn, this fluid amplifies the instability and triggers repeated shedding events, until equilibrium is reached once more. From the visualisations (see movie 3,  $tU_0/D \approx 670$ ), we see that recirculating fluid entrained by strong gap vortices will sometimes impinge on the shear layer on the same side of the gap at which it was entrained. This way, it enhances the roll-up process. Lower-momentum entrained fluid is mostly swallowed by the gap vortex forming on the opposite side.

It must be emphasised here that the gap shedding is different from the regular vortex shedding process (as detailed by Gerrard 1966), because the downstream cylinder impedes communication between the shear layers. The growing gap vortex is not able to draw the opposite shear layer fully across the gap, although fluid of oppositely signed vorticity does cross the centreline. As a result, the vortex is not cut off by the opposing vortex; rather it is convected downstream by the high-momentum fluid outside the gap. This is what allows the feedback mechanism which causes unstable child recurrence; that not all the recirculating fluid is entrained and shed during a single period. The formation length, in the instantaneous sense, of the shed vortices is not very different from the recirculating gap vortices, and that causes their primary frequencies to be quite close to one another.

### 3.3. *Spanwise mode coherence*

In figure 10(a,b), the time traces of the drag coefficients (in particular the downstream coefficient  $C_{Dd}$ ) have intervals of strong oscillations, their duration ranging from a couple of vortex shedding periods up to 16–20 periods. These intervals are associated with overall increased velocity fluctuations. We have compared the spanwise-averaged r.m.s. of the velocity fluctuations in the time interval  $378 \leq tU_0/D \leq 493$  with those of  $100 \leq tU_0/D \leq 215$ , during which  $C_{Dd}$  has relatively low-amplitude fluctuations. In the gap, at P2 the increase of spanwise-averaged  $u_{rms}$ ,  $v_{rms}$  and  $w_{rms}$  is 4.69, 34.82 and 26.31 %, respectively. In the wake, at P3, the corresponding changes are  $-1.11$ , 1.87 and 17.31 %.

The value of  $C_{Dd}$  remains negative throughout the entire simulation, although it nearly reaches zero on two occasions (marked in figure 10b). This implies that the flow remains within the reattachment regime, although vortex shedding occurs locally along the span. Near-zero values of  $C_{Dd}$  are accompanied by peaks in  $C_{Du}$  (figure 10a). The strong oscillations occur primarily in the drag force, and there is no indication of a corresponding amplitude increase in the lift time traces, shown in figure 12(a,b).

During the intervals of strong oscillations, there is increased spanwise coherence of the asymmetry in the gap, which is of great interest. An example is shown in figure 5(e), where the cross-flow velocity field has been averaged over approximately 16.5 vortex shedding cycles. In this plot, as opposed to the all-time average in figure 5(b), the mother cells emerge quite clearly and the asymmetry has the same sign along the entire span. Positive velocity in the centreplane towards the end of the gap implies that the vortex in the upper shear layer is stronger than its opposite, and thus has a more concentrated core. The opposite weaker vortex has a larger diameter, and thus expands above the centreplane. It must be noted that not all intervals are as strongly coherent as this one, but the tendency is clear.

Figure 11 gives an instantaneous view of the flow at a time when  $C_{Dd}$  is close to a local maximum ( $tU_0/D \approx 385$ , marked in figure 10b). We see that there is a large number of unstable children in the upper shear layer, spread along the entire cylinder span.



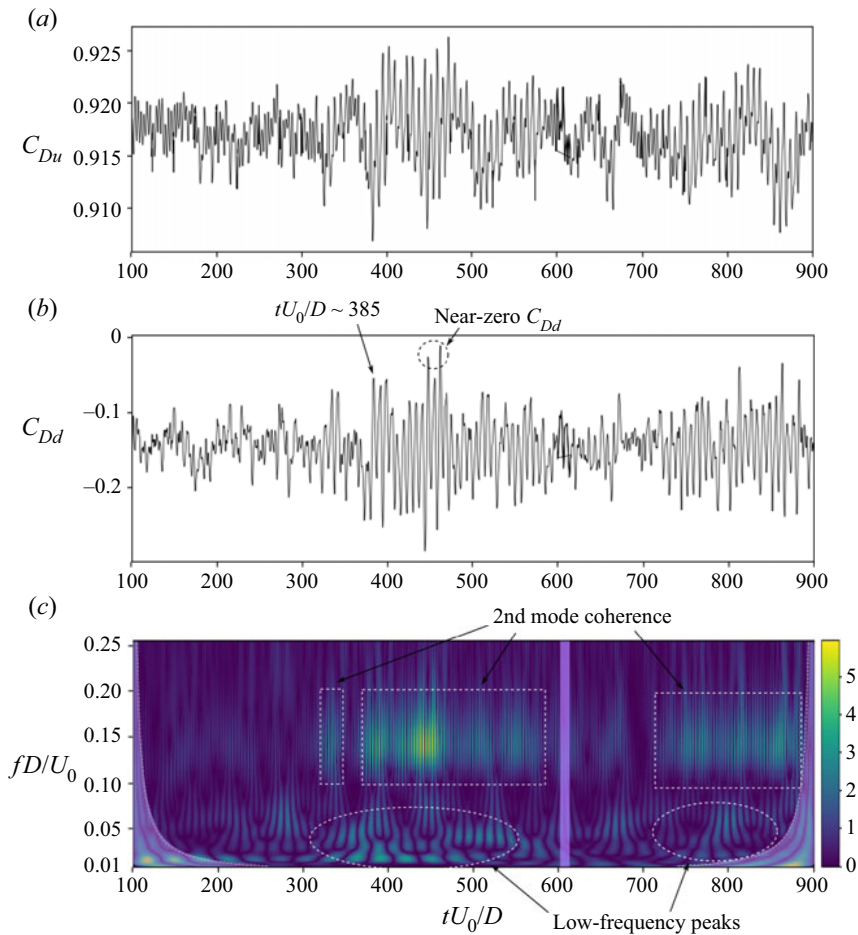


Figure 10. Time histories of (a) upstream and (b) downstream drag coefficients, and (c) wavelet map of  $C_{Dd}$ . The shaded region of the wavelet map marks the cone of influence. The flow is bi-stable throughout the time series, but intervals of strong  $C_{Dd}$  oscillations are associated with increased spanwise coherence of the second mode. A snapshot of the flow near  $tU_0/D = 385$  in figure 11 illustrates this mechanism. Periods of strong fluctuations are accompanied by an increase of spectral energy in the low-frequency components, which are related to variation of the reattachment and separation points on the downstream cylinder, as indicated in figure 13. (Aberrations due to the output writing error have been masked in the wavelet map.)

The streamwise and cross-flow velocity components are largely coherent along the span, except near  $z/D = -3$ . Here, the cross-flow and spanwise velocities indicate the presence of a comparably strong vortex loop in the near wake, which influences the gap region and disrupts the coherence, likely through secondary structures.

These results indicate that the intervals of strong oscillations of  $C_{Dd}$  are not a mode change *per se*, but arise when spanwise localised occurrences of the second mode are somehow coordinated, so that the spanwise coherence increases. Vortex roll-up in the gap at several spanwise locations necessarily leads to an increase of the (negative) drag. Conversely, spanwise coherent reattachment causes local drag minima.

The significant increase of spanwise velocity fluctuations in both gap and wake is attributed to the three-dimensional instability T3, which is given more space to develop during the second mode.

Asymmetric cellular bi-stability in tandem cylinder flow

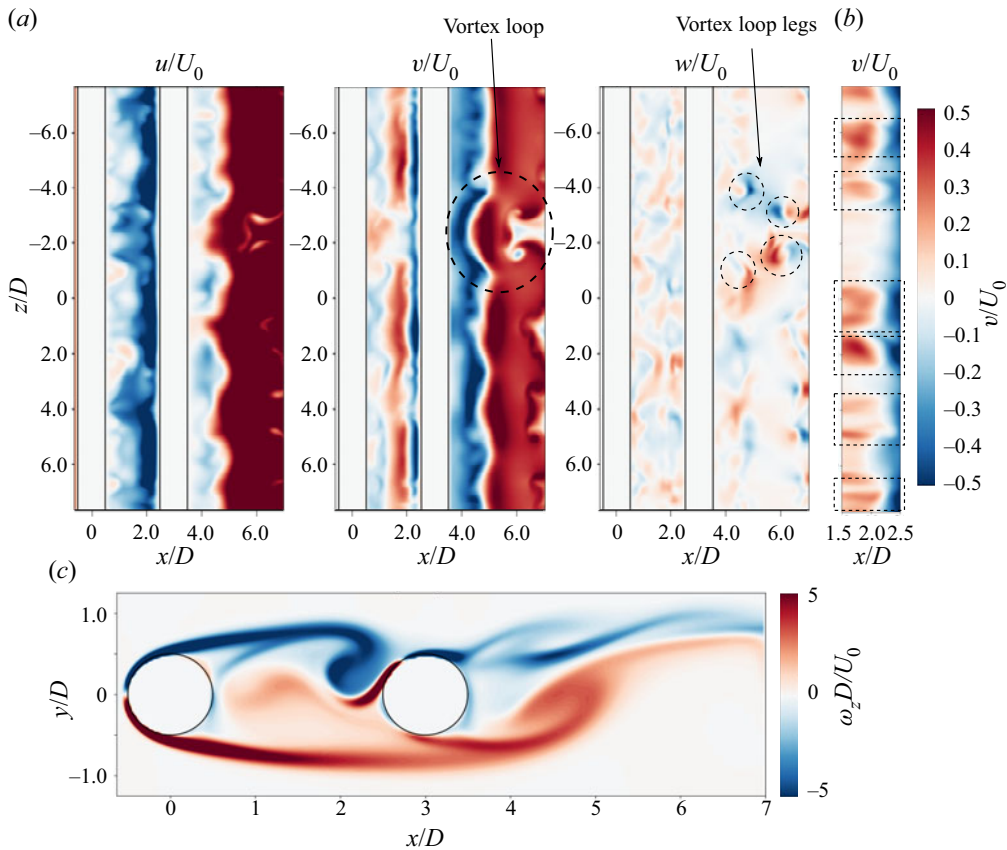


Figure 11. Snapshot of the flow at  $tU_0/D = 385.75$ . This time instant corresponds to a peak in  $C_{Dd}$ , which is likely due to spanwise coherence of the second mode. (a) Shows that the streamwise and cross-flow velocities are largely coherent in the gap. Unstable children in the top gap shear layer are marked by dashed rectangles in (b). Panel (c) illustrates strong roll-up in the gap at this time instant. When the gap shear layers detach from the downstream cylinder, this increases  $C_{Dd}$ , as observed in figure 10(b). A strong vortex loop disrupts the spanwise coherence near  $z/D = -3.0$ , as shown in (a). The velocity scale is exaggerated to make the spanwise structures clear; (a)  $y/D = 0$ , (b)  $y/D = 0.6$ , (c)  $z/D = 0$ .

Comparing the  $C_{Dd}$  and velocity time histories in figures 10(b) and 8, it is obvious that there is not always a correspondence between the increased force oscillations and velocity fluctuations at a given point. This is due to the cellular manifestation of the gap shedding. Plainly put, low fluctuations at the point probe combined with high fluctuations of the total drag force simply means that the mode switch occurs elsewhere along the span.

Although there is no appreciable impact of the second mode coherence on the downstream cylinder lift, the gap asymmetry influences the lift coefficient of the upstream cylinder, giving it a meandering, non-zero mean. This is clearly shown in figure 12. For example, during the time interval  $373 \leq tU_0/D \leq 493$ , the mean lift in the upstream cylinder is negative, with a value of  $\bar{C}_{Lu} = -0.013$ . A positive mean value is observed during  $720 \leq tU_0/D \leq 890$ , which is another time interval of significant spanwise coherence of the second mode, with  $\bar{C}_{Lu} = 0.012$ .

Phase diagrams of drag and lift are given in figure 12(c,d), for the upstream and downstream cylinders, respectively. The drag time histories of both cylinders contain multiple periods, and the quasi-periodicity of the upstream cylinder lift results in an

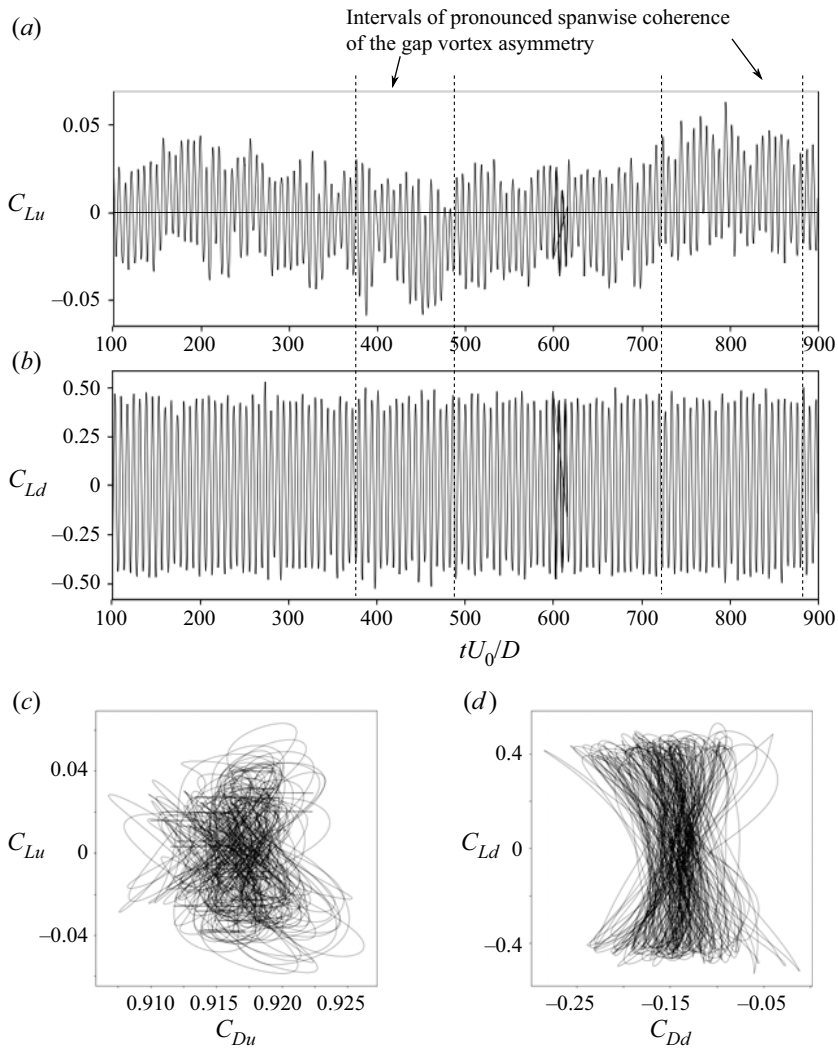


Figure 12. Time history of (a) upstream and (b) downstream cylinder lift coefficients. The second mode coherence has no obvious influence on  $C_{Ld}$ , but  $C_{Lu}$  is influenced by long-term asymmetry in the gap, so that the mean value is non-zero. Panels (c,d) show time traces in the  $C_D - C_L$  plane for the upstream and downstream cylinders, respectively.

irregular path in the  $C_D - C_L$  plane, as shown in figure 12(c);  $C_{Ld}$  is considerably less irregular than  $C_{Lu}$ , and its increased periodicity is evident in figure 12(d).

### 3.4. Low-frequency variations

When the first part of the simulation,  $100 \leq tU_0/D \leq 800$ , was evaluated, it was discovered that there are low-frequency peaks in the velocity spectra. Therefore, the simulation was run for 100 additional time units while an *in situ* FFT was carried out. A spectral map of selected frequencies are shown in figure 13.

Figure 13(a,b) display spectral maps of the lowest analysed frequencies,  $fD/U_0 = 0.02$  and 0.04, respectively. The plots in the plane  $z/D = 6$  show that the gap vortex in the lower shear layer was stronger during the time interval analysed. In figure 13(a), the spectral

Asymmetric cellular bi-stability in tandem cylinder flow

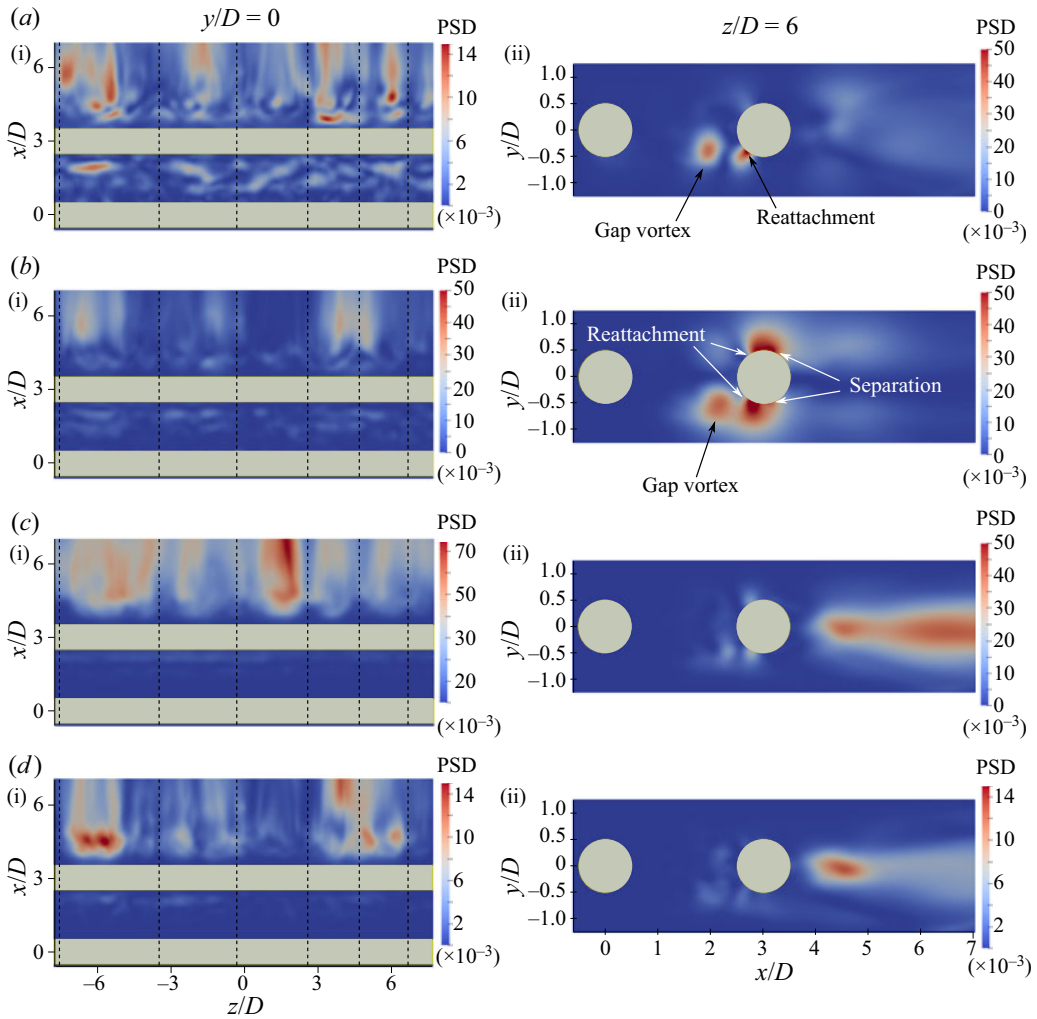


Figure 13. Spectral maps in the planes  $y/D = 0$  and  $z/D = 6$ , analysed over the time interval  $800 \leq tU_0/D \leq 900$ . Panels (a,b) show that there is low-frequency modulation of the reattachment and separation points on the downstream cylinder, which leads to slow variation of the vortex formation length. During this time interval, which covers approximately 14 von Kármán cycles, the gap vortex formation at  $z/D = 6$  is clearly asymmetric, favouring the lower vortex. The approximate boundaries of the mother cells are marked by dashed lines. Note that due to strong variation in spectral energy, the scales are not the same for all plots; (a)  $fU_0/D = 0.02$ , (b)  $fU_0/D = 0.04$ , (c)  $fU_0/D = 0.12$ , (d)  $fU_0/D = 0.14$ .

density is concentrated mostly around this gap vortex and the reattachment point on the same side. There are density concentrations in the corresponding points on the opposite side, but these are weak in comparison.

Meanwhile, figure 13(b) displays density concentrations around the downstream cylinder separation points, as well as around the reattachment point and the lower gap vortex. For the separation points, the highest spectral density is found on the opposite side of the strong gap vortex, and this indicates a relation with the gap shear layer overshoot mechanism.

Both  $fD/U_0 = 0.02$  and  $0.04$  have energy content in the near wake, but the distributions are different. In figure 13(a), we see that, in the near wake, the spectral energy is skewed

towards the opposite side of the strong gap vortex, but in [figure 13\(b\)](#) it is close to evenly distributed and mostly restricted to the downstream cylinder shear layers.

These findings indicate that there is low-frequency variation of the dynamics in the gap region, which in turn influences the formation of the wake vortices. This influence seems to operate both through modulation of the reattachment points, as well as through the overshooting mechanism, as indicated in [figure 13\(b\)](#). It is likely that this modulation is related to the bi-stable mode switch. Indeed, the wavelet map of  $C_{Dd}$  in [figure 10\(a\)](#) shows that the low frequencies gain energy during intervals of spanwise coherent secondary flow mode.

The work of Zhou & Yiu (2006) support our interpretation of the spectral analysis. They showed that the location of the reattachment points influences the strength of the wake vortices, because it determines the length over which the boundary layer develops before separation. The further upstream the reattachment point, the stronger the wake vortices. In the present study, a change in the streamwise location of roll-up in the gap gives a slight change of the reattachment point, and thus a small variation of strength of the wake vortex. This is likely why low-frequency content is seen in the wake, in the spectral maps of [figure 13\(a,b\)](#).

Low-frequency modulation of the vortex formation length is a known feature of bluff-body wakes, and previous studies have found that it is correlated with slow variation of the base pressure (Miau *et al.* 1999, 2004; Lehmkuhl *et al.* 2013; Cao & Tamura 2020). There is some variation in the reported modulation frequency. Miao *et al.* (2004) report modulation in the wake of a trapezoidal and a circular cylinder to be ‘one order of magnitude’ lower than the Strouhal number. This corresponds well with a value of  $0.14f_v$ , as reported by Cao & Tamura (2020) for a square cylinder, whereas the frequency found by Lehmkuhl *et al.* (2013) is substantially lower: approximately  $0.03f_v$ . The gap velocity spectra in both [figure 4\(a,b\)](#) have a peak near  $fD/U_0 = 0.005$ , corresponding well with the results by Lehmkuhl *et al.* (2013). Meanwhile, the low-frequency modulation of the gap and near wake discovered by the *in situ* FFT analysis are well in line with the results of Cao & Tamura (2020), in terms of value. In the present study,  $fD/U_0 = 0.02$  corresponds to  $0.14St$ . It is quite possible that there are different types of low-frequency phenomena at work, so that one might distinguish between the effects of bi-stability and a more general formation length modulation. Regrettably, the length of the present simulation is not sufficient to ascertain the nature of the lowest peak, so this is left for further study.

In the *in situ* FFT analysis, some frequencies near  $f_v$  were also considered. Because all frequencies have to be integer multiples of the lowest analysed frequency (in this case 0.02), we could not match the spectral peaks from [figure 8](#) exactly. Interestingly,  $fD/U_0 = 0.12$  has higher spectral density than  $fD/U_0 = 0.14$  during this time interval although, when the entire time series is considered, its spectral peak is lower, as seen from [figure 4\(b\)](#). This suggests a possible third mode, although we have not identified one with certainty. All in all, the spectral analysis, as well as the visualisations, indicate that there are several ongoing complex processes in the gap.

From [figure 13\(c,d\)](#) we see that the spanwise distribution of spectral energy roughly follows the mother cell structure. The energy concentrations in particular cells are likely caused by local mode switch.

#### 4. Discussion

At first glance it is not obvious how the unstable children are related to the intervals of the second mode spanwise coherence. There is generally a larger number of unstable cells per period during these intervals, but their cell length is not significantly changed.

We believe that there are two main mechanisms at work, which may amplify one another: the increase of spanwise velocity fluctuations and the recurrence of unstable children by the mechanism proposed in § 3.2.

One of the most conspicuous features of the second mode is the increase in spanwise velocity fluctuations. Recalling that the three-dimensional instability T3 (described in § 1) is cooperative, it follows that the enhanced strength of the vortices during the second mode, which allows increased interaction between the shear layers, leads to enhanced three-dimensionalisation of the gap flow.

Increased spanwise velocity fluctuations primarily leads to enhanced streamwise vorticity, but if we consider the vorticity equation, we see that some of this angular momentum is transferred to the spanwise vorticity through vortex tilting. In its inviscid form, the vorticity equation is given as

$$\frac{D\boldsymbol{\omega}}{Dt} = (\boldsymbol{\omega} \cdot \nabla) \mathbf{u}, \quad (4.1)$$

of which the spanwise component is

$$\frac{D\omega_z}{Dt} = \underbrace{\omega_x \frac{\partial w}{\partial x} + \omega_y \frac{\partial w}{\partial y}}_{\text{tilting}} + \underbrace{\omega_z \frac{\partial w}{\partial z}}_{\text{stretching}}. \quad (4.2)$$

Through induced velocity (primarily  $w$ ), an unstable child at one location may influence the velocity gradients at another location. From (4.2) it follows that these induced gradients may cause an increase of spanwise vorticity through vortex tilting, and thus precipitate a mode switch. That tilting occurs in the gap is easy to see from the small-scale structures visualised in figure 3.

In the event that several unstable children appear randomly along the span, the chance of triggering other unstable children by the above mechanism increases, as each of these random first occurrences contributes to increased spanwise velocity. This also increases the chances of recurrence, causing the spanwise coherence to become self-sustaining to a certain degree. This explains how the intervals of coherent second mode can be significantly longer than the observed number of periods in which an unstable child reappears during intervals of low spanwise coherence. The persistent gap asymmetry during such intervals supports this hypothesis.

We believe that the mechanism by which unstable children occur is the same as that which precipitates bi-stable switch between reattachment and co-shedding described in previous tandem cylinder studies (Igarashi 1981; Kitagawa & Ohta 2008; Carmo *et al.* 2010*a*). The difference is that this mechanism is at work much earlier than previously reported, in terms of the  $Re - L/D$  combination. Reattachment occurs exclusively on the upstream side of the downstream cylinder, which rules out the overshoot/reattachment bi-stability discovered by Xu & Zhou (2004). One might say that tandem cylinder flow defies simple classification. In the present case there is alternating overshoot/reattachment, a feature of low gap ratios, combined with a switch between reattachment and shedding in the gap (believed to be a feature of intermediate to high gap ratios and/or Reynolds numbers), but where vortices are shed repeatedly from just one shear layer, a phenomenon which has not been reported previously. No doubt, further peculiarities might be discovered by those who are willing to delve into the details of a single case.

The present study was carried out at a moderate Reynolds number. Whether the results are applicable to turbulent flow is unknown, although our previous results with tandem cylinders at  $Re = 10^4$  and  $L/D = 3.0$  indicated the presence of cellularity (and sparked the

present investigation). Unfortunately, tandem cylinder studies at high  $Re$  tend to have either insufficient spanwise length, or present only a cross-sectional view of their results. This makes comparison with the present study difficult. With the assumption that the presence of the unstable children and their cell length are related to the three-dimensional gap/wake instability mode T3, the fundamental question is whether or not this mode persists in the reattachment regime after transition to turbulence. For single cylinders, streamwise vortices that indicate the presence of mode B have been observed up to  $Re = 270 \times 10^5$  (Williamson 1996), but T3 has not been studied beyond  $Re = 500$ , to our knowledge. Thus, further investigations are required to conclude on this topic.

From figure 8(a,b), it appears as though there may be intermittent reversal of the asymmetry, so that when the upper shear layer exhibits the first mode, the lower shear layer exhibits the second mode and *vice versa*. Asymmetric wakes are found for several types of three-dimensional bluff bodies (Natarajan & Acrivos 1993; Bohorquez *et al.* 2011; Grandemange, Cadot & Gohlke 2012). In cases where there is a finite number of symmetry planes in the geometry, there may be bi-stable flipping of the wake from one side to the other (Haffner *et al.* 2020). Haffner *et al.* (2020) propose a mechanism for the wake reversal based on interaction between the shear layer and recirculation region, and they suggest this mechanism might be general, and not merely applicable to the geometry of that study (Ahmed body). By their reasoning, when the wake is asymmetric, the recirculating flow on one side amplifies the instability of the shear layer on the opposite side, causing increased entrainment through this layer. At some point, the roll-up of the triggered shear layer becomes strong enough to form a new recirculating flow opposing the original recirculation, which precipitates an unstable symmetrical state without coherent recirculating motion. From this state, the flow may be perturbed and revert to asymmetry on either side, although in most observed cases the asymmetry switches to the opposite of the original.

Naturally, there are several differences between the study by Haffner *et al.* (2020) and the present case, the most important being that the primary instability works in the gap, regardless of the long-term asymmetry. Moreover, at the present Reynolds number, the shear layers are laminar, so there is little or no entrainment through them. Entrainment occurs towards the end of the gap. However, there are similarities: asymmetry, interaction with a recirculating flow (the opposing gap vortex) and the apparent asymmetry reversal.

Bi-stability has also been observed in the case of a streamwise rotating sphere, for certain Reynolds number and rotation rates (Lorite-Díez & Jiménez-González 2020; Sierra-Ausín *et al.* 2022). Lorite-Díez & Jiménez-González (2020) found a switch between a quasi-periodic low-drag state and a more irregular high-drag state. Interestingly, low-frequency variation of the recirculation length was suggested as a trigger for the high-drag state. Both these results, alternating low-energy/high-energy states and low-frequency variation of the recirculation are similar to our observations herein. We also note that, in the study of Kitagawa & Ohta (2008), within the reattachment regime, a bi-stable switch was observed between a vortex-street wake and a symmetrical, non-shedding wake. The latter is qualitatively very similar to the unstable symmetrical state observed by Haffner *et al.* (2020). Together, these observations make an interesting topic of further study.

Finally, it is worth noting that our simulations had to run for quite a long time before an interval of spanwise coherence occurred that was long enough to attract our attention. Had we been content with statistics over, say, 40 vortex shedding cycles, this phenomenon might have gone unnoticed. The low-frequency modulations of the gap and wake also

underline the importance of simulation/measurement duration if one is intent on capturing the full range of flow physics of tandem cylinders.

## 5. Summary and concluding remarks

In the present study, we have investigated the possibility of cellular bi-stability for tandem cylinders near the drag-inversion spacing, and found that such a phenomenon does indeed exist. Vortex shedding in the gap occurs in short spanwise cells, which are predominantly asymmetric, so that shedding occurs solely from one shear layer. Interestingly, this process occurs repeatedly. Unstable spanwise vortex cells manifest in the same location, with approximately the same cell length, for several consecutive periods. This is likely caused by increased entrainment of high-momentum fluid when the shear layer rolls up, which then feeds the next vortex cycle as it is recirculated in the gap.

The study was carried out by means of DNS, for a gap ratio of  $L/D = 3$  and a Reynolds number of 500. Using a high grid resolution and long spanwise length allowed us to study the intricate flow interaction that arises in the gap and near wake in great detail.

A particularly interesting observation was made, where the second mode intermittently became spanwise coherent to a large extent, causing significant increase in the oscillation amplitude of the drag. The mechanisms behind this are likely the increased spanwise velocity fluctuations that arise from the three-dimensional instability when shedding is triggered, which in turn may trigger additional unstable vortices through momentum transfer. Coupled with the mechanism that causes recurrence of vortex shedding, this allows the intervals of second mode coherence to be surprisingly long.

These results show that, while tandem cylinders have been extensively investigated, there are physical phenomena within this framework that have not yet been described. A symmetrical geometry with cylinders of equal diameter, subjected to uniform inflow conditions, may produce a persistently asymmetric gap flow field. Such a wholly unexpected outcome goes to show that the fundamental flow cases still deserve our attention.

**Supplementary movies.** Supplementary movies are available at <https://doi.org/10.1017/jfm.2023.468>.

**Funding.** This work is supported by the Research Council of Norway through the Public Sector PhD Scheme, and the National Public Roads Administration, where the first author is an employee. Computational hours were granted by the Norwegian HPC project NN9191K.

**Declaration of interests.** The authors report no conflict of interest.

### Author ORCIDs.

 Tale E. Aasland <https://orcid.org/0000-0002-8504-930X>;

 Fengjian Jiang <https://orcid.org/0000-0002-5321-3275>.

## REFERENCES

- AASLAND, T.E., PETERSEN, B., ANDERSSON, H.I. & JIANG, F. 2022 Revisiting the reattachment regime: a closer look at tandem cylinder flow at  $Re = 10000$ . *J. Fluid Mech.* **953**, A18.
- ALAM, M.M. 2014 The aerodynamics of a cylinder submerged in the wake of another. *J. Fluids Struct.* **51**, 393–400.
- ALAM, M.M., MORIYA, M., TAKAI, K. & SAKAMOTO, H. 2003 Fluctuating fluid forces acting on two circular cylinders in a tandem arrangement at a subcritical Reynolds number. *J. Wind Engng Ind. Aerodyn.* **91**, 139–154.
- BOHORQUEZ, P., SANMIQUEL-ROJAS, E., SEVILLA, A., JIMÉNEZ-GONZÁLEZ, J. & MARTÍNEZ-BAZÁN, C. 2011 Stability and dynamics of the laminar wake past a slender blunt-based axisymmetric body. *J. Fluid Mech.* **676**, 110–114.



- CAO, Y. & TAMURA, T. 2020 Low-frequency unsteadiness in the flow around a square cylinder with critical angle of  $14^\circ$  at the Reynolds number of  $2.2 \times 10^4$ . *J. Fluids Struct.* **97**, 103087.
- CARMO, B.S. & MENEGHINI, J.R. 2006 Numerical investigation of the flow around two circular cylinders in tandem. *J. Fluids Struct.* **22**, 979–988.
- CARMO, B.S., MENEGHINI, J.R. & SHERWIN, S.J. 2010a Secondary instabilities in the flow around two circular cylinders. *J. Fluid Mech.* **644**, 395–431.
- CARMO, B.S., MENEGHINI, J.R. & SHERWIN, S.J. 2010b Possible states in the flow around two circular cylinders in tandem with separations in the vicinity of the drag inversion spacing. *Phys. Fluids* **22**, 054101.
- DENG, J., REN, A.-L., ZOU, J.-F. & SHAO, X.-M. 2006 Three-dimensional flow around two circular cylinders in tandem arrangement. *Fluid Dyn. Res.* **38** (6), 386–404.
- GERRARD, J.H. 1966 The mechanics of the formation region of vortices behind bluff bodies. *J. Fluid Mech.* **25**, 401–413.
- GRANDEMANGE, M., CADOT, O. & GOHLKE, M. 2012 Reflectional symmetry breaking of the separated flow over three-dimensional bluff bodies. *Phys. Rev. E* **86**, 035302.
- HAFFNER, Y., BORÉE, J., SPOHN, A. & CASTELAIN, T. 2020 Mechanics of bluff body drag reduction during transient near-wake reversals. *J. Fluid Mech.* **894**, A14.
- IGARASHI, T. 1981 Characteristics of the flow around two circular cylinders arranged in tandem (1st report). *Bull. JSME* **24** (188), 323–330.
- KITAGAWA, T. & OHTA, H. 2008 Numerical investigation on flow around circular cylinders in tandem arrangement at a subcritical Reynolds number. *J. Fluids Struct.* **24**, 680–699.
- LEE, T. & BASU, S. 1997 Nonintrusive measurements of the boundary layer developing on a single and two cylinders. *Exp. Fluids* **23**, 187–192.
- LEHMKUHL, O., RODRIGUES, I., BORRELL, R. & OLIVA, A. 2013 Low-frequency unsteadiness in the vortex formation region of a circular cylinder. *Phys. Fluids* **25**, 085109.
- LIN, J.-C., YANG, Y. & ROCKWELL, D. 2002 Flow past two cylinders in tandem: instantaneous and averaged flow structure. *J. Fluids Struct.* **16** (8), 1059–1071.
- LJUNGKRONA, L., NORBERG, C.H. & SUNDEN, B. 1991 Free-stream turbulence and tube spacing effect on surface pressure fluctuations for two tubes in an in-line arrangement. *J. Fluids Struct.* **5**, 701–727.
- LORITE-DÍEZ, M. & JIMÉNEZ-GONZÁLES, J.I. 2020 Description of the transitional wake behind a strongly streamwise rotating sphere. *J. Fluid Mech.* **896**, A18.
- MANHART, M. 2004 A zonal grid algorithm for DNS of turbulent boundary layers. *Comput. Fluids* **33**, 435–461.
- MIAU, J.J., WANG, J.T., CHOU, J.H. & WEI, C.Y. 1999 Characteristics of low-frequency variations embedded in vortex-shedding process. *J. Fluids Struct.* **13**, 339–359.
- MIAU, J.J., WU, S.J., HU, C.C. & CHOU, J.H. 2004 Low-frequency modulations associated with vortex shedding from flow over bluff body. *AIAA J.* **42**, 1388–1397.
- NATARAJAN, R. & ACRIVOS, A. 1993 The instability of steady flows past spheres and disks. *J. Fluid Mech.* **254**, 323–344.
- OKAJIMA, A. 1979 Flows around two tandem circular cylinders at very high Reynolds numbers. *Bull. JSME* **22**, 504–511.
- PAPAIOANNOU, G., YUE, D.K.P., TRIANTAFYLLOU, M.S. & KARNIADAKIS, G. 2006 Three-dimensionality effects in the flow around two tandem cylinders. *J. Fluid Mech.* **558**, 387–413.
- PELLER, N., LE DUC, A., TREMBLAY, T. & MANHART, M. 2006 High-order stable interpolations for immersed boundary methods. *Intl J. Numer. Meth. Fluids* **53**, 1175–1193.
- SIERRA-AUSÍN, J., LORITE-DÍEZ, M., JIMÉNEZ-GONZÁLES, J.I., CITRO, V. & FABRE, D. 2022 Unveiling the competitive role of global modes in the pattern formation of rotating sphere flows. *J. Fluid Mech.* **942**, A54.
- SONG, Y. & ZHU, R. 2017 A numerical study of flow patterns, drag and lift for low Reynolds number flow past tandem cylinders of various shapes. In *ASME 2017 Mech. Eng. Cong. and Expo. IMEC2017*. Tampa, Florida, USA, p. V007T09A058. ASME.
- SUMNER, D. 2010 Two circular cylinders in cross-flow: a review. *J. Fluids Struct.* **26**, 849–899.
- WANG, D., LIU, Y., LI, H. & XU, H. 2021 Secondary instability of channel-confined transition around dual-circular cylinders in tandem. *Intl J. Mech. Sci.* **208**, 106692.
- WANG, P., ZHOU, Q., ALAM, M.M., YANG, Y. & LI, M. 2022 Effects of streamwise gust amplitude on the flow around and forces on two tandem circular cylinders. *Ocean Engng* **261**, 112040.
- WILLIAMSON, C.H.K. 1996 Vortex dynamics in the cylinder wake. *Annu. Rev. Fluid Mech.* **28**, 477–539.
- XU, G. & ZHOU, Y. 2004 Strouhal numbers in the wake of two inline cylinders. *Exp. Fluids* **37**, 248–256.
- ZDRAVKOVICH, M.M. 1972 Smoke observations of wakes of tandem cylinders at low Reynolds numbers. *Aeronaut. J.* **76** (734), 108–114.

*Asymmetric cellular bi-stability in tandem cylinder flow*

- ZDRAVKOVICH, M.M. 1987 The effect of interference between circular cylinders in cross flow. *J. Fluids Struct.* **1**, 239–261.
- ZHOU, Y. & ALAM, M.M. 2016 Wake of two interacting circular cylinders: a review. *Intl J. Heat Fluid Flow* **62**, 510–537.
- ZHOU, Q., ALAM, M.M., CAO, S., LIAO, H. & LI, M. 2019 Numerical study of wake and aerodynamic forces on two tandem circular cylinders at  $Re = 10^3$ . *Phys. Fluids* **31**, 045103.
- ZHOU, Y. & YIU, M. 2006 Flow structure, momentum and heat transport in a two-tandem-cylinder wake. *J. Fluid Mech.* **548**, 17–48.



## Chapter 4

# Tandem cylinders with axial curvature



#### 4.1 Paper 3. Flow around curved tandem cylinders

Aasland, T. E., Pettersen, B., Andersson, H. I. & Jiang, F. 2022 Flow around curved tandem cylinders. *Journal of Fluids Engineering*, **144**, 121301. <https://doi.org/10.1115/1.4054890>

This paper is not included due to ASME copyright restrictions

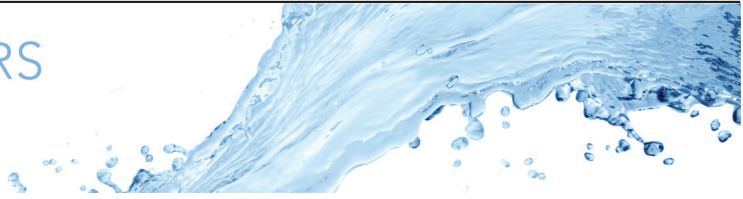


## 4.2 Paper 4. Flow topology in the gap and wake of convex curved tandem cylinders

Aasland, T. E., Pettersen, B., Andersson, H. I. & Jiang, F. 2023 Flow topology in the gap and wake of convex curved tandem cylinders. *Journal of Fluid Mechanics*, **976**, A32. <https://doi.org/10.1017/jfm.2023.933>







# Flow topology in the gap and wake of convex curved tandem cylinders

Tale E. Aasland<sup>1,†</sup>, Bjørnar Pettersen<sup>1</sup>, Helge I. Andersson<sup>1</sup> and Fengjian Jiang<sup>2</sup>

<sup>1</sup>Department of Marine Technology, Norwegian University of Science and Technology, NO-7491 Trondheim, Norway

<sup>2</sup>SINTEF Ocean, NO-7052 Trondheim, Norway

(Received 14 June 2023; revised 14 September 2023; accepted 3 November 2023)

---

Flow around curved tandem cylinders in the convex configuration has been studied by means of direct numerical simulations, for a Reynolds number of 500 and a nominal gap ratio of 3.0. Spanwise variation of flow regimes, as well as curvature-induced axial velocity, leads to an exceedingly complex vortex dynamics in the wake. Both parallel and oblique vortex shedding are observed. Oblique shedding is connected to repeated occurrences of dislocations. The dislocations are caused by two main mechanisms: frequency differences in the upper part of the curved geometry and shedding of gap vortices into the lower near wake. Both types of dislocations are closely associated with a mode switch in the gap. In parts of the gap, there is low-frequency quasi-periodic asymmetry of the gap vortices, where the flow is biased to one side of the gap for intervals of several wake vortex shedding periods. The switch from side to side is associated with a surge of the vertical velocity, and the frequency of the switch is similar to that of long-term variation of the recirculation length in the lower gap.

**Key words:** vortex dynamics, vortex interactions, vortex shedding

---

## 1. Introduction

The flow around multiple curved geometries covers highly interesting fundamental flow physics, and the topic has high relevance from an engineering point of view. The study of tandem curved cylinders encompasses both these perspectives. To date there are only two studies that investigate dual curved cylinders (Gao *et al.* 2021; Aasland *et al.* 2022a).

† Email address for correspondence: [tale.e.aasland@ntnu.no](mailto:tale.e.aasland@ntnu.no)

Therefore, an introduction to flow around a single curved cylinder is given; a geometry which has become the topic of quite a large number of studies in recent years.

Some basic concepts of the flow around two straight cylinders in tandem are also relevant when discussing the present results, and these are introduced in § 1.2.

### 1.1. Single curved cylinders

The major difference between a straight and a curved cylinder is the existence of curvature-induced flow along the cylinder axis, which influences the wake topology and forces acting on the curved cylinder. The direction and strength of the axial flow depend strongly on the inflow direction with respect to the plane of curvature. Therefore, the flow topology can change fundamentally with variation of the inflow direction (Miliou, Sherwin & Graham 2003a,b; Miliou *et al.* 2007; Ahmed 2010; Lee, Paik & Srinil 2020). Directing the incoming flow towards the outer face of the cylinder (convex configuration) results in a thoroughly different wake dynamics than directing it towards the inner face (concave configuration). Because the object of the present study is to investigate fixed curved tandem cylinders in the convex configuration, concave and oblique configurations are excluded from the present review, as are studies of vortex-induced vibrations of curved cylinders. Comprehensive studies of the concave configuration were carried out by, among others, Miliou *et al.* (2007), Shang *et al.* (2018), Jiang, Pettersen & Andersson (2018a, 2019), Jiang *et al.* (2018b), Chiatto *et al.* (2021, 2023) and Lee *et al.* (2020), who investigated a curved cylinder at several inflow angles. Vortex-induced vibration of curved cylinders was studied by de Vecchi, Sherwin & Graham (2008), Assi *et al.* (2014), Seyed-Aghazadeh, Budz & Modarres-Sadeghi (2015), Seyed-Aghazadeh *et al.* (2021), Srinil, Ma & Zhang (2018) and Ma & Srinil (2023).

Superficially, the wake of a single curved cylinder in the convex configuration is similar to that of a straight cylinder, as both wakes exhibit a von Kármán vortex street (see figure 1). One might perhaps have expected cellular shedding in the curved case, due to phase differences stemming from the local curvature, similar to the wake behind a tapered cylinder (Narasimhamurthy, Andersson & Pettersen 2009). Miliou *et al.* (2007), however, showed that, with the exception of a Reynolds number of 100 ( $Re = U_0 D / \nu$ , where  $U_0$  is the inflow velocity,  $D$  is the cylinder diameter and  $\nu$  is the kinematic viscosity), the vortices are in phase along the span, with no spanwise variation of the Strouhal number ( $St = f_v D / U_0$ , where  $f_v$  is the vortex shedding frequency). This result is related to weakening of the vortex strength with increasing axial flow. Strong axial flow in the lower part of the near wake inhibits communication between the shear layers, similar to a splitter plate (Cardell 1993), resulting in a weaker swirling flow. A similar non-shedding regime was described by Ramberg (1983) for a straight cylinder with inclination. Contrary to the lower wake, the spanwise vortices in the upper part of the wake, where the cylinder axis is nearly normal to the incoming flow, maintain a strength comparable to a straight cylinder. Thus, the wake is driven by the upper vortices. For a given Reynolds number, these vortices have a dominant frequency close to that of a straight cylinder (Miliou *et al.* 2007).

The orientation of the spanwise vortex cores can be normal to the incoming flow or inclined to align with the local curvature. Miliou *et al.* (2007) found straight cores at a Reynolds number of 100, and moderately inclined cores for  $Re = 500$ , as illustrated in figure 1(a). They suggested that the vortex cores align increasingly with the local curvature as the Reynolds number increases, which was corroborated by the results by Gallardo, Andersson & Pettersen (2014) at  $Re = 3900$ .

## Flow topology in the gap and wake

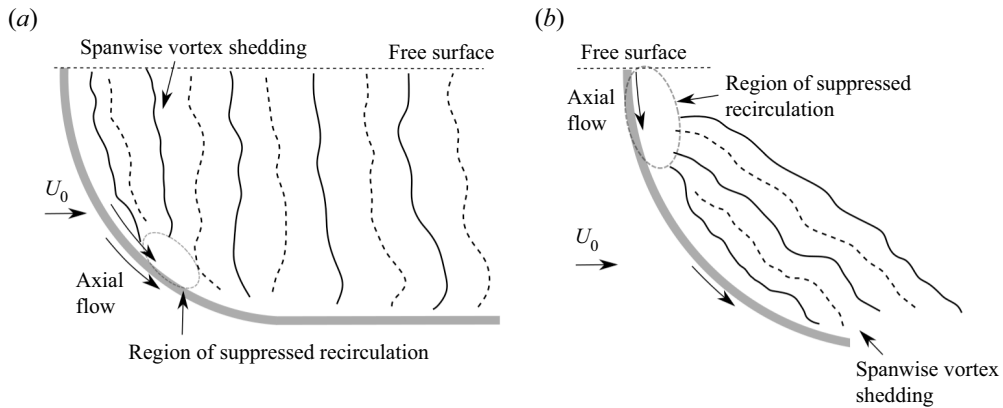


Figure 1. Schematic of the flow around convex curved cylinders. Adapted from flow visualisations by (a) Miliou *et al.* (2007) and (b) Shang, Stone & Smits (2018). The Reynolds numbers were 500 and 486, and the radii of curvature 12.5 and 22.9, respectively. The solid and dashed lines represent the cores of oppositely rotating vortex cells.

The axial flow can be quite significant. For instance, Miliou *et al.* (2007) estimated the downwards-deflected flow rate along the stagnation face to be approximately one third of the total flow rate. Because of the axial flow, the top boundary condition, be it numerical or experimental, is important. Shang *et al.* (2018) discovered that, in their experiment, vortex shedding was inhibited within a distance of up to  $6D$  away from the free surface, depending on the radius of curvature (concave cylinder). A corresponding result was found in numerical simulations by Gallardo, Pettersen & Andersson (2013). It was discovered that the free-slip condition on the top boundary of the computational domain influenced the vertical velocity component unless a straight  $6D$  long vertical extension was added to the upper geometry. When the extension was included, a mild upwelling was allowed to develop behind the upper part of the curved cylinder, which extended upwards along the straight part of the geometry.

With the inclusion of a straight vertical extension, spanwise vortex dislocations began to occur in the simulations of Gallardo *et al.* (2014). Such dislocations arise when local frequency and/or phase differences cause neighbouring vortex cells to move out of phase with each other, resulting in complex linking patterns between the vortex cores (Williamson 1989). In the wake of a straight cylinder, vortex dislocations develop spontaneously when the spanwise length is sufficient (Henderson 1997). This phenomenon may occur anywhere along the span, and the location varies with time. In the curved cylinder case, however, the dislocations always occurred near the intersection between the curved part and the straight vertical extension, and propagated downwards into the wake. It was discovered that the two cylinder parts had slightly different Strouhal numbers, and this was believed to be the cause of the dislocations (Gallardo *et al.* 2014).

An important question for investigations into curved cylinder flow has been the applicability of the independence principle for such geometries. The independence principle relies on the assumption that only the normal inflow component is important to the vortex dynamics, and that the axial flow can be neglected. For a curved cylinder, the constant change in local curvature would result in a different local Strouhal number for every section along the span, using this assumption. Thus, the validity of the independence principle was in essence refuted for a curved cylinder by Miliou *et al.* (2007), given that their results showed constant  $St$  along the span. However, Gallardo *et al.* (2014)

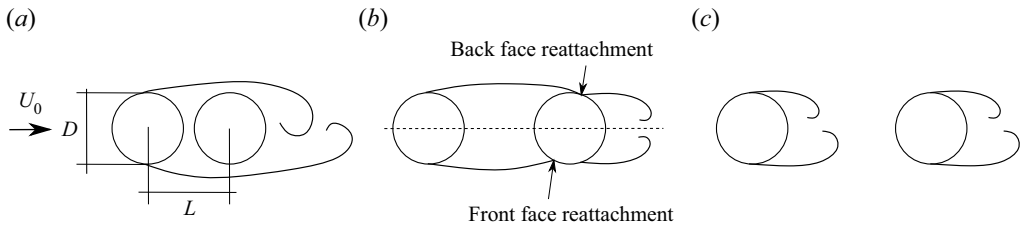


Figure 2. The main flow regimes of straight tandem cylinders: (a) overshoot/no reattachment, (b) reattachment and (c) co-shedding. Reattachment may occur on the back face or the front face of the downstream cylinder.

showed that the independence principle was valid along the upper part of the cylinder. The base pressure coefficient computed according to this principle began to deviate from the actual values approximately at the mid-span of the curved part of the geometry. The deviation point corresponded with the upper boundary of the region where recirculation was suppressed by the axial flow. Based on this result, a distinction between the upper and lower wake was suggested.

## 1.2. Straight tandem cylinders

Tandem cylinder flow comprises three main flow regimes: overshoot, reattachment and co-shedding, as shown in [figure 2](#). Within the overshoot regime, the upstream cylinder shear layers envelop the downstream cylinder and roll up in the wake, so that shedding is controlled by the upstream cylinder. When the gap spacing between the cylinders increases, the upstream cylinder shear layers begin to reattach onto the downstream cylinder. Shedding now occurs from the downstream cylinder alone. A further increase of the cylinder spacing leads to an upstream movement of the reattachment point, until finally, the upstream shear layers detach from the downstream cylinder, and shedding of large-scale vortices occurs from both cylinders. Tandem cylinder flow regimes are normally discussed in terms of the gap ratio,  $L/D$ , where  $L$  is the centre to centre spacing between the cylinders, and  $D$  is the cylinder diameter.

Because the shear layers and the entrainment demands of large-scale vortex formation are sensitive to the inflow velocity, the tandem cylinder regimes are Reynolds number dependent. This makes it challenging to characterise the different regimes by means of the gap ratio alone. Nevertheless, Zdravkovich (1987) suggested the following classification, which is still in wide use: overshoot  $1.0 \leq L/D \leq 1.2-1.8$ , reattachment  $1.2-1.8 \leq L/D \leq 3.4-3.8$  and co-shedding  $3.4-3.8 \leq L/D$ . Due to the Reynolds number dependency, Xu & Zhou (2004) later proposed that, instead of a range of gap ratios, the flow regimes of tandem cylinders should be described by means of ranges of Reynolds number and gap ratio combinations.

The gap ratio where co-shedding commences is traditionally called the critical spacing,  $L_c/D$ , or the drag-inversion spacing. The latter term refers to the fact that recirculation in the gap (which occurs during reattachment) leads to suction, resulting in a negative drag coefficient for the downstream cylinder. When there is shedding from both cylinders, the sign of the downstream cylinder drag coefficient is reversed, and becomes positive; hence 'drag inversion'. The critical spacing typically varies between 3.0 and 5.0 (Okajima 1979; Igarashi 1981; Xu & Zhou 2004; Alam 2014), depending on the Reynolds number and other factors, such as free-stream turbulence (Ljungkrona, Norberg & Sunden 1991) or inflow gust amplitude (Wang *et al.* 2022).

Reattachment of the upstream cylinder shear layers may be alternating, quasi-steady/symmetric or intermittent (Zdravkovich 1987). Alternating reattachment means that one shear layer reattaches, while the other overshoots the downstream cylinder. Within the reattachment regime, recirculating vortices form in the gap between the cylinders. For lower gap ratios, these are symmetric (Lin, Yang & Rockwell 2002). As the gap ratio is increased, the recirculating vortices become asymmetric/alternating (Lin *et al.* 2002; Zhou *et al.* 2019). Because they are restrained by the presence of the downstream cylinder, these vortices form repeatedly at the same streamwise location, whether they are symmetric or alternating. Therefore, they are typically dubbed quasi-stationary or quasi-steady in the literature. Herein, we simply call them ‘gap vortices’.

The transition between tandem cylinder flow regimes is subject to bi-stability, meaning that the flow intermittently jumps between regimes. Intermittent overshoot/reattachment was found by Xu & Zhou (2004), but has, to our knowledge, not been reported by others. Intermittent reattachment/co-shedding, however, is reported in a number of studies (Igarashi 1981; Xu & Zhou 2004; Kitagawa & Ohta 2008; Alam 2014; Afgan *et al.* 2023). When the term ‘bi-stability’ is used in the context of tandem cylinders, it usually refers to the jump between reattachment and co-shedding.

Igarashi (1981) reported that the bi-stable regime starts when the gap vortices become unstable, and shedding occurs intermittently (labelled regime D in that study). For a given Reynolds number, intervals of shedding in the gap became more frequent, with longer duration, as the gap ratio was increased. Bi-stability manifests itself as two distinct velocity spectral peaks, of similar magnitude. In Igarashi’s (1981) study, for a given gap ratio, these peaks start out close to one another, and gradually separate as the Reynolds number is increased.

The three-dimensionality of the gap and wake is important, in particular at moderate Reynolds numbers. Deng *et al.* (2006), Papaioannou *et al.* (2006) and Carmo & Meneghini (2006) all concluded that two-dimensional simulations failed to predict the correct drag-inversion spacing for a three-dimensional wake. Moreover, Papaioannou *et al.* (2006) discovered that there are strong spanwise phase variations in the gap and wake within the reattachment regime, with a clear periodic spanwise structure. A similar result was recently reported by Wang *et al.* (2021), for channel-confined tandem cylinders. The results of Aasland *et al.* (2022*b*) indicated the possibility of spanwise localised bi-stability near the critical spacing, where shedding in the gap occurs in spanwise cells. This was confirmed by Aasland *et al.* (2023), who found that bi-stability manifests not only spanwise localised, but also asymmetrically in the gap; shedding may occur repeatedly from just one gap shear layer.

For further details, the reader is encouraged to peruse the comprehensive reviews of Sumner (2010), and Zhou & Alam (2016).

### 1.3. *Motivation for the present investigation*

Due to their relevance to the aerospace industry (typically as simplified configurations of aircraft landing gear), non-parallel tandem cylinders have been investigated by several researchers (Thakur, Liu & Marshall 2004; Wilkins, Hogan & Hall 2013; Younis, Alam & Zhou 2016; Alam *et al.* 2022), but there are still very few investigations concerning curved dual cylinders. The lack of literature is possibly due to the complexity of the subject. Meticulous attention to the set-up is required, and in the case of numerical investigations, the demand on grid refinement is large. Gao *et al.* (2021) investigated side-by-side cylinders at different spacings, for Reynolds numbers of 100 and 500. The study of Zhu *et al.* (2019) is concerned with a symmetrical, hanging riser segment of

different curvatures (i.e. different distances between the end points), at a Reynolds number of 100. For high curvatures, the cylinder end segments are close enough that the flow resembles that of tandem cylinders, with a concave cylinder in the wake of a convex one.

An initial study of curved tandem cylinders at a gap ratio of 3.0 was conducted by Aasland *et al.* (2022a), which was concerned mainly with the forces. Spanwise variation of tandem flow regimes, due to a gradual change in the effective gap ratio along the span, was discovered. There was low-frequency variation of the drag coefficients, and it was suggested that this may be caused by a slow meandering of the location at which gap vortex shedding starts.

The aim of the present study is to characterise the flow topology of the gap and wake; in particular, intricate interaction between these two flow regions, and how bi-stability in the gap influences the wake region. Moreover, the source of the low-frequency variations described by Aasland *et al.* (2022a) is investigated, along with the hypothesis of meandering gap shedding inception.

## 2. Flow problem formulation and computational aspects

The present geometry consists of two curved tandem cylinders of equal diameter, with the inflow in the plane of curvature of the cylinders. The convex configuration is studied, and the gap ratio is  $L/D = 3.0$ . A Reynolds number of 500 was chosen, based on previous investigations with a single and dual curved cylinders (Miliou *et al.* 2007; Jiang *et al.* 2018a,b; Lee *et al.* 2020; Gao *et al.* 2021; Aasland *et al.* 2022a). For this combination of gap ratio and Reynolds number, alternating overshoot/reattachment is expected for straight tandem cylinders (Aasland *et al.* 2023), with the three-dimensional gap/wake instability mode T3 (Carmo, Meneghini & Sherwin 2010a).

### 2.1. Governing equations and numerical method

In the present study, the full Navier–Stokes equations for incompressible flow are solved by means of direct numerical simulations (DNS)

$$\frac{\partial u_i}{\partial x_i} = 0, \quad (2.1)$$

$$\frac{\partial u_i}{\partial t} + u_j \frac{\partial u_i}{\partial x_j} = -\frac{1}{\rho} \frac{\partial P}{\partial x_i} + \frac{\partial}{\partial x_j} \left( \nu \left[ \frac{\partial u_i}{\partial x_j} + \frac{\partial u_j}{\partial x_i} \right] \right), \quad i, j = 1, 2, 3, \quad (2.2)$$

where  $u$  is velocity and  $P$  is pressure. All simulations were carried out using the MGLET (multi grid large eddy turbulence) flow solver. MGLET is based on a finite volume formulation of the incompressible Navier–Stokes equations, and uses a staggered Cartesian grid (Manhart 2004). Solid bodies are introduced through an immersed boundary method (Peller *et al.* 2006), where the boundary is discretised using a cut-cell approach (Unglehrt *et al.* 2022). A third-order low-storage explicit Runge–Kutta time integration scheme is used for time stepping, and the Poisson equation is solved using an iterative, strongly implicit procedure. MGLET has previously been used for convex (Gallardo *et al.* 2014; Aasland *et al.* 2022a) and concave (Jiang *et al.* 2018a, 2019) curved cylinder studies.

Free-slip boundary conditions are used on all computational domain boundaries except the inlet and outlet. Uniform inflow is imposed at the inlet, and a Neumann condition is imposed on the velocity components at the outlet. No-slip and impermeability conditions were enforced on the cylinder surfaces.

## Flow topology in the gap and wake

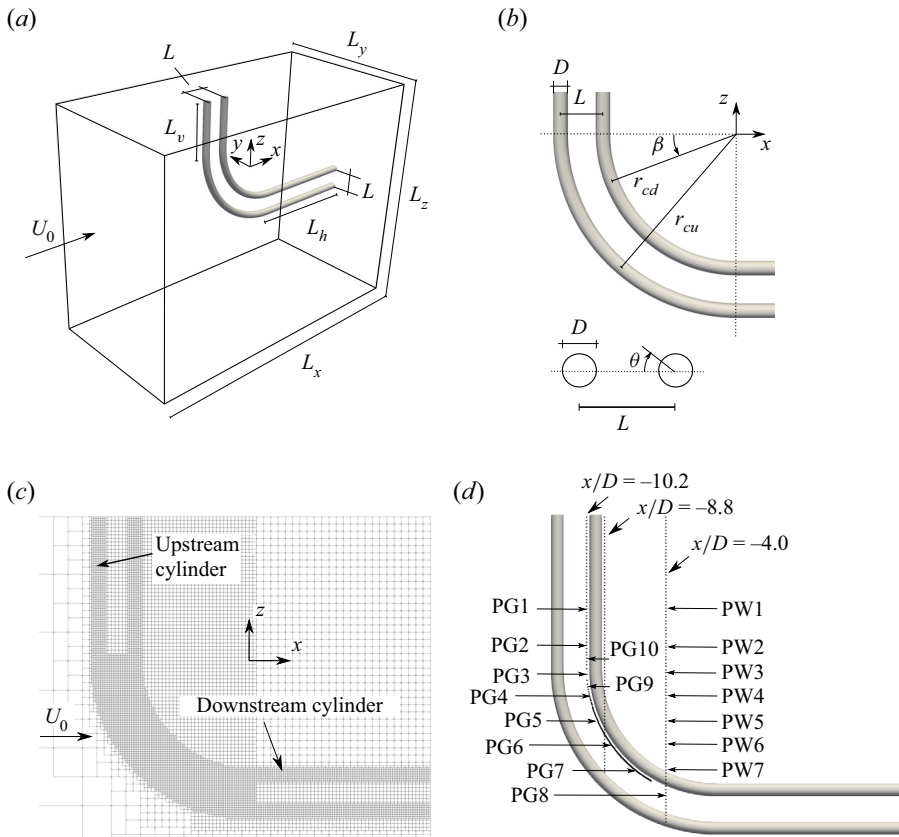


Figure 3. (a) Computational domain, (b) definitions, (c) computational grid schematic and (d) location of velocity probes. Probes PG1–7 are on the same  $z/D$  levels as their counterparts in the wake PW1–7, ranging from  $z/D = 5$  to  $z/D = -8$ . PG8, PG9 and PG10 are located at  $z/D = -10$ ,  $-1.2$  and  $1.0$ , respectively.

During the first  $650 tU_0/D$ , the time step was gradually adjusted to obtain a target Courant number of 0.6. The final time step was  $dt = 0.00247D/U_0$ . After initialisation, sampling of statistics was carried out for 3150 time units, which corresponds to approximately 450 large-scale vortex shedding cycles. The long initialisation and sampling times are required due to low-frequency variations in the flow field, similar to the findings of previous studies (Gallardo *et al.* 2014; Aasland *et al.* 2022a).

Herein, all reported frequencies are based on discrete Fourier transform of velocity time traces sampled at probe lines in the gap and wake, as shown in figure 3(d). Vertical wake probe lines were located along  $(x/D, y/D) = (-4.0, 0.0)$  and  $(-8.8, 0.0)$ . In the gap, the probes were always located  $0.2D$  away from the downstream cylinder stagnation point, at  $y/D = 0$ , spanning  $-9.0 \leq z/D \leq 12.0$ . The internal probe spacing was  $0.25D$  in the wake and the vertical part of the gap. In the curved part of the gap, the spacing was  $0.03125D$ . The frequency resolution can be computed as  $df = 1/(dt \times Nt)$ , where  $Nt$  is the number of sampling points in the time series. Probe data were sampled at every time step, which means  $Nt = 3150/dt$ , so that  $df = 1/3150 = 3.16 \times 10^{-4}$ . Because the geometry is fully three-dimensional, spanwise averaging of spectra (commonly used for straight cylinders), is not appropriate in the present case. Therefore, spectral noise was reduced by means of Welch's method, using a Hamming window with 50% overlap. *In situ* fast Fourier transform (FFT) analysis was carried out, in order to investigate the



distribution of certain frequencies within the flow. The advantage of this method, which is carried out as an integrated part of the simulations, is that the analysis does not depend on specific probes; the results are given for the entire computational domain. The drawback is that the frequencies to be investigated must be specified in advance, and they must all be integer multiples of the lowest specified frequency. Moreover, they cannot be changed without restarting sampling of statistics. For these reasons, *in situ* FFT was first carried out during the main simulation, using a first guess of frequencies. This gave a spectral map of frequencies that were fairly close to the frequencies measured by the probes, although not completely accurate. Then, a new simulation was started from the flow field of the main simulation and run for 150 time units, using target frequencies that were adjusted according to the probe data. This resulted in a more accurate spectral map for the *in situ* FFT, although with the drawback of a shorter sampling time.

## 2.2. Geometry, computational domain and grid

The curved part of each cylinder is a quarter segment of ring with a radius of curvature  $r_c$ . The upstream cylinder has a radius of curvature of  $r_{cu} = 12.5D$ , similar to previous studies with a single curved cylinder (Miliou *et al.* 2007; Gallardo *et al.* 2014). In order to ensure a constant gap ratio along the entire geometry, a curvature of  $r_{cd} = 9.5D$  is used for the downstream cylinder. Due to the uniform inflow condition, the effective gap ratio varies along the curved part of the cylinders. Therefore, the chosen gap ratio is referred to as the nominal gap ratio henceforth.

To minimise the influence from the computational boundaries, the curved tandem cylinders were fitted with straight vertical extensions of  $L_v = 12D$ , as well as horizontal extensions of  $L_h = 15D$ . An evaluation of the required vertical extension length was carried out, and the results are shown in the [Appendix](#).

The computational domain and geometry are depicted in [figure 3](#), as well as a schematic representation of the grid structure. The total domain size is  $43D$ ,  $24D$  and  $43.2D$  in the  $x$ ,  $y$  and  $z$  directions, respectively.

A detailed grid refinement study was carried out by Aasland *et al.* (2022a). It was found that the flow was significantly influenced by the refinement level in the curved part of the gap, where the velocity and pressure gradients are strong. Thus, the final grid featured a refinement of this region to the same grid cell size as in the boundary layers near the solid bodies. The same grid resolution and refinement regions are used in the present study, the only difference being a longer  $L_v$ . The smallest element size is  $dx = dy = dz = 0.0075D$ , which is also the grid resolution inside the boundary layer. The total number of elements is approximately  $704 \times 10^6$ .

## 2.3. Definitions

Herein, the  $x$ ,  $y$  and  $z$  directions are referred to as streamwise, cross-flow and vertical. Vortices that align with the vertical direction are dubbed spanwise. When vortex shedding modes are discussed, ‘parallel’ means that the spanwise orientation of the vortices is parallel to the straight vertical extension, i.e. normal to the inflow direction, and ‘oblique’ in this context means the vortices have an angle in the  $y$ -plane.

Different parts of the gap are referred to in terms of the different parts of the cylinder geometry. ‘Vertical gap’ refers to the gap between the straight vertical extensions, while ‘curved gap’ refers to the gap between the curved cylinder parts and ‘horizontal gap’ refers to the gap between the straight horizontal extensions.

Subscripts  $u$  and  $d$  refer to the upstream and downstream cylinders, respectively.

### 3. Results

#### 3.1. Overview of the flow topology

The wake of curved tandem cylinders is very complex, owing to the spanwise variation of flow regimes, as well as the axial flow. [Figure 4](#) shows the wake topology at two time instances. The basic tandem flow regime, which is found in the upper part of the flow domain, is alternating overshoot/reattachment. Further down, there is a gradual transition from reattachment to gap vortex shedding. The approximate location of gap shedding inception is marked in [figure 4\(a\)](#). Similar to single curved cylinders in the convex configuration, there is a clear von Kármán vortex street in the wake, and the spanwise vortices may be oblique, with a shedding angle  $\alpha$ , or parallel, as depicted in the middle panels of [figures 4\(a\)](#) and [4\(b\)](#), respectively.

Strong downdrafts in the lower gap and wake cause the vortices in these regions to have significant streamwise vorticity, a phenomenon which is clearly shown when the time-averaged vorticity is considered, depicted in [figure 5](#). We see that, although the spanwise vorticity is stronger, the streamwise component cannot be neglected. This is also clear from [figure 4](#), where the vortices in the lower gap and near wake align with the local curvature of the cylinders. Time-averaged fields, the extent of the recirculation region and the stagnation points of the vertical velocity will be further discussed in § 3.6.

In the upper wake, the spanwise vortices are bridged by counter-rotating streamwise vortex pairs, as shown in inset B of [figure 4\(b\)](#). The wavelength of the streamwise vortex pairs appears to be approximately one diameter; a topology reminiscent of the single cylinder three-dimensional instability mode B, described by Williamson (1996). However, if we consider the spanwise vortex undulations in [figure 4\(b\)](#), they seem to have a wavelength close to  $4D$ . According to Carmo *et al.* (2010a), the three-dimensional instability for tandem cylinders at  $L/D = 3.0$ ,  $Re = 500$  is mode T3, with a spanwise wavelength of approximately  $5D$ . This corresponds well with the wavelength of the spanwise vortices in [figure 4\(b\)](#). We believe that the short wavelength of the streamwise structures can be attributed to the large number of secondary vortices that arise from the interaction between the gap shear layers and near wake within the alternating reattachment/overshoot regime, previously described by Aasland *et al.* (2023) for the wake behind straight tandem cylinders.

Vortex dislocations occur frequently in the near wake, predominantly in the region  $-4 \leq z/D \leq 0$ , along the upper portion of the curved cylinder, but also in the lower wake, typically below  $z/D = -6.5$ . These regions represent generation of dislocations by means of two different mechanisms: in the upper region the dislocations stem from spanwise frequency differences, whereas in the lower region they occur due to gap vortex shedding. These dislocations will be referred to as type 1 and type 2, respectively. An example of a type 1 dislocation forming in the upper region of the near wake is shown in [figure 4\(a\)](#).

From [figure 6](#), we see that the occurrence of a dislocation is often followed by others, so that time intervals of reasonably straight vortex lines are followed by intervals of comparable disorder. These events are related to flow mode variations in the gap, something which will be further discussed in § 3.3. [Figure 6](#) also shows incidents where the two dislocation types occur nearly simultaneously.

The inherent three-dimensionality of the geometry enhances bending and tilting of the vortex cores in the wake, resulting in almost knitting-like patterns, especially in the lower part of the wake. Here, three-dimensionality is further strengthened by the interaction with the gap vortices (see inset C of [figure 4b](#)), as well by friction from the cylinder surface which causes retardation. Such a ‘knitting pattern’ is highlighted in inset A of [figure 4\(a\)](#),

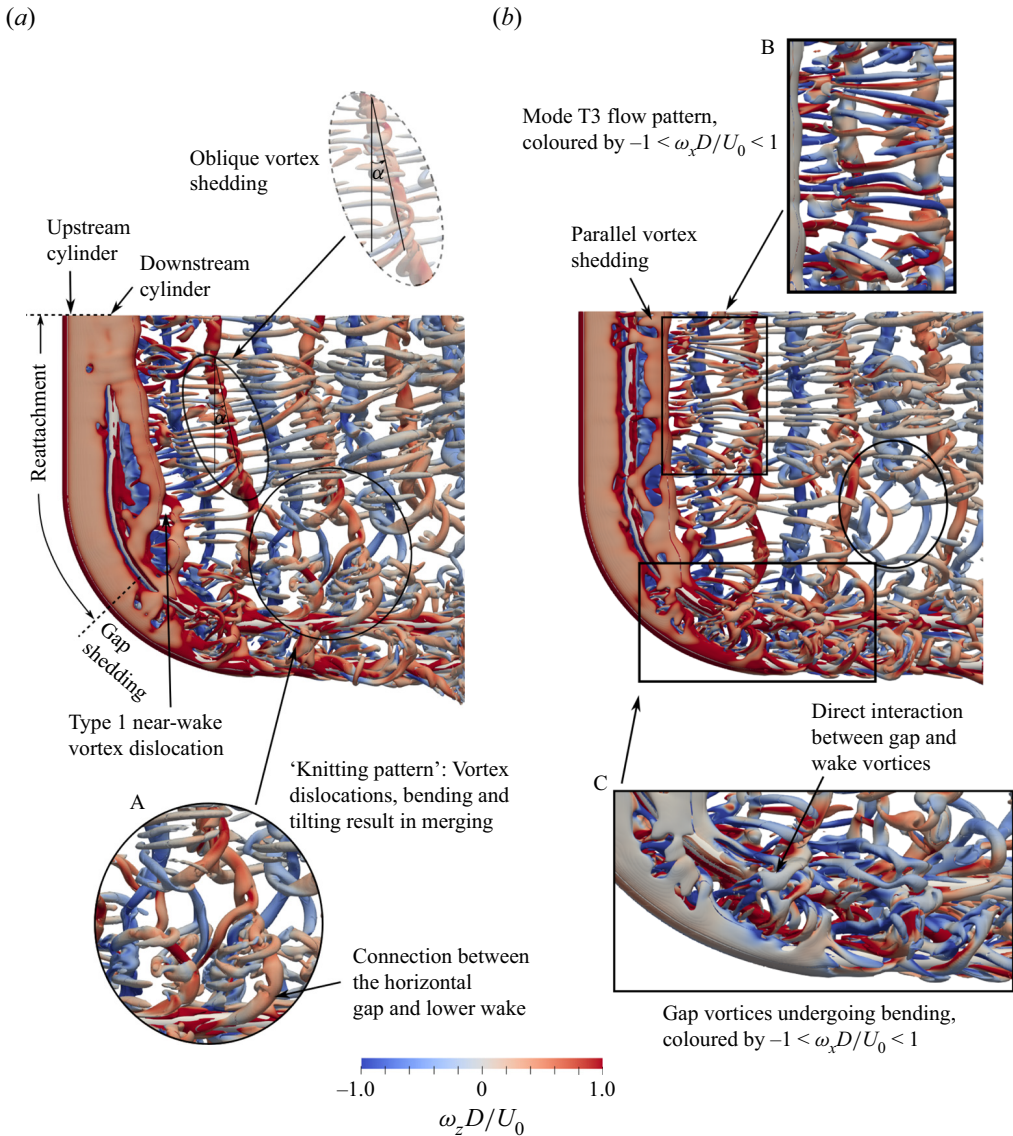


Figure 4. Instantaneous flow field, represented by isosurfaces of  $Q(D/U_0)^2 = 0.02$  coloured by the vertical vorticity. Two distinct shedding modes are found in the wake: (a) oblique mode, at  $tU_0/D = 850$  and (b) parallel mode, at  $tU_0/D = 2450$ . The vortex dynamics of the wake is extremely complex, due to vortex dislocations, bending, tilting and interaction between the structures in the lower wake and the horizontal gap. Dislocations are caused by two separate mechanisms, namely frequency differences (type 1,  $-4 \leq z/D \leq 0$ ) and gap vortex shedding (type 2,  $z/D \leq -6.5$ ).

where spanwise vortex dislocations, combined with bending and tilting of the streamwise vortices, results in merging of spanwise and streamwise structures.

Although the primary vortex shedding frequency persists unchanged along the entire gap, there are secondary frequencies, and these are particularly strong in the region  $-4 \leq z/D \leq 0$  (a comprehensive spectral analysis is given in § 3.4). The resulting spanwise phase differences cause bending of the spanwise vortices which can be quite substantial. This is shown in figure 7(a), where massive bending of the vortices seems to propagate from the region near  $z/D = -2$ . The bending of the spanwise vortices causes rotation of

Flow topology in the gap and wake

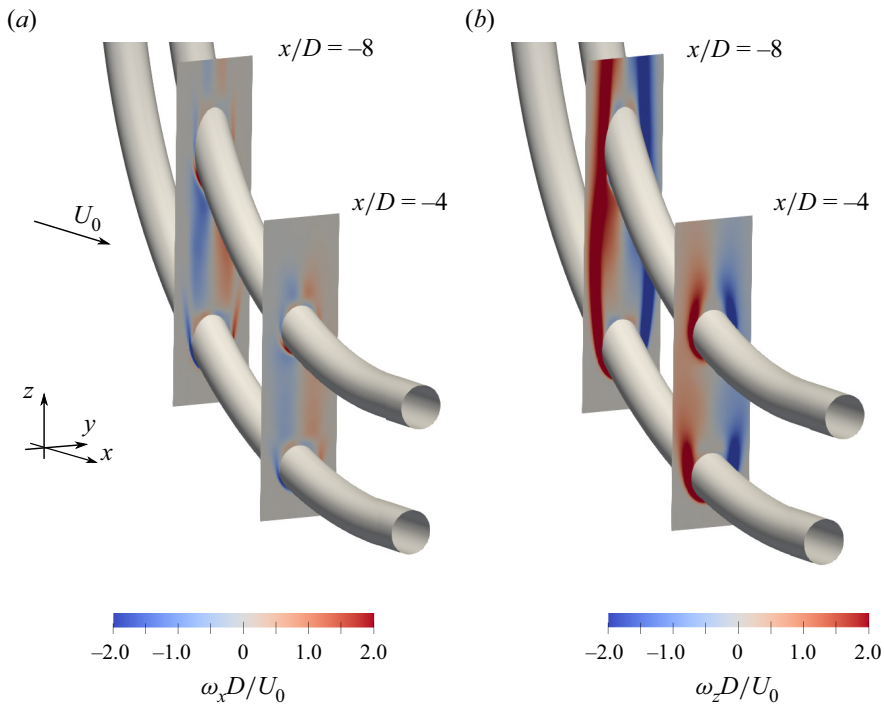


Figure 5. Time-averaged (a) streamwise and (b) spanwise vorticity in two planes in the lower gap and wake. It is clear from (a) that the vorticity of the gap vortices has a strong streamwise component due to the curvature-induced axial velocity.

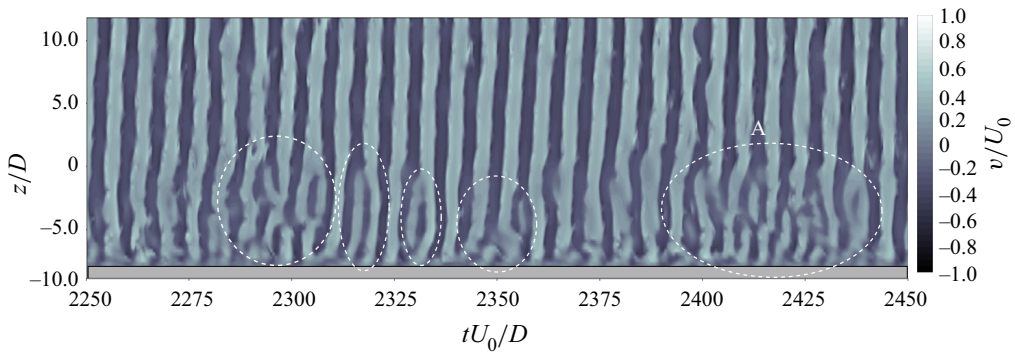


Figure 6. Temporal development of the cross-flow velocity along the probe line at  $x/D = -4$ , over an interval of 200 time units. The downstream cylinder is marked in grey. Spanwise vortex dislocations, marked by white dashed ovals, are frequent in the wake. During the event marked A, dislocations of both type 1 and type 2 occur simultaneously. This particular event can also be observed in figures 7(a) and 7(b).

the streamwise vortices in the braid region at an angle  $\gamma \approx 16^\circ$  at the upper boundary. At the lower boundary, the angle is somewhat larger, due to the retardation of the vortices by the horizontal part of the downstream cylinder. This finding corresponds rather well to the results of Williamson (1992) for forced symmetrical dislocations at a Reynolds number of 300. Measured visually, the half-angle of the  $\Delta$ -shaped dislocation was  $12^\circ$ , whereas using a definition based on the streamwise velocity fluctuations gave an angle of  $18^\circ$ . One must keep in mind, however, that in Williamson's (1992) study, dislocations occurred periodically, being forced, whereas in an unforced transitional wake they are intermittent.

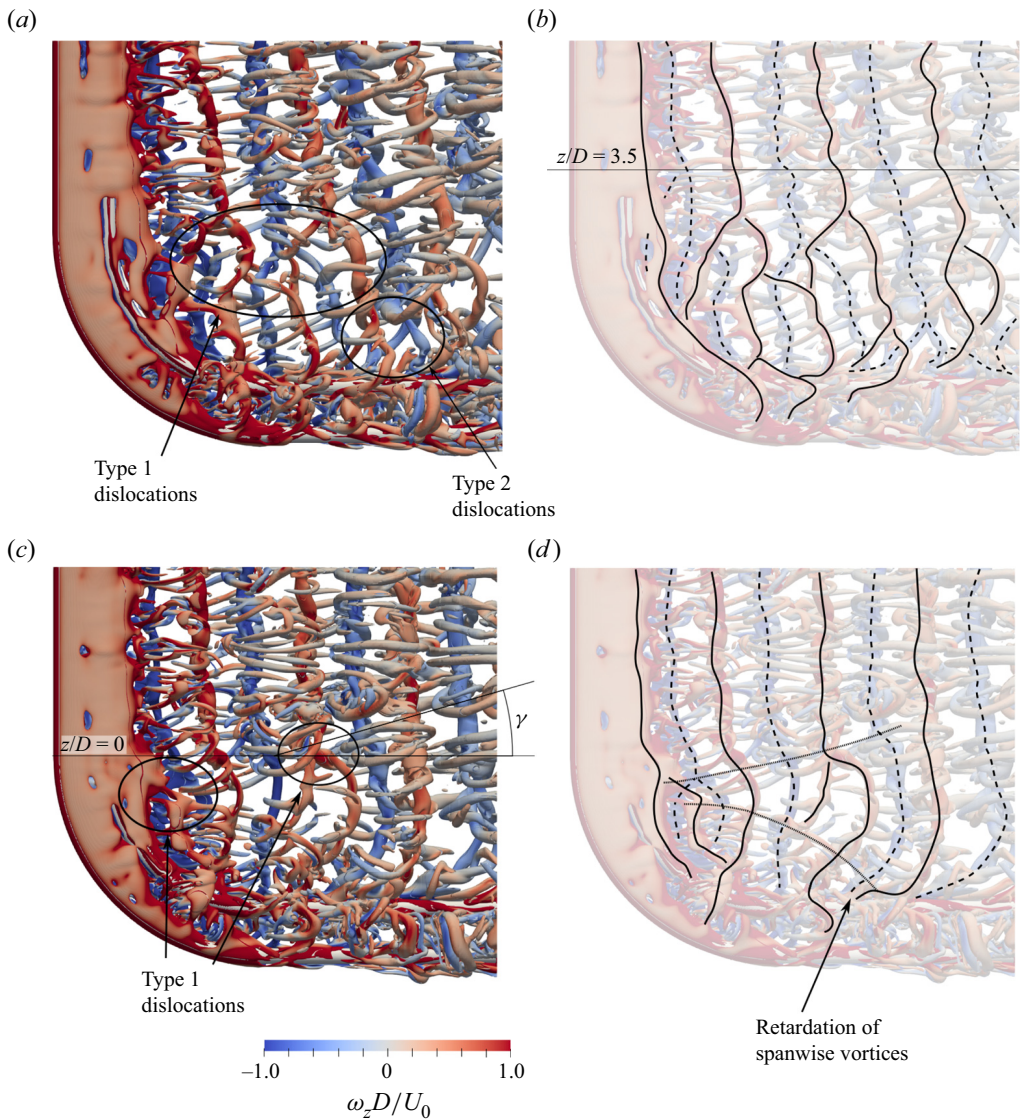


Figure 7. Instantaneous flow field at (a)  $tU_0/D = 1250$  and (c)  $tU_0/D = 3800$ , represented by isosurfaces of  $Q(D/U_0)^2 = 0.02$  coloured by the spanwise vorticity. In (b) and (d), solid lines trace vortex cores of positive spanwise vorticity, while vortex cores of negative spanwise vorticity are traced by dashed lines. In (a), both types of dislocations can be identified in the wake. Moreover, a type 1 dislocation occurs as high up as  $z/D \approx 3.5$ , easily seen in (b). Due to frequency and phase differences, as well as retardation due to the horizontal cylinder part, the spanwise vortices in (d) undergo massive bending in the  $y/D$  plane. This is highlighted by the vertically dashed lines. The bending of spanwise vortices leads to rotation of the streamwise vortices in the braid region. In the present snapshot, the rotation angle is  $\gamma \approx 16^\circ$ .

Both types of spanwise vortex dislocations identified in the present study can be observed in the wake of figure 7(b). This cluster of dislocations is in fact the same event which was captured some periods earlier by the probe line at  $x/D = -4$ , shown in figure 6. In the simplified figure 7(b), we see an uncharacteristic occurrence of a spanwise vortex dislocation along the straight vertical extension, near  $z/D = 3.5$ . Supplementary material and movie 1, available at <https://doi.org/10.1017/jfm.2023.933>, illustrate the development of dislocations in the lower wake.

## 3.2. Spanwise development of flow regimes

The spanwise variation of flow regimes is visualised in [figure 8](#). The flow pattern changes gradually from alternating overshoot/reattachment ([figure 8a–c](#)), to stable reattachment ([figure 8d,e](#)), until vortex shedding finally commences in the gap (starting from [figure 8f](#)).

Compared with the wake at  $z/D = 5$  in [figure 8\(a\)](#), the wake at  $z/D = 2$  and  $z/D = 0$  (shown in [figures 8\(c\)](#) and [8\(d\)](#), respectively) is intricate. This region, which is located directly below the rectangle which marks inset B in [figure 4\(b\)](#), features significant bending and tilting of streamwise eddies, so that these gain a clear spanwise vorticity component, resulting in clusters of secondary vortices in the planes  $z/D = 2$  and  $z/D = 0$ .

The small wake vortex observed in [figures 8\(d\)](#) and [8\(e\)](#) is one leg of a spanwise vortex dislocation, marked by an oval in [figure 4\(b\)](#). In fact, this particular vortex exhibits both type 1 and type 2 dislocations (see [figure 7a](#)). The small vortex cluster in [figure 8\(e\)](#) consists of two vortices twisting around each other in a helical manner. Higher up, in [figure 8\(d\)](#), they have paired.

In [figure 8\(f\)](#), the flow is bi-stable with one-sided reattachment, meaning that vortices are repeatedly shed from a single shear layer, while the opposite shear layer reattaches. Some of these vortices are marked in [figure 8\(f\)](#). Far downstream it becomes increasingly hard to distinguish gap vortices from other vortical structures in the lower wake. In the case of straight tandem cylinders, a so-called binary vortex street is formed for gap ratios between the critical spacing and  $L/D = 6$  (Zdravkovich 1987). Here, vortices from the upstream cylinder are convected downstream alongside downstream cylinder vortices of the same vorticity sign, without merging. From [figure 8\(f\)](#), the wake can be described as loosely binary (on one side), although the gap and wake vortices are staggered. However, one must keep in mind the three-dimensionality of the flow. The gap vortices in the lower wake form the legs of type 2 dislocations.

Near-wake vortex shedding persists down to approximately  $z/D = -8$ , as seen in [figure 8\(g\)](#). Here, the axial flow has grown strong enough to partially inhibit communication between the shear layers, and true shedding only occurs intermittently. A mere  $0.5D$  lower, in [figure 8\(h\)](#), there is no longer vortex shedding in the near wake. The gradual change from von Kármán shedding to non-shedding causes narrowing of the wake width, so that the spanwise vortices have a slight inclination away from the symmetry plane. It is worth noting that, from a statistical point of view, near-wake vortex shedding is suppressed already at  $z/D = -6$ , an observation which is discussed in § 3.6. However, there are large temporal variations.

The character of the vortex formation in the gap gradually changes between  $z/D = -7$  and  $-9.5$  ([figures 8f](#) and [8i](#), respectively), as both the effective gap ratio and the vertical velocity increase. Reattachment occurs intermittently at both  $z/D = -7$  and  $-8$ , something which will shortly be discussed in some detail, while further down, the vortices of both gap shear layers undergo complete roll up. The formation length of the vortices shortens as the gap ratio increases, so that at  $z/D = -9.5$  a short wake is formed in the gap. The strong axial flow imposes additional stress and strain on the gap vortices in this region, which accelerates the transition to turbulence and hastens vortex breakdown, as seen in [figure 8\(i\)](#). With increased vertical velocity comes an increase of small secondary eddies in the gap, as vorticity is transferred from the large-scale gap vortices. This is seen in [figures 8\(g\)](#) and [8\(h\)](#).

In the horizontal gap, the structure of the vortices is extremely complex. In [figure 8\(j\)](#), we see that a vortex street forms in the wake of the upstream cylinder, which features a

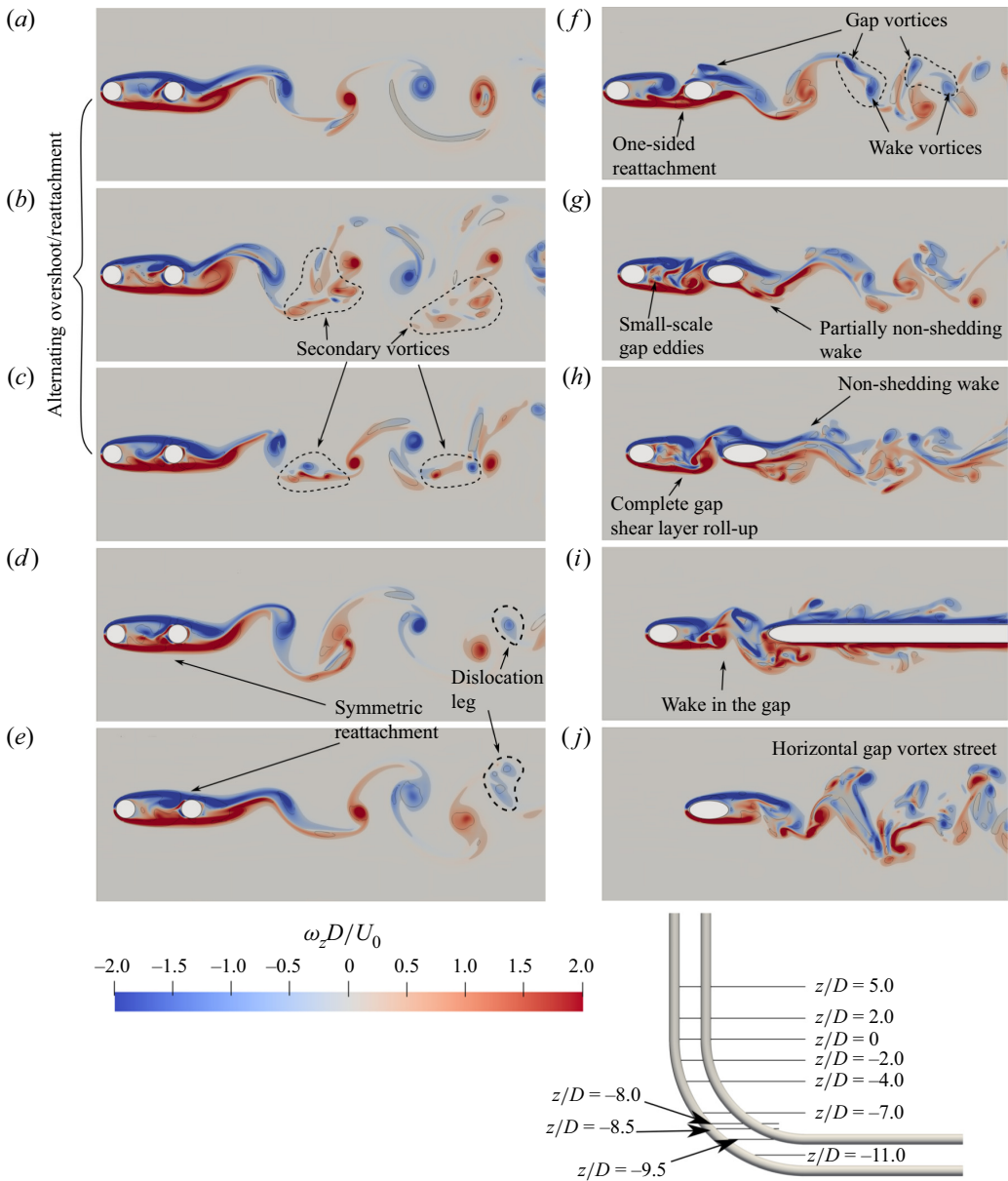


Figure 8. Spanwise development of the instantaneous wake flow at  $tU_0/D = 2450$ , represented by vertical vorticity and contours of  $Q(D/U_0)^2 = 0.1$ . Along the straight vertical extension, (a–c), there is alternating overshoot/reattachment. The flow regime changes to symmetric reattachment between  $z/D = 0$  and  $-2$ , (c) and (d), respectively. Symmetric reattachment persists in (e). Panel (f) shows a one-sided bi-stable regime where gap and wake vortices form staggered pairs (marked by dashed lines). Vortices are shed from both sides of the gap in (g), though communication between the shear layers is still partly inhibited. Depending on the flow mode, shedding may occur in the near wake. In (h) there is complete roll-up of the gap vortices, but the axial flow prevents vortex shedding in the near wake. A wake forms in the gap in (i). Panel (j) shows the vortex street in the horizontal part of the gap. Along the curved part, the effective gap spacing  $L_e$  has been computed by measuring the spacing from the upstream cylinder back to the downstream cylinder front and adding  $1D$ . (a)  $z/D = 5.0$ ,  $L/D = 3.0$ , (b)  $z/D = 2.0$ ,  $L/D = 3.0$ , (c)  $z/D = 0$ ,  $L/D = 3.0$ , (d)  $z/D = -2.0$ ,  $L_e/D = 3.2$ , (e)  $z/D = -4.0$ ,  $L_e/D = 3.6$ , (f)  $z/D = -7.0$ ,  $L_e/D = 4.2$ , (g)  $z/D = -8.0$ ,  $L_e/D = 4.6$ , (h)  $z/D = -8.5$ ,  $L_e/D = 4.8$ , (i)  $z/D = -9.5$ ,  $L_e/D = 6.1$  and (j)  $z/D = -11.0$ .

large number of secondary structures. This wake is in fact wider than the lower wake of the downstream cylinder. This is because the vortices in the horizontal gap loop outwards, away from the symmetry plane, as seen in [figure 4\(b\)](#).

In the present study, it is not just the effective gap ratio that changes along the span, but also the cross-sectional shape of the cylinders in the  $z/D$  planes. For a straight inclined cylinder, it is first and foremost the axial velocity that influences the shedding regime, not the local cross-sectional shape (Shirakashi, Hasegawa & Wakiya 1986). Meanwhile, the case of curved tandem cylinders is more complex, due to the fact that the cross-sectional shape of the downstream cylinder influences the interaction between the gap and wake flows.

Because the upstream and downstream cylinders have different radii of curvature, their cross-sections do not change at the same rate. The change is much faster in the downstream cylinder, with a lower  $r_c$  resulting in a configuration with a slightly elliptical cylinder upstream and an increasingly elongated cross-section downstream (see [figures 8f–8h](#)). This occurs within the gap shedding region, and has two different implications: (i) an elongated downstream body gives the structures from the upstream shear layer more time to interact with the downstream cylinder boundary layer, (ii) vortices shed in the gap impinge at different locations than they would have on a circular downstream cylinder cross-section. One example is the staggered binary vortex pairs in [figure 8\(f\)](#).

### 3.3. Flow bi-stability

In the present study, the flow is bi-stable. It is important to note that this does not merely encompass the switch between reattachment and shedding which occurs in the lower gap; bi-stability is present along the entire span, including the region of alternating overshoot/reattachment. This is consistent with the results of Aasland *et al.* (2023), who showed that there are two flow modes in the gap and near wake of straight tandem cylinders at  $L/D = 3$  and  $Re = 500$ .

Within the reattachment region, the second flow mode generally manifests itself in stronger vortex interactions, stronger velocity fluctuations and wider widths of the gap and wake. Moreover, gap shear layer overshoot penetrates further into the near wake. In accordance with Aasland *et al.* (2023), the second mode may manifest locally, but in the present case the axial velocity enhances communication along the span, and this may trigger a switch of flow modes at additional spanwise locations. In the supplementary material and movie 2, the mode switch first occurs at  $z/D = 0$ , subsequently at  $z/D = -6$  and then finally at  $z/D = -8$ . The second mode is associated with increased vertical velocity fluctuations. While the time-averaged vertical velocity at  $z/D = 0$  is positive (see [figure 17](#)), strong gap vortices have a significant streamwise vorticity component even at this  $z/D$  level. Second mode time intervals correspond to an increase in the number of dislocations of both types, such as the event depicted in [figure 7\(d\)](#).

In the lower gap, the switch between modes is similar to the prevailing understanding of tandem cylinder bi-stability, namely a switch between reattachment and true vortex shedding in the gap. This is exemplified in [figure 9](#), for  $z/D = -8$ . Here, periods of relatively calm flow, with mostly reattachment or one-sided reattachment, are followed by periods of chaotic flow with shedding from both gap shear layers and strong interaction with the near wake. The downstream cylinder shear layer oscillations increase during intervals of the second mode, and may precipitate intermittent near-wake vortex shedding at  $z/D = -8$ .

The time instances shown in [figure 9](#) are chosen to highlight some typical features of the temporal development of the lower gap flow. [Figures 9\(a\)–9\(e\)](#) are part of an interval



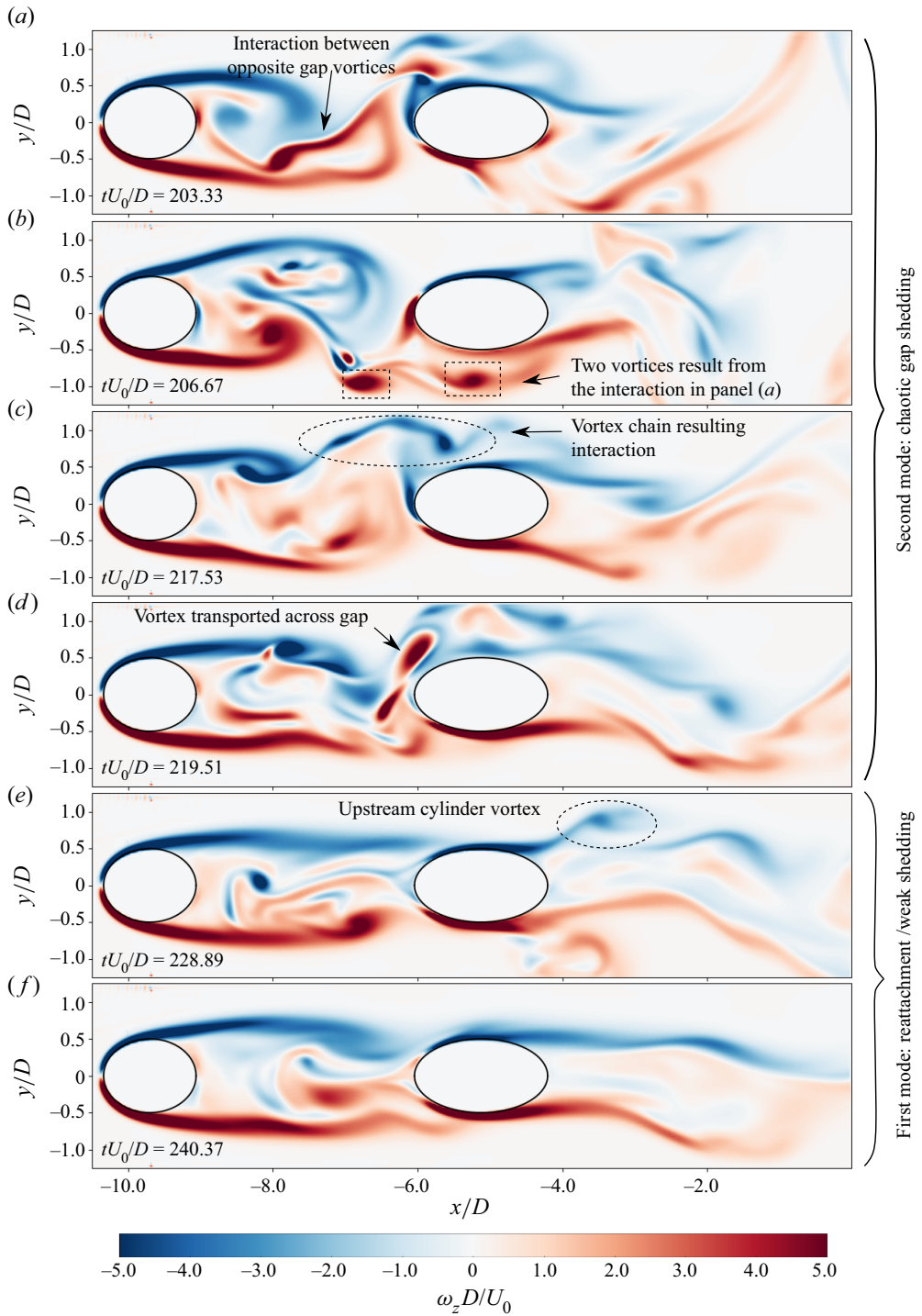


Figure 9. Selected time instances of the flow in the plane  $z/D = -8$ , represented by vertical vorticity. Panels (a–d) depict a chaotic period of strong gap shedding. In panel (e), this period is coming to a close, with the flow returning to a state of variation between weak gap shedding and reattachment. In panel (f), the flow is in the middle of a calm period.

of chaotic gap shedding which lasts for some 30 time units, corresponding to roughly 5 large-scale vortex shedding periods. In [figure 9\(a\)](#), the large-scale vortex forming in the upper shear layer interferes with the vortex that has recently formed in the lower shear layer (event marked by black arrow). Instead of being cleanly shed, this vortex is cut into two separate, smaller vortices, marked by dashed rectangles in [figure 9\(b\)](#). A similar event occurs later in the chaotic interval, resulting in a chain of smaller vortices, this time in the upper shear layer, as seen in [figure 9\(c\)](#) (dashed oval). Moreover, the interaction between the gap shear layers results in the formation of structures of opposite rotation which are sucked into the flow passed the upper side of the downstream cylinder (black arrow in [figure 9d](#)). [Figure 9\(e\)](#) depicts a much calmer flow, towards the end of the chaotic time interval, and in [figure 9\(f\)](#), the flow is back to weak gap shedding interspersed with reattachment. Note that the vortex in the upper shear layer of the downstream cylinder [figure 9\(e\)](#) (dashed oval) originates from the upstream cylinder.

### 3.4. Spectral analysis

Spectra of the cross-flow velocity, computed from probe time traces, are shown in [figure 10](#). The spectral peaks in the present study reproduce those of Aasland *et al.* (2023), where the dominant frequency is  $fD/U_0 = 0.143$ , with secondary peaks of  $fD/U_0 = 0.147$  and  $0.155$ . This is clearly shown in inset G, in the lower right of [figure 10](#). The secondary peaks are connected to the mode switch phenomena described in § 3.3, and their relative importance grows in the lower gap and wake, as mode switches become more frequent.

Not only are the dominant and secondary frequencies the same as for straight tandem cylinders; their value also remains nearly constant along the gap and wake. From single curved cylinder studies in the literature, we know that the vortex shedding in the lower wake is largely governed by the frequency of the shedding in the upper wake (Miliou *et al.* 2007; Gallardo *et al.* 2014). The same appears to be true for tandem curved cylinders, where the vortices along the straight vertical extension govern the frequencies in the rest of the flow.

The degree to which the vortices in the upper part of the gap and wake dominate the Strouhal number likely depends on the length of the straight vertical extension. A longer length favours strong vortices with an orientation normal to the inflow direction. Moreover, the fact that the dominant frequencies are near identical to those in the straight tandem cylinder case indicates that the parallel vortex shedding is more common than oblique shedding.

In the wake, there are two secondary broadband peaks, centred approximately on  $fD/U_0 = 0.18$  and  $0.23$ . These peaks are not present to any significant degree along the straight vertical extension, but are well defined in the region  $-4 \leq z/D \leq 0$ . The peaks are caused by vortex dislocations of type 1, which occur frequently in this spanwise region. If we consider [figure 6](#), we see that a point probe in the wake located for instance at  $z/D = -3$  is passed by a larger number of vortex cores during the given time interval than a probe higher up in the wake.

Wavelet analysis of the cross-flow velocity confirms the existence of rather long intervals of dislocations (such as event A in [figure 6](#)). From the spectral map in [figure 11](#), we see that  $f_v$  does not necessarily co-exist in time with the secondary peaks. In inset A of [figure 11](#), the secondary frequencies dominate  $f_v$  over an interval of some 130 time units. This is quite a long time, considering that it covers 18 vortex shedding cycles, using  $f_v$  as a reference. Most of the intervals are shorter than the one shown in inset A, however. The typical duration of these dislocation intervals seems to correspond well to the observed lifetime

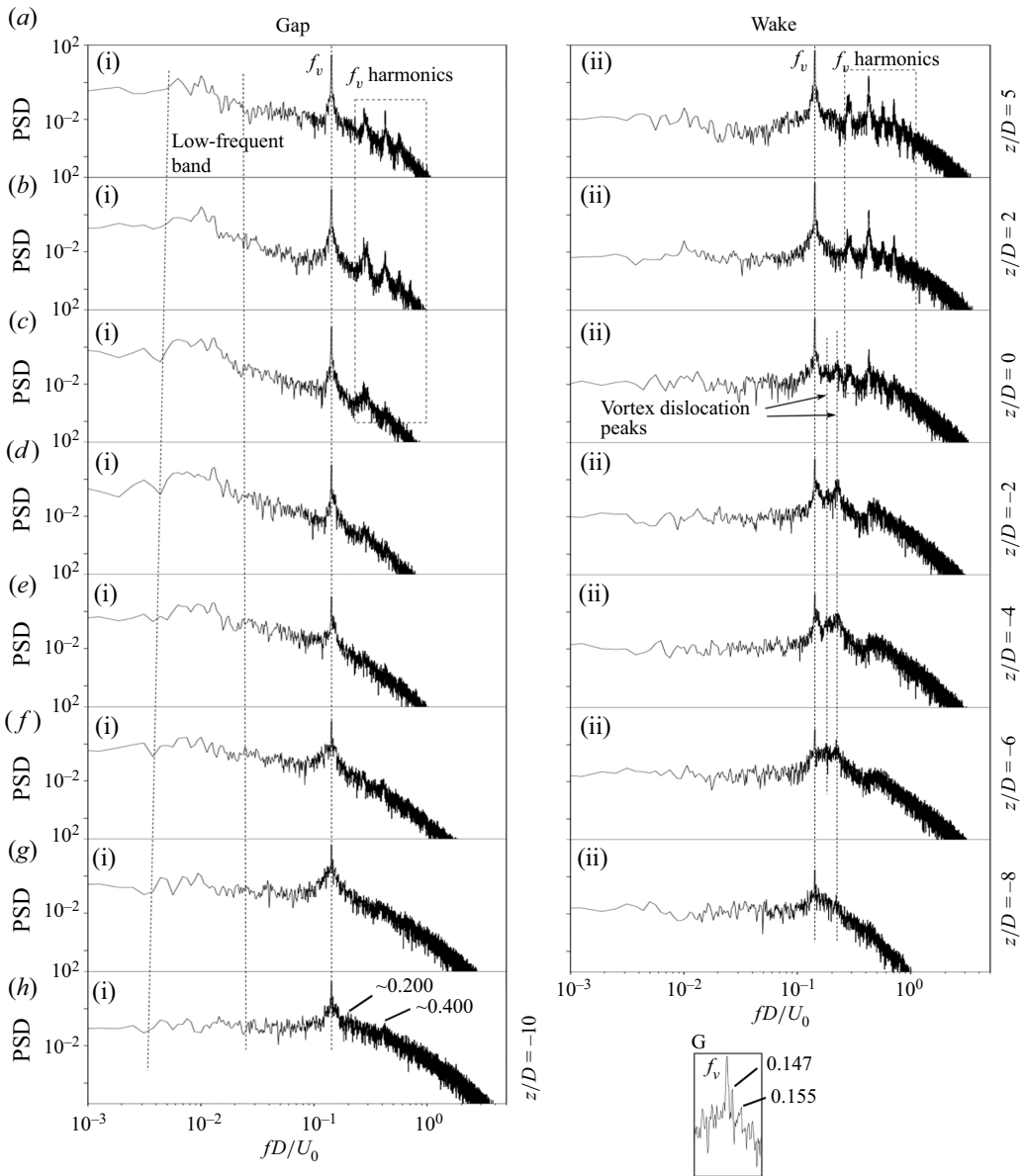


Figure 10. Cross-flow velocity spectra taken at  $y/D = 0.0$ , at various  $z/D$  locations in the gap and wake (probes PG1–8 and PW1–7, see figure 3d). Inset G shows a close up of the spectral peaks in (g). The secondary peaks occur owing to the flow bi-stability. There is significant low-frequency content, and its power spectral density (PSD) is highest in the gap.

of the mode switches described in § 3.3, which underlines the connection between these two phenomena.

There is significant low-frequency activity in the flow, which is clearly shown in the cross-flow velocity spectra of figure 10. The low frequencies appear in a broad band, but there are also distinct spectral peaks within this band. The energy of the low-frequency spectral band is significantly higher in the gap than in the wake. If we look at figure 10(a–h), we see that there is a gradual shift towards lower frequencies as we

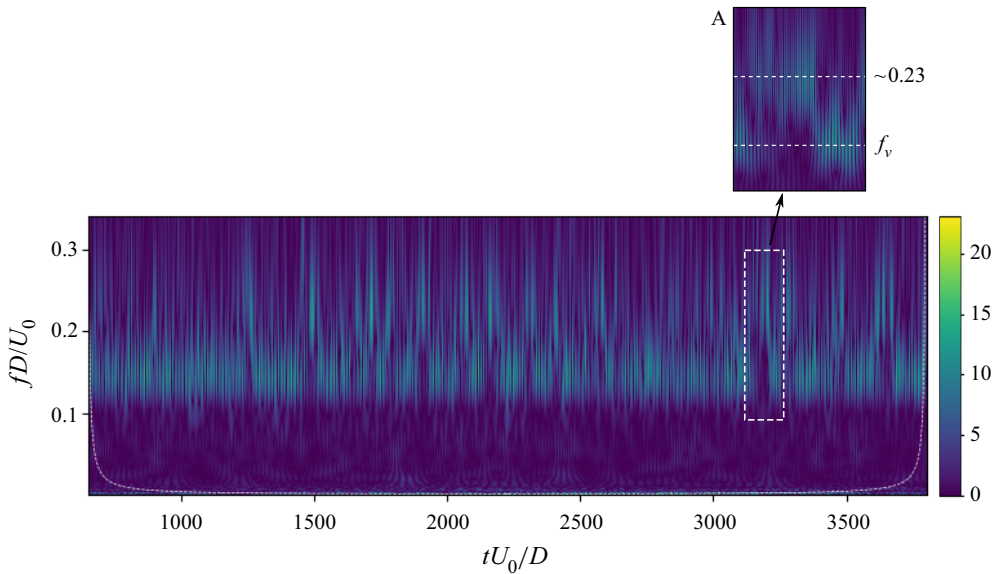


Figure 11. Wavelet map of the cross-flow velocity at wake probe PW3. The corresponding spectrum is shown in figure 10(dii). During certain time intervals, the higher frequency peaks seen in the spectrum become significantly stronger than  $f_v$ , as seen in inset A. The inset covers the time interval  $3130 \leq tU_0/D \leq 3260$ , which corresponds to around 18 cycles of  $f_v$ . The broken lines mark the cone of influence.

move downwards in the gap, while the overall spectral energy within the band decreases somewhat.

The *in situ* FFT analysis shows that, for the lowest analysed frequency,  $fD/U_0 = 0.0089$ , the spectral content is mainly concentrated in the lower part of the curved gap, as depicted in figure 12(a). However, there is also significant spectral energy associated with the gap shear layers and gap vortices at higher  $z/D$ , as seen in figures 12(b) and 12(c). The same holds true for  $fD/U_0 = 0.0178$  and  $0.0356$ , but only the lowest frequency is shown herein, for brevity.

Within the gap shedding region, in figure 12(e), we see that the highest spectral energy of  $fD/U_0 = 0.0089$  seems to be clustered near the cores of the swirling gap vortices. There is a second type of cluster along the gap centreline, which is located upstream of the gap vortices. This is connected to long-term variation of the axial flow.

At  $z/D = -8$ , shown in figure 12(d), the spectral energy cluster is located around the streamwise extent of the vortex formation region, but it is distinctly asymmetrical. The frequency  $fD/U_0 = 0.0089$  was captured during the second set of *in situ* FFT analyses, which only ran for 150 time units. Thus, only a single period of this very low frequency was analysed. However, this result indicates that there may be cross-flow meandering of the vortex formation region whose frequency is too low to appear in the visualisations.

At the probe shown in figure 10(h), which is located nearly in the horizontal part of the gap, the downstream cylinder is no longer directly in the wake of the upstream cylinder; the geometrical constraints are now above and below. Moreover, the local cross-section is no longer circular; it is elliptical with an aspect ratio of approximately  $AR = 0.47$ , where  $AR$  is defined as the ratio between the minor ( $y$ -direction) and major ( $x$ -direction) axes of the ellipsis.

The frequencies are still dominated by vortices along the straight vertical extension. However, figure 10(h) shows a broad-banded secondary peak, centred on  $fD/U_0 = 0.200$ , and its harmonic  $fD/U_0 = 0.400$ . This frequency is not significant higher up in the gap.

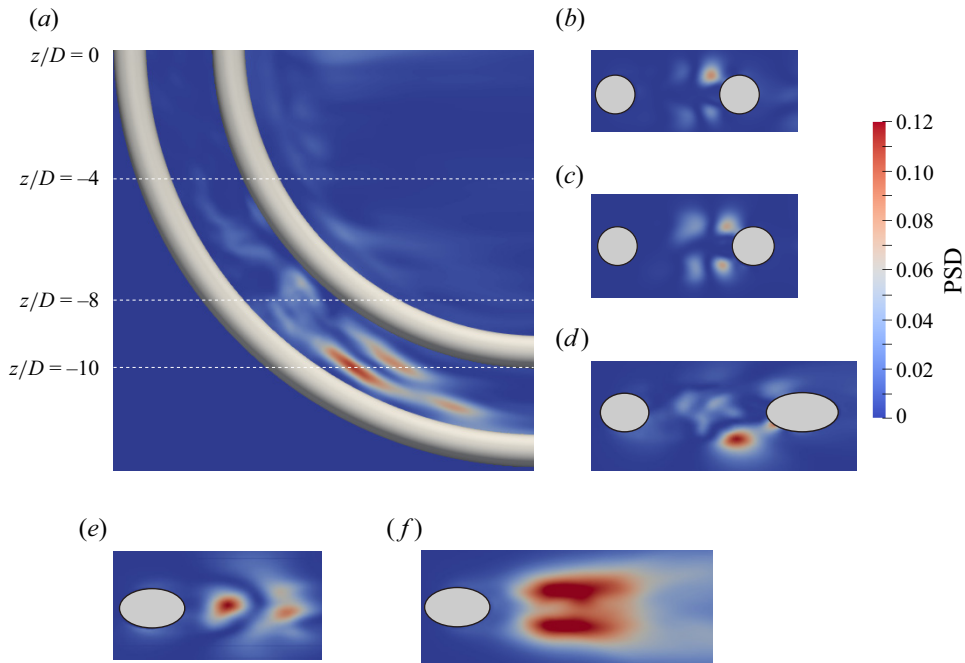


Figure 12. (a–e) Spectral map of the frequency  $fD/U_0 = 0.0089$ . The energy of this low frequency is mainly concentrated in the lower part of the curved gap, in the vortex formation region of the upstream cylinder, but it is also significant for the formation of gap vortices in the upper part of the curved gap. (f) Spectral map of  $fD/U_0 = 0.2175$ . This frequency is part of a broad-banded spectral peak centred around  $fD/U_0 = 0.20$ . In (d), the asymmetry with respect to the gap centreline is a result of the short sampling period. Panels show (a)  $y/D = 0$ , (b)  $z/D = 0$ , (c)  $z/D = -4$ , (d)  $z/D = -8$ , (e)  $z/D = -10$  and (f)  $z/D = -10$ .

The *in situ* FFT analysis has captured a spectral map of  $fD/U_0 = 0.2175$ , shown in figure 12(f), which is part of the broad-banded peak. In the figure we see that the spectral energy is primarily clustered in the shear layers of the upstream cylinder, in the formation region of the swirling vortices. This indicates that the formation length varies. We believe the broad-banded peak may result from a mode switch where the most unstable mode represents a flow similar to a single bluff body wake, in this case an elliptical cylinder.

A wavelet map of the cross-flow velocity in the probe from figure 10(h), along with all three velocity components, is shown in figure 13. In figure 13(c), we see that the cross-flow velocity time trace is quasi-periodic, consisting of relatively high-amplitude intervals interspersed with irregular intervals of low-amplitude fluctuations. Comparing the time trace with the wavelet map, we see that the irregular intervals correspond to a downward shift of the dominant frequency. An upward shift of the dominant frequency, towards  $fD/U_0 \approx 0.2$ , accompanies intervals of stronger, more regular velocity fluctuations, which is indicative of a shorter vortex formation length. Intuitively, a shorter formation length in this part of the gap allows increased flow along the downstream cylinder front face, and figure 13(a) shows that strong cross-flow and vertical velocity fluctuations are accompanied by an increase of the streamwise velocity ( $u/U_0$  is predominantly positive in this part of the gap).

Though we cannot conclude firmly with the available data, the high-frequency intervals are believed to represent the ‘single bluff body’ mode suggested above. It would have been beneficial to compare the frequency of the broad-banded peak with the dominant frequency of an elliptical cylinder. Regrettably, we have found no studies of elliptical

## Flow topology in the gap and wake

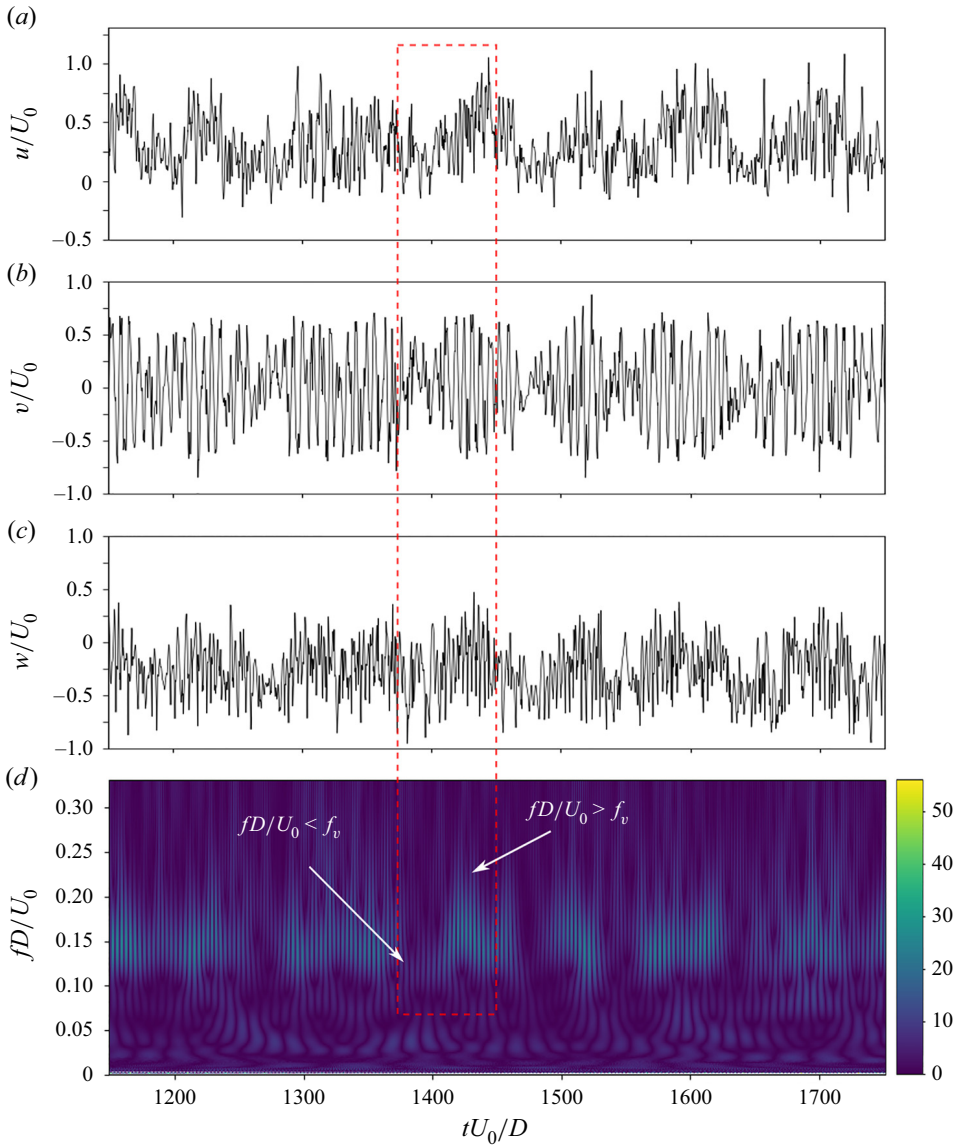


Figure 13. (a) Streamwise, (b) cross-flow and (c) vertical velocity time traces, as well as (d) the cross-flow velocity wavelet map at probe PG8, in the lower curved gap. Intervals of irregular low-amplitude velocity fluctuations correspond to a lowering of the dominant frequency. Conversely, high-amplitude fluctuations correspond with an increase in the dominant frequency. The spectrum at this probe is shown in [figure 10\(h\)](#).

cylinders with comparable conditions that report  $St$ . A study with a Reynolds number of 150 found  $St \approx 0.17$  for  $AR = 0.5$  (Shi, Alam & Bai 2020), but at such a low  $Re$  the flow is two-dimensional.

### 3.5. Low-frequency quasi-periodic gap asymmetry

In the upper part of the gap (above  $z/D \approx -2$ ), vortices are often shed repeatedly from one shear layer. This long-term asymmetry results in an asymmetry of the transverse position

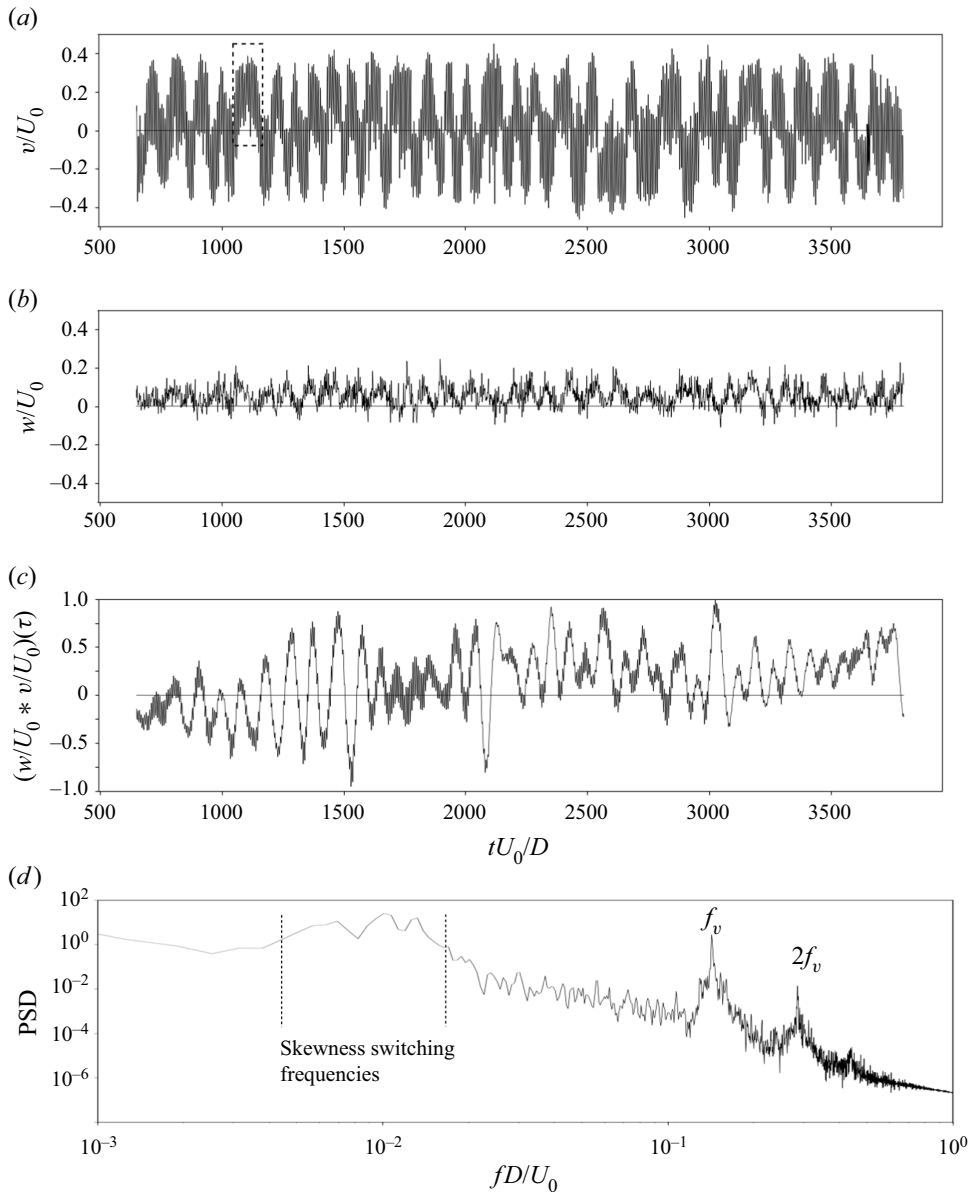


Figure 14. Time traces of (a) cross-flow and (b) vertical velocities at probe PG3 in the gap, at the intersection between the curved and straight cylinder parts. (c) Shows the cross-correlation between the velocities, and (d) shows the spectrum of the cross-correlation. The cross-flow is skewed with respect to the  $v/U_0 = 0$  line, for long periods of time. In the dashed rectangle, for example, it is positive for several vortex shedding periods. Here,  $v$  and  $w$  are clearly correlated, and a switch in the skewness across the  $v/U_0 = 0$  line is normally accompanied by a surge in  $|w/U_0|$ .

of the gap backflow region, which meanders on a time scale longer than that of the wake shedding. These results are consistent with the study of Aasland *et al.* (2023) on straight tandem cylinders, who showed that the asymmetry was caused by a mode switch in one shear layer. In that study, the mode switch occurred intermittently, while in the present study, the mode switch occurs quasi-periodically, so that the long-term asymmetry moves

between gap shear layers with a period of approximately 100 time units. This is clearly shown in [figure 14\(a\)](#), which shows the cross-flow time trace of a probe in the gap, at the intersection between the straight vertical extensions and curved cylinders. Although the long-term average may be zero, the cross-flow velocity is skewed to either side of the  $v/U_0 = 0$  line during several vortex shedding periods at a time. The temporal evolution of the flow field is exemplified in supplementary material and movie 3.

In [figure 14\(b\)](#), the vertical velocity is plotted. Close inspection reveals that a switch of the asymmetry is normally accompanied by a surge of  $|w/U_0|$ . The cross-flow and vertical velocities are clearly correlated, as shown in [figure 14\(c\)](#). Running an FFT of the cross-correlation produces a triple low-frequency spectral peak centred around  $fD/U_0 = 0.01$ , with secondary peaks at  $fD/U_0 = 0.0065$  and  $0.013$ , shown in [figure 14\(d\)](#). This frequency range corresponds well with the low-frequency band observed in the spectra in [figures 10\(a\)–10\(g\)](#), particularly within the reattachment region of the gap (i.e. above  $z/D \approx -6$ ).

Behaviour similar to that of the time trace in [figure 14\(a\)](#) is found to a certain degree in the cross-flow velocity for all probes above  $z/D = -4$  (shown for  $-2 \leq z/D \leq 1$  in [figure 15](#)). However, the transverse switch is most clearly defined in the range  $-4.0 \leq z/D \leq 0$ . This is the range within which the bi-stability frequencies are most pronounced, as shown in the spectra of [figures 10\(c\)–10\(e\)](#), and also the range within which type 1 dislocations most frequently develop.

[Figure 15](#) shows that the transverse switch is slightly out of phase along the span. It occurs first in the upper curved gap, and propagates upwards along the straight vertical extension.

### 3.6. Recirculation and secondary flows

In the time-averaged sense, the larger part of the gap region falls under the reattachment regime, which persists along the entire vertical extension and down to gap shedding angle,  $\beta_{GS} = 38.1^\circ$ , as shown in [figure 16\(a\)](#). The following gap recirculation bubble is suppressed at  $\beta_{ru} = 45.6^\circ$ . In comparison, recirculation in the wake is suppressed at  $\beta_{rd} = 37.4^\circ$ . These values are based on the time-averaged flow in the centreplane, and do not take the swirling vortices in the lower gap into account. The extent of the swirling vortices is shown in [figure 18](#), which plots the zero shear stress contour on the cylinder surfaces. Their inception corresponds with the recirculation suppression.

The non-zero values of cross-flow velocity in the centreplane ([figure 16b](#)) are caused primarily by the long-term asymmetry of the gap vortices. The values are small compared with the straight tandem cylinder case of (Aasland *et al.* 2023). Long-term asymmetry is not confined to the reattachment region, with non-zero values of  $V/U_0$  also appearing in the lower gap. This is consistent with the in situ FFT results shown in [figure 12\(d\)](#).

In [figure 16\(c\)](#), we see that there is upwelling in the entire part of the vertical gap and near wake, which penetrates down to the stagnation points at  $\beta_{stgu} = 44.7^\circ$  and  $\beta_{stgd} = 34.3^\circ$ , respectively. The upwelling velocities are low compared with the downdraft in the lower gap and wake, something which is clearly shown in [figure 17](#). In both the gap and the wake, the stagnation points are located slightly higher than the point of suppressed recirculation. In the present study, the region of maximum upwelling velocity is found along the straight vertical extension, near  $z/D = 2$ . This differs from the single curved cylinder case of Gallardo *et al.* (2014), where the maximum upwelling velocities were found along the curved part of the cylinder, in the region that corresponds to  $-6 \leq z/D \leq -2$  in the present study.



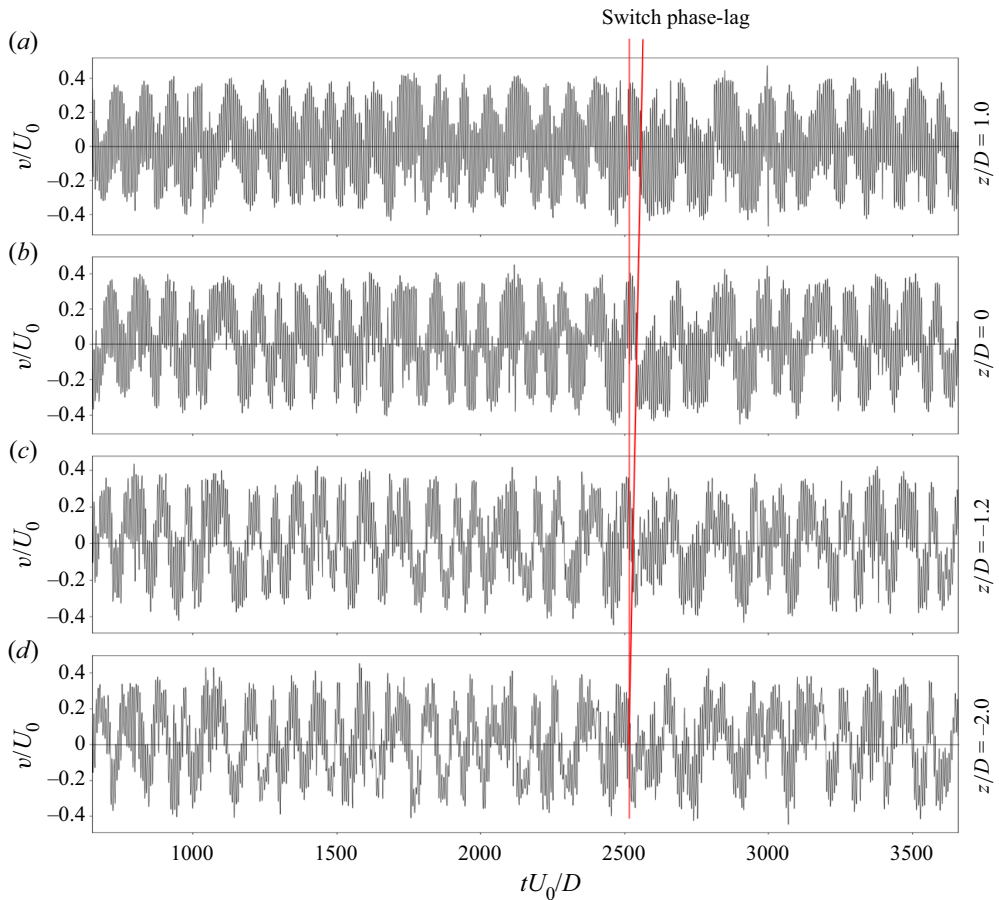


Figure 15. Time traces of cross-flow velocity at various  $z/D$  locations along the gap (probes PG10, PG3, PG9 and PG4). The quasi-periodic asymmetry switch in the gap is slightly out of phase along the span, as indicated by the red lines, with the switch first occurring in upper curved gap, then propagating upwards along the straight vertical extension.

There is a second upwelling zone in the wake, marked in [figure 16\(c\)](#), which spreads from the lower part of the vertical extension with a wedge-like shape. In this region, there is significant bending and helical twisting of the vortices, associated with the spanwise vortex dislocations. For a straight vortex tube, the induced velocity is purely circumferential, but when two vortices twist around each other in a helical manner (which happens when the dislocations legs join together), the induced velocity has a component along the vortex core axis (see [figure 25](#) of [Williamson 1992](#)). Note that the upper boundary of the upwelling region has approximately the same angle as the rotated streamwise vortices of [figure 7](#).

In [figure 16\(a\)](#), the contours in the near wake show that the streamwise extension of the recirculation bubble is considerably longer along the curved part of the downstream cylinder than along the straight vertical extension. This is quite different from the turbulent wake behind a single curved cylinder studied by [Gallardo \*et al.\* \(2014\)](#), where the recirculation bubble has approximately the same streamwise length down to the region of swirling flow, where it is gradually attenuated. The increase in recirculation length actually starts along the lower part of the straight vertical extension, near  $z/D = 1$ . It is also worth noting that the strongest backflow velocities are found in the region  $-4 \leq z/D \leq 0$ , which is also where the recirculation length is at its longest. The backflow velocities along the

## Flow topology in the gap and wake

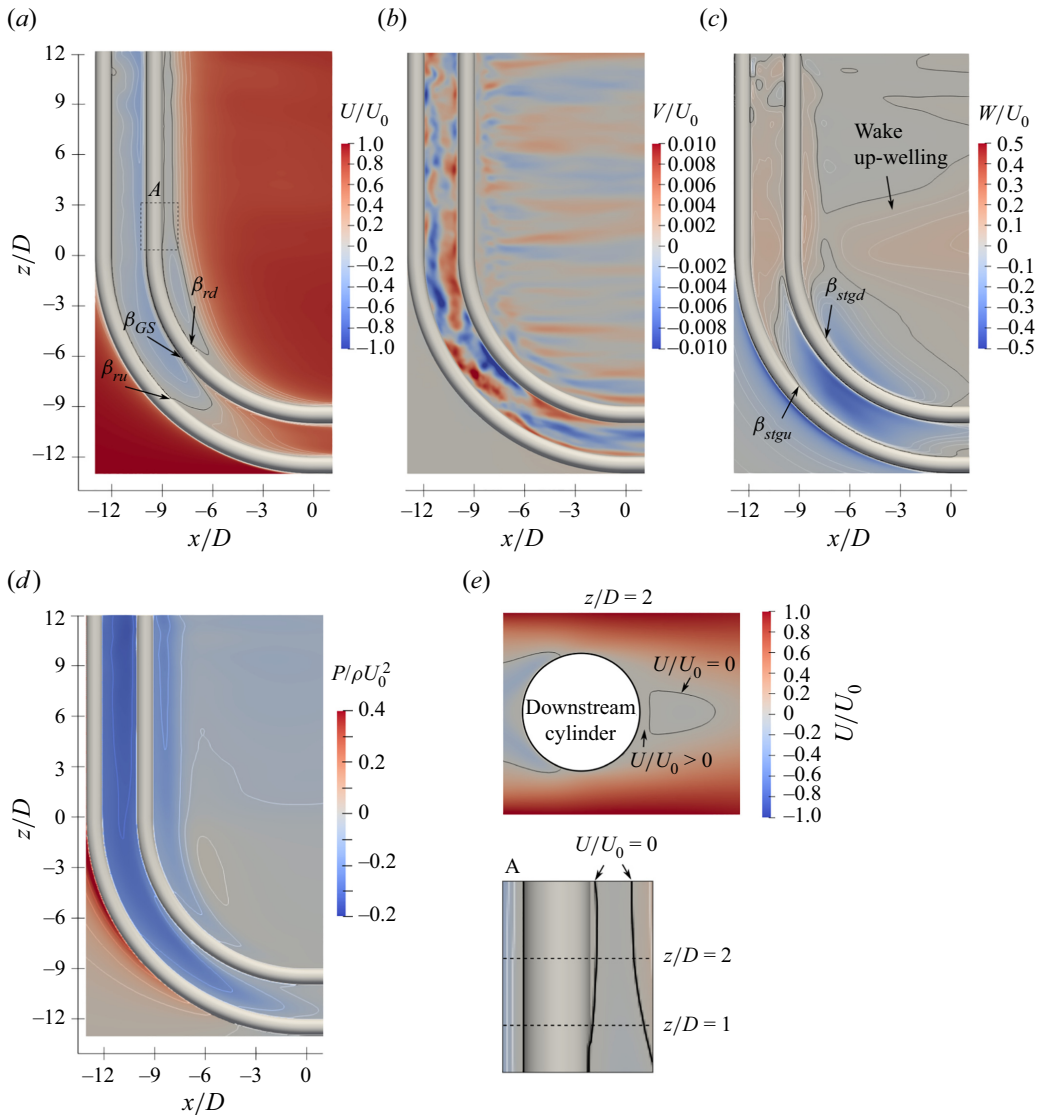


Figure 16. Time-averaged (a) streamwise, cross-flow and (c) vertical velocity, as well as (d) pressure in the symmetry plane. Black contour lines mark  $U/U_0 = 0$  and  $W/U_0 = 0$  in (a) and (c), respectively. (e) Shows the time-averaged streamwise velocity around the downstream cylinder in the plane  $z/D = 2.0$ . The contour  $U/U_0 = 0$ , shows that the recirculation bubble in the downstream cylinder wake is displaced by a region of low, positive streamwise velocities. Inset A, taken from (a), shows a close-up of the downstream cylinder in the region where this displacement starts.

straight vertical extension are low in comparison. This is different from the gap, where the strength of the backflow is nearly evenly distributed along the length of the reattachment region. This result is also in opposition to that of Gallardo *et al.* (2014), where the backflow is strongest along the straight vertical extension.

If we consider the pressure distribution in the symmetry plane, shown in figure 16(d), we see that the suction in the near wake is strongest along the straight vertical extension. It is well known that lowering the base pressure results in a shorter recirculation length (Gerrard 1966). Previously, it was found that, for straight tandem cylinders, the base

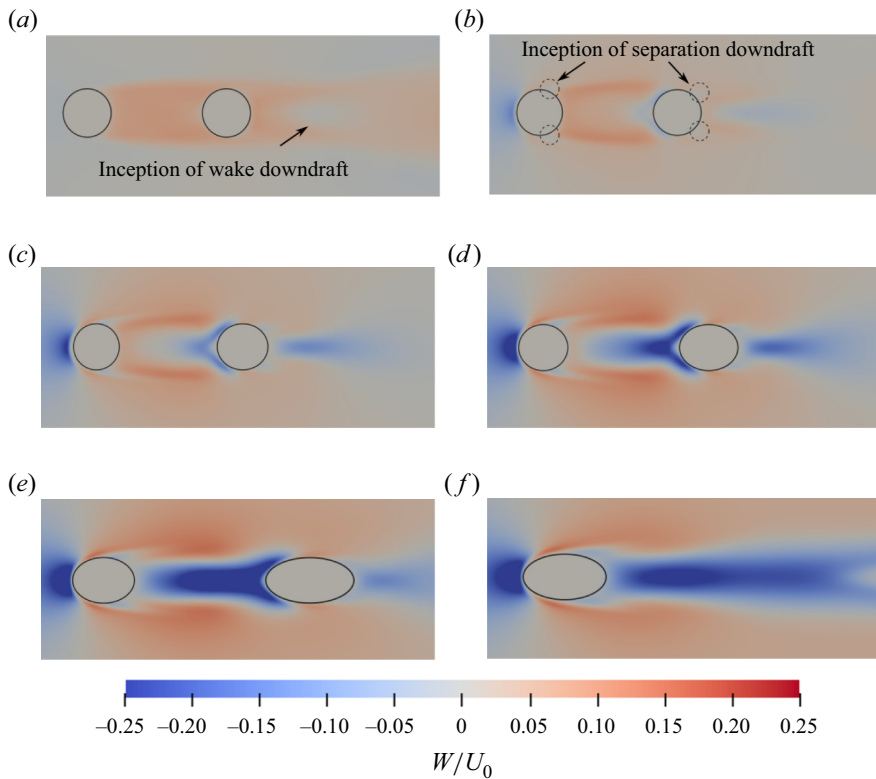


Figure 17. Time-averaged vertical velocity in various  $z/D$  planes. In the gap, downdraft along the downstream cylinder front face begins near  $z/D = -1.5$  (see figure 16c). Along the entire gap, there is upwelling in the outer regions of the shear layers of both cylinders. Downdraft near the separation points begins around  $z/D = -2$ , marked by dashed circles. The velocity scale is exaggerated for better visibility. The minimum vertical velocity is approximately  $W/U_0 = -0.45$ . Panels show (a)  $z/D = 0$ , (b)  $z/D = -2$ , (c)  $z/D = -4$ , (d)  $z/D = -6$ , (e)  $z/D = -8$  and (f)  $z/D = -10$ .

pressure of the downstream cylinder is lower for alternating overshoot/reattachment than for steady reattachment and bi-stable flow (Igarashi 1981). These observations correspond well with our result regarding the recirculation length. Note that the increase in  $L_r$  starts around  $z/D = 1$ , although in the instantaneous snapshots in figure 8, this region appears to fall within alternating the reattachment/overshoot regime. This is attributed to time variation of the boundaries between regimes and the cellular manifestation of modes.

A new finding in the present study is a streamwise secondary flow in the very near wake of the downstream cylinder, along the straight vertical extension. A positive streamwise velocity develops around  $z/D = 1$ , as shown in inset A in the lower right of figure 16. This secondary flow is associated with downstream displacement of the recirculation bubble clearly shown in figure 16(c). Although the scales are small, it is clear that the largest downstream displacement is found in the region of maximum upwelling velocity in the near wake. A related flow feature was described briefly by Gallardo *et al.* (2014), who reported that a near-zero, albeit negative, streamwise velocity plateau with a length of some  $0.5D$  preceded the recirculation bubble.

Separation and reattachment lines, defined as zero shear stress iso-lines, are marked in figure 18. The reattachment point does not change significantly until  $\beta \approx 21^\circ$ , in the upper part of the curved gap, near  $z/D = -3.5$ . This is the region where symmetric

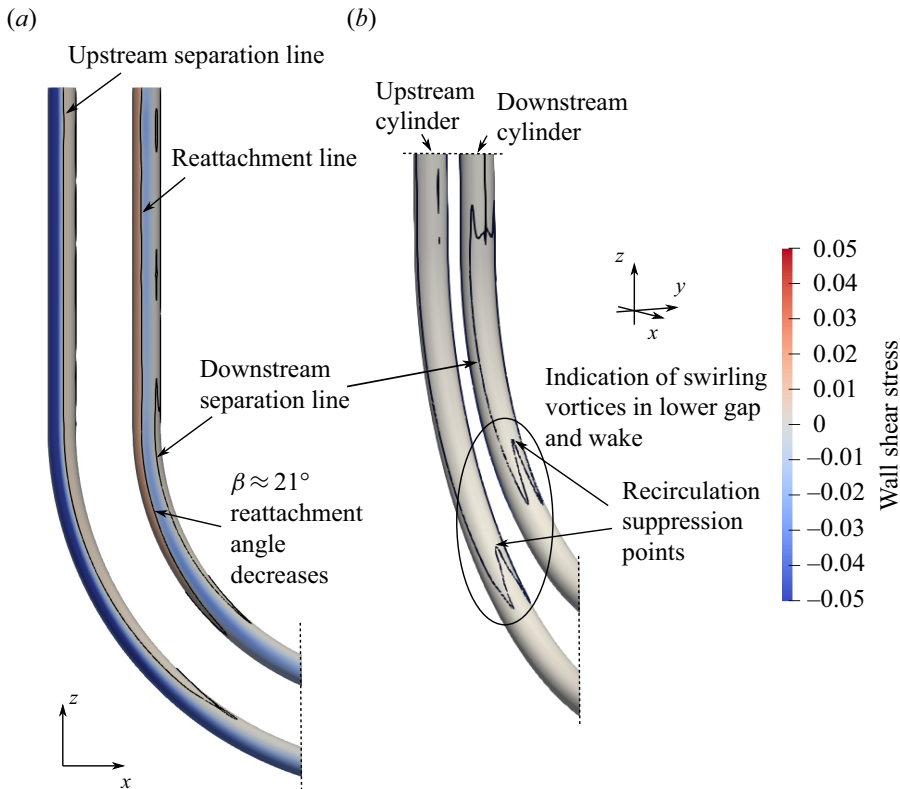


Figure 18. Time-averaged shear stress on the cylinder surfaces. (a) Side view (b) view from downstream. The black contour marks lines of zero shear stress. Here,  $\theta_R$  is nearly constant until  $\beta \approx 21^\circ$ .

reattachment gradually transitions to gap shedding. Along the vertical extension the value is  $\theta_R = 68^\circ$ , very similar to straight tandem cylinders (Aasland *et al.* 2023). Separation from the downstream cylinder occurs near  $135^\circ$ . Note that, along most of the straight vertical extension, figure 18 shows no time-averaged separation line. This is due to the positive secondary streamwise flow in the near wake.

#### 4. Discussion

Both Papaioannou *et al.* (2006) and Aasland *et al.* (2023) found that the flow in the gap of straight tandem cylinders within the reattachment regime has a basic spanwise cell structure. Aasland *et al.*'s (2023) study showed that this structure was very persistent in time, and could be easily discerned in the time-averaged velocity field. There is little evidence of such a structure in the present study, even along the straight vertical extension, although the instantaneous wake structure in the upper wake is similar to that of Aasland *et al.* (2023). This indicates that the axial flow does influence the three-dimensional instability in the gap and wake, even if the effect is slight.

Carmo *et al.* (2010a) found that mode T3 is a cooperative elliptical instability, 'cooperative' meaning that the instability depends on interaction between the shear layers. Mode T3 initiates in the gap, and placing a splitter plate directly upstream of the downstream cylinder can suppress it completely (Carmo *et al.* 2010a). The upwelling in the gap and near wake works in a similar way, reducing, although not entirely disrupting,

the communication between the shear layers. In this context, axial flow can be expected to act as a stabilising factor.

Within the co-shedding regime for tandem cylinders, the three-dimensional instability of the gap and wake is the same as for a single cylinder: mode A or mode B, depending on the Reynolds number (Carmo *et al.* 2010a). Moreover, while the downstream cylinder works as a stabiliser within the reattachment regime, it works as a de-stabiliser after the critical spacing (Papaioannou *et al.* 2006). This means that transition from mode A to mode B occurs earlier, in terms of Reynolds number, for tandem cylinders within the co-shedding regime than for a single cylinder. Intuitively, this should lead to a transition from mode T3 to mode B in the lower gap and wake of the present study, when the gap widens sufficiently to allow shedding. However, the vortex dislocations, as well as the strong downdraft in this region, alters the topology of the vortices to a point where visual observation is no longer useful to determine wavelengths etc. In order to finally determine the type of instability observed in the flow, a fully fledged stability analysis would be required, which is outside the scope of the present study. In this context, it is also important to note that the possible existence of critical points for higher Reynolds numbers than the present study is unknown. For straight tandem cylinders, no systematic studies of the three-dimensional wake instability exist for Reynolds numbers beyond 500 (Carmo, Meneghini & Sherwin 2010b), to the knowledge of the authors. Furthermore, the issue of critical points for the wake topology has not been addressed at all for single convex curved cylinders; a possible topic of further study.

The quasi-periodicity of the long-term gap flow asymmetry is a puzzle, since the bi-stable switch between tandem cylinder states is a random process. Thus, if it occurs periodically, it must be triggered by another periodic phenomenon. Zhu *et al.* (2019) observed a low-frequency switch between reattachment and co-shedding, which was assumed to be triggered by fluctuations of the axial velocity. Our own observations regarding the correlation between the cross-flow and vertical velocities (see figure 14) indicate a similar relation. As to the cause of the vertical velocity fluctuations, we believe it can be found in the lower gap. Previous studies of single bluff bodies have found low-frequency modulation of the vortex formation length (Miau *et al.* 1999, 2004; Lehmkühl *et al.* 2013; Cao & Tamura 2020). The occurrence of such processes in the lower gap may alter the vertical velocity in a quasi-periodic fashion, which is subsequently transmitted along the span. This hypothesis is supported by the spectral analysis, which shows that the energy of the low frequencies is strongest in the gap shedding region. However, low-frequency variation of the reattachment points seems to be an inherent trait of tandem cylinder flow at the present Reynolds number (Aasland *et al.* 2023). The velocity spectra in the gap of Aasland *et al.* (2022a) also have clearly defined low-frequency peaks around  $fD/U_0 = 0.01$ , indicating that such a phenomenon extends into the subcritical Reynolds number range. This means that a straightforward relationship between the low-frequency variations in the lower gap and the quasi-periodic asymmetry is nearly impossible to determine, although clearly there is interaction between the two.

We see from figure 16(c) that the vertical velocity in the symmetry plane is negative below  $z/D \approx -1.5$ . Assuming that information is carried along the span by means of the axial velocity, this implies that in this region information is convected away from the upper part of the gap, towards the lower part. Conversely, above the stagnation line of the vertical velocity, information is carried upwards. From figure 8, however, we see that, outside the symmetry plane, in the regions that roughly correspond to the lateral position of the shear layers, there is positive vertical velocity all throughout the gap. Thus, it is possible to convey information in both directions along the gap by means of the axial velocity.

Aasland *et al.* (2022a) observed low-frequency variations in the drag and vertical force on the downstream cylinder, and suggested that these variations may be caused by a slow meandering of the angle at which gap shedding starts (i.e.  $\beta_{GS}$ ) in the lower gap. The reasoning was that a larger reattachment region leads to increased gap suction and *vice versa*. We have not been able to directly observe such a meandering, though the same type of low-frequency drag variation occurs in the present study (not shown). The mode changes in the lower gap, as described in § 3.3 impact the drag, and the dominant low frequencies of the forces correspond well to the low-frequency content in the lower gap. However, the phenomenon appears to be more complex than previously assumed, since mode switches may occur locally (described in § 3.3 and for straight tandem cylinders by Aasland *et al.* 2023).

Some previous studies of straight tandem cylinders have suggested that, within the reattachment regime, it is the frequency of the gap vortices that drives the frequency of the wake vortices (Xu & Zhou 2004; Aasland *et al.* 2022b), similar to the ‘lock-in’ effect found for straight tandem cylinders within the co-shedding regime. This hypothesis was implicitly challenged by Hosseini, Griffith & Leontini (2021). In their investigation, a third body was placed in the near wake of tandem cylinders at  $L/D = 5$  and  $Re = 200$ , a combination of gap ratio and  $Re$  which normally results in co-shedding. Provided that this third body was placed within the region of absolute instability of the downstream cylinder, vortex shedding could be entirely suppressed in the gap, resulting in a reattachment regime instead. We are inclined to believe in the view put forward by Hosseini *et al.* (2021). This suggests that the gap vortices for relatively small gap ratios are driven by the vortex shedding from the downstream cylinder, and not the other way around. This upstream feedback can result from fluctuations in the pressure field. If so, this would entail that the vortex formation in both the upper and lower gap in the present study is driven by the vortices in the upper wake. This interpretation further explains why the gap vortices in the lower gap have the same dominant frequency as those of the upper gap, even if the lower gap vortices are stronger, in terms of vorticity.

Finally, the independence principle is clearly invalid for the present case. This is underlined by the change of reattachment regime type which occurs in the upper part of the curved geometry, where the normal velocity and the corresponding local Reynolds number are quite similar to the nominal values. Below  $z/D = -4$ , these values decrease rapidly, while the dominant frequency remains virtually unchanged. Both Papaioannou *et al.* (2006) and Carmo *et al.* (2010b) predict a critical spacing of  $L/D \approx 3.8$  for  $Re = 500$ . Herein, a corresponding effective gap ratio occurs in the vicinity of  $z/D = -5$ . This is close to the point of recirculation suppression in the near wake, so that a true co-shedding regime does not exist. It is obvious that the axial flow cannot be ignored in any part of the flow. This corresponds to the results of Alam *et al.* (2022), who concluded that the independence principle is invalid within the reattachment and bi-stable range for non-parallel yawed tandem cylinders.

## 5. Summary and concluding remarks

In the present study, the flow around curved tandem cylinders in the convex configuration has been investigated by means of DNS, at a Reynolds number of 500 and a nominal gap ratio of 3.0. Due to a gradual change in the effective gap ratio along the curved part of the span, there is a variation of tandem cylinder flow regimes from alternating reattachment/overshoot, through symmetric reattachment until shedding of vortices commences in the lower part of the gap. Similar to a single curved cylinder in the convex

configuration, vortex shedding is inhibited in the lower near wake, due to strong downdraft. A non-shedding swirling vortex regime prevails in this region.

Axial flow and spanwise flow regime variation lead to an intricate wake topology, with alterations between parallel and oblique spanwise vortex shedding. Communication between the shear layers is partially inhibited by the axial flow, and this influences the three-dimensional instability mechanism of the gap and wake, so that the spanwise cellular structure, which is typical for straight tandem cylinders at moderate Reynolds numbers, no longer occurs. That being said, the large-scale vortex shedding is governed by the vortices along the straight vertical extension, whose dominant and secondary frequencies are the same as for straight tandem cylinders at the same Reynolds number.

Spanwise vortex dislocations occur by two distinct physical mechanisms, one being spanwise frequency differences in the gap and wake, the other being shedding of gap vortices into the lower wake. Both may be present in the flow simultaneously, and along with bending and tilting of the streamwise vortices, this leads to extremely complex flow patterns in the wake. The topology is further complicated by interaction between the lower wake and the vortices in the horizontal part of the gap, which have a strong streamwise component.

Our results indicate that the flow is multi-stable, predominantly due to the spanwise flow regime variation. Alternating reattachment/overshoot, which is the governing regime along the straight vertical extensions, is in itself a bi-stable flow, with cellular manifestations of one-sided gap vortex shedding. In a previous study of straight tandem cylinders (Aasland *et al.* 2023), this caused long-term asymmetric vortex formation in the gap, intermittently switching from side to side. In the present study, the same type of asymmetry occurs, but the switch is quasi-periodic. The frequency at which the switch occurs is mirrored by low-frequency variations of the velocity fluctuations in the lower gap, which we believe result from slow variation of the recirculation length in the gap shedding region. This low-frequency variation may be transmitted along the span by means of the vertical velocity component. The asymmetry switch is seen to be accompanied by a surge of the vertical velocity.

Given the sensitivity of a single curved cylinder to the curvature and inflow direction, it seems likely that the flow around curved tandem cylinders, which is inherently more complex, should also be sensitive to these parameters. Moreover, the present study was carried out at a transitional Reynolds number, and the effect of turbulent flow is yet to be clarified.

**Supplementary material and movies.** Supplementary material and movies are available at <https://doi.org/10.1017/jfm.2023.933>.

**Acknowledgements.** The authors would like to thank Dr J. Gallardo (PRDW, Santiago, Chile) for insightful discussions regarding the origin of the low-frequency variations.

**Funding.** This work is supported by the Research Council of Norway through the Public Sector PhD Scheme (grant no. 258721/H40), and the Norwegian Public Roads Administration, where the first author is an employee. Computational hours were granted by the Norwegian HPC project NN9191K.

**Declaration of interest.** The authors report no conflict of interest.

**Author ORCID.**

• Tale E. Aasland <https://orcid.org/0000-0002-8504-930X>;

• Fengjian Jiang <https://orcid.org/0000-0002-5321-3275>.

## Flow topology in the gap and wake

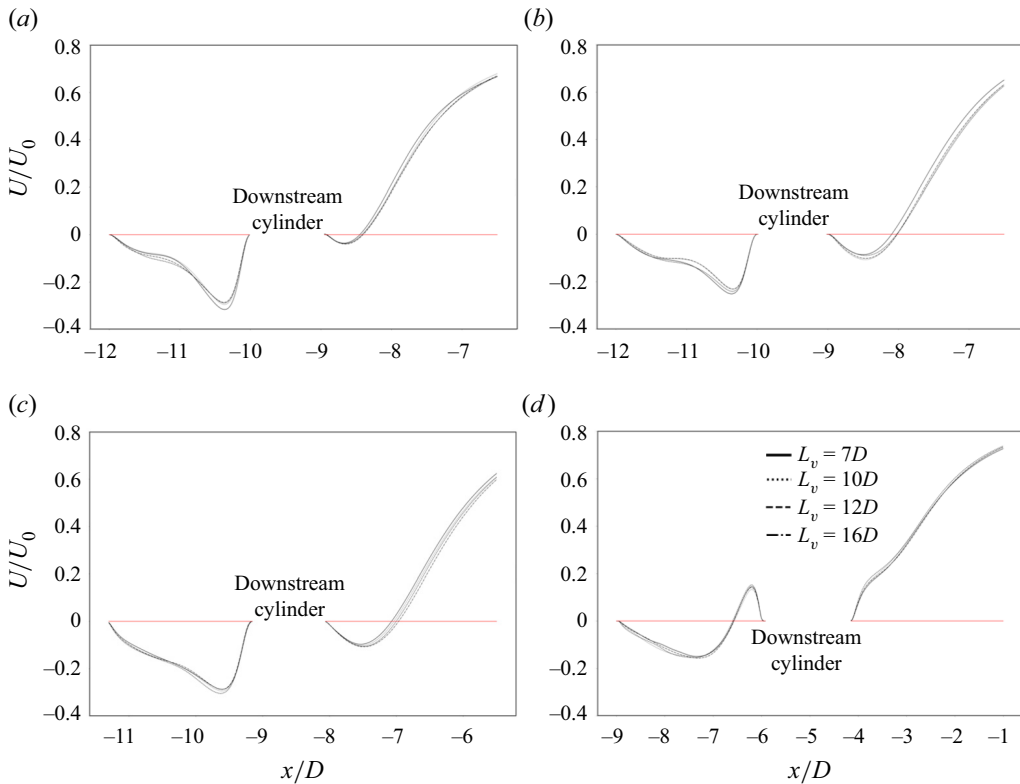


Figure 19. Comparison of time-averaged streamwise velocity profiles for different  $L_v$  at  $y/D = 0$  and (a)  $z/D = 5$ , (b)  $z/D = 0$ , (c)  $z/D = -4$  and (d)  $z/D = -8$ . In each of the plots, the horizontal extent of the downstream cylinder cross-section is cut out of the profiles.

### Appendix. Effect of the straight vertical extension length

Because of spurious flow in the upper part of the domain discovered in the initial study (Aasland *et al.* 2022a), an investigation of the effect of  $L_v$  was carried out. Recalling that Gallardo *et al.* (2013) discovered that the main effect of vertical blockage was to suppress the upwelling in the near wake, the  $L_v$  parameter study focused on the time-averaged secondary flow features, which are all related to the vertical velocity component. Four different lengths were tested:  $L_v = 7D$ ,  $10D$ ,  $12D$  and  $16D$ . For these simulations, sampling of statistics started after 250 time units, and was carried out for 550 time units, corresponding to some 100 von Kármán vortex shedding cycles.

The effect of the boundary condition is, naturally, most significant in the upper part of the domain. Horizontal profiles of the streamwise velocity, shown in figure 19, show that the influence penetrates rather far down into the domain, although the differences in recirculation length are small. Down to  $z/D = -4$ , a slight increase of the recirculation bubble was observed as  $L_v$  was increased. At  $z/D = -8$ , the differences are negligible.

Figure 20 shows the upwelling velocity along the straight vertical extension in the gap and wake. The adverse influence of the top boundary condition is evident in the profiles of  $L_v = 7D$  and  $10D$ , especially in the gap. The same is true for the region of low positive streamwise velocity in the very near wake of the downstream cylinder, shown in figure 21. The effect is less prominent, although still visible, for  $L_v = 12D$  and  $16D$ . Increased  $L_v$  seems to cause stronger upwelling in the gap, but weaker upwelling in



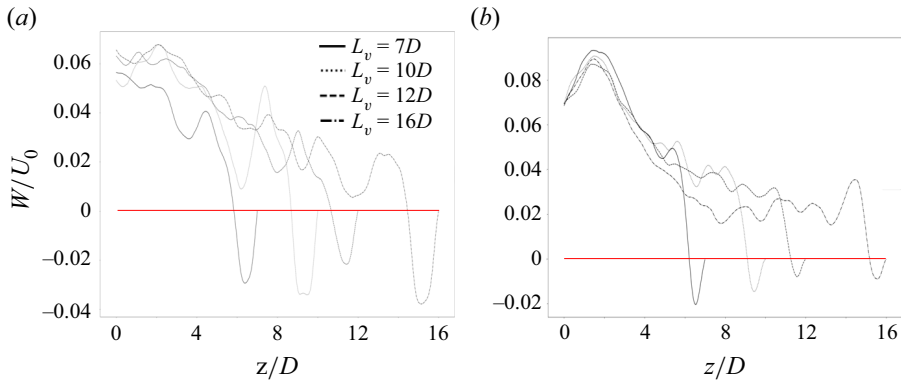


Figure 20. Effect of  $L_v$  on the upwelling in the near wake of the (a) upstream and (b) downstream cylinders. Panels show (a)  $x/D = -11.8$  and (b)  $x/D = 8.8$ .

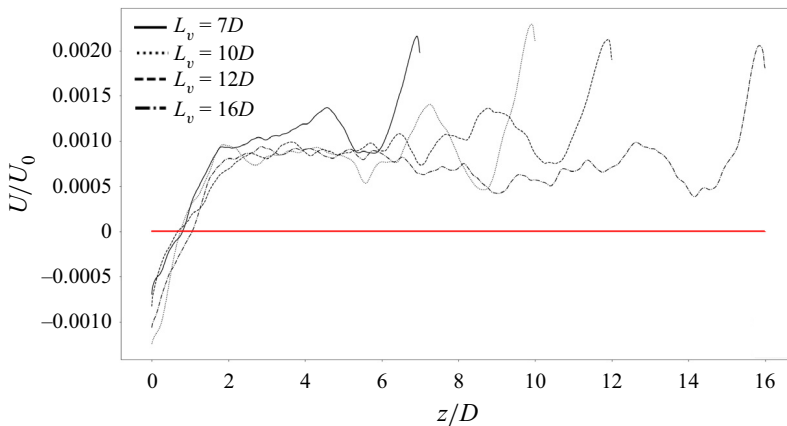


Figure 21. Effect of  $L_v$  on the positive  $U/U_0$  in the very near wake of the downstream cylinder, at  $x/D = -8.98$ .

the wake, although the differences are smaller. Moreover, a slight decrease of  $St$  (based on the cross-flow forces) was found as  $L_v$  was increased, consistent with the increased recirculation length shown in figure 19. The values were  $St = 0.152, 0.149, 0.148$  and  $0.146$  for  $L_v = 7D, 10D, 12D$  and  $16D$ , respectively.

There is no way to completely negate the blockage effect from the top boundary, so a compromise must be made between accuracy and computational cost. From figures 20 and 21, we see that, below  $z/D = 5.0$ , the influence from the upper boundary condition is small for  $L_v = 12D$  and  $L_v = 16D$ . Further, the differences between the two  $L_v$  cases are small in this region. Thus, we conclude that  $L_v = 12D$  gives acceptable accuracy vs cost for the present study.

#### REFERENCES

- AASLAND, T.E., PETERSEN, B., ANDERSSON, H.I. & JIANG, F. 2022a Flow around curved tandem cylinders. *Trans. ASME J. Fluids Engng* **144** (12), 121301.
- AASLAND, T.E., PETERSEN, B., ANDERSSON, H.I. & JIANG, F. 2022b Revisiting the reattachment regime: a closer look at tandem cylinder flow at  $Re = 10\,000$ . *J. Fluid Mech.* **953**, A18.

- AASLAND, T.E., PETERSEN, B., ANDERSSON, H.I. & JIANG, F. 2023 Asymmetric cellular bistability in the gap between tandem cylinders. *J. Fluid Mech.* **966**, A39.
- AFGAN, I., KAHIL, Y., BENHAMADOUCHE, S., ALI, M., ALKAABI, A., BERROUK, A.S. & SAGAUT, P. 2023 Cross flow over two heated cylinders in tandem arrangements at subcritical Reynolds number using large eddy simulations. *Intl J. Heat Fluid Flow* **100**, 109115.
- AHMED, A. 2010 On the wake of a circular cylinder with nodal and saddle attachment. *J. Fluids Struct.* **26**, 41–49.
- ALAM, M.M. 2014 The aerodynamics of a cylinder submerged in the wake of another. *J. Fluids Struct.* **51**, 393–400.
- ALAM, M.M., RASTAN, M.R., WANG, L. & ZHOU, Y. 2022 Flows around two nonparallel tandem circular cylinders. *J. Wind Engng Ind. Aerodyn.* **220**, 104870.
- ASSI, G.R.S., SRINIL, N., FREIRE, C.M. & KORKISCHKO, I. 2014 Wake dynamics of external flow past a curved circular cylinder with the free-stream aligned to the plane of curvature. *J. Fluids Struct.* **41**, 52–66.
- CAO, Y. & TAMURA, T. 2020 Low-frequency unsteadiness in the flow around a square cylinder with critical angle of  $14^\circ$  and a Reynolds number of  $2.2 \times 10^4$ . *J. Fluids Struct.* **97**, 103087.
- CARDELL, G.S. 1993 Flow past a circular cylinder with a permeable wake splitter plate. PhD thesis, California Institute of Technology.
- CARMO, B.S. & MENEGHINI, J.R. 2006 Numerical investigation of the flow around two circular cylinders in tandem. *J. Fluids Struct.* **22**, 979–988.
- CARMO, B.S., MENEGHINI, J.R. & SHERWIN, S.J. 2010a Secondary instabilities in the flow around two circular cylinders. *J. Fluid Mech.* **644**, 395–431.
- CARMO, B.S., MENEGHINI, J.R. & SHERWIN, S.J. 2010b Possible states in the flow around two circular cylinders in tandem with separations in the vicinity of the drag inversion spacing. *Phys. Fluids* **22**, 054101.
- CHIATTO, M., CARDINALE, C., SHANG, J.K. & GRASSO, F. 2023 Analysis of the wake flow behind concave curved cylinders with velocity measurements by particle image velocimetry and modal decomposition. *Phys. Fluids* **35**, 075153.
- CHIATTO, M., SHANG, J.K., DE LUCA, L. & GRASSO, F. 2021 Insights into low Reynolds flow past finite curved cylinders. *Phys. Fluids* **33**, 035150.
- DENG, J., REN, A.-L., ZOU, J.-F. & SHAO, X.-M. 2006 Three-dimensional flow around two circular cylinders in tandem arrangement. *Fluid Dyn. Res.* **38** (6), 386–404.
- GALLARDO, J.P., ANDERSSON, H.I. & PETERSEN, B. 2014 Turbulent wake behind a curved circular cylinder. *J. Fluid Mech.* **742**, 192–229.
- GALLARDO, J.P., PETERSEN, B. & ANDERSSON, H.I. 2013 Effect of free-slip boundary conditions on the flow around a curved circular cylinder. *Comput. Fluids* **86**, 389–394.
- GAO, Y., HE, J., ONG, M.C., ZHAO, M. & WANG, L. 2021 Three-dimensional numerical investigation on flow past two side-by-side curved cylinders. *Ocean Engng* **234**, 109167.
- GERRARD, J.H. 1966 The mechanics of the formation region of vortices behind bluff bodies. *J. Fluid Mech.* **25**, 401–413.
- HENDERSON, R.D. 1997 Nonlinear dynamics and pattern formation in turbulent wake transition. *J. Fluid Mech.* **352**, 65–112.
- HOSSEINI, N., GRIFFITH, M.D. & LEONTINI, J.S. 2021 Flow states and transitions in flows past arrays of tandem cylinders. *J. Fluid Mech.* **910**, A34.
- IGARASHI, T. 1981 Characteristics of the flow around two circular cylinders arranged in tandem (1st report). *Bull. JSME* **24** (188), 323–330.
- JIANG, F., PETERSEN, B. & ANDERSSON, H.I. 2018a Influences of upstream extensions on flow around a curved cylinder. *Eur. J. Mech. (B/Fluids)* **67**, 79–86.
- JIANG, F., PETERSEN, B. & ANDERSSON, H.I. 2019 Turbulent wake behind a concave curved cylinder. *J. Fluid Mech.* **878**, 663–699.
- JIANG, F., PETERSEN, B., ANDERSSON, H.I., KIM, J. & KIM, S. 2018b Wake behind a concave curved cylinder. *Phys. Rev. Fluids* **3**, 094804.
- KITAGAWA, T. & OHTA, H. 2008 Numerical investigation on flow around circular cylinders in tandem arrangement at a subcritical Reynolds number. *J. Fluids Struct.* **24**, 680–699.
- LEE, S., PAIK, K.-J. & SRINIL, N. 2020 Wake dynamics of a 3D curved cylinder in oblique flows. *Intl J. Naval Arch. Ocean Engng* **12**, 501–517.
- LEHMKUHL, O., RODRIGUES, I., BORRELL, R. & OLIVA, A. 2013 Low-frequency unsteadiness in the vortex formation region of a circular cylinder. *Phys. Fluids* **25**, 085109.
- LIN, J.-C., YANG, Y. & ROCKWELL, D. 2002 Flow past two cylinders in tandem: instantaneous and averaged flow structure. *J. Fluids Struct.* **16** (8), 1059–1071.
- LJUNGKRONA, L., NORBERG, C. & SUNDEN, B. 1991 Free-stream turbulence and tube spacing effect on surface pressure fluctuations for two tubes in an in-line arrangement. *J. Fluid Struct.* **5**, 701–727.

- MA, B. & SRINIL, N. 2023 Prediction model for multidirectional vortex-induced vibrations of catenary riser in convex/concave and perpendicular flows. *J. Fluids Struct.* **117**, 103826.
- MANHART, M. 2004 A zonal grid algorithm for DNS of turbulent boundary layers. *Comput. Fluids* **33**, 435–461.
- MIAU, J.J., WANG, J.T., CHOU, J.H. & WEI, C.Y. 1999 Characteristics of low-frequency variations embedded in vortex-shedding process. *J. Fluids Struct.* **13**, 339–359.
- MIAU, J.J., WU, S.J., HU, C.C. & CHOU, J.H. 2004 Low-frequency modulations associated with vortex shedding from flow over bluff body. *AIAA J.* **42**, 1388–1397.
- MILIOU, A., DE VECCHI, A., SHERWIN, S.J. & GRAHAM, J.M.R. 2007 Wake dynamics of external flow past a curved cylinder with free stream aligned with the plane of curvature. *J. Fluid Mech.* **592**, 89–115.
- MILIOU, A., SHERWIN, S.J. & GRAHAM, J.M.R. 2003a Fluid dynamic loading on curved riser pipes. *Trans. ASME J. Offshore Mech. Arctic Engng* **18** (1), 29–40.
- MILIOU, A., SHERWIN, S.J. & GRAHAM, J.M.R. 2003b Wake topology of curved cylinders at low Reynolds numbers. *Flow Turbul. Combust.* **71**, 157–160.
- NARASIMHAMURTHY, V.D., ANDERSSON, H.I. & PETERSEN, B. 2009 Cellular vortex shedding behind a tapered circular cylinder. *Phys. Fluids* **21** (4), 044106.
- OKAJIMA, A. 1979 Flows around two tandem circular cylinders at very high Reynolds numbers. *Bull. JSME* **22**, 504–511.
- PAPAIOANNOU, G., YUE, D.K.P., TRIANTAFYLLOU, M. & KARNIADAKIS, G.E. 2006 Three-dimensionality effects in flow around two tandem cylinders. *J. Fluid Mech.* **558**, 387–413.
- PELLER, N., LE DUC, A., TREMBLAY, T. & MANHART, M. 2006 High-order stable interpolations for immersed boundary methods. *Intl. J. Numer. Meth. Fluids* **53**, 1175–1193.
- RAMBERG, S.E. 1983 The effects of yaw and finite length upon the vortex wakes of stationary and vibrating circular cylinders. *J. Fluid Mech.* **128**, 81–107.
- SEYED-AGHAZADEH, B., BENNER, B., GJOKOLLARI, X. & MODERRES-SADEGHI, Y. 2021 An experimental investigation of vortex-induced vibration of a curved flexible cylinder. *J. Fluids Mech.* **927**, A21.
- SEYED-AGHAZADEH, B., BUDZ, C. & MODARRES-SADEGHI, Y. 2015 The influence of higher harmonic flow forces on the response of a curved circular cylinder undergoing vortex-induced vibration. *J. Sound Vib.* **353**, 395–406.
- SHANG, J.K., STONE, H.A. & SMITS, A.J. 2018 Flow past finite cylinders of constant curvature. *J. Fluid Mech.* **837**, 896–915.
- SHI, X., ALAM, M. & BAI, H. 2020 Wakes of elliptical cylinders at low Reynolds number. *Intl. J. Heat Fluid Flow* **82**, 108553.
- SHIRAKASHI, M., HASEGAWA, A. & WAKIYA, S. 1986 Effect of secondary flow on Kármán vortex shedding from a yawed cylinder. *Bull. JSME* **29**, 1124–1132.
- SRINIL, N., MA, B. & ZHANG, L. 2018 Experimental investigation on in-plane/out-of-plane vortex-induced vibrations of curved cylinder in parallel and perpendicular flows. *J. Sound Vib.* **421**, 275–299.
- SUMNER, D. 2010 Two circular cylinders in cross-flow: a review. *J. Fluids Struct.* **26**, 849–899.
- THAKUR, A., LIU, X. & MARSHALL, J.S. 2004 Wake flow of single and multiple yawed cylinders. *Trans. ASME J. Fluids Engng* **126**, 861–870.
- UNGLEHRT, L., JENSSEN, U., KURZ, F., SCHANDERL, W., KREUZINGER, J., SCHWERTFIRM, F. & MANHART, M. 2022 Large-eddy simulation of the flow inside a scour hole around a circular cylinder using a cut cell immersed boundary method. *Flow Turbul. Combust.* **109**, 893–929.
- DE VECCHI, A., SHERWIN, S.J. & GRAHAM, J.M.R. 2008 Wake dynamics of external flow past a curved circular cylinder with the free-stream aligned to the plane of curvature. *J. Fluids Struct.* **24**, 1262–1270.
- WANG, D., LIU, Y., LI, H. & XU, H. 2021 Secondary instability of channel-confined transition around dual-circular cylinders in tandem. *Intl. J. Mech. Sci.* **208**, 106692.
- WANG, P., ZHOU, Q., ALAM, M.M., YANG, Y. & LI, M. 2022 Effects of streamwise gust amplitude on the flow around and forces on two tandem circular cylinders. *Ocean Engng* **261**, 112040.
- WILKINS, S.J., HOGAN, J.D. & HALL, J.W. 2013 Vortex shedding in a tandem circular cylinder system with a yawed downstream cylinder. *Trans. ASME J. Fluids Engng* **135**, 071202.
- WILLIAMSON, C.H.K. 1989 Oblique and parallel modes of vortex shedding in the wake of a circular cylinder at low Reynolds numbers. *J. Fluid Mech.* **206**, 579–627.
- WILLIAMSON, C.H.K. 1992 The natural and forced formation of spot-like ‘vortex dislocations’ in the transition of a wake. *J. Fluid Mech.* **243**, 393–441.
- WILLIAMSON, C.H.K. 1996 Vortex dynamics in the cylinder wake. *Annu. Rev. Fluid Mech.* **28**, 477–539.
- XU, G. & ZHOU, Y. 2004 Strouhal numbers in the wake of two inline cylinders. *Exp. Fluids* **37**, 248–256.
- YOUNIS, Y., ALAM, M. & ZHOU, Y. 2016 Flow around two nonparallel tandem cylinders. *Phys. Fluids* **28** (12), 125106.

*Flow topology in the gap and wake*

- ZDRAVKOVICH, M.M. 1987 The effect of interference between circular cylinders in cross flow. *J. Fluids Struct.* **1**, 239–261.
- ZHOU, Y. & ALAM, M. 2016 Wake of two interacting circular cylinders: a review. *Intl J. Heat Fluid Flow* **62**, 510–537.
- ZHOU, Q., ALAM, M.M., CAO, S., LIAO, H. & LI, M. 2019 Numerical study of wake and aerodynamic forces on two tandem circular cylinders at  $Re = 10^3$ . *Phys. Fluids* **31**, 045103.
- ZHU, H., WANG, R., BAO, Y., ZHOU, D., PING, H., HAN, Z. & SHERWIN, S.J. 2019 Flow over a symmetrically curved circular cylinder with the free stream parallel to the plane of curvature at low Reynolds number. *J. Fluids Struct.* **87**, 23–38.



### 4.3 Paper 5. Turbulent flow around convex curved tandem cylinders

Aasland, T. E., Pettersen, B., Andersson, H. I. & Jiang, F. Turbulent flow around convex curved tandem cylinders. *Under consideration in an international journal*



# Turbulent flow around convex curved tandem cylinders

Tale E. Aasland<sup>1</sup>†, Bjørnar Pettersen<sup>1</sup>, Helge I. Andersson<sup>1</sup>, and Fengjian Jiang<sup>2</sup>

<sup>1</sup>Department of Marine Technology, Norwegian University of Science and Technology, NO-7491, Trondheim, Norway

<sup>2</sup>SINTEF Ocean, NO-7052, Trondheim, Norway

(Received xx; revised xx; accepted xx)

Turbulent flow around curved tandem cylinders has been studied for the first time, by means of DNS. The convex configuration was used, with a nominal gap ratio of  $L/D = 3$ , and a Reynolds number of 3900. Along the span, the flow regimes vary from alternating overshoot/reattachment to co-shedding. Three distinct Strouhal numbers coexist in the flow, that are tied directly to different tandem cylinder flow regimes. This result differs substantially from convex curved tandem cylinders at a transitional Reynolds number, where only a single dominant frequency is found. All regimes exhibit some degree of instability, so that the flow can be considered multi-stable. A mode switch from alternating overshoot/reattachment to symmetric reattachment is found. Complex interactions are observed between the primary instability, the shear layer instability, and the flow mode alterations. As opposed to previous investigations with single and tandem straight cylinders in the subcritical flow regime, our results indicate that there may be direct feedback from the primary instability to the shear layer instability. The downdraft region in the gap exhibits slow meandering, and travel upstream and amplify the shear layer instability, causing early transition in the gap shear layer. This downdraft is governed by the slow modulations of the vortex formation region in the lower gap, meaning that the vortex dynamics of this region may indirectly influence the shear layer instability higher up in the gap.

**Key words:** vortex shedding, vortex dynamics, separated flows

---

## 1. Introduction

Flow around multiple bluff bodies has been widely studied, both because of its obvious importance in various engineering applications and because it provides an opportunity to study the interaction between several fundamental fluid dynamics phenomena. Of the many and varied geometries and configurations within this field, the case of two cylinders in tandem is perhaps one of the most canonical. Even after decades of research, this flow remains an object of interest for engineers and physicists alike.

Flow around straight tandem cylinders of equal diameter is characterised by three main flow regimes: overshoot (also called extended-body regime), reattachment and co-shedding. When the cylinders are closely spaced, the shear layers from the upstream cylinder overshoot the downstream cylinder and roll up in its wake, so that vortex shedding essentially occurs from the upstream cylinder alone. When the spacing between the cylinders increases, the

† Email address for correspondence: tale.e.aasland@ntnu.no



upstream cylinder shear layers reattach onto the downstream cylinder. Vortex shedding now occurs solely from the downstream cylinder. Reattachment may be alternating, quasi-steady/symmetric or intermittent (Zdravkovich 1987). Initially, the reattachment points are located on the back face of the downstream cylinder, but the points move upstream, onto the front face, with increased spacing and/or higher Reynolds number (Xu & Zhou 2004; Zhou & Yiu 2006). Finally, when the spacing between the cylinders is sufficiently large, the upstream cylinder shear layers roll up in the gap, and vortex shedding occurs from both cylinders.

Tandem cylinder flow regimes are normally discussed in terms of the gap ratio  $L/D$ , where  $L$  is the center-to-center spacing between the cylinders and  $D$  is the cylinder diameter. The gap ratio at which co-shedding first occurs is traditionally referred to as the critical spacing,  $L_c/D$ . Because the flow depends strongly on the Reynolds number ( $Re = U_0 D/\nu$ , where  $U_0$  is the inflow velocity, and  $\nu$  is the kinematic viscosity) (Xu & Zhou 2004), and other factors such as free-stream turbulence (Ljungkrona *et al.* 1991) or inflow gust amplitude (Wang *et al.* 2022), there is quite a spread in the reported values of  $L_c/D$ . Typically, the critical spacing varies between  $3.0D$  and  $5.0D$  (Okajima 1979; Igarashi 1981; Xu & Zhou 2004; Alam 2014). Owing to the Reynolds number dependency, defining the extent of the regimes exclusively in terms of the gap ratio is challenging. Nonetheless, the following classification by Zdravkovich (1987) remains in wide use: overshoot  $1.0 \leq L/D \leq 1.2 - 1.8$ , reattachment  $1.2 - 1.8 \leq L/D \leq 3.4 - 3.8$  and co-shedding  $3.4 - 3.8 \leq L/D$ . Specific gap ratio and Reynolds number ranges exist where vortices are fully formed on the upstream cylinder, but are unable to be shed due to the interference of the downstream body. This particular case does not fit neatly into the reattachment nor co-shedding categories. Behara *et al.* (2022) reported a similar situation, but in the completely different case of two tandem rotating cylinders.

Transition between the different flow regimes of straight tandem cylinders is unstable and hysteretic (Carmo *et al.* 2010). Near a transition point, the flow jumps intermittently between regimes, and these may persist for short or long time intervals, depending on the Reynolds number and gap ratio (Igarashi 1981). The co-existence of two flow regimes near a transition point manifests itself as two distinct velocity spectral peaks of similar magnitude. Igarashi (1981) coined the term "bi-stability" for intermittent switch between reattachment and co-shedding, but a second type of bi-stability was reported by Xu & Zhou (2004), namely a switch between overshoot and reattachment. The latter has not been reported by others, to the knowledge of the authors, but the reattachment/co-shedding bi-stability is reported in a number of studies (Igarashi 1981; Xu & Zhou 2004; Kitagawa & Ohta 2008; Alam 2014; Afgan *et al.* 2023).

It is worth noting that summaries of the literature on tandem cylinder flow will often, for the sake of brevity, skip the complexity of the different flows grouped under the bi-stable regime. Igarashi (1981), for instance, reported that in the beginning of the bi-stable regime, the gap vortices become unstable, and shedding occurs intermittently. This regime is labeled "regime D" in that study, and the illustration portrays a gap flow where one shear layer reattaches, while the opposite shear layer overshoots the downstream cylinder and at the same time allows a gap vortex to escape and be convected into the near wake. True intermittent roll-up of the gap shear layers occurs within the next regime, labelled "regime E". Similarly, the bi-stable flow described by Kitagawa & Ohta (2008) consists of a switch between symmetric reattachment, with a highly turbulent non-shedding wake, and a state where small vortices are shed from the gap shear layers, combined with a vortex street in the wake. In the illustrations of the latter, one gap shear layer clearly forms a vortex, while the opposite shear layer overshoots. A similar flow regime was reported by Aasland *et al.* (2023a), who found that vortex shedding may occur repeatedly from just one gap shear layer,

while the opposite shear layer reattaches or overshoots the downstream cylinder. Moreover, this flow regime may be spanwise-localised, so that bi-stability manifests in short spanwise cells.

The inherent intricacies of tandem cylinder flow contribute to a substantial increase of complexity when non-uniformity of the geometry is introduced, such as for non-parallel or curved tandem cylinders. There are still very few studies that investigate such flows. Flow around non-parallel tandem cylinders was studied by Younis *et al.* (2016) and Alam *et al.* (2022) at subcritical Reynolds numbers. Curved tandem cylinders in the convex configuration (meaning that the inflow is directed at the outside of the curved cylinders and parallel to the plane of curvature) at  $Re = 500$  was the topic of two papers by the present authors (Aasland *et al.* 2022a, 2023b). Another relevant study is that of Zhu *et al.* (2019), which is concerned with a symmetrical, hanging riser segment of different curvatures (i.e. different distances between the end points) at  $Re = 100$ . For high curvatures, the cylinder end segments are close enough that the flow resembles that of tandem cylinders, with a concave cylinder in the wake of a convex one.

What these flows have in common is that different tandem cylinder flow regimes co-exist and interact along the span of the same geometry. Information may travel along the span by means of axial flow (induced either by curvature or yaw angle, depending on the geometry), and this alters the dynamics of the flow regimes (Aasland *et al.* 2023b). In the study of Alam *et al.* (2022), the transitions between flow regimes were accelerated in terms of gap ratio, compared with straight tandem cylinder at a similar Reynolds number. Moreover, the gap ratio range over which reattachment/co-shedding bi-stability could be found, was significantly increased. Both Zhu *et al.* (2019) and Aasland *et al.* (2022a, 2023b) reported low-frequency periodicity of flow mode switches that are normally considered random processes for straight tandem cylinders.

The wake of convex curved tandem cylinders shares some important features with the wakes of their single cylinder counterparts (Aasland *et al.* 2022a, 2023b). The wakes of convex curved single cylinders are superficially similar to the wakes of straight single cylinders at the same Reynolds number, in that both wakes exhibit a von Kármán vortex street (Miliou *et al.* 2007; Gallardo *et al.* 2014; Shang *et al.* 2018). The major difference between the two is the curvature-induced axial flow along the front and back face of the curved cylinder. There is a strong downdraft in the lower part of the near wake, and this downdraft impedes communication between the shear layers (Gallardo *et al.* 2014), so that the flow in this region resembles the swirling non-shedding flow regime reported by Ramberg (1983) for a yawed single cylinder with a free end. Vortex shedding is then re-established further downstream. The swirling vortices are weaker than the vortices in the upper part of the wake, which are nearly normal to the incoming flow. In the study of Miliou *et al.* (2007) for  $Re = 500$ , the weakening of the lower wake vortices caused the vortex shedding to be dominated by the vortices in the upper wake, so that the Strouhal number ( $f_v D/U_0$ , where  $f_v$  is the vortex shedding frequency) turned out to be the same along the entire span. Gallardo *et al.* (2014) found nearly the same result, although in their study, the inclusion of a straight vertical extension on top of the curved cylinder lead to a slightly different  $St$  along this extension. This caused vortex dislocations to develop in the wake.

When the straight vertical extension was included (Gallardo *et al.* 2013, 2014), a low-velocity upwelling was allowed to develop in the very near wake, along the upper part of the curved cylinder and the extension. The flow now exhibited a vertical velocity stagnation point along the curved cylinder. The wake vortices in the study of Miliou *et al.* (2007) were normal to the incoming flow for  $Re = 100$ , but had a slight inclination for  $Re = 500$ . This lead to the hypothesis that the wake vortices would align increasingly with the local cylinder curvature

with increasing Reynolds number, which was confirmed by the study of Gallardo *et al.* (2014) for  $Re = 3900$ .

The flow features described above are recognisable also for convex curved tandem cylinders at  $Re = 500$ , though the spanwise regime variation leads to a significantly more intricate flow field. In this case, there is strong downdraft in the lower wake as well as in the lower gap along the back face of the upstream cylinder and the front face of the downstream cylinder. There is upwelling in the entire upper part of the gap, and along the upper part of the near wake. Vortex shedding is largely governed by the upper wake vortices, although bi-stability leads to the occurrence of several secondary frequencies, in particular along the upper part of the curved cylinders. These frequency variations, along with the shedding of gap vortices into the lower wake, causes frequent vortex dislocations, and alterations between parallel and oblique wake vortex shedding. Because of the suppression of vortex shedding in the lower wake, true co-shedding was not observed for convex curved tandem cylinders at  $Re = 500$  (Aasland *et al.* 2022a, 2023b).

To further investigate the complex flow field interaction in the gap and wake of convex curved tandem cylinders, it is natural to extend our previous work to a subcritical Reynolds number; in this case  $Re = 3900$ . At this Reynolds number, transition to turbulence is expected to occur in the shear layers for straight and curved single cylinders (Dong *et al.* 2006; Gallardo *et al.* 2014), and the wake is turbulent. It is of particular interest, therefore, to study the interaction between the shear layer instability and the multi-stable processes in the gap region. Moreover, the effect of the curvature-induced axial flow on this interaction, and the effect of the shear layer instability on the near wake are investigated herein.

## 2. Flow problem formulation and computational aspects

The geometry consists of curved tandem cylinders of equal diameter, with a gap ratio of  $L/D = 3$ . The cylinders are placed in the convex configuration, with the inflow parallel to the plane of curvature of the cylinders.

### 2.1. Governing equations and numerical method

In the present study, direct numerical simulations are carried out using the MGLET (Multi Grid Large Eddy Turbulence) flow solver. MGLET is based on a finite volume formulation of the incompressible Navier-Stokes equations. The governing equations are

$$\frac{\partial u_i}{\partial x_i} = 0, \quad (2.1)$$

$$\frac{\partial u_i}{\partial t} + u_j \frac{\partial u_i}{\partial x_j} = -\frac{1}{\rho} \frac{\partial P}{\partial x_i} + \frac{\partial}{\partial x_j} \left( \nu \left[ \frac{\partial u_i}{\partial x_j} + \frac{\partial u_j}{\partial x_i} \right] \right), \quad i, j = 1, 2, 3 \quad (2.2)$$

MGLET uses a staggered Cartesian grid (Manhart 2004), and solid bodies are introduced through an immersed boundary method (Peller *et al.* 2006). The surface of solid bodies is discretised using a cut-cell approach (Unglehart *et al.* 2022). A third-order low-storage explicit Runge-Kutta time integration scheme is used for time stepping, and the Poisson equation is solved using an iterative, strongly implicit procedure (SIP). MGLET has previously been used for convex (Gallardo *et al.* 2014; Aasland *et al.* 2022a, 2023b) and concave (Jiang *et al.* 2018, 2019) curved cylinder studies.

Free-slip boundary conditions are used on all computational domain boundaries except the inlet and outlet. Uniform inflow is imposed at the inlet, and a Neumann condition is imposed on the velocity components at the outlet. No-slip and impermeability conditions are enforced on the tandem cylinder surfaces.

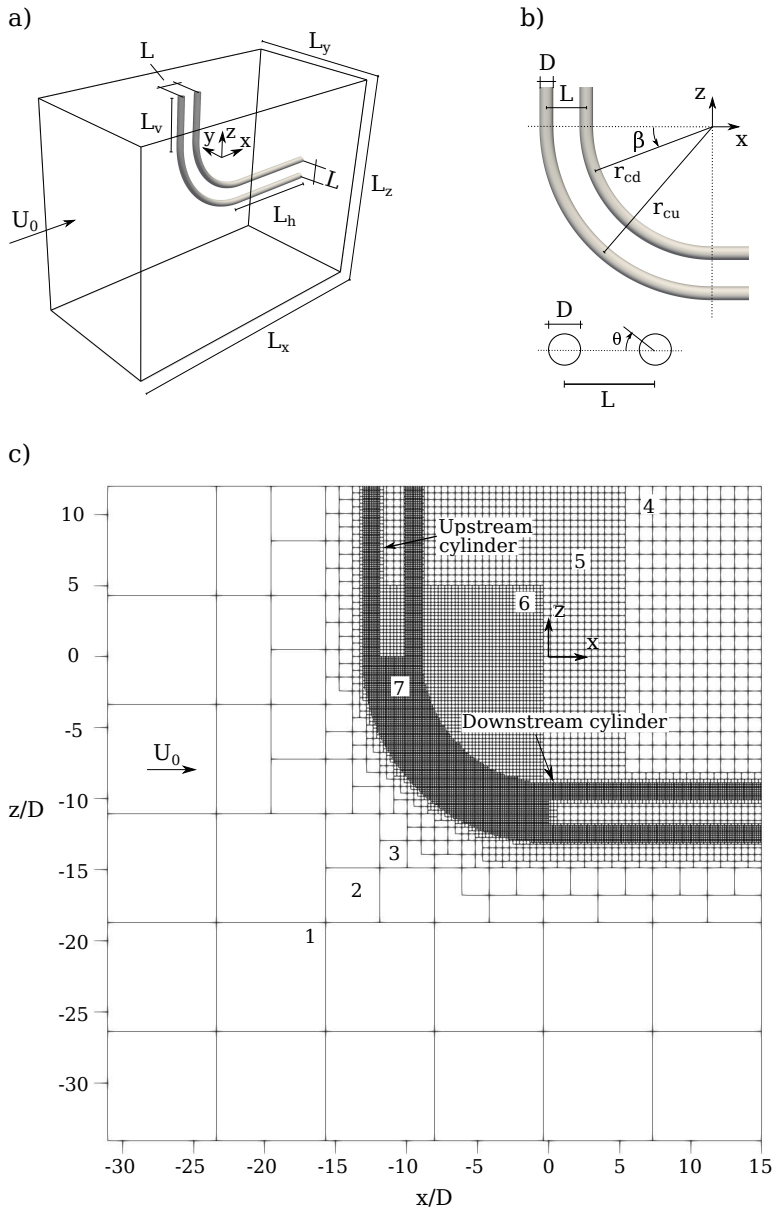


Figure 1: a) Computational domain, b) definitions, and c) computational grid schematic. This schematic does not show the actual grid resolution, only the extent of the grid blocks. The most refined grid block contains approximately  $2365 \times 10^6$  cells, and the second most refined block contains approximately  $974 \times 10^6$  cells. The cells are cubic, and the smallest cell size is  $0.00375D$ . The largest cell is  $0.24D$ . There are seven grid levels in total, where each level has half the grid cell size of the previous level. These levels are marked in c).

## 2.2. Computational domain and grid

As shown in figure 1a, each cylinder consists of a quarter-segment of a ring, fitted with horizontal and vertical extensions in order to reduce influence from the computational domain boundaries. Based on previous computational studies (Gallardo *et al.* 2013, 2014; Aasland *et al.* 2023b), the chosen length of the horizontal and vertical extensions are

Grid	$\Delta_{min}/D$	no. elem. $\times 10^6$	$\overline{C}_D$	$C_{Lrms}$	$\overline{C}_z$	$St$
<i>Upstream cylinder</i>						
coarse	0.015	482	0.592	0.014	0.118	0.150
medium	0.0075	944	0.726	0.011	0.132	0.170/0.190/0.210
fine	0.00375	3890	0.710	0.009	0.128	0.173/0.190/0.206
<i>Downstream cylinder</i>						
coarse	0.015	482	0.034	0.047	-0.002	0.150
medium	0.075	944	-0.177	0.072	-0.021	0.170/0.190/0.210
fine	0.00375	3890	-0.175	0.081	-0.021	0.173/0.190/0.206

Table 1: Results of grid convergence study. Three Strouhal numbers are captured by the medium and fine grids, due to spanwise mode variation.

$L_h = 15D$  and  $L_v = 12D$ , respectively. In order to ensure a constant gap ratio along the span, the curved cylinders have different radii of curvature, as shown in figure 1b. The radii of the upstream and downstream cylinders are  $r_{cu} = 12.5D$  and  $r_{cd} = 9.5D$ , respectively.

The computational domain is sketched in figures 1a. The size of the domain is  $L_x = 46.08D$ ,  $L_y = 30.72D$  and  $L_z = 47.08D$ . The distance between the inflow plane and the upstream cylinder front face is  $18.08D$ .

The computational grid, shown in figure 1c consists of nested grid blocks, where each child block has half the cell size as its parent block. Grid elements have the same length in  $x$ ,  $y$  and  $z$  direction. A previous study of curved tandem cylinders showed that refinement in the curved gap region is crucial to capture the flow physics (Aasland *et al.* 2022a), due to the sensitivity of the gap shear layers, as well as the curvature-induced axial velocity. For this reason, the grid cell size in the curved gap region is the same as the cell size on the solid bodies and in the boundary layers.

A grid convergence study was carried out in three steps, and the results are listed in table 1. With each refinement, the cell size of the smallest grid element  $\Delta_{min}/D$  was cut in half. In order to save computational hours, a start-up simulation with a very coarse grid was first run for 900 time units. This grid had the same smallest element size as the coarse grid in table 1, but with little refinement in the gap and wake. Afterwards, the simulations with each refined grid was started from the flow field of the previous grid. The time step was adjusted before sampling of statistics began, in order to ensure a maximum Courant number of 0.5. Sampling of statistics started after 100 time units  $D/U_0$  for each of the three grids in table 1. For the coarse and medium grids, statistics were sampled for 800 time units. A sampling time of 815 time units was used for the finest grid, but due to a writing error in the force output which led to loss of data, the force coefficients in table 1 are only computed over 585 time units.

The coarsest grid is obviously insufficient, giving coefficient values that differ substantially from the medium and fine grids. This coarse grid resolution is unable to resolve the flow physics in the gap region, thereby failing to capture the mode alterations that take place therein. The differences between the medium and fine grids are much less pronounced, although there is 22 percent difference in the root mean square (rms) of upstream cylinder lift, with a corresponding 11 percent difference for the downstream cylinder. This is likely

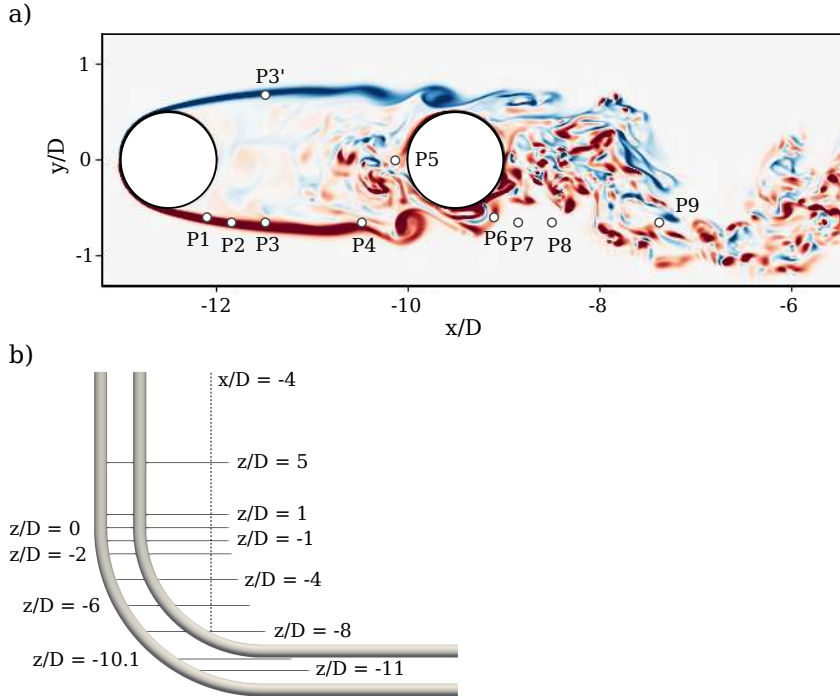


Figure 2: a) Positions of point probes at  $z/D = 5.0$ . The other  $z/D$  levels discussed have corresponding probes with the same streamwise distances from the cylinder center, and equal lateral positions. The streamwise coordinates of the probes P1 - P4 w.r.t. the upstream cylinder center are as follows:  $[0.4D, 0.65D, 1.0D, 2.0D]$ . Similarly, probes P6 - P9 have the following streamwise coordinates, w.r.t. the downstream cylinder center:  $[0.4D, 0.65D, 1.0D, 2.0D]$ . P1 and P6 are located at  $y/D = -0.6$ , whereas the remaining shear layer probes are located at  $y/D = -0.65$ . P5 is located  $0.1D$  upstream of the downstream cylinder front face, at  $y/D = 0$ . b) spanwise locations and streamwise extent of  $z/D$  planes used for visualisation, as well as the position of the probe line at  $x/D = -4$ , which is used to compute velocity spectra in the wake. The distance between probes in the line is  $0.25D$ .

caused by insufficient refinement along the straight vertical extension for the medium grid. Since the von Kármán vortices are generally stronger along the straight vertical extension for convex curved cylinders, single or tandem (Gallardo *et al.* 2014; Aasland *et al.* 2023b) it makes sense that less refinement in this region should affect the overall lift. Given the discrepancies between the medium and fine grid, it may have been beneficial to test a fourth, even finer grid. However, the computational cost precludes further refinement, and it is the results from the fine grid that are used herein.

Three Strouhal numbers are captured, due to mode variations. A run-time of 815 time units corresponds to approximately 138 von Kármán vortex shedding cycles, using the lowest St. The non-dimensional time-step of the present computation was  $dt = 6.6 \times 10^{-4}$ .

The computations were carried out on the supercomputer Betzy, run by the Norwegian Research Infrastructure Services (NRIS). One time-step typically required between 0.5 and 0.6 seconds, and the fine grid case alone required approximately 1 500 000 time steps. All in all, the required computational resources amount to nearly 10 million CPU hours.

### 2.3. Data sampling

Time histories of the velocity were sampled at a number of point probes within the gap and near-wake, close to the shear layers. The probe locations are illustrated in figure 2a. Probes were sampled every second time-step, giving a frequency resolution of approximately  $df = 0.00128$ .

Herein, all frequencies and spectra have been computed using discrete Fourier transform (DFT) of the velocity data from the probes. Because the present geometry is fully three-dimensional, spanwise-averaging of spectra is inappropriate. In order to reduce spectral leakage, Welch's method with a Hamming window is employed. The data was partitioned into 4 or 8 segments, to compute spectra in the wake and shear layers, respectively.

Visualisation of the flow field in various planes (based on arrays of probes) are presented herein, and the spanwise locations of these planes are illustrated in figure 2b, for reference.

### 2.4. Definitions

Herein, the  $x$ ,  $y$  and  $z$  directions are referred to as streamwise, crossflow and vertical. Vortices that align with the vertical direction are dubbed spanwise. When vortex shedding modes are discussed, "parallel" means that the spanwise orientation of the vortices are parallel to the straight vertical extension, i.e. normal to the inflow direction, and "oblique" in this context means the vortices have an angle in the  $y$ -plane.

Force coefficients are defined as  $C_F = 2F/\rho U_0^2 A$ , where  $F$  is the force component in question,  $\rho$  is the fluid density and  $A$  is the projected frontal area. Subscripts  $D$  and  $L$  denote drag and lift, respectively, and subscript  $z$  denotes vertical force. Note that "lift" implies crossflow (i.e.  $y$ ) direction in the present study. Subscripts  $u$  and  $d$  refer to the upstream and downstream cylinders, respectively.

## 3. Results

### 3.1. Flow field overview

An overview of the flow field is given in figure 3a. The wake is turbulent, though there is a clear von Kármán vortex street, similar to the case of a single convex curved cylinder (Gallardo *et al.* 2014). In figure 3b, we see that the von Kármán vortices have a slight backwards slant, though the shedding angles are sufficiently small so that the vortices can be considered nearly parallel to the  $z$ -axis. Truly oblique shedding does occur, however, similar to the  $Re = 500$  case (Aasland *et al.* 2022a, 2023b). This shedding mode is discussed in section 3.3.

Transition to turbulence initiates in the gap shear layers, by the Kelvin Helmholtz (K-H) instability. The characteristic shear-layer vortices form in the gap between the cylinders, as seen in figure 3a. These vortices subsequently become unstable and break down into a myriad of small-scale eddies that make up the bulk of the von Kármán vortices in the wake. The shear layer vortex breakdown process, shown in figure 3c, works by vortex stretching, similar to the development of streamwise vortices in mixing layers and transitional wakes of single cylinders (Williamson 1995). The development of small-scale horse-shoe vortex loops during breakdown is evident in figure 3c. We see that although the shear layer vortices are surprisingly spanwise coherent within the gap (the longest unbroken core stretching almost  $10D$  in figure 3a), the breakdown process commences within shorter spanwise cells.

In the upper part of the curved gap, as well as in the gap along the straight vertical extension, the shear layer vortices maintain an orientation parallel to the  $z$ -axis. However, once these vortices have been convected past the downstream cylinder, their orientation alters to align with the spanwise vortices forming in the near-wake, as shown in figure 3c. In the lower

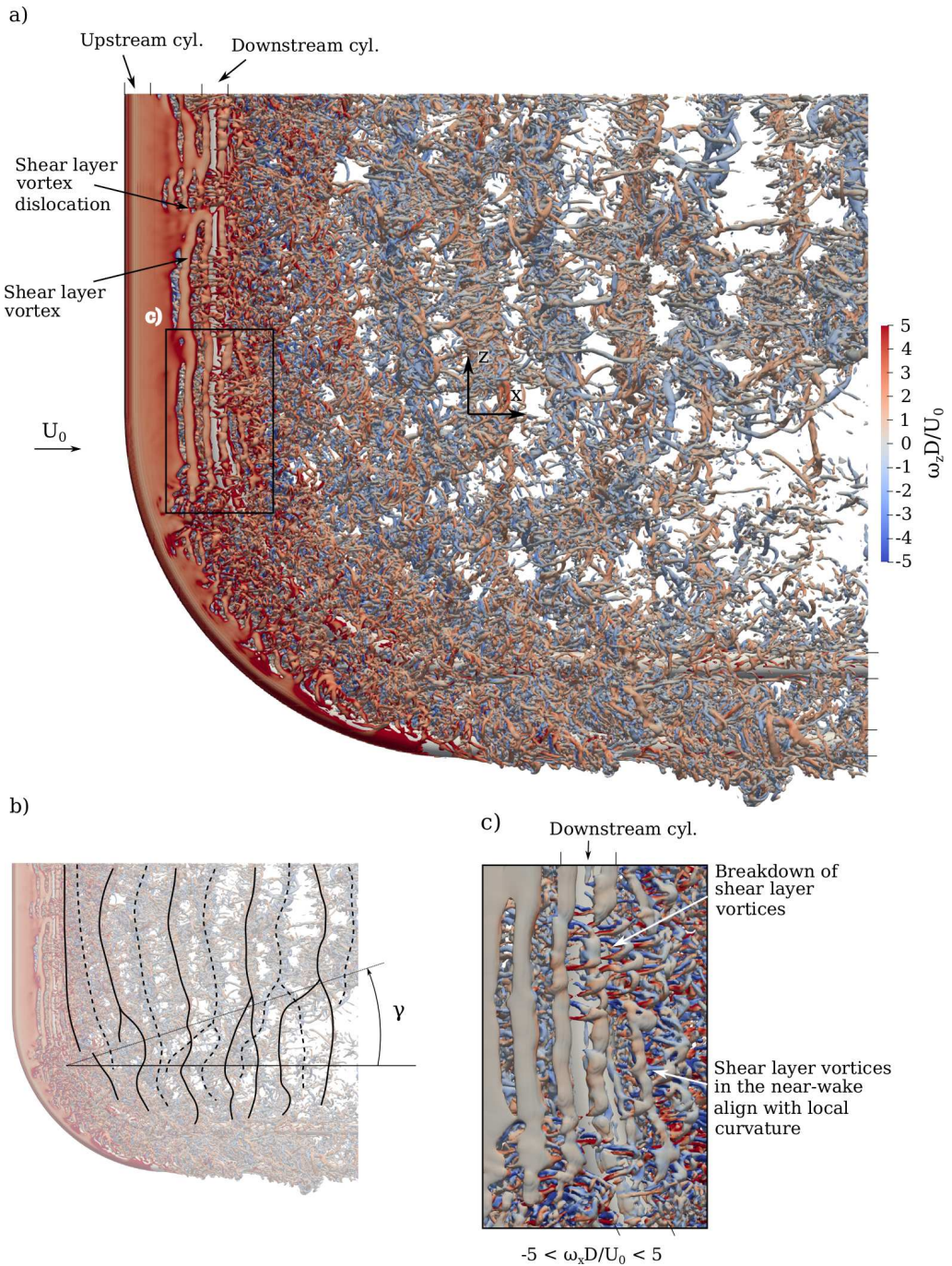


Figure 3: a) Isosurfaces of  $Q = 0.5$  for  $tU_0/D = 915$ , coloured by the spanwise vorticity  $\omega_z D / U_0$ . b) Spanwise wake vortices marked for clarity. Solid lines have positively signed spanwise vorticity. Dashed lines have negatively signed spanwise vorticity. Vortex dislocations propagate from the midspan of the curved cylinders with an angle of  $\gamma \approx 19^\circ$ . c) Close-up of the gap shear layer vortices from a), coloured by the streamwise vorticity  $\omega_x D / U_0$ . In the gap, these vortices are mostly parallel to the  $z$ -axis, but when convected into the near wake, they align with the local axial curvature.



gap, the shear layer vortices align somewhat with the local curvature of the cylinder, and are thus shed with slightly oblique angles. This result agrees quite well with the study of Prasad & Williamson (1997a), who found that the shear layer instability was mostly parallel with the cylinder axis, even when the large-scale vortex shedding itself was oblique. The shear layer instability and the associated vortices play an important role in the dynamics, and the spacial and temporal development of these flow features is discussed in detail in section 3.4.

Similar to convex curved tandem cylinders at  $Re = 500$  (Aasland *et al.* 2022a, 2023b), there is spanwise variation of flow regimes as the effective gap ratio widens (for decreasing  $z/D$ ), from alternating overshoot/reattachment, via symmetric reattachment to vortex shedding in the gap. However, the transition between regimes is accelerated, due to the increased Reynolds number in the present study, so that these transitions occur at higher  $z/D$  (i.e. lower effective gap ratios). The accelerated transition leads to the occurrence of co-shedding, which was not found for  $Re = 500$ . The spanwise flow regime variations are detailed in section 3.2.

The time-averaged velocity and pressure fields are presented in figure 4. Key parameters are summarized in table 2 and compared with other convex curved cylinder cases. As with convex curved tandem cylinders at  $Re = 500$ , the flow is characterised by recirculation zones in the gap and wake, strong downdraft in the lower gap and wake, and a low-velocity up-welling in the upper part of the gap and wake (Aasland *et al.* 2023b).

In figure 4a, we see that a recirculation zone bounded by the cylinders fills the entire vertical gap, and a large part of the curved gap. Within this zone, there is reattachment of the upstream cylinder shear layer onto the downstream cylinder. Reattachment causes suction in the gap, as shown in figure 4c, which leads to a negative drag coefficient for the downstream cylinder (see table 1), similar to straight tandem cylinders. Gap shedding starts near  $z/D = -6$ . Recirculation in both gap and wake is eventually suppressed by the downdraft along the curved cylinders, where the vortices attain the non-shedding, swirling characteristics discussed in section 1.

Figure 4d shows the surface pressure on the cylinders, seen from upstream. On the downstream cylinder, the surface pressure in the gap is predominantly negative, but a region of positive surface pressure develops for  $\beta \geq 15^\circ$ . This is caused by increasing prevalence of symmetric reattachment or gap shedding regimes.

Non-zero vertical velocities along the entire span entails that the gap and wake vortices have a non-zero streamwise vorticity component nearly everywhere, though this component is certainly strongest along the curved cylinders. In figure 5 time-averaged streamlines coloured by the streamwise vorticity shows the swirling flow in the gap and along the back face of the downstream cylinder, for the curved portion of the cylinder span. The downdraft increases near the midspan, as seen in figure 4b, and this is also reflected in the magnitude of the vorticity.

From table 2, we see that the gap shedding inception angle, as well as recirculation suppression angles in the gap and wake, are all lower for  $Re = 3900$  than for  $Re = 500$ . The vertical velocity stagnation point in the wake is located significantly higher for  $Re = 3900$ ; it now occurs along the straight vertical extension. In the gap, however, the stagnation point is moved slightly lower. This is likely due to more frequent gap shedding, where the slanted vortices induce up-welling.

The primary contribution to vertical forces comes from the curved portion of the cylinders, mainly due to the curvature-induced downdraft. Vertical forces on the straight extensions are nearly negligible. If we, for instance, calculate  $\overline{C_z}$  on the upstream cylinder separately for all parts of the geometry, we get  $(C_{zv}, C_{zc}, C_{zh}) = (0.0004, 0.2596, -0.0026)$  for the vertical, curved and horizontal cylinders, respectively. Taking a look at the time-averaged pressure in

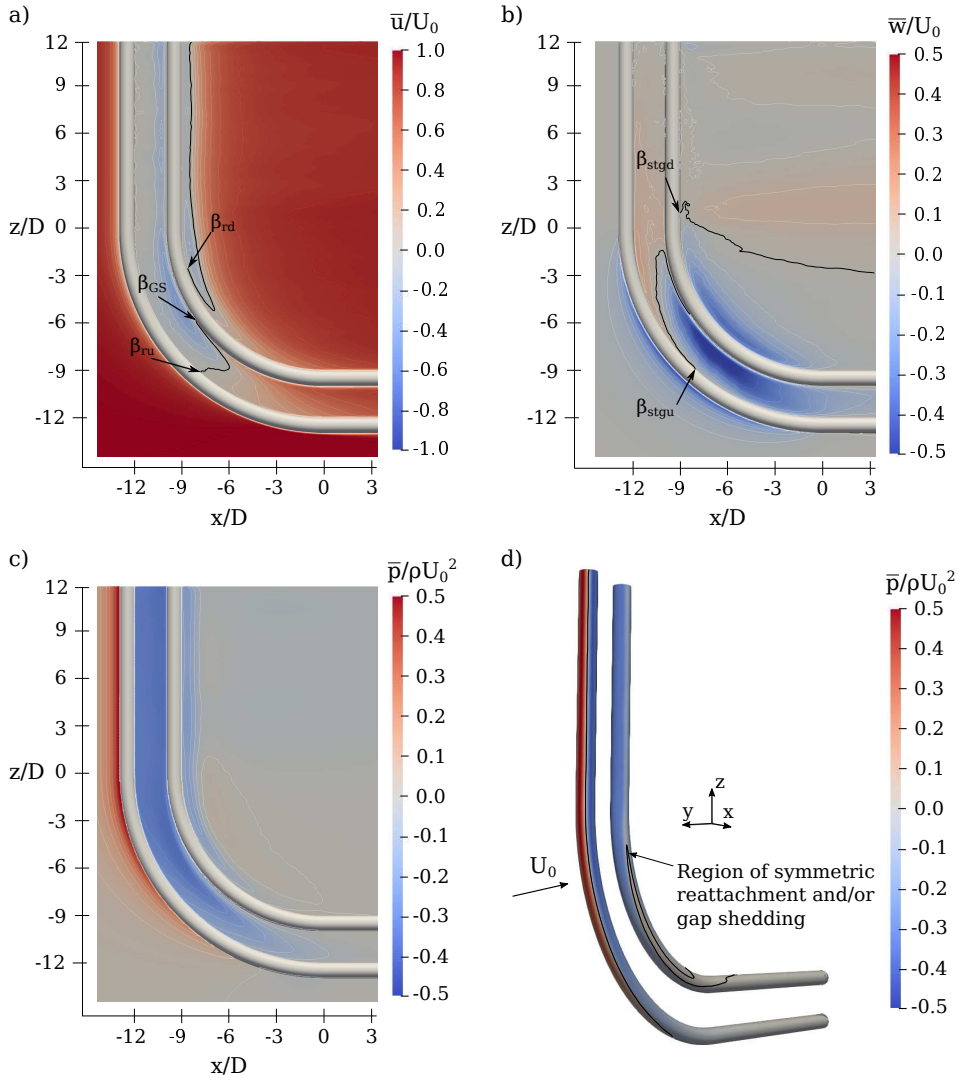


Figure 4: a)-c) Time-averaged field in the symmetry plane. a) Streamwise velocity. The extent of the recirculation region is marked in black.  $\beta_{GS}$  denotes the angle of gap shedding inception, whereas  $\beta_{ru}$  and  $\beta_{rd}$  refer to the angle where recirculation is suppressed in the gap and wake, respectively (defined as  $\bar{u}/U_0 > 0$  along the cylinder back face). b) Vertical velocity. The black contour lines mark the boundaries between up-welling and downdraft in the gap and lower wake, where  $\beta_{stgu}$  and  $\beta_{stgd}$  refer to the stagnation points near the cylinder surfaces. c) Pressure. d) Isometric view the time-averaged pressure on the cylinder surfaces. The black contour lines mark  $\bar{p}/\rho U_0^2 = 0$ .

figure 4c, we see that the suction region in the curved gap gives positive pressure gradients for the upstream cylinder, and negative pressure gradients for the downstream cylinder. The location of the pressure minima in the gap correspond well with the vertical velocity minima in figure 4b. However, the downdraft is not the only contribution to the suction; the gap vortices also play a role.

Compared with  $Re = 500$ , the recirculation lengths along both the straight vertical extension and curved cylinder are shorter in the present study. This is likely an effect of increased entrainment which follows from transition to turbulence in the shear layers.

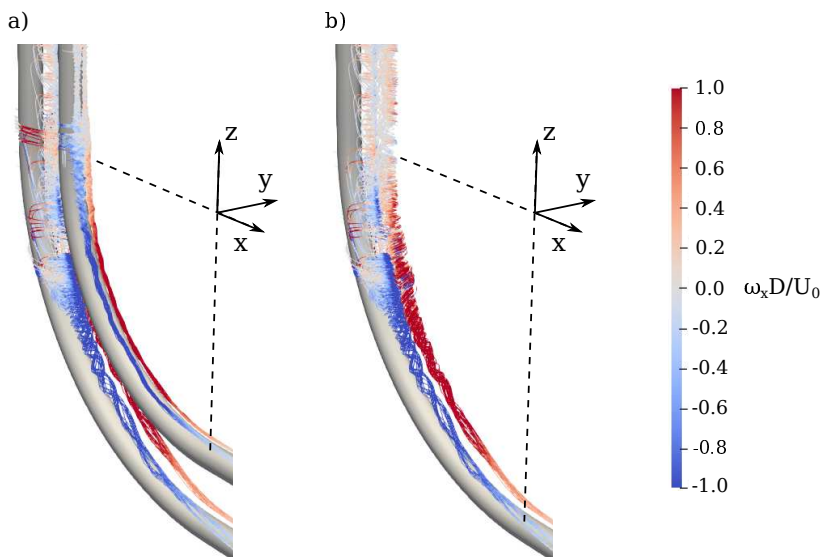


Figure 5: Time-averaged streamlines showing the swirling flow along the curved span, coloured by the streamwise vorticity  $\omega_x D/U_0$ . a) shows both cylinders, whereas b) shows the upstream cylinder alone, for a better view of the gap flow. The scale of  $\omega_x D/U_0$  is exaggerated for visibility.

$Re$	Convex curved tandem cylinders		Single convex curved cylinder
	500	3900	3900
$f_v$	0.143/0.155	0.173/0.190/0.206	0.213/0.223
$\beta_{gs}$	38.1°	35.6°	-
$\beta_{ru}$	45.6°	40.5°	-
$\beta_{rd}$	37.4°	25°	45°
$\beta_{stgu}$	44.7°	48°	-
$\beta_{stgd}$	34.3°	-5.1°	38°
$Lrv/D$	0.634	0.522	1.60
$Lrc/D$	1.197	0.820	1.95

Table 2: Comparison between main results for convex curved tandem cylinders at  $Re = 500$  (Aasland *et al.* 2022a, 2023b) and the present study at  $Re = 3900$ . Values from a single convex curved cylinder study at  $Re = 3900$  (Gallardo *et al.* 2014) are included for reference.  $Lrv/D$  and  $Lrc/D$  denote the recirculation lengths in the wake along the straight vertical extension and along the curved span, respectively, measured at  $z/D = 5$  and at  $z/D = -1$ , for the curved tandem cylinder cases, and at  $z/D = 4$  and  $z/D = -1$  for the single curved cylinder case. The negative value of  $\beta_{stgd}$  for  $Re = 3900$  implies that the stagnation point is located along the straight vertical extension.

### 3.2. Spanwise development of the flow-field

The spanwise development of the flow-field in the gap and near wake is shown in figure 6. As seen in figures 6a and 6b, alternating overshoot/reattachment persists along the straight vertical extension, even at this high Reynolds number. However, the shear layer reattachment is symmetric along the upper part of the curved cylinders (see figure 6c - 6e). From the flow visualizations, we see that intermittent co-shedding has commenced at  $z/D = -4$  (see supplementary movie 1), though the shedding from the gap remains one-sided. The same

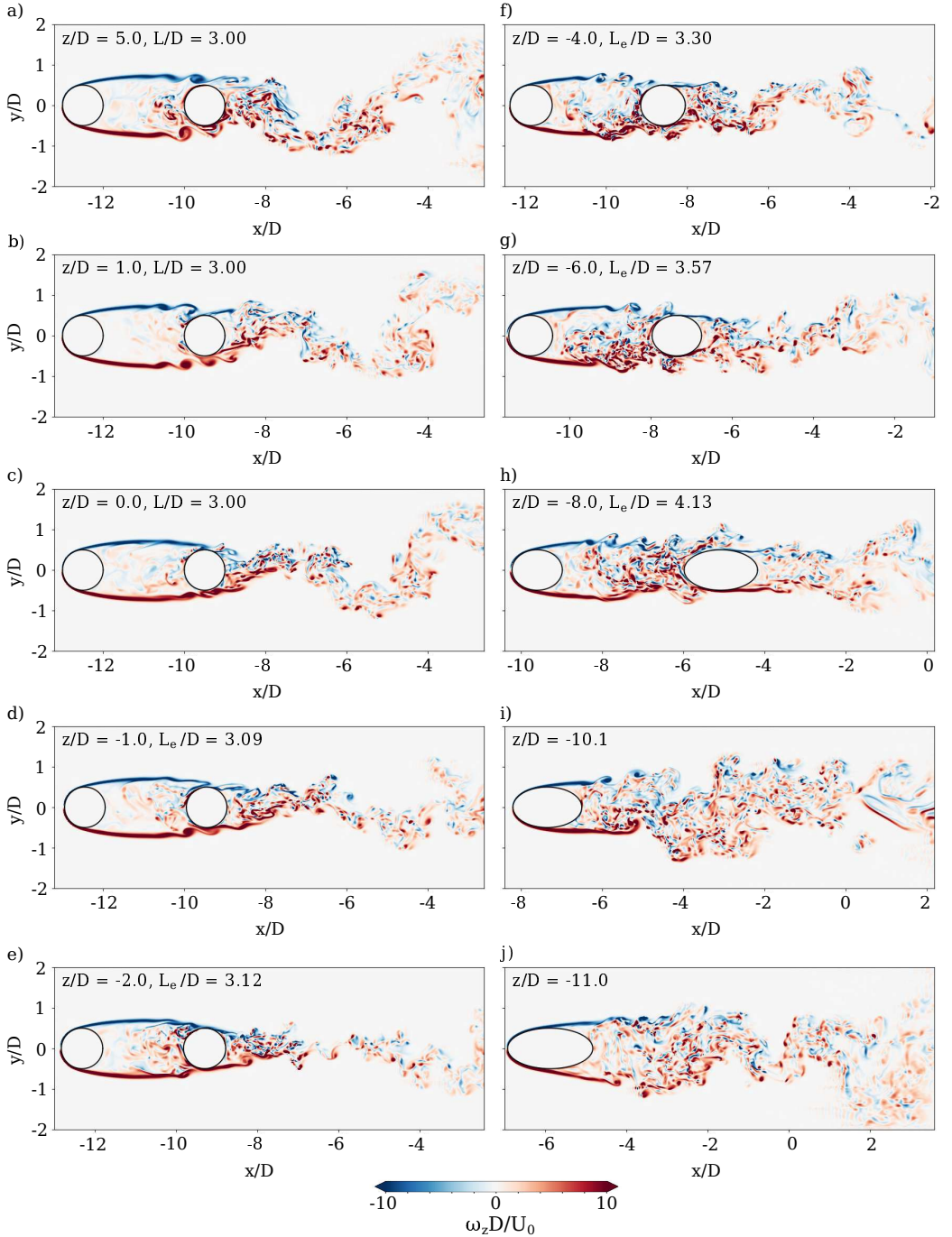


Figure 6: Spanwise vorticity  $\omega_z D/U_0$  in various  $z/D$  planes at  $tU_0/D = 915.066$  (directly after the snapshot in figure 3). The local flow regime changes from alternating overshoot/reattachment in a) and b), to symmetric reattachment in c)- e), before shedding of gap vortices begins in f). The regimes in f) and g) can be considered bi-stable co-shedding regimes. Increased axial flow contributes to a considerable increase of the shear layer separation angles, with a corresponding widening of the wake, in the lower gap, in j). The spanwise locations of the  $z/D$  planes are illustrated in figure 1d. Along the curved part, the effective gap spacing  $L_e$  has been computed by measuring the spacing from the upstream cylinder back to the downstream cylinder front and adding  $1D$ .

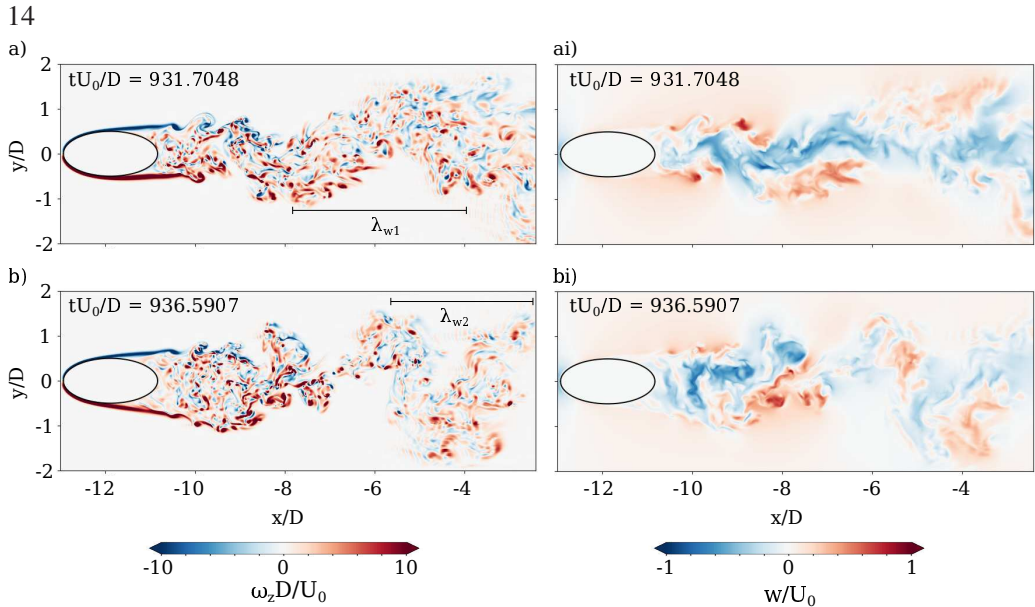


Figure 7: Snapshots of the flow field at  $z/D = -11$ , showing a) narrow and b) wide near wake modes. The narrow wake mode is accompanied by a shorter vortex formation region and transverse motion of the shear layers. Snapshot b) is taken approximately one vortex shedding period after snapshot a). The shortening of the formation length has clearly reduced the streamwise wave length of the wake, so that  $\lambda_{w1} > \lambda_{w2}$ , and the braid regions are narrow compared to those in a). The short formation length in a) is associated with a slight weakening of the vertical velocities in the near wake, as seen when comparing ai) and bi).

type of local regime was observed by Aasland *et al.* (2023b), though lower into the wake, at  $z/D = -7$ . Beyond  $z/D = -4$ , the flow regime is considered to be a weak form of intermittent co-shedding where the streamwise location of roll-up in the gap meanders. owing to the strong axial flow in the near wake, communication between the shear layers becomes increasingly inhibited, so that shedding occurs intermittently down to  $z/D = -6$  (figure 6g) and not at all at  $z/D = -8$  (figure 6h) and below. The wake still oscillates somewhat, due to forcing from vortices higher up in the wake, as evidenced by the wake structure figure 6h.

In the lower part of the gap, the downstream cylinder is no longer in the wake of the upstream cylinder. This means that the wake of the upstream cylinder wake can develop more freely. The cylinders do still represent constraints within the horizontal gap, but in the vertical direction. We see from figure 6j that the wake is quite wide in the lower gap region. The separation angle of the shear layers is higher than within the reattachment region. This angle is quite steady, and does not change significantly in time. However, transverse motion of the shear layers due to vortex shedding, similar to what is found for straight single cylinders (Prasad & Williamson 1997a), occurs intermittently. Such transverse motion is seen during time intervals when the instantaneous vortex formation region shortens, as shown in figure 7a. During these intervals, the local flow regime resembles that of a straight elliptic cylinder with an aspect ratio of 0.4 (see flow visualisations by Fonesca *et al.* (2013) or Durante *et al.* (2021)). The shortening of the formation region is associated with a momentary weakening of the vertical velocity in the near wake of the upstream cylinder. This can be observed in figures figure 7ai and figure 7bi. A variation of the vortex formation length also leads to a variation of the streamwise wavelength of the wake, which is clearly shown in figure 7a and figure 7b. The variation of the vertical velocity in the gap has a significant impact on the

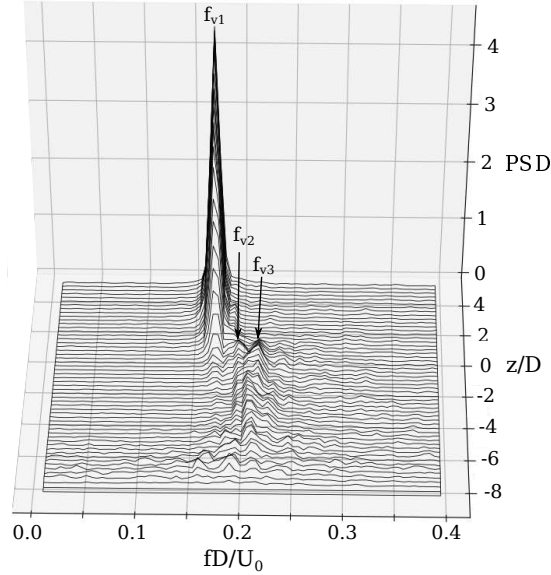


Figure 8: Spectra of the crossflow velocity  $v/U_0$  from a line of probes in the wake of the downstream cylinder, at  $(x/D, y/D) = (-4, 0)$ . The wake contains three independent frequencies,  $f_{v1}$ ,  $f_{v2}$  and  $f_{v3}$ , which represent different flow modes. The relative importance of these frequencies shifts along the cylinder span, so that higher frequencies dominate in the lower wake.

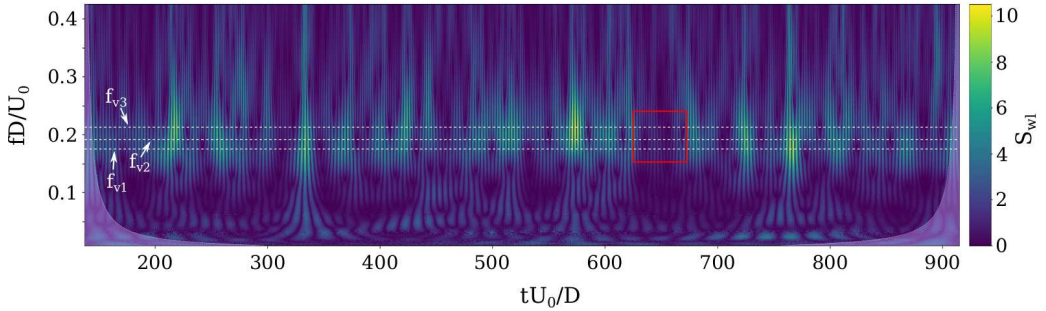


Figure 9: Wavelet map of the crossflow velocity in the wake of the downstream cylinder at  $z/D = 0$  (probe position P9). The spectral peak shifts between  $f_{v1}$ ,  $f_{v2}$  and  $f_{v3}$  (represented by horizontal dashed lines), though there are time intervals when neither of these frequencies contain significant wavelet energy  $S_{wl}$ . The red rectangle marks such an interval, which corresponds roughly to event A in figure 10b.

behavior of the gap shear layers at higher  $z/D$ , something which will be further discussed in section 3.5.

The spanwise regime variation engenders a multi-stable flow field, where three independent vortex shedding frequencies are found in the wake (the same frequencies are found in the force spectra, though this is not shown here). From figure 8, we see that  $f_{v1} = 0.173U_0/D$  dominates the flow along the upper part of the straight vertical extension. The secondary frequency  $f_{v2} = 0.190U_0/D$  develops as we move downwards along the straight vertical extension. At  $z/D = 0$ , the third frequency  $f_{v3} = 0.206U_0/D$  has already grown to match the spectral energy of  $f_{v2}$ . At this level,  $f_{v2}$  and  $f_{v3}$  are almost as energetic as  $f_{v1}$ . Below

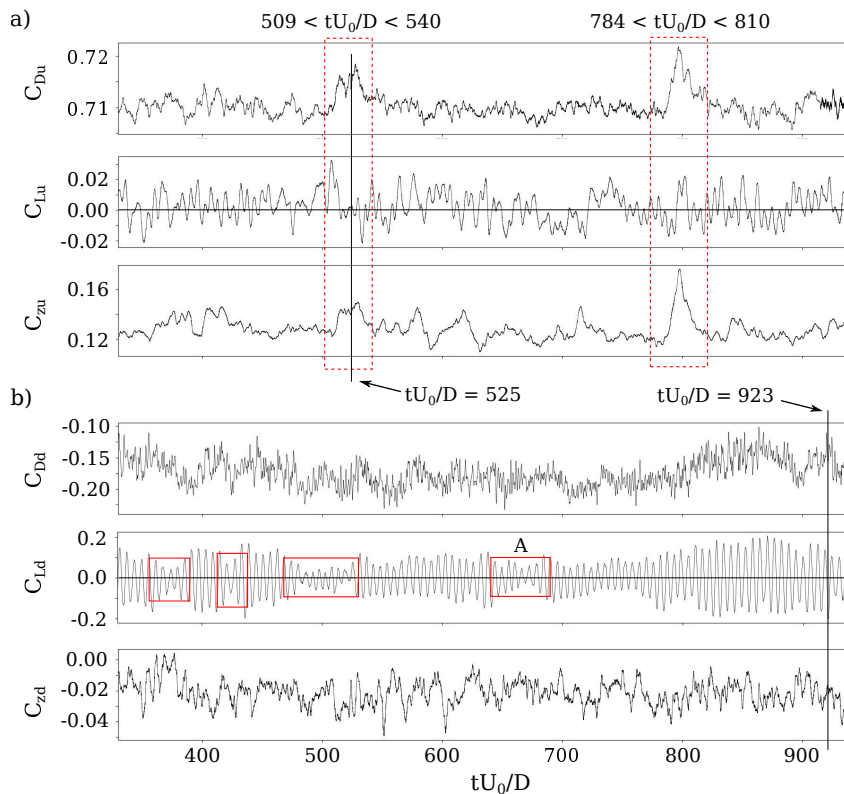


Figure 10: Time histories of the forces for the a) upstream and b) downstream cylinders.

There is alteration between high and low amplitude lift modes for the downstream cylinder. Intervals of significantly reduced lift are marked by red rectangles in b). The low amplitude lift intervals are associated with oblique wake vortex shedding and an increased number of spanwise vortex dislocations. These phenomena are closely coupled to the mode switches in the gap.  $C_{Du}$  and  $C_{zu}$  exhibit two significant peaks, each lasting approximately 5 vortex shedding cycles, marked by dashed red rectangles in a).

$z/D = 0$ , the higher frequencies dominate the flow, while  $f_{v1}$  gradually diminishes. For  $z/D \leq -2$  there is a shift of  $f_{v3}$  towards a slightly lower frequency.

Figure 9 shows the wavelet transform of the signal in probe P9 at  $z/D = 0$ . We see that the broad banded spectral peaks are generally centered on either  $f_{v1}$ ,  $f_{v2}$  or  $f_{v3}$ , though there are time intervals when neither frequency contains significant spectral energy. The three frequencies  $f_{v1}$ ,  $f_{v2}$  and  $f_{v3}$  represent three different main flow regimes, or modes, that interact and that may trigger one another. Such interactions are further discussed in section 3.5.

If we compare with previous studies of straight tandem cylinders, we see that  $f_{v1}$  corresponds with co-shedding directly after the critical spacing at a comparable Reynolds number (Xu & Zhou 2004).  $f_{v2}$  and  $f_{v3}$  approach the dominant frequency of a single cylinder within the subcritical Reynolds number regime, which is typical for co-shedding regimes as  $L/D$  increases (Sumner 2010).

### 3.3. Temporal variation of the forces

In figure 10b, we see that the downstream cylinder lift exhibits alteration between high and low amplitudes. Intervals of high amplitude lift are accompanied by an increase in  $C_{Dd}$  (i.e.

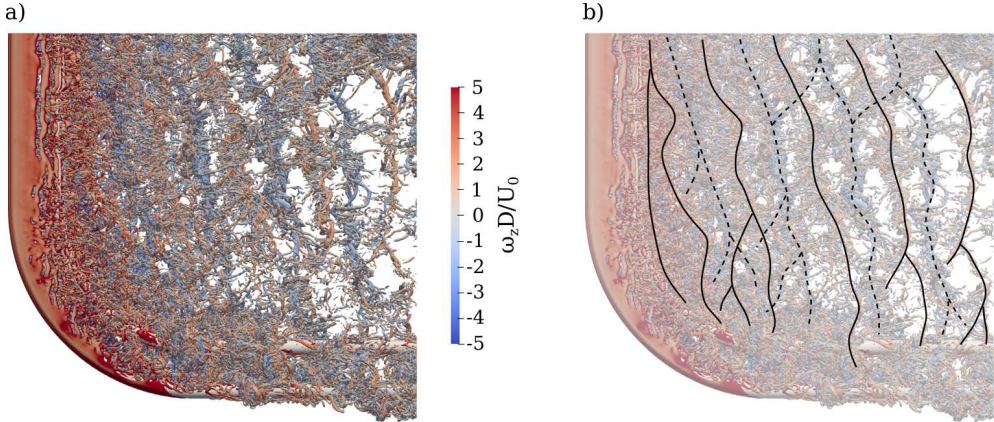


Figure 11: a) Isosurfaces of  $Q = 0.5$  for  $tU_0/D = 525$ , colored by the spanwise vorticity. b) Solid lines indicate positive  $\omega_z D/U_0$ , while dashed lines indicate negative  $\omega_z D/U_0$ . The wake exhibits oblique shedding with a large amount of vortex dislocations, even along the straight vertical extension. This time instant occurs at the end of interval of low lift on the downstream cylinder, as shown in figure 10b, and corresponds to an interval of markedly high drag on the upstream cylinder (see figure 10a).

decreased suction, as  $C_{Dd}$  is exclusively negative). Two high peaks stand out in the time traces of drag and vertical force on the upstream cylinder, in figure 10a. These peaks are by no means instantaneous events, but persist over several vortex shedding cycles. The first peak occurs within the interval  $509 \leq tU_0/D \leq 540$  and the second within  $784 \leq tU_0/D \leq 810$ . It is worth noting that both these peaks are correlated in time with a transition from low to higher amplitude lift on the downstream cylinder. However, transitions from low to high amplitude lift are not uniquely associated with local peaks in  $C_{Du}$  and  $C_{zu}$ .

We have no direct observations of the flow field during the last, most prominent, peak. However, we have a snapshot of the flow at  $tU_0/D = 525$ , shown in figure 11. The difference between the wake structure at  $tU_0/D = 525$  and 915 (figure 3a) is quite striking. While the latter exhibits a comparably more orderly wake with nearly parallel vortex shedding and coherent gap shear layer vortices, the former is significantly more chaotic. The spanwise vortices have a distinct oblique shedding angle, and there is a high number of vortex dislocations. These dislocations occur, not just in the lower wake, but also quite high up along the straight vertical extension. Also noticeable is the development of the gap shear layers, with accelerated breakdown, spanwise undulations and dislocations. The loss of coherence associated with oblique vortex shedding and spanwise dislocations leads to reduced lift on straight bluff bodies (Prasad & Williamson 1997b). The same mechanisms appear to be responsible for the low amplitude lift intervals experienced by the downstream cylinder. For example, the event marked A in figure 10b corresponds to a time interval of localised low periodicity in the wake at  $z/D = 0$ , as seen in figure 9. Meanwhile, at various lower  $z/D$  locations, the wake exhibits strong quasi-periodic fluctuations at frequencies centered on  $f_{v3}$  during the same time interval.

Figure 12 shows the instantaneous pressure field in the flow at  $tU_0/D = 525$  for various  $z/D$  levels. There is substantial variation of the flow regimes along the span, even within relatively short spanwise distances. For instance, gap vortices form on opposite sides of the gap at  $z/D = 0$  and  $z/D = -2$ , shown in figure 12c and 12d, respectively. If we consider the pressure around the downstream cylinder, it is clear that the lift force on the cylinder cannot be in phase along the span, which lowers the total lift.

The above conclusion does not, however, directly explain the occurrence of the two



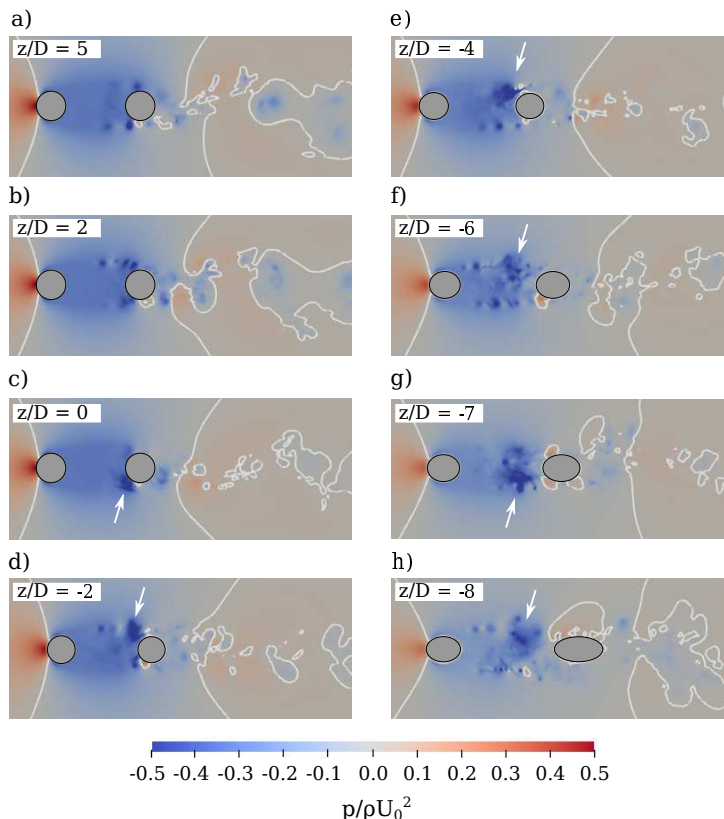


Figure 12: Instantaneous pressure field at various  $z/D$  levels, at  $tU_0/D = 525$ . The white contour line marks  $p/\rho U_0^2 = 0$ . The flow regime varies substantially with  $z/D$  and the formation of gap vortices (marked by white arrows) is clearly not in phase along the span. From the pressure distribution around the downstream cylinder, it is obvious that the lift force on the cylinder is also out of phase, which leads to low-amplitude total lift.

distinctive peaks in the drag and vertical forces on the upstream cylinder, seen in figure 10a. For straight tandem cylinders, the transition from reattachment to co-shedding is associated with a jump in the drag on the upstream cylinder (Igarashi 1981). Intuitively, if co-shedding occurred along larger portions of the curved span, this would increase the drag on the upstream cylinder. At  $tU_0/D = 525$  there is indeed one-sided co-shedding as high as  $z/D = -2$ , as shown in figure 12b, with  $f_{v3}$  as the dominant frequency of the surrounding time trace envelope (not shown for brevity). Because the vortices within the gap shedding region are to some degree aligned with the local curvature, a portion of the forces exerted on the upstream cylinder by these vortices will work in the vertical direction. This may be the reason why we also see vertical force peaks on the upstream cylinder simultaneously with the drag peaks.

There is an important difference between the peaks at  $tU_0/D \approx 525$  and  $tU_0/D \approx 800$ , and that is the behavior of the upstream cylinder lift. The former is preceded by a peak in  $C_{Lu}$ , whereas during the actual event, the lift amplitude is quite low for both cylinders. This corresponds well with the loss of spanwise coherence described above. The peak at  $tU_0/D \approx 800$ , however, is in-phase with a significant local peak in  $C_{Lu}$ . This indicates that the two peaks may have altogether different origins.

### 3.4. Development of the shear layers

From figure 3a, we see that shear layer vortices are shed along the entire straight vertical extension, and the shedding also persists along nearly the entire curved cylinder span. The inception point of the shear layer instability seems to move further upstream as we move downwards into the curved gap.

Figure 13 shows excerpts of the time history of band-pass filtered crossflow velocity fluctuations  $v'/U_0$  in the  $y/D < 0$  shear layer at various  $z/D$  levels, and these can be used to assess the behavior of the transition region. It is well known that the shear layer transition region in a straight single cylinder near wake exhibits random streamwise meandering (Prasad & Williamson 1997a), due to intermittent amplification of the shear layer instability by small-scale eddies in the recirculation region (Rai 2010). This implies that when point measurements are made in the shear layer close to the cylinder base, the shear layer instability manifests itself as short intervals of strong velocity fluctuations, such as the ones seen in figure 13. These fluctuations are conventionally called 'packets'. When the measurement point is moved downstream, the number of observed fluctuation packets increases, as well as the fluctuation amplitudes (Prasad & Williamson 1997a). In figure 13, the probe has the same distance to the upstream cylinder center for all  $z/D$  levels. As such, an increase in the number of packets and their amplitude indicates an upstream movement of the shear layer transition region.

Placing a second body in the wake of a cylinder has a stabilising effect on the shear layers. Previous studies have shown that a splitter plate (Cardell 1993) or a second cylinder (Aasland *et al.* 2022b) can lessen the meandering of the shear layer transition region, and move this region downstream. Oblique vortex shedding has a similar effect, and may delay the critical Reynolds number for inception of transition in the shear layers (Prasad & Williamson 1997a). The stabilising effect is related to the strength of the von Kármán vortices. Both oblique shedding and interference in the formation region weaken the vortex strength, which means that the strength of small-scale eddies in the recirculation region is lowered. Thus, there are fewer perturbations with sufficient strength to trigger the shear layer instability (Rai 2010).

In the present study, stabilising of the gap shear layers comes primarily from the presence of the downstream cylinder, whose effect is particularly strong within the reattachment region. From figures 13a - 13c, we see that along the straight vertical extension, the number of strong shear layer fluctuations is quite low. The number of fluctuations, their amplitude, and the duration of the packets grow into the lower gap. This effect is especially eye-catching between  $z/D = -4$  and  $z/D = -8$  (figure 13f - 13h), where gap shedding events gradually become more frequent. The upstream movement of the shear layer transition region is caused in part by the widening gap, decreasing the stabilising influence of the downstream cylinder, and in part by the increase of the vertical velocity component in the recirculation region of the upstream cylinder, as seen in figure 4b. The existence of a downdraft region towards the end of the gap means that shear layer vortices and other small eddies are to some degree convected downwards, where they may contribute to further amplification of the shear layer instability. A similar mechanism was observed by Gallardo *et al.* (2014) in the lower wake of a single convex curved cylinder.

The strongest fluctuations, in terms of amplitude and duration, are found at  $z/D = -8$ . Fluctuations at  $z/D = -11$  are not as strong, as seen in figure 13i, though they are more plentiful. A larger number of packets at  $z/D = -11$  makes sense, since the shear layers are no longer stabilised by the downstream cylinder at this level. At  $z/D = -8$ , there is still some influence from the downstream cylinder, which leads to more stable shear layers. The high amplitude of the fluctuations at  $z/D = -8$ , compared to  $z/D = -11$  is likely attributed to the

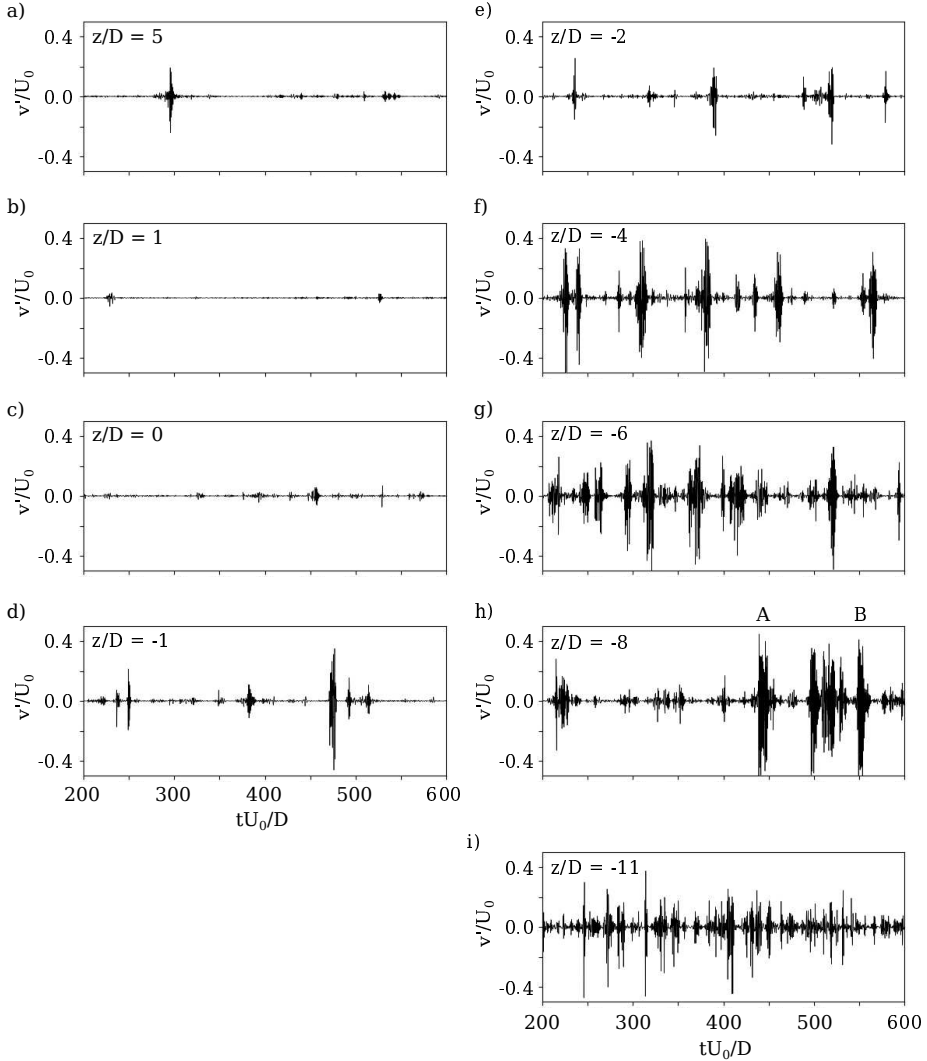


Figure 13: Time traces of the band-pass filtered crossflow velocity fluctuations  $v'/U_0$ , sampled at probe P3 in the upstream cylinder shear layer, at various  $z/D$ . The increase of fluctuations with decreasing  $z/D$  correspond to an upstream movement of the shear layer transition region in the gap. Probe P3 is quite close to the upstream cylinder base (see figure 2), so that few fluctuations are expected along the straight vertical extension. The low and high cutoff frequencies of the band-pass filter were  $fD/U_0 = 0.45$  and  $3.00$ , respectively.

strength of the large-scale gap vortices at this level. These vortices are significantly stronger than the more streamwise-oriented vortices at  $z/D = -11$ .

Interestingly, some of the strongest packets at  $z/D = -8$  (marked A and B in figure 13h) are felt in both shear layers, as shown in figure 14. Shear layer amplification events are normally not in phase for a straight single cylinder (Rai 2010). That events A and B are in phase may be the result of particularly strong gap shedding events. Gap shedding increases entrainment into the recirculation region of the upstream cylinder, and may thus amplify the shear layer instability through strong small-scale eddies. At this level, the vertical velocity component is significant. Figure 14b shows that  $v'/U_0$  and  $w'/U_0$  have very similar amplitudes, and that

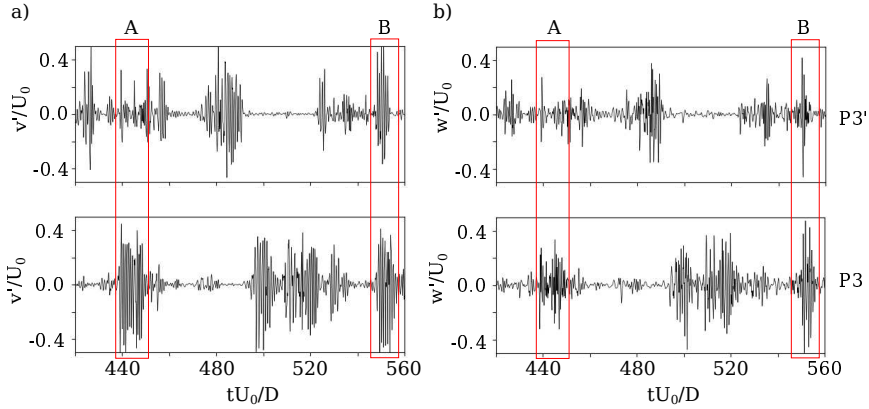


Figure 14: Time traces of the band-pass filtered a) crossflow velocity fluctuations  $v'/U_0$  and b) vertical velocity fluctuations  $w'/U_0$ , sampled at probes P3' and P3 in the upstream cylinder shear layers, at opposite sides of the gap at  $z/D = -8$ . We see that events A and B, marked in figure 13h, are felt in both shear layers. This is believed to be caused by strong gap shedding events.

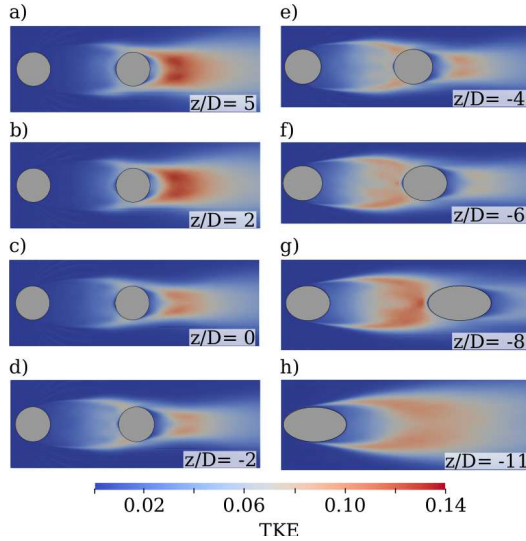


Figure 15: Turbulent kinetic energy (TKE) at various  $z/D$ . TKE is strongest in the near wake along the straight vertical extension. As the effective gap ratio widens with decreasing  $z/D$ , the local maxima of TKE move into the gap. This reflects the change of spanwise localised flow regime from reattachment to gap shedding.

events A and B are significant in the traces of both velocity components. Strong gap shedding events in the lower gap generally coincide with increased vertical velocity magnitudes, and upstream movement of the downdraft region. It is possible that this influences the shear-layer instability so that amplification occurs in phase across the gap. Event B, which is more symmetric across the gap than event A, also has stronger vertical velocity amplitudes. Unfortunately, we do not have visualisation of the flow field for events like A and B, so we cannot conclude firmly.

At the same time as the transition region moves upstream in the gap shear layers, the near wake vortices gradually weaken due to the increasing axial flow. This is reflected in the spanwise development of the turbulent kinetic energy (TKE), displayed in figure 15. The

maxima of TKE are found along the straight vertical extension. However, the energy quickly declines in the near wake for  $z/D \leq 2$ , and the local maxima of TKE gradually move into the gap. In the gap, the highest levels of TKE are found in the vicinity of  $z/D = -8$ , as shown in figure 15g. This agrees well with our previous observations regarding the strength of the gap vortices in this spanwise region.

Unsurprisingly, the spanwise development of the gap shear layers differs substantially from the shear layers behind a single convex curved cylinder, due to the presence of the downstream cylinder. In the study of Gallardo *et al.* (2014), the shear layer fluctuations were strongest, and occurred most commonly, in the lower wake and, secondly, along the straight vertical extension, at the  $z/D$  values that are equivalent to  $z/D = 3$  and  $z/D = -10$  in the present study. The fluctuations at the  $z/D$  values corresponding to  $z/D = -2$  and  $z/D = -6$  were substantially weaker. This was attributed to the local inclination of the wake vortices. In the present study, as we have seen, this region has an increase in the fluctuations compared to the straight vertical extension. The effect of local inclination of the gap vortices seems to be overshadowed by the effect of the downstream cylinder and the tandem flow regimes. It may be that the oblique shedding in the wake has an effect on the shear layers of the downstream cylinder, but this is impossible to evaluate, due to interference from the upstream cylinder shear layers.

The shear layer frequency  $f_{sl}$  of straight tandem cylinders in the reattachment regime does not differ from that of a single cylinder at the same Reynolds number (Aasland *et al.* 2022b). In the present study, however,  $f_{sl}$  is affected by the curvature. Crossflow velocity spectra sampled in the gap shear layer, at probes P1-P4 (see figure 2), are given in figure 16. The broad-banded main peak of the shear layer frequency, centered on  $f_{sl1}D/U_0 \approx 1.07$ , remains nearly constant along the straight vertical extension, down to  $z/D = -1$ . This value is similar to  $f_{sl}$  in the gap of straight tandem cylinders at  $Re = 4200$  and  $L/D = 2$  (Xu & Zhou 2004). In the curved part of the gap, however, there is a gradual shift towards higher frequencies down to  $z/D \approx -4$ , with a main peak  $f_{sl2}D/U_0 \approx 1.3$  followed by a decrease towards  $f_{sl1}$ . At  $z/D = -6$ ,  $f_{sl1}$  and  $f_{sl2}$  co-exist, and at  $z/D = -11$ , the shear layer frequencies consist of one broad-banded peak centered on  $f_{sl1}$ .

In the study of Gallardo *et al.* (2014), the shear layer frequency along the straight vertical extension corresponds well with results from straight single cylinder studies at a similar Reynolds numbers (Norberg 1987; Dong *et al.* 2006). Downwards along the curved span, however, there is a gradual transition to a lower frequency. As we have just seen, the situation is very different in the present study. While  $f_{sl}$  seems to decrease with axial flow for a single convex curved cylinder, there is no obvious relation between the shear layer frequency and the axial flow in the present study.  $f_{sl2}$  is first detected at a  $z/D$  level where there is still primarily upwelling in the gap, as seen in figure 4b. Although this frequency dominates where the vertical velocity increases rapidly, its relative importance declines again in the region of maximum downdraft. This phenomenon may be related to interaction with the primary instability in the wake, and will be further discussed in section 4.

Along the straight vertical extension, the difference-frequency of the shear layer and von Kármán shedding,  $f_\Delta = f_{sl1} - f_{v1}$ , is large, indicating non-linear interaction between the two (Miksad *et al.* 1982). In figure 16a, we see that the difference-frequency grows with  $x/D$ , so that its energy is higher than that of  $f_{sl1}$  at probe P4, towards the end of the gap. This is consistent with the findings of Kourta *et al.* (1987) for a single straight cylinder at subcritical Reynolds numbers. Beyond  $z/D = -1$ , non-linear interaction is not easily discernible in the curved part of the gap.

The shear layers of the downstream cylinder are buffeted by shear layer vortices from the gap shear layers, whose strength, coherence and frequency depend on  $z/D$ . Figure 17 shows the crossflow velocity spectra sampled at probes P5-P7, located in the downstream cylinder

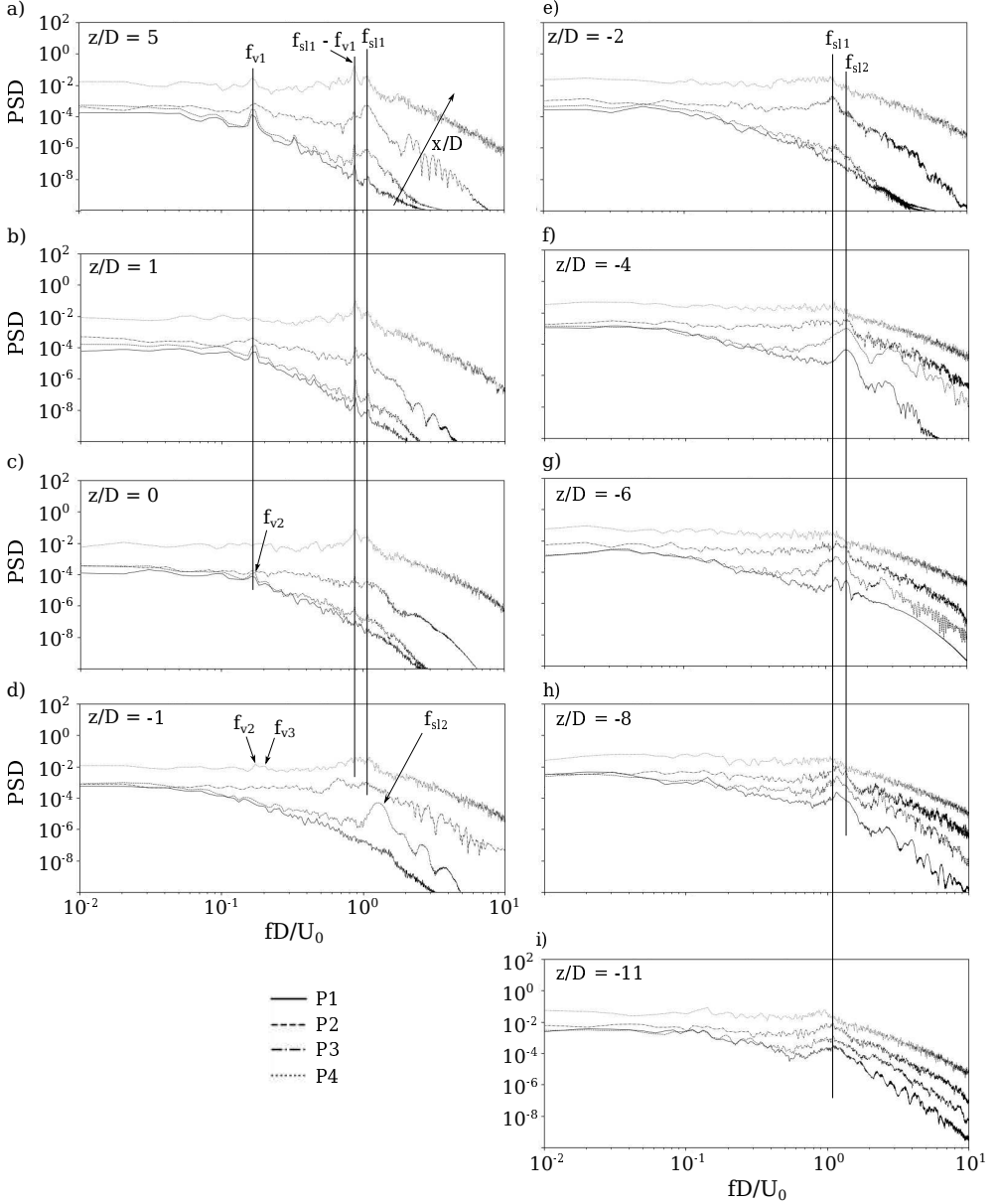


Figure 16: Spectra of the crossflow velocity  $v/U_0$  sampled in the gap shear layer at various  $z/D$ , at probes P1-P4 (see figure 2).  $f_{sl}$  is nearly constant along the straight vertical extension, but changes to a slightly higher value,  $f_{slc}$ , in the curved gap.  $f_{slc}$  varies somewhat along the span. The inception point of the KH instability moves upstream in the shear layer as we move downwards in the gap, due to an increased effective gap ratio and triggering by the vertical velocity. This is also shown by the time traces in figure 13. There is significant non-linear interaction between the shear layer frequencies and the primary vortex shedding frequency and its harmonics.

shear layer. We see that the peaks become increasingly broad banded in the lower wake, as the shear layer transition region in the gap moves further upstream. This corresponds well with the results of Khabbouchi *et al.* (2014), who found that increasing the free-stream turbulence increased the bandwidth of the shear layer frequency peak. The upstream buffeting also

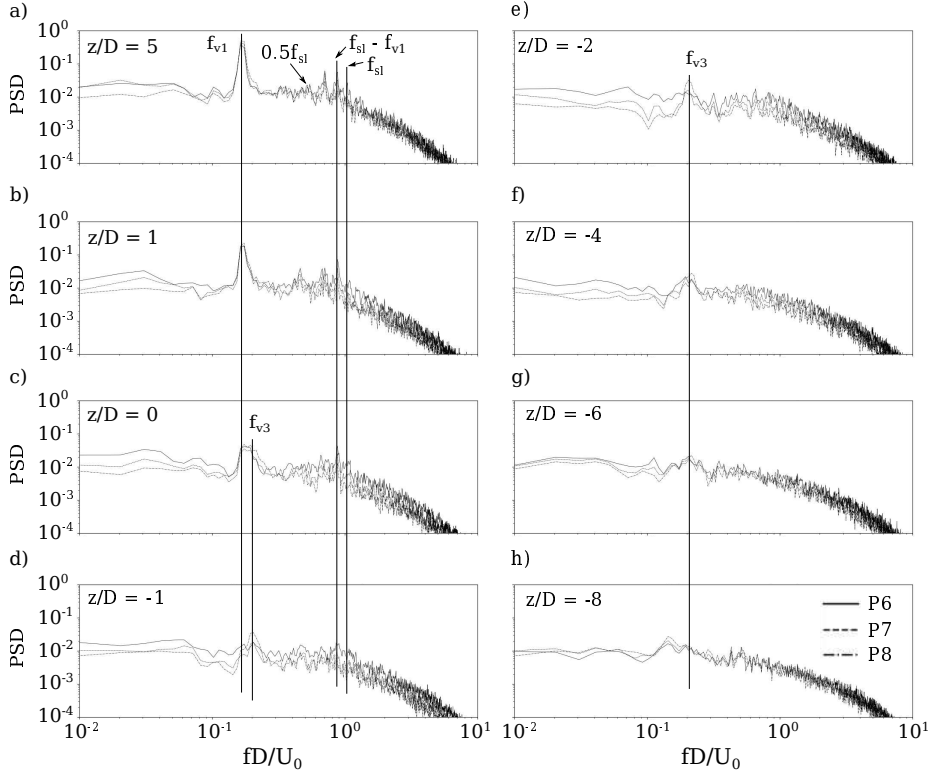


Figure 17: Spectra of the crossflow velocity  $v/U_0$  sampled in the downstream cylinder shear layer (probes P6-P8, see figure 2) at various  $z/D$ .

means that there is very little difference in the spectral energy levels at the probes along the wake shear layers, as opposed to the gap shear layers where the inflow is nearly smooth.

In figures 17a-17d, we see that non-linear interaction, indicated by the difference-frequency peak, occurs along the same range of  $z/D$  as in the gap shear layer. At  $z/D = 5$ , in figure 17a, the subharmonic of the shear-layer frequency is seen. The occurrence of the subharmonic is associated with shear-layer vortex pairing (Ho & Huang 1982). Looking at figure 6a, it is easy to see that pairing is possible in the overshooting gap shear layer at  $z/D = 5$ , as well as at  $z/D = 1$  (figure 6b). Here, the streamwise distance between the shear-layer transition and the merging of the upstream and downstream shear layers is sufficiently long to permit pairing, in accordance with the observations of Cardell (1993). This is not the case with the symmetric reattachment seen in figures 6c - 6e. Intuitively, shear layer vortex pairing might also occur further down in the curved gap, when the transition region moves upstream, similar to straight tandem cylinders at a higher subcritical Reynolds number (Aasland *et al.* 2022b). However, the overall turbulence level in this region makes it hard to distinguish the subharmonic in the spectra, as seen in figures 17f - 17h. Pairing events at  $z/D = 1$  have been recorded, and some of these are shown in figure 18.

### 3.5. Flow modes and the interaction between them

The presence of mode switches in the flow has been established through examination of the force time traces and crossflow velocity spectra, as well as flow visualisations (for example in the snapshots at  $z/D = -11$  in figure 7). In the following, we examine the characteristics

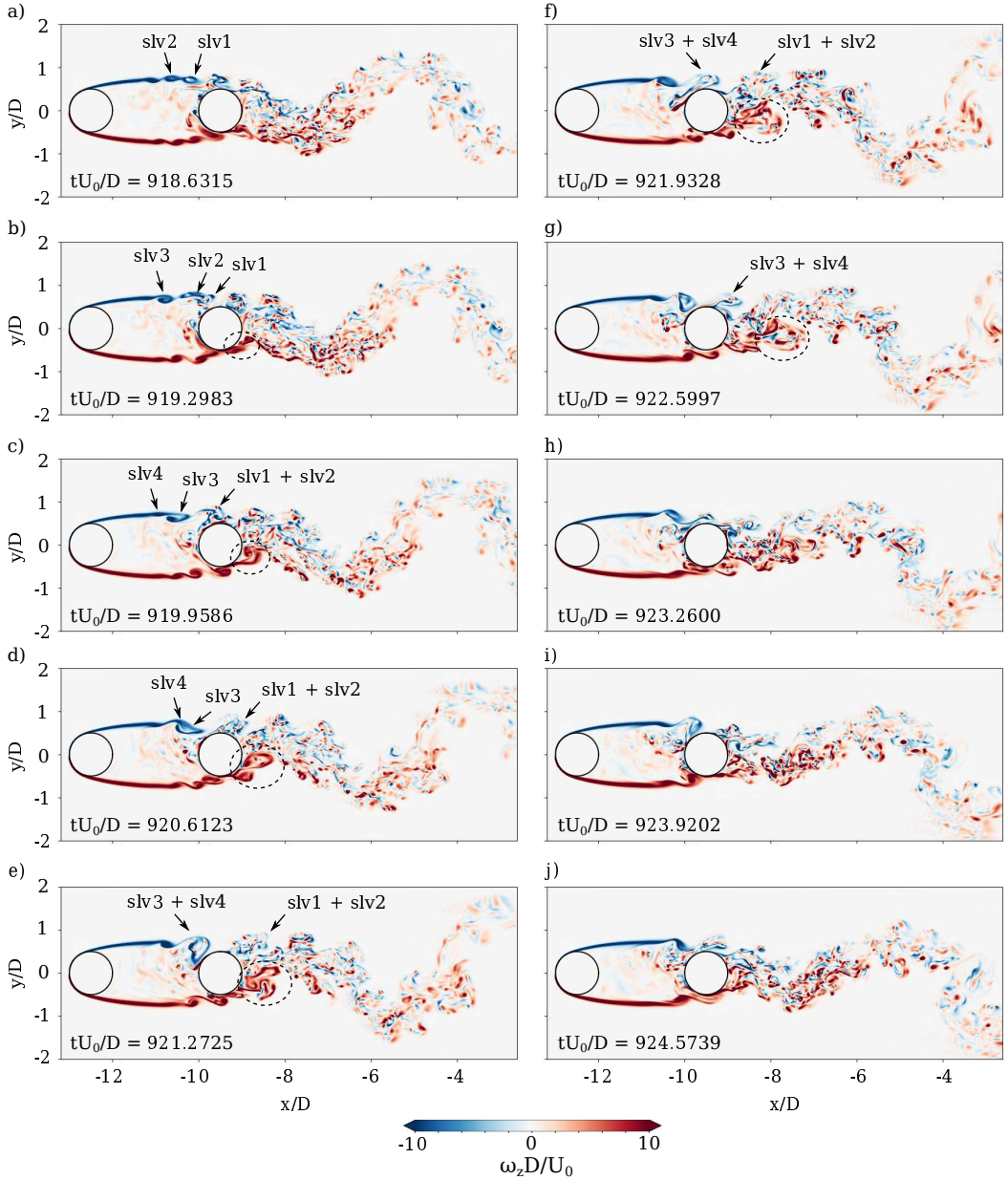


Figure 18: Temporal development of the flow field at  $z/D = 1$ , visualised by the spanwise vorticity. Pairing of shear layer vortices occurs twice during the depicted time interval. First the vortices  $slv1$  and  $slv2$  undergo pairing between a) and c).  $slv3$  and  $slv4$  subsequently pair, between c) and e). The paired structures are convected into the near wake. Between h) and i), there is a switch from alternating to symmetric reattachment. This mode change occurs simultaneous with a decrease of the global lift force on the downstream cylinder, as shown in figure 10b. In panels b)-g) we see that shear layer vortices from the upstream cylinder are fed directly into the near wake so that the forming wake vortex consists primarily of such vortices (dashed oval). This may affect the shedding frequency.



of these mode switches and how they influence other co-existing regimes along the cylinder span.

Our flow visualisations indicate that loss of spanwise coherence discussed in section 3.3 results from one or several mode switches. At  $z/D = 1$ , around  $tU_0/D = 923.5$ , we observe a switch from strong to weak wake vortex shedding, accompanied by a narrower wake width. This is clearly shown in figure 18h - 18j, as well as in supplementary movie 2. The switch directly precedes a reduction of the global downstream lift amplitude, as shown in figure 10b. When the weak shedding begins, the shear layers become more symmetrically reattached, and the shear layer instability in both shear layers appears to be fairly synchronized in both time and streamwise position.

Meanwhile, at other spanwise locations, different types of mode switches occur simultaneously, though none appear to be as persistent in time as the one observed at  $z/D = 1$ . At  $z/D = -1$ , where the basic flow regime is symmetric reattachment there is a significant reduction of the shear layer instability (see figure 19b), around the time of the mode switch at  $z/D = 1$ . The shear layers remain laminar, and shear layer vortices only form at the very end of the gap. This scenario lasts for approximately one vortex shedding period, after which the shear layer transition region moves upstream in the gap. All simultaneous mode variations cannot be displayed herein, but supplementary movies (see movies 3-5) show the development of the flow field in additional  $z/D$  planes. In the range  $-4 \leq z/D \leq -1$ , a temporary weakening of the wake vortex shedding is found.

Mode switches along the span appear to be closely related to the variations of the vertical velocity component, which gives a clue as to how modes may interact and influence each other. In the curved part of the gap, both positive and negative vertical velocities exist at all  $z/D$  levels, meaning information can be carried both upwards and downwards along the span. The mode switch described above, for instance, is directly preceded by a strong gap shedding event observed at  $z/D = -6$  and  $z/D = -8$ , which influences the vertical velocity component  $w/U_0$  in the gap region. At the same time, the near wake at  $z/D = -11$  undergoes a massive widening.  $w/U_0$  is generally positive in the upstream cylinder shear layers. Towards the gap centerline, however, a downdraft region develops, growing larger in the lower gap.

At  $z/D = -1$ , upwelling is prevalent in the gap, except in a small region of downdraft near the front face of the downstream cylinder. Figure 19 shows a gradual upstream shift of this downdraft region, which occurs around the same time as the previously described mode switch. At the same time as moving upstream, this region slowly diffuses and breaks up into smaller regions (figure 19ci). The gap shear layers subsequently undergo a distinct change from being relatively calm and stable to a state of strong instability, with a significant upstream shift of the transition region, shown in figure 19d. We see that amplification of the shear layer instability occurs when smaller downdraft regions move into contact with the shear layers.

If we consider the inviscid vorticity equation

$$\frac{D\boldsymbol{\omega}}{Dt} = (\boldsymbol{\omega} \cdot \nabla) \mathbf{u} \quad (3.1)$$

and its spanwise component

$$\frac{D\omega_z}{Dt} = \underbrace{\omega_x \frac{\partial w}{\partial x} + \omega_y \frac{\partial w}{\partial y}}_{\text{tilting}} + \underbrace{\omega_z \frac{\partial w}{\partial z}}_{\text{stretching}} \quad (3.2)$$

we see that the downdraft  $w$  can amplify the spanwise vorticity of the shear layer in several ways. All three vorticity components are non-zero in the majority of the gap and wake flow,

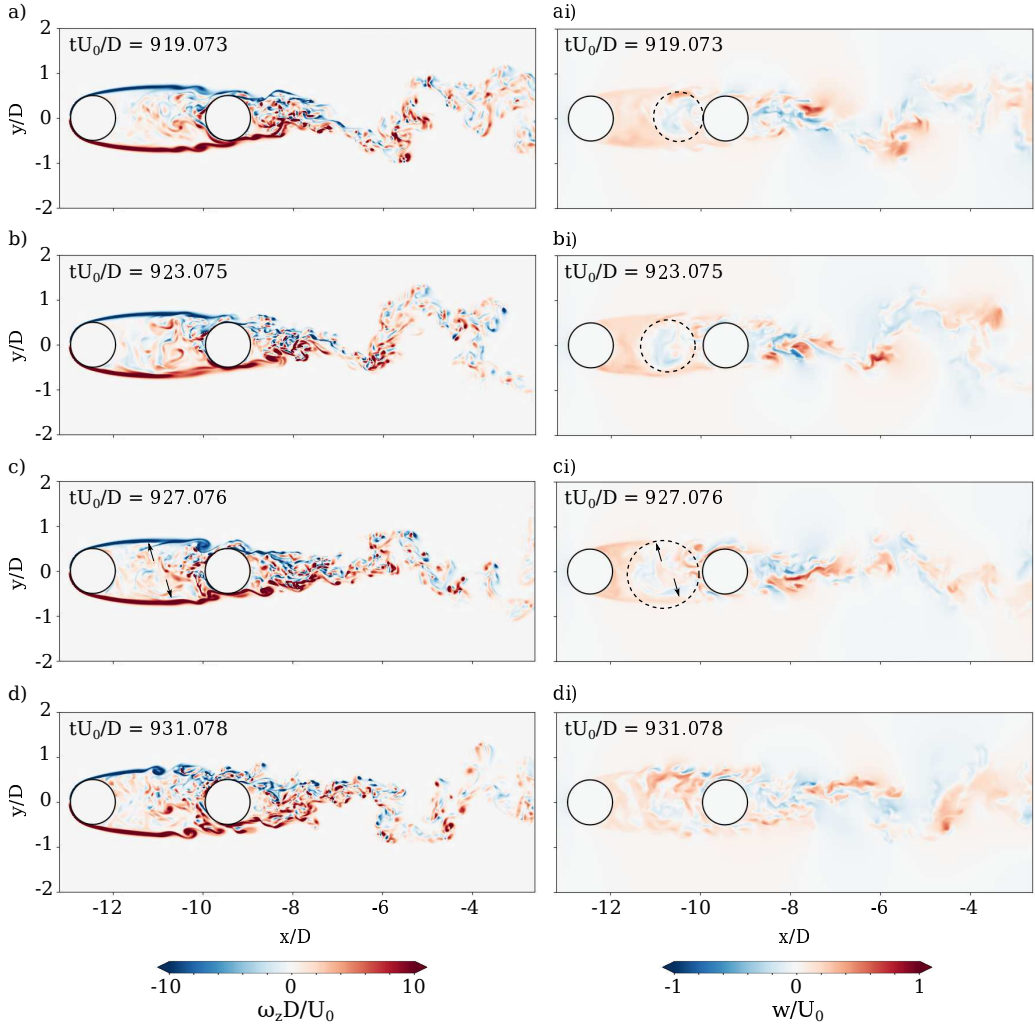


Figure 19: Instantaneous spanwise vorticity (left) and vertical velocity (right) at  $z/D = -1$ . The downdraft region, marked by a dashed circle, along the downstream cylinder front face meanders upstream between ai) and bi) and breaks up into smaller regions. In ci), some of these small downdraft regions come into contact with the shear layer near the black arrows, and trigger the Kelvin-Helmholtz instability. This causes the shear layer transition region to shift upstream, as seen in d). The shown time interval covers a little more than two vortex shedding cycles.

so that neither of the right-hand side terms of equation 3.2 are zero unless the gradients of the vertical velocity are zero. As seen in figure 19ai, the vertical velocity is positive in the larger part of the gap region at  $z/D = -1$ , with slightly higher values towards the outer part of the shear layer. When a downdraft region comes into contact with a shear layer region with positively signed vertical velocity (such as in figure 19ci), this creates a strong gradient of the vertical velocity in the  $y$ -direction. We also see from figure 19ci, that there must be a gradient of the vertical velocity in the  $x$ -direction, albeit weaker. These two vertical velocity gradients contribute to amplification of the shear layer instability through vortex tilting (first two terms of equation 3.2). While the vertical velocity gradient in  $z$ -direction may not be very strong, the spanwise vorticity certainly is, meaning that a significant contribution to the

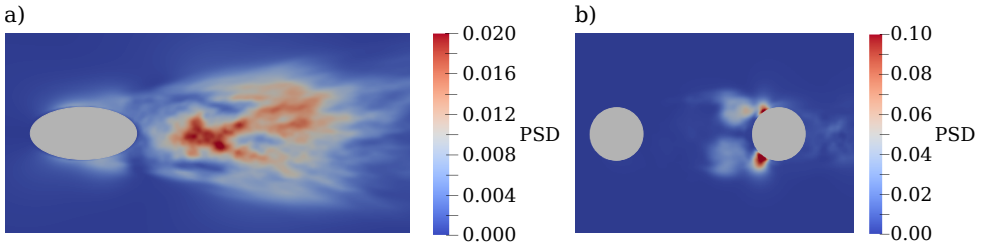


Figure 20: Spectral energy map of  $fU_0/D = 0.010625$  at a)  $z/D = -11$  and b)  $z/D = -1$  (see figure 2b). A cluster of low-frequency spectral energy in the vortex formation region at  $z/D = -11$  implies a slow variation of the formation length. This type of mode variation is visualised in figure 7. The mode variation in the lower gap causes modulation of the vertical velocity, which in turn influences the position of the shear layer transition region, as shown in figure 19

shear layer amplification can also come from vortex stretching (last term of equation 3.2). This is in keeping with the results of Rai (2010) regarding amplification of the shear layer instability.

The slow meandering of the downdraft region observed in figure 19 corresponds with the results of Aasland *et al.* (2023b) for curved tandem cylinders at  $Re = 500$ . In that study, it was suggested that a low-frequency variation of the vortex formation length in the lower part of the gap influenced the downdraft along the front face of the downstream cylinder. Such low-frequency variation in the lower gap is indicated by the flow visualizations in figure 7, as well as the spectral analysis herein. Figure 20 shows maps of the spectral density of  $fU_0/D = 0.010625$ , captured during the simulations by in-situ FFT analysis. At  $z/D = -11$ , the spectral energy is clustered in the vortex formation region, whereas at  $z/D = -1$ , the energy is clustered near the reattachment points and in the shear layer towards the end of the gap. We have seen that the vertical velocity in the gap impact the stability of the gap shear layers, and that this vertical velocity is coupled with low-frequency mode variations in the lower gap. Together, these results imply that the vortex dynamics of the lower gap may influence the shear layer instability at higher  $z/D$  levels, through modulation of the vertical velocity. Furthermore, these dynamics may influence the near wake, since an upstream shift of the transition region in the gap shear layers leads to increased fluid entrainment into the wake vortices, similar to free-stream turbulence (Khabbouchi *et al.* 2014).

The modulation of the vertical velocity component in the low- $Re$  study of Aasland *et al.* (2023b) also contributed to low-frequency quasi-periodic asymmetry of the large-scale gap vortices, so that the gap recirculation region was biased towards one side for several vortex shedding periods. The bias switched with a period of some 100 time units. A similar type of asymmetry is seen in the present study, corresponding to one-sided formation and/or shedding, depending on the effective gap ratio. The obvious quasi-periodicity observed in the previous study is not present, however, due to the co-existence of several modes at the same spanwise location (such as at  $z/D = 0$ ). Time traces taken at the gap centreline, directly upstream of the downstream cylinder front face (probe P5) are presented in figure 21. At  $z/D = 1$ , in figure 21b, a similar bias as for  $Re = 500$ , with approximately the same period is observed. The behavior is not consistent, however, as other flow modes intermittently become dominant. Gap asymmetry is most prominent in the range  $-4 \leq z/D \leq -1$ , as seen in figures 21d - 21f. This is where one-sided co-shedding starts to occur frequently. At  $z/D = -6$ , in figure 21g, we see longer intervals of non-biased  $v/U_0$ , which is indicative of roll-up of both gap shear layers. Finally, at  $z/D = -8$ , roll-up of both shear layers is the dominant flow mode in the gap, as seen in figure 21h.

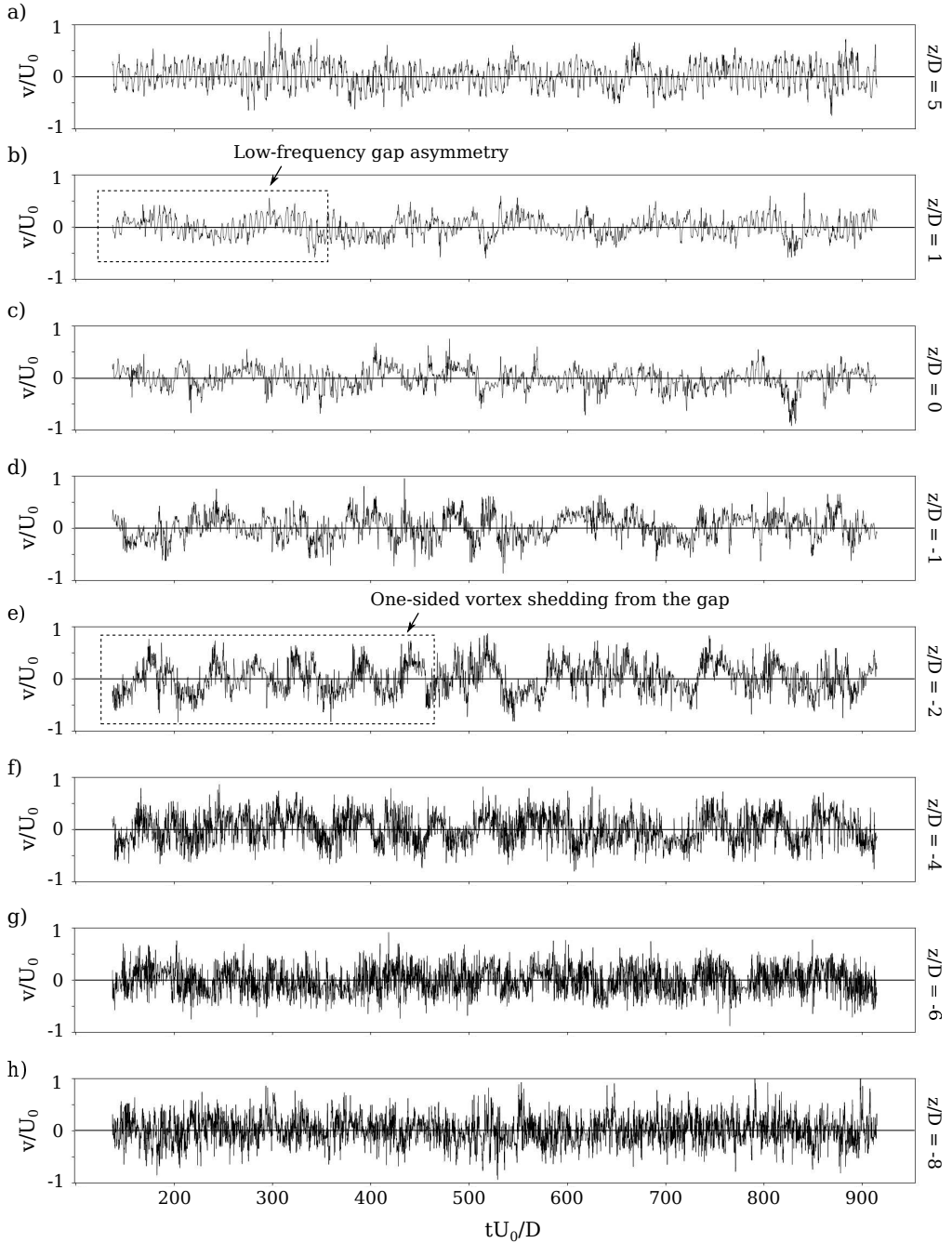


Figure 21: Time traces of the crossflow velocity  $v/U_0$  on the gap centreline (probe P5) at various  $z/D$  locations. Bias of the time trace away from the centreline occurs for several vortex shedding periods is observed along the entire gap, and indicates one-sided formation or shedding of gap vortices. Due to the co-existence of flow modes, the bias is intermittent.

#### 4. Discussion

We have seen that the present study has several features in common with convex curved tandem cylinders at  $Re = 500$  (Aasland *et al.* 2023b), though transition to turbulence in the shear layers has a significant impact. An important difference between the gap and wake dynamics of the present and previous studies, however, is that for  $Re = 500$  the vortex formation is entirely dominated by the frequency of the vortices in the upper wake, so that  $St = 0.143$  dominates along the entire span. For  $Re = 3900$ , on the other hand, there is a gradual shift of the dominant frequency along the span, and this is reflected in the instantaneous flow field. Three separate main modes have been identified, each with their distinct dominant frequency. We have seen that although these modes are localized in the sense that one will dominate along a given spanwise section, they do co-exist. Given that alternating overshoot/reattachment can also be a bi-stable flow regime for  $L/D = 3$ , both for straight (Aasland *et al.* 2023a) and curved tandem cylinders (Aasland *et al.* 2023b), this result implies that there is no truly stable flow regime anywhere along the span.

There is communication along the span by means of the vertical velocity component, which causes local regimes to interact and influence each other. One can readily imagine that an unstable local regime might switch to its closest neighbour regime when perturbed. At  $z/D = 1$ , for example, that regime is symmetric reattachment, which occurs near the transition between the straight vertical extension and the curved cylinders. Thus, a mode switch between alternating overshoot/reattachment and symmetric reattachment is observed. Such a mode switch has not previously been reported for straight tandem cylinders, nor was it seen for curved tandem cylinders at a lower Reynolds number. Since the switch seems closely related to the instability of the shear layers, it cannot be expected to occur at a Reynolds number at which the shear layers are stable. There is, however, no reason to believe that a bi-stable switch between alternating overshoot/reattachment and symmetric reattachment should be non-existing for straight tandem cylinders at a subcritical Reynolds number, considering the variation of mode switches already observed (Igarashi 1981; Xu & Zhou 2004; Kitagawa & Ohta 2008; Aasland *et al.* 2023a).

We have seen that the shear layer instability in the gap may have a profound influence on the near wake vortex dynamics. In light of this observation, it is an interesting question whether the reverse is true; i.e. do the large-scale vortex dynamics influence the shear layer instability in the gap, and if so, in what way? Kourta *et al.* (1987) found that non-linear interaction between the primary instability and the shear layer instability persisted even with a splitter plate in the wake. However, the basic shear layer frequency was not changed, contrary to the primary instability, which exhibits a lower dominant frequency when a splitter plate is introduced. This result indicated that there was no direct feedback from the von Kármán vortex shedding. The same conclusion was drawn by Aasland *et al.* (2022a), when comparing the shear layer frequencies for straight single and tandem cylinders at  $Re = 10^4$ . This may not be the case in the present study, however, due to the cylinder curvature.

To shed more light on this matter, we consider first possible reasons why the shear layer frequency decreased in the lower gap in the single convex curved cylinder study of Gallardo *et al.* (2014). The results showed a slight decrease in  $f_v$  in the lower wake, which coincided with weakening of the wake vortices. If  $f_v$  and  $f_{sl}$  are de-coupled, like in the splitter plate case, a decrease of  $f_v$  cannot be the cause of a decrease in  $f_{sl}$ . The change in  $f_{sl}$  may, however, be related to the axial flow itself, either along the cylinder front face, or in the near wake. In the case of straight single cylinders,  $f_{sl}$  decreases with decreasing Reynolds number (Bloor 1964; Prasad & Williamson 1997a). Like Prasad & Williamson (1997a), we assume that the shear layer frequency scales with the velocity outside the boundary layer at separation  $U_{sep}$ , and the momentum thickness of the shear layer at the point where the K-H

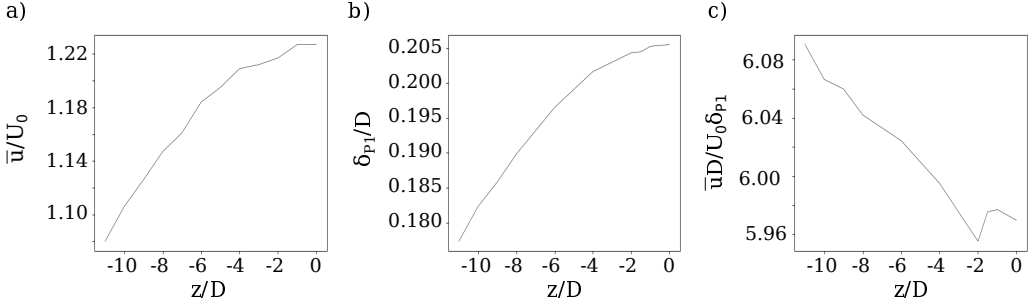


Figure 22: Spanwise variation of a) time-averaged streamwise outside the boundary layer at separation on the upstream cylinder, b) non-dimensional momentum thickness at the probe P1,  $\delta_{p1}/D$  and c) the ratio between  $\bar{u}/U_0$  and  $\delta_{p1}/D$ .

instability is first triggered  $\delta_{kh}$ , so that

$$f_{sl} \sim \frac{U_{sep}}{\delta_{kh}}. \quad (4.1)$$

Note that  $\delta_{kh}$  is not the momentum thickness where transition to turbulence occurs, but the thickness at the inception of the linear K-H instability, in accordance with the definition by Sato (1965). From 4.1, we gather that the decrease of  $f_{sl}$  downwards along the span in the study of Gallardo *et al.* (2014) should be related to either a decrease in the velocity outside the boundary layer, which may occur due to curvature-induced axial flow, or an increase in momentum thickness. Such data are not presented in that study, however, so we cannot draw any firm conclusions.

In the present study, however, we can calculate the momentum thickness by

$$\delta_{kh} = \int_0^\infty \frac{u(y)}{U_\infty} \left(1 - \frac{u(y)}{U_\infty}\right) dy \quad (4.2)$$

where  $U_\infty$  is the velocity just outside the shear layer. With the available data, we cannot accurately determine the position of inception of the linear K-H instability, so we have used probe P1 as the reference position. The drawback of this method is that the transition region moves upstream with decreasing  $z/D$ , which must necessarily have an effect on the momentum thickness at probe P1.

The time-averaged velocity outside the boundary layer of the upstream cylinder at separation and the calculated momentum thickness  $\delta_{p1}$  are shown in figure 22a and 22b, respectively. We see that both variables decline with decreasing  $z/D$ . The ratio between  $\bar{u}/U_0$  and  $\delta_{p1}/D$  is plotted in figure 22c. Apart from the dip at  $z/D = -2$ , there is a steady increase downwards into the gap. According to equation 4.1, there should have been an increase in the frequency. From section 3.4, however, we recall that the shear layer frequency increases between  $z/D = -1$  and  $z/D = -4$ , and then decreases to its former value into the lower curved gap. Even with the uncertainty added from using P1, it is clear that equation 4.1 cannot explain the spanwise variation of the shear layer frequency in the present study. Thus, the explanation must be found elsewhere.

A notable feature of the shear layer frequencies herein is that they are all very close to the higher harmonics of the von Kármán vortices, and they seem to be tied to the dominant local Strouhal number. The increase of the gap shear layer frequency along the curved cylinder span follows the Strouhal number shift towards  $f_{v3}$ , so that the relative importance of  $f_{sl2}$  grows. When the strength of  $f_{v3}$  diminishes in the more broad banded cross velocity spectra in the lower wake (see figure 8h), the strength of  $f_{sl2}$  declines in favor of  $f_{sl1}$ . These observations

indicate that the large-scale vortex dynamics truly may exercise an influence on the shear layer instability, possibly through fluctuations in the pressure field. One may hypothesise that the gap shear layers are more susceptible to external forcing in the present case, compared to straight tandem cylinders, because of the de-stabilising effect of the vertical velocity demonstrated in section 3.5.

## 5. Concluding remarks

In the present study, turbulent flow around curved tandem cylinders has been studied for the first time, by means of DNS. The convex configuration was considered, with a nominal gap ratio of  $L/D = 3$ . The Reynolds number was  $Re = 3900$ .

There is spanwise variation of flow regimes, and three distinct Strouhal numbers are found in the flow, corresponding to alternating overshoot/reattachment, symmetric reattachment and co-shedding. This situation is quite different from a single convex curved cylinder and convex curved tandem cylinders at a lower Reynolds number, where the vortices in the upper wake govern the flow so that only one dominant frequency is found. An important finding is that though one of the three modes is normally dominant along a given spanwise section, a minimum of two modes co-exist along the majority of the span. Given that alternating overshoot/reattachment is a bi-stable flow regime for  $L/D = 3$ , this implies that there is no truly stable flow regime anywhere along the span. Near the transition between the curved cylinder and the straight vertical extension, all three modes co-exist and have approximately equal spectral densities, indicating multi-stability. A mode switch between alternating overshoot/reattachment and symmetric reattachment is directly observed. This type of bi-stability has not been reported for straight tandem cylinders.

Random alterations between parallel and oblique shedding are found, and these are closely connected to spanwise vortex dislocations in the wake, caused by mode switches. The dislocations may occur along the entire height of the wake, and result in extended time intervals of low-amplitude lift fluctuations on the downstream cylinder.

At  $Re = 3900$ , transition to turbulence initiates in the shear layers, and a key objective of the present investigation has been to characterise the effect of the shear layer instability and on this intrinsically complex flow field. Detailed numerical results reveal that there are complex interactions between the primary instability, the shear layer instability, and the alterations between different tandem cylinder flow modes along the span. Amplification of the shear layer instability in the gap results in increased forcing on the downstream cylinder shear layers, which may in turn influence the wake vortex formation process and trigger an intermittent switch of tandem cylinder flow regimes. Conversely, the spectral analysis indicates that there may be direct feedback from the vortices in the near wake to the shear layer instability, so that the shear layer frequency is to some degree governed by the local dominant Strouhal number.

The axial velocity in the gap plays an integral role in the interaction between the shear layer instability and the flow modes, because it contributes to amplification of the shear layer instability through vortex tilting and stretching. In particular, the downdraft region along the front face of the downstream cylinder exhibits slow streamwise meandering, governed by the low-frequency variation of the vortex formation length in the lower gap region. When this downdraft region travels upstream in the gap, it may trigger early transition to turbulence in the shear layer, and thus modify the the gap and near wake flow field. This means that the dynamics of the lower gap region may in fact influence the shear layer instability much higher up in the gap.

## 6. Funding and declaration of interests

This work is supported by the Research Council of Norway through the Public Sector PhD Scheme, and the National Public Roads Administration, where the first author is an employee. Computational hours were granted by the Norwegian HPC project NN9191K. The authors report no conflict of interests.

## Supplementary material

Supplementary movies are available online.

## REFERENCES

- AASLAND, T. E., PETTERSEN, B., ANDERSSON, H. I. & JIANG, F. 2022a Flow around curved tandem cylinders. *J. Fluids Eng.* **144** (12), 121301.
- AASLAND, T. E., PETTERSEN, B., ANDERSSON, H. I. & JIANG, F. 2022b Revisiting the reattachment regime: A closer look at tandem cylinder flow at  $Re = 10\,000$ . *J. Fluid Mech.* **953**, A18.
- AASLAND, T. E., PETTERSEN, B., ANDERSSON, H. I. & JIANG, F. 2023a Asymmetric cellular bistability in the gap between tandem cylinders. *J. Fluid Mech.* **966**, A39.
- AASLAND, T. E., PETTERSEN, B., ANDERSSON, H. I. & JIANG, F. 2023b Flow topology in the gap and wake of convex curved tandem cylinders. *J. Fluid Mech.* **976**.
- AFGAN, I., KAHIL, Y., BENHAMADOUCHE, S., ALI, M., ALKAABI, A., BERROUK, A. S. & SAGAUT, P. 2023 Cross flow over two heated cylinders in tandem arrangements at subcritical Reynolds number using large eddy simulations. *Int. J. Heat Fluid Flow* **100**, 109115.
- ALAM, M. M. 2014 The aerodynamics of a cylinder submerged in the wake of another. *J. Fluids Struct.* **51**, 393–400.
- ALAM, M. M., RASTAN, M. R., WANG, L. & ZHOU, Y. 2022 Flows around two nonparallel tandem circular cylinders. *J. Wind Eng. Ind. Aero.* **220**, 104870.
- BEHARA, S., CHANDRA, V. & PRASHANTH 2022 Three-dimensional transition in the wake of two tandem rotating cylinders. *J. Fluid Mech.* **951**, A29.
- BLOOR, S. 1964 The transition to turbulence in the wake of a circular cylinder. *J. Fluid Mech.* **19**, 290–301.
- CARDELL, G. S. 1993 Flow past a circular cylinder with a permeable wake splitter plate. PhD thesis, California Institute of Technology.
- CARMO, B. S., MENEGHINI, J. R. & SHERWIN, S. J. 2010 Possible states in the flow around two circular cylinders in tandem with separations in the vicinity of the drag inversion spacing. *Phys. Fluids* **22**, 054101, 1–7.
- DONG, S., KARNIADAKIS, G. E., EKMEKCI, A. & ROCKWELL, D. 2006 A combined direct numerical simulation - particle image velocimetry study of the turbulent near wake. *J. Fluid Mech.* **569**, 185–207.
- DURANTE, D., GIANNOPOULOU, O. & COLAGROSSI, A. 2021 Regimes identification of the viscous flow past an elliptic cylinder for Reynolds number up to 10000. *Commun. Nonlinear Sci. Numer. Simulat.* **102**, 105902.
- FONESCA, F. B., MANSUR, S. S. & VIEIRA, E. D. R. 2013 Flow around elliptical cylinders in moderate Reynolds numbers. In *22nd International Congress of Mechanical Engineering (COBEM 2013), November 3-7, 2013, Ribeirão Preto, SP, Brazil*, pp. 4089–4100.
- GALLARDO, J.P., ANDERSSON, H. I. & PETTERSEN, B. 2014 Turbulent wake behind a curved circular cylinder. *J. Fluid Mech.* **742**, 192–229.
- GALLARDO, J.P., PETTERSEN, B. & ANDERSSON, H. I. 2013 Effect of free-slip boundary conditions on the flow around a curved circular cylinder. *Comput. Fluids* **86**, 389–394.
- HO, C.-M. & HUANG, L.-S. 1982 Subharmonics and vortex merging in mixing layers. *J. Fluid Mech.* **119**, 443–473.
- IGARASHI, T. 1981 Characteristics of the flow around two circular cylinders arranged in tandem (1st report). *Bull. JSME* **24** (188), 323–330.
- JIANG, F., PETTERSEN, B. & ANDERSSON, H. I. 2018 Influences of upstream extensions on flow around a curved cylinder. *Eur. J. Mech. / B Fluids* **67**, 79–86.
- JIANG, F., PETTERSEN, B. & ANDERSSON, H. I. 2019 Turbulent wake behind a concave curved cylinder. *J. Fluid Mech.* **878**, 663–699.



- KHABBOUCHI, I., FELLOUAH, H., FERCHICHI, M. & GUELLOUZ, M. S. 2014 Effects of free-stream turbulence and Reynolds number on the separated shear layer from a circular cylinder. *J. Wind Eng. Ind. Aerodyn.* **135**, 46–56.
- KITAGAWA, T. & OHTA, H. 2008 Numerical investigation on flow around circular cylinders in tandem arrangement at a subcritical Reynolds number. *J. Fluids Struct.* **24**, 680–699.
- KOURTA, A., BOISSIN, H. C., CHASSING, P. & HA MINH, H. 1987 Nonlinear interaction and the transition to turbulence in the wake of a circular cylinder. *J. Fluid Mech.* **181**, 141–161.
- LJUNGKRONA, L., NORBERG, C. & SUNDEN, B. 1991 Free-stream turbulence and tube spacing effect on surface pressure fluctuations for two tubes in an in-line arrangement. *J. Fluid Struct.* **5**, 701–727.
- MANHART, M. 2004 A zonal grid algorithm for DNS of turbulent boundary layers. *Comput. Fluids* **33**, 435–461.
- MIKSAD, R. W., JONES, F. L., POWERS, E. J., KIM, Y. C. & KHADRA, L. 1982 Experiments on the role of amplitude and phase modulations during transition to turbulence. *J. Fluid Mech.* **123**, 1–29.
- MILIOU, A., DE VECCHI, A., SHERWIN, S. J. & GRAHAM, J. M. R. 2007 Wake dynamics of external flow past a curved cylinder with free stream aligned with the plane of curvature. *J. Fluid Mech.* **592**, 89–115.
- NORBERG, C. 1987 Effects of Reynolds number and low-intensity freestream turbulence on the flow around a circular cylinder. PhD thesis, Chalmers Tekniska Högskola.
- OKAJIMA, A. 1979 Flows around two tandem circular cylinders at very high Reynolds numbers. *Bull. JSME* **22**, 504–511.
- PELLER, N., LE DUC, A., TREMBLAY, T. & MANHART, M. 2006 High-order stable interpolations for immersed boundary methods. *Int. J. Num. Meth. Fluids* **53**, 1175–1193.
- PRASAD, A. & WILLIAMSON, C. H. K. 1997a The instability of the shear layer separating from a bluff body. *J. Fluid Mech.* **333**, 375–402.
- PRASAD, A. & WILLIAMSON, C. H. K. 1997b Three-dimensional effects in turbulent bluff-body wakes. *J. Fluid Mech.* **343**, 235–265.
- RAI, M. M. 2010 A computational investigation of the instability of the detached shear layers in the wake of a circular cylinder. *J. Fluid Mech.* **659**, 375–404.
- RAMBERG, S. E. 1983 The effects of yaw and finite length upon the vortex wakes of stationary and vibrating circular cylinders. *J. Fluid Mech.* **128**, 81–107.
- SATO, H. 1965 Experimental investigation on the transition of laminar separated shear layer. *J. Phys. Soc. Japan* **11**, 702.
- SHANG, J. K., STONE, H. A. & SMITS, A. J. 2018 Flow past finite cylinders of constant curvature. *J. Fluid Mech.* **837**, 896–915.
- SUMNER, D. 2010 Two circular cylinders in cross-flow: A review. *J. Fluids Struct.* **26**, 849–899.
- UNGLEHRT, L., JENSSEN, U., KURZ, F., SCHANDERL, W., KREUZINGER, J., SCHWERTFIRM, F. & MANHART, M. 2022 Large-eddy simulation of the flow inside a scour hole around a circular cylinder using a cut cell immersed boundary method. *Flow Turb. Comb.* **109**, 893–929.
- WANG, P., ZHOU, Q., ALAM, M. M., YANG, Y. & LI, M. 2022 Effects of streamwise gust amplitude on the flow around and forces on two tandem circular cylinders. *Ocean Eng.* **261**, 112040.
- WILLIAMSON, C. H. K. 1995 Scaling of streamwise structures in wakes. *Phys. Fluids* **7**, 2307.
- XU, G. & ZHOU, Y. 2004 Strouhal numbers in the wake of two inline cylinders. *Exp. Fluids* **37**, 248–256.
- YOUNIS, Y., ALAM, M. & ZHOU, Y. 2016 Flow around two nonparallel tandem cylinders. *Phys. Fluids* **28** (12), 125106.
- ZDRAVKOVICH, M. M. 1987 The effect of interference between circular cylinders in cross flow. *J. Fluids Struct.* **1**, 239–261.
- ZHOU, Y. & YIU, M. 2006 Flow structure, momentum and heat transport in a two-tandem-cylinder wake. *J. Fluid Mech.* **548**, 17–48.
- ZHU, H., WANG, R., BAO, Y., ZHOU, D., PING, H., HAN, Z. & SHERWIN, S. J. 2019 Flow over a symmetrically curved circular cylinder with the free stream parallel to the plane of curvature at low Reynolds number. *J. Fluids Struct.* **87**, 23–38.

**Previous PhD theses published at the Department of Marine Technology  
(earlier: Faculty of Marine Technology)  
NORWEGIAN UNIVERSITY OF SCIENCE AND TECHNOLOGY**

<b>Report No.</b>	<b>Author</b>	<b>Title</b>
	Kavlie, Dag	Optimization of Plane Elastic Grillages, 1967
	Hansen, Hans R.	Man-Machine Communication and Data-Storage Methods in Ship Structural Design, 1971
	Gisvold, Kaare M.	A Method for non-linear mixed -integer programming and its Application to Design Problems, 1971
	Lund, Sverre	Tanker Frame Optimization by means of SUMT-Transformation and Behaviour Models, 1971
	Vinje, Tor	On Vibration of Spherical Shells Interacting with Fluid, 1972
	Lorentz, Jan D.	Tank Arrangement for Crude Oil Carriers in Accordance with the new Anti-Pollution Regulations, 1975
	Carlsen, Carl A.	Computer-Aided Design of Tanker Structures, 1975
	Larsen, Carl M.	Static and Dynamic Analysis of Offshore Pipelines during Installation, 1976
UR-79-01	Brigt Hatlestad, MK	The finite element method used in a fatigue evaluation of fixed offshore platforms. (Dr.Ing. Thesis)
UR-79-02	Erik Pettersen, MK	Analysis and design of cellular structures. (Dr.Ing. Thesis)
UR-79-03	Sverre Valsgård, MK	Finite difference and finite element methods applied to nonlinear analysis of plated structures. (Dr.Ing. Thesis)
UR-79-04	Nils T. Nordsve, MK	Finite element collapse analysis of structural members considering imperfections and stresses due to fabrication. (Dr.Ing. Thesis)
UR-79-05	Ivar J. Fylling, MK	Analysis of towline forces in ocean towing systems. (Dr.Ing. Thesis)
UR-79- x	Finn Gunnar Nielsen, MH	Hydrodynamic problems related to oil barriers for offshore application
UR-80-06	Nils Sandsmark, MM	Analysis of Stationary and Transient Heat Conduction by the Use of the Finite Element Method. (Dr.Ing. Thesis)
UR-80-09	Sverre Haver, MK	Analysis of uncertainties related to the stochastic modeling of ocean waves. (Dr.Ing. Thesis)
UR-81-15	Odland, Jonas	On the Strength of welded Ring stiffened cylindrical Shells

		primarily subjected to axial Compression
UR-82-17	Engesvik, Knut	Analysis of Uncertainties in the fatigue Capacity of Welded Joints
UR-82-18	Rye, Henrik	Ocean wave groups
UR-83-30	Eide, Oddvar Inge	On Cumulative Fatigue Damage in Steel Welded Joints
UR-83-33	Mo, Olav	Stochastic Time Domain Analysis of Slender Offshore Structures
UR-83-34	Amdahl, Jørgen	Energy absorption in Ship-platform impacts
UR-84-37	Mørch, Morten	Motions and mooring forces of semi submersibles as determined by full-scale measurements and theoretical analysis
UR-84-38	Soares, C. Guedes	Probabilistic models for load effects in ship structures
UR-84-39	Aarsnes, Jan V.	Current forces on ships
UR-84-40	Czujko, Jerzy	Collapse Analysis of Plates subjected to Biaxial Compression and Lateral Load
UR-85-46	Alf G. Engseth, MK	Finite element collapse analysis of tubular steel offshore structures. (Dr.Ing. Thesis)
UR-86-47	Dengody Sheshappa, MP	A Computer Design Model for Optimizing Fishing Vessel Designs Based on Techno-Economic Analysis. (Dr.Ing. Thesis)
UR-86-48	Vidar Aanesland, MH	A Theoretical and Numerical Study of Ship Wave Resistance. (Dr.Ing. Thesis)
UR-86-49	Heinz-Joachim Wessel, MK	Fracture Mechanics Analysis of Crack Growth in Plate Girders. (Dr.Ing. Thesis)
UR-86-50	Jon Taby, MK	Ultimate and Post-ultimate Strength of Dented Tubular Members. (Dr.Ing. Thesis)
UR-86-51	Walter Lian, MH	A Numerical Study of Two-Dimensional Separated Flow Past Bluff Bodies at Moderate KC-Numbers. (Dr.Ing. Thesis)
UR-86-52	Bjørn Sortland, MH	Force Measurements in Oscillating Flow on Ship Sections and Circular Cylinders in a U-Tube Water Tank. (Dr.Ing. Thesis)
UR-86-53	Kurt Strand, MM	A System Dynamic Approach to One-dimensional Fluid Flow. (Dr.Ing. Thesis)
UR-86-54	Arne Edvin Løken, MH	Three Dimensional Second Order Hydrodynamic Effects on Ocean Structures in Waves. (Dr.Ing. Thesis)
UR-86-55	Sigurd Falch, MH	A Numerical Study of Slamming of Two-Dimensional Bodies. (Dr.Ing. Thesis)
UR-87-56	Arne Braathen, MH	Application of a Vortex Tracking Method to the Prediction of Roll Damping of a Two-Dimension Floating Body.

(Dr.Ing. Thesis)

UR-87-57	Bernt Leira, MK	Gaussian Vector Processes for Reliability Analysis involving Wave-Induced Load Effects. (Dr.Ing. Thesis)
UR-87-58	Magnus Småvik, MM	Thermal Load and Process Characteristics in a Two-Stroke Diesel Engine with Thermal Barriers (in Norwegian). (Dr.Ing. Thesis)
MTA-88-59	Bernt Arild Bremdal, MP	An Investigation of Marine Installation Processes – A Knowledge - Based Planning Approach. (Dr.Ing. Thesis)
MTA-88-60	Xu Jun, MK	Non-linear Dynamic Analysis of Space-framed Offshore Structures. (Dr.Ing. Thesis)
MTA-89-61	Gang Miao, MH	Hydrodynamic Forces and Dynamic Responses of Circular Cylinders in Wave Zones. (Dr.Ing. Thesis)
MTA-89-62	Martin Greenhow, MH	Linear and Non-Linear Studies of Waves and Floating Bodies. Part I and Part II. (Dr.Techn. Thesis)
MTA-89-63	Chang Li, MH	Force Coefficients of Spheres and Cubes in Oscillatory Flow with and without Current. (Dr.Ing. Thesis)
MTA-89-64	Hu Ying, MP	A Study of Marketing and Design in Development of Marine Transport Systems. (Dr.Ing. Thesis)
MTA-89-65	Arild Jæger, MH	Seakeeping, Dynamic Stability and Performance of a Wedge Shaped Planing Hull. (Dr.Ing. Thesis)
MTA-89-66	Chan Siu Hung, MM	The dynamic characteristics of tilting-pad bearings
MTA-89-67	Kim Wikstrøm, MP	Analysis av projekteringen for ett offshore projekt. (Licenciat-avhandling)
MTA-89-68	Jiao Guoyang, MK	Reliability Analysis of Crack Growth under Random Loading, considering Model Updating. (Dr.Ing. Thesis)
MTA-89-69	Arnt Olufsen, MK	Uncertainty and Reliability Analysis of Fixed Offshore Structures. (Dr.Ing. Thesis)
MTA-89-70	Wu Yu-Lin, MR	System Reliability Analyses of Offshore Structures using improved Truss and Beam Models. (Dr.Ing. Thesis)
MTA-90-71	Jan Roger Hoff, MH	Three-dimensional Green function of a vessel with forward speed in waves. (Dr.Ing. Thesis)
MTA-90-72	Rong Zhao, MH	Slow-Drift Motions of a Moored Two-Dimensional Body in Irregular Waves. (Dr.Ing. Thesis)
MTA-90-73	Atle Minsaas, MP	Economical Risk Analysis. (Dr.Ing. Thesis)
MTA-90-74	Knut-Arild Farnes, MK	Long-term Statistics of Response in Non-linear Marine Structures. (Dr.Ing. Thesis)
MTA-90-75	Torbjørn Sotberg, MK	Application of Reliability Methods for Safety Assessment of Submarine Pipelines. (Dr.Ing. Thesis)
MTA-90-76	Zeuthen, Steffen, MP	SEAMAID. A computational model of the design process in a constraint-based logic programming environment. An

		example from the offshore domain. (Dr.Ing. Thesis)
MTA-91-77	Haagensen, Sven, MM	Fuel Dependant Cyclic Variability in a Spark Ignition Engine - An Optical Approach. (Dr.Ing. Thesis)
MTA-91-78	Løland, Geir, MH	Current forces on and flow through fish farms. (Dr.Ing. Thesis)
MTA-91-79	Hoen, Christopher, MK	System Identification of Structures Excited by Stochastic Load Processes. (Dr.Ing. Thesis)
MTA-91-80	Haugen, Stein, MK	Probabilistic Evaluation of Frequency of Collision between Ships and Offshore Platforms. (Dr.Ing. Thesis)
MTA-91-81	Sødahl, Nils, MK	Methods for Design and Analysis of Flexible Risers. (Dr.Ing. Thesis)
MTA-91-82	Ormberg, Harald, MK	Non-linear Response Analysis of Floating Fish Farm Systems. (Dr.Ing. Thesis)
MTA-91-83	Marley, Mark J., MK	Time Variant Reliability under Fatigue Degradation. (Dr.Ing. Thesis)
MTA-91-84	Krokstad, Jørgen R., MH	Second-order Loads in Multidirectional Seas. (Dr.Ing. Thesis)
MTA-91-85	Molteberg, Gunnar A., MM	The Application of System Identification Techniques to Performance Monitoring of Four Stroke Turbocharged Diesel Engines. (Dr.Ing. Thesis)
MTA-92-86	Mørch, Hans Jørgen Bjelke, MH	Aspects of Hydrofoil Design: with Emphasis on Hydrofoil Interaction in Calm Water. (Dr.Ing. Thesis)
MTA-92-87	Chan Siu Hung, MM	Nonlinear Analysis of Rotordynamic Instabilities in Highspeed Turbomachinery. (Dr.Ing. Thesis)
MTA-92-88	Bessason, Bjarni, MK	Assessment of Earthquake Loading and Response of Seismically Isolated Bridges. (Dr.Ing. Thesis)
MTA-92-89	Langli, Geir, MP	Improving Operational Safety through exploitation of Design Knowledge - an investigation of offshore platform safety. (Dr.Ing. Thesis)
MTA-92-90	Sævik, Svein, MK	On Stresses and Fatigue in Flexible Pipes. (Dr.Ing. Thesis)
MTA-92-91	Ask, Tor Ø., MM	Ignition and Flame Growth in Lean Gas-Air Mixtures. An Experimental Study with a Schlieren System. (Dr.Ing. Thesis)
MTA-86-92	Hessen, Gunnar, MK	Fracture Mechanics Analysis of Stiffened Tubular Members. (Dr.Ing. Thesis)
MTA-93-93	Steinebach, Christian, MM	Knowledge Based Systems for Diagnosis of Rotating Machinery. (Dr.Ing. Thesis)
MTA-93-94	Dalane, Jan Inge, MK	System Reliability in Design and Maintenance of Fixed Offshore Structures. (Dr.Ing. Thesis)
MTA-93-95	Steen, Sverre, MH	Cobblestone Effect on SES. (Dr.Ing. Thesis)
MTA-93-96	Karunakaran, Daniel, MK	Nonlinear Dynamic Response and Reliability Analysis of

		Drag-dominated Offshore Platforms. (Dr.Ing. Thesis)
MTA-93-97	Hagen, Arnulf, MP	The Framework of a Design Process Language. (Dr.Ing. Thesis)
MTA-93-98	Nordrik, Rune, MM	Investigation of Spark Ignition and Autoignition in Methane and Air Using Computational Fluid Dynamics and Chemical Reaction Kinetics. A Numerical Study of Ignition Processes in Internal Combustion Engines. (Dr.Ing. Thesis)
MTA-94-99	Passano, Elizabeth, MK	Efficient Analysis of Nonlinear Slender Marine Structures. (Dr.Ing. Thesis)
MTA-94-100	Kvålsvold, Jan, MH	Hydroelastic Modelling of Wetdeck Slamming on Multihull Vessels. (Dr.Ing. Thesis)
MTA-94-102	Bech, Sidsel M., MK	Experimental and Numerical Determination of Stiffness and Strength of GRP/PVC Sandwich Structures. (Dr.Ing. Thesis)
MTA-95-103	Paulsen, Hallvard, MM	A Study of Transient Jet and Spray using a Schlieren Method and Digital Image Processing. (Dr.Ing. Thesis)
MTA-95-104	Hovde, Geir Olav, MK	Fatigue and Overload Reliability of Offshore Structural Systems, Considering the Effect of Inspection and Repair. (Dr.Ing. Thesis)
MTA-95-105	Wang, Xiaozhi, MK	Reliability Analysis of Production Ships with Emphasis on Load Combination and Ultimate Strength. (Dr.Ing. Thesis)
MTA-95-106	Ulstein, Tore, MH	Nonlinear Effects of a Flexible Stern Seal Bag on Cobblestone Oscillations of an SES. (Dr.Ing. Thesis)
MTA-95-107	Solaas, Frøydis, MH	Analytical and Numerical Studies of Sloshing in Tanks. (Dr.Ing. Thesis)
MTA-95-108	Hellan, Øyvind, MK	Nonlinear Pushover and Cyclic Analyses in Ultimate Limit State Design and Reassessment of Tubular Steel Offshore Structures. (Dr.Ing. Thesis)
MTA-95-109	Hermundstad, Ole A., MK	Theoretical and Experimental Hydroelastic Analysis of High Speed Vessels. (Dr.Ing. Thesis)
MTA-96-110	Bratland, Anne K., MH	Wave-Current Interaction Effects on Large-Volume Bodies in Water of Finite Depth. (Dr.Ing. Thesis)
MTA-96-111	Herfjord, Kjell, MH	A Study of Two-dimensional Separated Flow by a Combination of the Finite Element Method and Navier-Stokes Equations. (Dr.Ing. Thesis)
MTA-96-112	Æsøy, Vilmar, MM	Hot Surface Assisted Compression Ignition in a Direct Injection Natural Gas Engine. (Dr.Ing. Thesis)
MTA-96-113	Eknes, Monika L., MK	Escalation Scenarios Initiated by Gas Explosions on Offshore Installations. (Dr.Ing. Thesis)
MTA-96-114	Erikstad, Stein O., MP	A Decision Support Model for Preliminary Ship Design. (Dr.Ing. Thesis)
MTA-96-115	Pedersen, Egil, MH	A Nautical Study of Towed Marine Seismic Streamer Cable Configurations. (Dr.Ing. Thesis)
MTA-97-	Moksnes, Paul O., MM	Modelling Two-Phase Thermo-Fluid Systems Using Bond

116		Graphs. (Dr.Ing. Thesis)
MTA-97-117	Halse, Karl H., MK	On Vortex Shedding and Prediction of Vortex-Induced Vibrations of Circular Cylinders. (Dr.Ing. Thesis)
MTA-97-118	Igland, Ragnar T., MK	Reliability Analysis of Pipelines during Laying, considering Ultimate Strength under Combined Loads. (Dr.Ing. Thesis)
MTA-97-119	Pedersen, Hans-P., MP	Levendefiskteknologi for fiskefartøy. (Dr.Ing. Thesis)
MTA-98-120	Vikestad, Kyrre, MK	Multi-Frequency Response of a Cylinder Subjected to Vortex Shedding and Support Motions. (Dr.Ing. Thesis)
MTA-98-121	Azadi, Mohammad R. E., MK	Analysis of Static and Dynamic Pile-Soil-Jacket Behaviour. (Dr.Ing. Thesis)
MTA-98-122	Ulltang, Terje, MP	A Communication Model for Product Information. (Dr.Ing. Thesis)
MTA-98-123	Torbergsen, Erik, MM	Impeller/Diffuser Interaction Forces in Centrifugal Pumps. (Dr.Ing. Thesis)
MTA-98-124	Hansen, Edmond, MH	A Discrete Element Model to Study Marginal Ice Zone Dynamics and the Behaviour of Vessels Moored in Broken Ice. (Dr.Ing. Thesis)
MTA-98-125	Videiro, Paulo M., MK	Reliability Based Design of Marine Structures. (Dr.Ing. Thesis)
MTA-99-126	Mainçon, Philippe, MK	Fatigue Reliability of Long Welds Application to Titanium Risers. (Dr.Ing. Thesis)
MTA-99-127	Haugen, Elin M., MH	Hydroelastic Analysis of Slamming on Stiffened Plates with Application to Catamaran Wetdecks. (Dr.Ing. Thesis)
MTA-99-128	Langhelle, Nina K., MK	Experimental Validation and Calibration of Nonlinear Finite Element Models for Use in Design of Aluminium Structures Exposed to Fire. (Dr.Ing. Thesis)
MTA-99-129	Berstad, Are J., MK	Calculation of Fatigue Damage in Ship Structures. (Dr.Ing. Thesis)
MTA-99-130	Andersen, Trond M., MM	Short Term Maintenance Planning. (Dr.Ing. Thesis)
MTA-99-131	Tveiten, Bård Wathne, MK	Fatigue Assessment of Welded Aluminium Ship Details. (Dr.Ing. Thesis)
MTA-99-132	Søreide, Fredrik, MP	Applications of underwater technology in deep water archaeology. Principles and practice. (Dr.Ing. Thesis)
MTA-99-133	Tønnessen, Rune, MH	A Finite Element Method Applied to Unsteady Viscous Flow Around 2D Blunt Bodies With Sharp Corners. (Dr.Ing. Thesis)
MTA-99-134	Elvekrok, Dag R., MP	Engineering Integration in Field Development Projects in the Norwegian Oil and Gas Industry. The Supplier Management of Norne. (Dr.Ing. Thesis)
MTA-99-135	Fagerholt, Kjetil, MP	Optimeringsbaserte Metoder for Ruteplanlegging innen skipsfart. (Dr.Ing. Thesis)
MTA-99-	Bysveen, Marie, MM	Visualization in Two Directions on a Dynamic Combustion

136		Rig for Studies of Fuel Quality. (Dr.Ing. Thesis)
MTA-2000-137	Storteig, Eskild, MM	Dynamic characteristics and leakage performance of liquid annular seals in centrifugal pumps. (Dr.Ing. Thesis)
MTA-2000-138	Sagli, Gro, MK	Model uncertainty and simplified estimates of long term extremes of hull girder loads in ships. (Dr.Ing. Thesis)
MTA-2000-139	Tronstad, Harald, MK	Nonlinear analysis and design of cable net structures like fishing gear based on the finite element method. (Dr.Ing. Thesis)
MTA-2000-140	Kroneberg, André, MP	Innovation in shipping by using scenarios. (Dr.Ing. Thesis)
MTA-2000-141	Haslum, Herbjørn Alf, MH	Simplified methods applied to nonlinear motion of spar platforms. (Dr.Ing. Thesis)
MTA-2001-142	Samdal, Ole Johan, MM	Modelling of Degradation Mechanisms and Stressor Interaction on Static Mechanical Equipment Residual Lifetime. (Dr.Ing. Thesis)
MTA-2001-143	Baarholm, Rolf Jarle, MH	Theoretical and experimental studies of wave impact underneath decks of offshore platforms. (Dr.Ing. Thesis)
MTA-2001-144	Wang, Lihua, MK	Probabilistic Analysis of Nonlinear Wave-induced Loads on Ships. (Dr.Ing. Thesis)
MTA-2001-145	Kristensen, Odd H. Holt, MK	Ultimate Capacity of Aluminium Plates under Multiple Loads, Considering HAZ Properties. (Dr.Ing. Thesis)
MTA-2001-146	Greco, Marilena, MH	A Two-Dimensional Study of Green-Water Loading. (Dr.Ing. Thesis)
MTA-2001-147	Heggelund, Svein E., MK	Calculation of Global Design Loads and Load Effects in Large High Speed Catamarans. (Dr.Ing. Thesis)
MTA-2001-148	Babalola, Olusegun T., MK	Fatigue Strength of Titanium Risers – Defect Sensitivity. (Dr.Ing. Thesis)
MTA-2001-149	Mohammed, Abuu K., MK	Nonlinear Shell Finite Elements for Ultimate Strength and Collapse Analysis of Ship Structures. (Dr.Ing. Thesis)
MTA-2002-150	Holmedal, Lars E., MH	Wave-current interactions in the vicinity of the sea bed. (Dr.Ing. Thesis)
MTA-2002-151	Rognebakke, Olav F., MH	Sloshing in rectangular tanks and interaction with ship motions. (Dr.Ing. Thesis)
MTA-2002-152	Lader, Pål Furset, MH	Geometry and Kinematics of Breaking Waves. (Dr.Ing. Thesis)
MTA-2002-153	Yang, Qinzhen, MH	Wash and wave resistance of ships in finite water depth. (Dr.Ing. Thesis)
MTA-2002-154	Melhus, Øyvinn, MM	Utilization of VOC in Diesel Engines. Ignition and combustion of VOC released by crude oil tankers. (Dr.Ing. Thesis)
MTA-2002-155	Ronæss, Marit, MH	Wave Induced Motions of Two Ships Advancing on Parallel Course. (Dr.Ing. Thesis)
MTA-	Økland, Ole D., MK	Numerical and experimental investigation of whipping in



2002-156		twin hull vessels exposed to severe wet deck slamming. (Dr.Ing. Thesis)
MTA-2002-157	Ge, Chunhua, MK	Global Hydroelastic Response of Catamarans due to Wet Deck Slamming. (Dr.Ing. Thesis)
MTA-2002-158	Byklum, Eirik, MK	Nonlinear Shell Finite Elements for Ultimate Strength and Collapse Analysis of Ship Structures. (Dr.Ing. Thesis)
IMT-2003-1	Chen, Haibo, MK	Probabilistic Evaluation of FPSO-Tanker Collision in Tandem Offloading Operation. (Dr.Ing. Thesis)
IMT-2003-2	Skaugset, Kjetil Bjørn, MK	On the Suppression of Vortex Induced Vibrations of Circular Cylinders by Radial Water Jets. (Dr.Ing. Thesis)
IMT-2003-3	Chezian, Muthu	Three-Dimensional Analysis of Slamming. (Dr.Ing. Thesis)
IMT-2003-4	Buhaug, Øyvind	Deposit Formation on Cylinder Liner Surfaces in Medium Speed Engines. (Dr.Ing. Thesis)
IMT-2003-5	Tregde, Vidar	Aspects of Ship Design: Optimization of Aft Hull with Inverse Geometry Design. (Dr.Ing. Thesis)
IMT-2003-6	Wist, Hanne Therese	Statistical Properties of Successive Ocean Wave Parameters. (Dr.Ing. Thesis)
IMT-2004-7	Ransau, Samuel	Numerical Methods for Flows with Evolving Interfaces. (Dr.Ing. Thesis)
IMT-2004-8	Soma, Torkel	Blue-Chip or Sub-Standard. A data interrogation approach of identity safety characteristics of shipping organization. (Dr.Ing. Thesis)
IMT-2004-9	Ersdal, Svein	An experimental study of hydrodynamic forces on cylinders and cables in near axial flow. (Dr.Ing. Thesis)
IMT-2005-10	Brodtkorb, Per Andreas	The Probability of Occurrence of Dangerous Wave Situations at Sea. (Dr.Ing. Thesis)
IMT-2005-11	Yttervik, Rune	Ocean current variability in relation to offshore engineering. (Dr.Ing. Thesis)
IMT-2005-12	Fredheim, Arne	Current Forces on Net-Structures. (Dr.Ing. Thesis)
IMT-2005-13	Heggernes, Kjetil	Flow around marine structures. (Dr.Ing. Thesis)
IMT-2005-14	Fouques, Sebastien	Lagrangian Modelling of Ocean Surface Waves and Synthetic Aperture Radar Wave Measurements. (Dr.Ing. Thesis)
IMT-2006-15	Holm, Håvard	Numerical calculation of viscous free surface flow around marine structures. (Dr.Ing. Thesis)
IMT-2006-16	Bjørheim, Lars G.	Failure Assessment of Long Through Thickness Fatigue Cracks in Ship Hulls. (Dr.Ing. Thesis)
IMT-2006-17	Hansson, Lisbeth	Safety Management for Prevention of Occupational Accidents. (Dr.Ing. Thesis)

IMT-2006-18	Zhu, Xinying	Application of the CIP Method to Strongly Nonlinear Wave-Body Interaction Problems. (Dr.Ing. Thesis)
IMT-2006-19	Reite, Karl Johan	Modelling and Control of Trawl Systems. (Dr.Ing. Thesis)
IMT-2006-20	Smogeli, Øyvind Notland	Control of Marine Propellers. From Normal to Extreme Conditions. (Dr.Ing. Thesis)
IMT-2007-21	Storhaug, Gaute	Experimental Investigation of Wave Induced Vibrations and Their Effect on the Fatigue Loading of Ships. (Dr.Ing. Thesis)
IMT-2007-22	Sun, Hui	A Boundary Element Method Applied to Strongly Nonlinear Wave-Body Interaction Problems. (PhD Thesis, CeSOS)
IMT-2007-23	Rustad, Anne Marthine	Modelling and Control of Top Tensioned Risers. (PhD Thesis, CeSOS)
IMT-2007-24	Johansen, Vegar	Modelling flexible slender system for real-time simulations and control applications
IMT-2007-25	Wroldsen, Anders Sunde	Modelling and control of tensegrity structures. (PhD Thesis, CeSOS)
IMT-2007-26	Aronsen, Kristoffer Høye	An experimental investigation of in-line and combined inline and cross flow vortex induced vibrations. (Dr. avhandling, IMT)
IMT-2007-27	Gao, Zhen	Stochastic Response Analysis of Mooring Systems with Emphasis on Frequency-domain Analysis of Fatigue due to Wide-band Response Processes (PhD Thesis, CeSOS)
IMT-2007-28	Thorstensen, Tom Anders	Lifetime Profit Modelling of Ageing Systems Utilizing Information about Technical Condition. (Dr.ing. thesis, IMT)
IMT-2008-29	Refsnes, Jon Erling Gorset	Nonlinear Model-Based Control of Slender Body AUVs (PhD Thesis, IMT)
IMT-2008-30	Berntsen, Per Ivar B.	Structural Reliability Based Position Mooring. (PhD-Thesis, IMT)
IMT-2008-31	Ye, Naiquan	Fatigue Assessment of Aluminium Welded Box-stiffener Joints in Ships (Dr.ing. thesis, IMT)
IMT-2008-32	Radan, Damir	Integrated Control of Marine Electrical Power Systems. (PhD-Thesis, IMT)
IMT-2008-33	Thomassen, Paul	Methods for Dynamic Response Analysis and Fatigue Life Estimation of Floating Fish Cages. (Dr.ing. thesis, IMT)
IMT-2008-34	Pákozdi, Csaba	A Smoothed Particle Hydrodynamics Study of Two-dimensional Nonlinear Sloshing in Rectangular Tanks. (Dr.ing.thesis, IMT/ CeSOS)
IMT-2007-35	Grytøyr, Guttorm	A Higher-Order Boundary Element Method and Applications to Marine Hydrodynamics. (Dr.ing.thesis, IMT)
IMT-2008-36	Drummen, Ingo	Experimental and Numerical Investigation of Nonlinear Wave-Induced Load Effects in Containerships considering

		Hydroelasticity. (PhD thesis, CeSOS)
IMT-2008-37	Skejic, Renato	Maneuvering and Seakeeping of a Singel Ship and of Two Ships in Interaction. (PhD-Thesis, CeSOS)
IMT-2008-38	Harlem, Alf	An Age-Based Replacement Model for Repairable Systems with Attention to High-Speed Marine Diesel Engines. (PhD-Thesis, IMT)
IMT-2008-39	Alsos, Hagbart S.	Ship Grounding. Analysis of Ductile Fracture, Bottom Damage and Hull Girder Response. (PhD-thesis, IMT)
IMT-2008-40	Graczyk, Mateusz	Experimental Investigation of Sloshing Loading and Load Effects in Membrane LNG Tanks Subjected to Random Excitation. (PhD-thesis, CeSOS)
IMT-2008-41	Taghipour, Reza	Efficient Prediction of Dynamic Response for Flexible amd Multi-body Marine Structures. (PhD-thesis, CeSOS)
IMT-2008-42	Ruth, Eivind	Propulsion control and thrust allocation on marine vessels. (PhD thesis, CeSOS)
IMT-2008-43	Nystad, Bent Helge	Technical Condition Indexes and Remaining Useful Life of Aggregated Systems. PhD thesis, IMT
IMT-2008-44	Soni, Prashant Kumar	Hydrodynamic Coefficients for Vortex Induced Vibrations of Flexible Beams, PhD thesis, CeSOS
IMT-2009-45	Amlashi, Hadi K.K.	Ultimate Strength and Reliability-based Design of Ship Hulls with Emphasis on Combined Global and Local Loads. PhD Thesis, IMT
IMT-2009-46	Pedersen, Tom Arne	Bond Graph Modelling of Marine Power Systems. PhD Thesis, IMT
IMT-2009-47	Kristiansen, Trygve	Two-Dimensional Numerical and Experimental Studies of Piston-Mode Resonance. PhD-Thesis, CeSOS
IMT-2009-48	Ong, Muk Chen	Applications of a Standard High Reynolds Number Model and a Stochastic Scour Prediction Model for Marine Structures. PhD-thesis, IMT
IMT-2009-49	Hong, Lin	Simplified Analysis and Design of Ships subjected to Collision and Grounding. PhD-thesis, IMT
IMT-2009-50	Koushan, Kamran	Vortex Induced Vibrations of Free Span Pipelines, PhD thesis, IMT
IMT-2009-51	Korsvik, Jarl Eirik	Heuristic Methods for Ship Routing and Scheduling. PhD-thesis, IMT
IMT-2009-52	Lee, Jihoon	Experimental Investigation and Numerical in Analyzing the Ocean Current Displacement of Longlines. Ph.d.-Thesis, IMT.
IMT-2009-53	Vestbøstad, Tone Gran	A Numerical Study of Wave-in-Deck Impact usin a Two-Dimensional Constrained Interpolation Profile Method, Ph.d.thesis, CeSOS.

IMT-2009-54	Bruun, Kristine	Bond Graph Modelling of Fuel Cells for Marine Power Plants. Ph.d.-thesis, IMT
IMT 2009-55	Holstad, Anders	Numerical Investigation of Turbulence in a Sekwed Three-Dimensional Channel Flow, Ph.d.-thesis, IMT.
IMT 2009-56	Ayala-Uraga, Efren	Reliability-Based Assessment of Deteriorating Ship-shaped Offshore Structures, Ph.d.-thesis, IMT
IMT 2009-57	Kong, Xiangjun	A Numerical Study of a Damaged Ship in Beam Sea Waves. Ph.d.-thesis, IMT/CeSOS.
IMT 2010-58	Kristiansen, David	Wave Induced Effects on Floaters of Aquaculture Plants, Ph.d.-thesis, CeSOS.
IMT 2010-59	Ludvigsen, Martin	An ROV-Toolbox for Optical and Acoustic Scientific Seabed Investigation. Ph.d.-thesis IMT.
IMT 2010-60	Hals, Jørgen	Modelling and Phase Control of Wave-Energy Converters. Ph.d.thesis, CeSOS.
IMT 2010-61	Shu, Zhi	Uncertainty Assessment of Wave Loads and Ultimate Strength of Tankers and Bulk Carriers in a Reliability Framework. Ph.d. Thesis, IMT/ CeSOS
IMT 2010-62	Shao, Yanlin	Numerical Potential-Flow Studies on Weakly-Nonlinear Wave-Body Interactions with/without Small Forward Speed, Ph.d.thesis,CeSOS.
IMT 2010-63	Califano, Andrea	Dynamic Loads on Marine Propellers due to Intermittent Ventilation. Ph.d.thesis, IMT.
IMT 2010-64	El Khoury, George	Numerical Simulations of Massively Separated Turbulent Flows, Ph.d.-thesis, IMT
IMT 2010-65	Seim, Knut Sponheim	Mixing Process in Dense Overflows with Emphasis on the Faroe Bank Channel Overflow. Ph.d.thesis, IMT
IMT 2010-66	Jia, Huirong	Structural Analysis of Intect and Damaged Ships in a Collision Risk Analysis Perspective. Ph.d.thesis CeSoS.
IMT 2010-67	Jiao, Linlin	Wave-Induced Effects on a Pontoon-type Very Large Floating Structures (VLFS). Ph.D.-thesis, CeSOS.
IMT 2010-68	Abrahamsen, Bjørn Christian	Sloshing Induced Tank Roof with Entrapped Air Pocket. Ph.d.thesis, CeSOS.
IMT 2011-69	Karimirad, Madjid	Stochastic Dynamic Response Analysis of Spar-Type Wind Turbines with Catenary or Taut Mooring Systems. Ph.d.-thesis, CeSOS.
IMT -2011-70	Erlend Meland	Condition Monitoring of Safety Critical Valves. Ph.d.-thesis, IMT.
IMT – 2011-71	Yang, Limin	Stochastic Dynamic System Analysis of Wave Energy Converter with Hydraulic Power Take-Off, with Particular Reference to Wear Damage Analysis, Ph.d. Thesis, CeSOS.

IMT – 2011-72	Visscher, Jan	Application of Particle Image Velocimetry on Turbulent Marine Flows, Ph.d.Thesis, IMT.
IMT – 2011-73	Su, Biao	Numerical Predictions of Global and Local Ice Loads on Ships. Ph.d.Thesis, CeSOS.
IMT – 2011-74	Liu, Zhenhui	Analytical and Numerical Analysis of Iceberg Collision with Ship Structures. Ph.d.Thesis, IMT.
IMT – 2011-75	Aarsæther, Karl Gunnar	Modeling and Analysis of Ship Traffic by Observation and Numerical Simulation. Ph.d.Thesis, IMT.
Imt – 2011- 76	Wu, Jie	Hydrodynamic Force Identification from Stochastic Vortex Induced Vibration Experiments with Slender Beams. Ph.d.Thesis, IMT.
Imt – 2011- 77	Amini, Hamid	Azimuth Propulsors in Off-design Conditions. Ph.d.Thesis, IMT.
IMT – 2011-78	Nguyen, Tan-Hoi	Toward a System of Real-Time Prediction and Monitoring of Bottom Damage Conditions During Ship Grounding. Ph.d.thesis, IMT.
IMT- 2011- 79	Tavakoli, Mohammad T.	Assessment of Oil Spill in Ship Collision and Grounding, Ph.d.thesis, IMT.
IMT- 2011- 80	Guo, Bingjie	Numerical and Experimental Investigation of Added Resistance in Waves. Ph.d.Thesis, IMT.
IMT- 2011- 81	Chen, Qiaofeng	Ultimate Strength of Aluminium Panels, considering HAZ Effects, IMT
IMT- 2012-82	Kota, Ravikiran S.	Wave Loads on Decks of Offshore Structures in Random Seas, CeSOS.
IMT- 2012-83	Sten, Ronny	Dynamic Simulation of Deep Water Drilling Risers with Heave Compensating System, IMT.
IMT- 2012-84	Berle, Øyvind	Risk and resilience in global maritime supply chains, IMT.
IMT- 2012-85	Fang, Shaoji	Fault Tolerant Position Mooring Control Based on Structural Reliability, CeSOS.
IMT- 2012-86	You, Jikun	Numerical studies on wave forces and moored ship motions in intermediate and shallow water, CeSOS.
IMT- 2012-87	Xiang ,Xu	Maneuvering of two interacting ships in waves, CeSOS
IMT- 2012-88	Dong, Wenbin	Time-domain fatigue response and reliability analysis of offshore wind turbines with emphasis on welded tubular joints and gear components, CeSOS

IMT-2012-89	Zhu, Suji	Investigation of Wave-Induced Nonlinear Load Effects in Open Ships considering Hull Girder Vibrations in Bending and Torsion, CeSOS
IMT-2012-90	Zhou, Li	Numerical and Experimental Investigation of Station-keeping in Level Ice, CeSOS
IMT-2012-91	Ushakov, Sergey	Particulate matter emission characteristics from diesel engines operating on conventional and alternative marine fuels, IMT
IMT-2013-1	Yin, Decao	Experimental and Numerical Analysis of Combined In-line and Cross-flow Vortex Induced Vibrations, CeSOS
IMT-2013-2	Kurniawan, Adi	Modelling and geometry optimisation of wave energy converters, CeSOS
IMT-2013-3	Al Ryati, Nabil	Technical condition indexes doe auxiliary marine diesel engines, IMT
IMT-2013-4	Firoozkoohi, Reza	Experimental, numerical and analytical investigation of the effect of screens on sloshing, CeSOS
IMT-2013-5	Ommani, Babak	Potential-Flow Predictions of a Semi-Displacement Vessel Including Applications to Calm Water Broaching, CeSOS
IMT-2013-6	Xing, Yihan	Modelling and analysis of the gearbox in a floating spar-type wind turbine, CeSOS
IMT-7-2013	Balland, Océane	Optimization models for reducing air emissions from ships, IMT
IMT-8-2013	Yang, Dan	Transitional wake flow behind an inclined flat plate---- Computation and analysis, IMT
IMT-9-2013	Abdillah, Suyuthi	Prediction of Extreme Loads and Fatigue Damage for a Ship Hull due to Ice Action, IMT
IMT-10-2013	Ramirez, Pedro Agustin Pérez	Ageing management and life extension of technical systems- Concepts and methods applied to oil and gas facilities, IMT
IMT-11-2013	Chuang, Zhenju	Experimental and Numerical Investigation of Speed Loss due to Seakeeping and Maneuvering. IMT
IMT-12-2013	Etemaddar, Mahmoud	Load and Response Analysis of Wind Turbines under Atmospheric Icing and Controller System Faults with Emphasis on Spar Type Floating Wind Turbines, IMT
IMT-13-2013	Lindstad, Haakon	Strategies and measures for reducing maritime CO2 emissions, IMT
IMT-14-2013	Haris, Sabril	Damage interaction analysis of ship collisions, IMT
IMT-15-2013	Shainee, Mohamed	Conceptual Design, Numerical and Experimental Investigation of a SPM Cage Concept for Offshore Mariculture, IMT

IMT-16-2013	Gansel, Lars	Flow past porous cylinders and effects of biofouling and fish behavior on the flow in and around Atlantic salmon net cages, IMT
IMT-17-2013	Gaspar, Henrique	Handling Aspects of Complexity in Conceptual Ship Design, IMT
IMT-18-2013	Thys, Maxime	Theoretical and Experimental Investigation of a Free Running Fishing Vessel at Small Frequency of Encounter, CeSOS
IMT-19-2013	Aglen, Ida	VIV in Free Spanning Pipelines, CeSOS
IMT-1-2014	Song, An	Theoretical and experimental studies of wave diffraction and radiation loads on a horizontally submerged perforated plate, CeSOS
IMT-2-2014	Rogne, Øyvind Ygre	Numerical and Experimental Investigation of a Hinged 5-body Wave Energy Converter, CeSOS
IMT-3-2014	Dai, Lijuan	Safe and efficient operation and maintenance of offshore wind farms ,IMT
IMT-4-2014	Bachynski, Erin Elizabeth	Design and Dynamic Analysis of Tension Leg Platform Wind Turbines, CeSOS
IMT-5-2014	Wang, Jingbo	Water Entry of Freefall Wedged – Wedge motions and Cavity Dynamics, CeSOS
IMT-6-2014	Kim, Ekaterina	Experimental and numerical studies related to the coupled behavior of ice mass and steel structures during accidental collisions, IMT
IMT-7-2014	Tan, Xiang	Numerical investigation of ship's continuous- mode icebreaking in level ice, CeSOS
IMT-8-2014	Muliawan, Made Jaya	Design and Analysis of Combined Floating Wave and Wind Power Facilities, with Emphasis on Extreme Load Effects of the Mooring System, CeSOS
IMT-9-2014	Jiang, Zhiyu	Long-term response analysis of wind turbines with an emphasis on fault and shutdown conditions, IMT
IMT-10-2014	Dukan, Fredrik	ROV Motion Control Systems, IMT
IMT-11-2014	Grimsmo, Nils I.	Dynamic simulations of hydraulic cylinder for heave compensation of deep water drilling risers, IMT
IMT-12-2014	Kvittem, Marit I.	Modelling and response analysis for fatigue design of a semisubmersible wind turbine, CeSOS
IMT-13-2014	Akhtar, Juned	The Effects of Human Fatigue on Risk at Sea, IMT
IMT-14-2014	Syahroni, Nur	Fatigue Assessment of Welded Joints Taking into Account Effects of Residual Stress, IMT
IMT-1-2015	Bøckmann, Eirik	Wave Propulsion of ships, IMT

IMT-2-2015	Wang, Kai	Modelling and dynamic analysis of a semi-submersible floating vertical axis wind turbine, CeSOS
IMT-3-2015	Fredriksen, Arnt Gunvald	A numerical and experimental study of a two-dimensional body with moonpool in waves and current, CeSOS
IMT-4-2015	Jose Patricio Gallardo Canabes	Numerical studies of viscous flow around bluff bodies, IMT
IMT-5-2015	Vegard Longva	Formulation and application of finite element techniques for slender marine structures subjected to contact interactions, IMT
IMT-6-2015	Jacobus De Vaal	Aerodynamic modelling of floating wind turbines, CeSOS
IMT-7-2015	Fachri Nasution	Fatigue Performance of Copper Power Conductors, IMT
IMT-8-2015	Oleh I Karpa	Development of bivariate extreme value distributions for applications in marine technology, CeSOS
IMT-9-2015	Daniel de Almeida Fernandes	An output feedback motion control system for ROVs, AMOS
IMT-10-2015	Bo Zhao	Particle Filter for Fault Diagnosis: Application to Dynamic Positioning Vessel and Underwater Robotics, CeSOS
IMT-11-2015	Wenting Zhu	Impact of emission allocation in maritime transportation, IMT
IMT-12-2015	Amir Rasekhi Nejad	Dynamic Analysis and Design of Gearboxes in Offshore Wind Turbines in a Structural Reliability Perspective, CeSOS
IMT-13-2015	Arturo Jesùs Ortega Malca	Dynamic Response of Flexibles Risers due to Unsteady Slug Flow, CeSOS
IMT-14-2015	Dagfinn Husjord	Guidance and decision-support system for safe navigation of ships operating in close proximity, IMT
IMT-15-2015	Anirban Bhattacharyya	Ducted Propellers: Behaviour in Waves and Scale Effects, IMT
IMT-16-2015	Qin Zhang	Image Processing for Ice Parameter Identification in Ice Management, IMT
IMT-1-2016	Vincentius Rumawas	Human Factors in Ship Design and Operation: An Experiential Learning, IMT
IMT-2-2016	Martin Storheim	Structural response in ship-platform and ship-ice collisions, IMT



IMT-3-2016	Mia Abrahamsen Prsic	Numerical Simulations of the Flow around single and Tandem Circular Cylinders Close to a Plane Wall, IMT
IMT-4-2016	Tufan Arslan	Large-eddy simulations of cross-flow around ship sections, IMT
IMT-5-2016	Pierre Yves-Henry	Parametrisation of aquatic vegetation in hydraulic and coastal research,IMT
IMT-6-2016	Lin Li	Dynamic Analysis of the Instalation of Monopiles for Offshore Wind Turbines, CeSOS
IMT-7-2016	Øivind Kåre Kjerstad	Dynamic Positioning of Marine Vessels in Ice, IMT
IMT-8-2016	Xiaopeng Wu	Numerical Analysis of Anchor Handling and Fish Trawling Operations in a Safety Perspective, CeSOS
IMT-9-2016	Zhengshun Cheng	Integrated Dynamic Analysis of Floating Vertical Axis Wind Turbines, CeSOS
IMT-10-2016	Ling Wan	Experimental and Numerical Study of a Combined Offshore Wind and Wave Energy Converter Concept
IMT-11-2016	Wei Chai	Stochastic dynamic analysis and reliability evaluation of the roll motion for ships in random seas, CeSOS
IMT-12-2016	Øyvind Selnes Patricksson	Decision support for conceptual ship design with focus on a changing life cycle and future uncertainty, IMT
IMT-13-2016	Mats Jørgen Thorsen	Time domain analysis of vortex-induced vibrations, IMT
IMT-14-2016	Edgar McGuinness	Safety in the Norwegian Fishing Fleet – Analysis and measures for improvement, IMT
IMT-15-2016	Sepideh Jafarzadeh	Energy efficiency and emission abatement in the fishing fleet, IMT
IMT-16-2016	Wilson Ivan Guachamin Acero	Assessment of marine operations for offshore wind turbine installation with emphasis on response-based operational limits, IMT
IMT-17-2016	Mauro Candeloro	Tools and Methods for Autonomous Operations on Seabed and Water Coumn using Underwater Vehicles, IMT
IMT-18-2016	Valentin Chabaud	Real-Time Hybrid Model Testing of Floating Wind Tubines, IMT
IMT-1-2017	Mohammad Saud Afzal	Three-dimensional streaming in a sea bed boundary layer
IMT-2-2017	Peng Li	A Theoretical and Experimental Study of Wave-induced Hydroelastic Response of a Circular Floating Collar

IMT-3-2017	Martin Bergström	A simulation-based design method for arctic maritime transport systems
IMT-4-2017	Bhushan Taskar	The effect of waves on marine propellers and propulsion
IMT-5-2017	Mohsen Bardestani	A two-dimensional numerical and experimental study of a floater with net and sinker tube in waves and current
IMT-6-2017	Fatemeh Hoseini Dadmarzi	Direct Numerical Simulation of turbulent wakes behind different plate configurations
IMT-7-2017	Michel R. Miyazaki	Modeling and control of hybrid marine power plants
IMT-8-2017	Giri Rajasekhar Gunnu	Safety and efficiency enhancement of anchor handling operations with particular emphasis on the stability of anchor handling vessels
IMT-9-2017	Kevin Koosup Yum	Transient Performance and Emissions of a Turbocharged Diesel Engine for Marine Power Plants
IMT-10-2017	Zhaolong Yu	Hydrodynamic and structural aspects of ship collisions
IMT-11-2017	Martin Hassel	Risk Analysis and Modelling of Allisions between Passing Vessels and Offshore Installations
IMT-12-2017	Astrid H. Brodtkorb	Hybrid Control of Marine Vessels – Dynamic Positioning in Varying Conditions
IMT-13-2017	Kjersti Bruserud	Simultaneous stochastic model of waves and current for prediction of structural design loads
IMT-14-2017	Finn-Idar Grøtta Giske	Long-Term Extreme Response Analysis of Marine Structures Using Inverse Reliability Methods
IMT-15-2017	Stian Skjong	Modeling and Simulation of Maritime Systems and Operations for Virtual Prototyping using co-Simulations
IMT-1-2018	Yingguang Chu	Virtual Prototyping for Marine Crane Design and Operations
IMT-2-2018	Sergey Gavrilin	Validation of ship manoeuvring simulation models
IMT-3-2018	Jeevith Hegde	Tools and methods to manage risk in autonomous subsea inspection, maintenance and repair operations
IMT-4-2018	Ida M. Strand	Sea Loads on Closed Flexible Fish Cages
IMT-5-2018	Erlend Kvinge Jørgensen	Navigation and Control of Underwater Robotic Vehicles

IMT-6-2018	Bård Stovner	Aided Inertial Navigation of Underwater Vehicles
IMT-7-2018	Erlend Liavåg Grotle	Thermodynamic Response Enhanced by Sloshing in Marine LNG Fuel Tanks
IMT-8-2018	Børge Rokseth	Safety and Verification of Advanced Maritime Vessels
IMT-9-2018	Jan Vidar Ulveseter	Advances in Semi-Empirical Time Domain Modelling of Vortex-Induced Vibrations
IMT-10-2018	Chenyu Luan	Design and analysis for a steel braceless semi-submersible hull for supporting a 5-MW horizontal axis wind turbine
IMT-11-2018	Carl Fredrik Rehn	Ship Design under Uncertainty
IMT-12-2018	Øyvind Ødegård	Towards Autonomous Operations and Systems in Marine Archaeology
IMT-13-2018	Stein Melvær Nornes	Guidance and Control of Marine Robotics for Ocean Mapping and Monitoring
IMT-14-2018	Petter Norgren	Autonomous Underwater Vehicles in Arctic Marine Operations: Arctic marine research and ice monitoring
IMT-15-2018	Minjoo Choi	Modular Adaptable Ship Design for Handling Uncertainty in the Future Operating Context
MT-16-2018	Ole Alexander Eidsvik	Dynamics of Remotely Operated Underwater Vehicle Systems
IMT-17-2018	Mahdi Ghane	Fault Diagnosis of Floating Wind Turbine Drivetrain-Methodologies and Applications
IMT-18-2018	Christoph Alexander Thieme	Risk Analysis and Modelling of Autonomous Marine Systems
IMT-19-2018	Yugao Shen	Operational limits for floating-collar fish farms in waves and current, without and with well-boat presence
IMT-20-2018	Tianjiao Dai	Investigations of Shear Interaction and Stresses in Flexible Pipes and Umbilicals
IMT-21-2018	Sigurd Solheim Pettersen	Resilience by Latent Capabilities in Marine Systems
IMT-22-2018	Thomas Sauder	Fidelity of Cyber-physical Empirical Methods. Application to the Active Truncation of Slender Marine Structures
IMT-23-2018	Jan-Tore Horn	Statistical and Modelling Uncertainties in the Design of Offshore Wind Turbines

IMT-24-2018	Anna Swider	Data Mining Methods for the Analysis of Power Systems of Vessels
IMT-1-2019	Zhao He	Hydrodynamic study of a moored fish farming cage with fish influence
IMT-2-2019	Isar Ghamari	Numerical and Experimental Study on the Ship Parametric Roll Resonance and the Effect of Anti-Roll Tank
IMT-3-2019	Håkon Strandenes	Turbulent Flow Simulations at Higher Reynolds Numbers
IMT-4-2019	Siri Mariane Holen	Safety in Norwegian Fish Farming – Concepts and Methods for Improvement
IMT-5-2019	Ping Fu	Reliability Analysis of Wake-Induced Riser Collision
IMT-6-2019	Vladimir Krivopolianski	Experimental Investigation of Injection and Combustion Processes in Marine Gas Engines using Constant Volume Rig
IMT-7-2019	Anna Maria Kozłowska	Hydrodynamic Loads on Marine Propellers Subject to Ventilation and out of Water Condition.
IMT-8-2019	Hans-Martin Heyn	Motion Sensing on Vessels Operating in Sea Ice: A Local Ice Monitoring System for Transit and Stationkeeping Operations under the Influence of Sea Ice
IMT-9-2019	Stefan Vilsen	Method for Real-Time Hybrid Model Testing of Ocean Structures – Case on Slender Marine Systems
IMT-10-2019	Finn-Christian W. Hanssen	Non-Linear Wave-Body Interaction in Severe Waves
IMT-11-2019	Trygve Olav Fossum	Adaptive Sampling for Marine Robotics
IMT-12-2019	Jørgen Bremnes Nielsen	Modeling and Simulation for Design Evaluation
IMT-13-2019	Yuna Zhao	Numerical modelling and dynamic analysis of offshore wind turbine blade installation
IMT-14-2019	Daniela Myland	Experimental and Theoretical Investigations on the Ship Resistance in Level Ice
IMT-15-2019	Zhengru Ren	Advanced control algorithms to support automated offshore wind turbine installation
IMT-16-2019	Drazen Polic	Ice-propeller impact analysis using an inverse propulsion machinery simulation approach
IMT-17-2019	Endre Sandvik	Sea passage scenario simulation for ship system performance evaluation

IMT-18-2019	Loup Suja-Thauvin	Response of Monopile Wind Turbines to Higher Order Wave Loads
IMT-19-2019	Emil Smilden	Structural control of offshore wind turbines – Increasing the role of control design in offshore wind farm development
IMT-20-2019	Aleksandar-Sasa Milakovic	On equivalent ice thickness and machine learning in ship ice transit simulations
IMT-1-2020	Amrit Shankar Verma	Modelling, Analysis and Response-based Operability Assessment of Offshore Wind Turbine Blade Installation with Emphasis on Impact Damages
IMT-2-2020	Bent Oddvar Arnesen Haugaløkken	Autonomous Technology for Inspection, Maintenance and Repair Operations in the Norwegian Aquaculture
IMT-3-2020	Seongpil Cho	Model-based fault detection and diagnosis of a blade pitch system in floating wind turbines
IMT-4-2020	Jose Jorge Garcia Agis	Effectiveness in Decision-Making in Ship Design under Uncertainty
IMT-5-2020	Thomas H. Viuff	Uncertainty Assessment of Wave-and Current-induced Global Response of Floating Bridges
IMT-6-2020	Fredrik Mentzoni	Hydrodynamic Loads on Complex Structures in the Wave Zone
IMT-7-2020	Senthuran Ravinthrakumar	Numerical and Experimental Studies of Resonant Flow in Moonpools in Operational Conditions
IMT-8-2020	Stian Skaalvik Sandøy	Acoustic-based Probabilistic Localization and Mapping using Unmanned Underwater Vehicles for Aquaculture Operations
IMT-9-2020	Kun Xu	Design and Analysis of Mooring System for Semi-submersible Floating Wind Turbine in Shallow Water
IMT-10-2020	Jianxun Zhu	Cavity Flows and Wake Behind an Elliptic Cylinder Translating Above the Wall
IMT-11-2020	Sandra Hogenboom	Decision-making within Dynamic Positioning Operations in the Offshore Industry – A Human Factors based Approach
IMT-12-2020	Woongshik Nam	Structural Resistance of Ship and Offshore Structures Exposed to the Risk of Brittle Failure
IMT-13-2020	Svenn Are Tuttøren Værnø	Transient Performance in Dynamic Positioning of Ships: Investigation of Residual Load Models and Control Methods for Effective Compensation
IMT-14-2020	Mohd Atif Siddiqui	Experimental and Numerical Hydrodynamic Analysis of a Damaged Ship in Waves
IMT-15-2020	John Marius Hegseth	Efficient Modelling and Design Optimization of Large Floating Wind Turbines

IMT-16-2020	Asle Natskär	Reliability-based Assessment of Marine Operations with Emphasis on Sea Transport on Barges
IMT-17-2020	Shi Deng	Experimental and Numerical Study of Hydrodynamic Responses of a Twin-Tube Submerged Floating Tunnel Considering Vortex-Induced Vibration
IMT-18-2020	Jone Torsvik	Dynamic Analysis in Design and Operation of Large Floating Offshore Wind Turbine Drivetrains
IMT-1-2021	Ali Ebrahimi	Handling Complexity to Improve Ship Design Competitiveness
IMT-2-2021	Davide Proserpio	Isogeometric Phase-Field Methods for Modeling Fracture in Shell Structures
IMT-3-2021	Cai Tian	Numerical Studies of Viscous Flow Around Step Cylinders
IMT-4-2021	Farid Khazaeli Moghadam	Vibration-based Condition Monitoring of Large Offshore Wind Turbines in a Digital Twin Perspective
IMT-5-2021	Shuaishuai Wang	Design and Dynamic Analysis of a 10-MW Medium-Speed Drivetrain in Offshore Wind Turbines
IMT-6-2021	Sadi Tavakoli	Ship Propulsion Dynamics and Emissions
IMT-7-2021	Haoran Li	Nonlinear wave loads, and resulting global response statistics of a semi-submersible wind turbine platform with heave plates
IMT-8-2021	Einar Skiftestad Ueland	Load Control for Real-Time Hybrid Model Testing using Cable-Driven Parallel Robots
IMT-9-2021	Mengning Wu	Uncertainty of machine learning-based methods for wave forecast and its effect on installation of offshore wind turbines
IMT-10-2021	Xu Han	Onboard Tuning and Uncertainty Estimation of Vessel Seakeeping Model Parameters
IMT-01-2022	Ingunn Marie Holmen	Safety in Exposed Aquaculture Operations
IMT-02-2022	Prateek Gupta	Ship Performance Monitoring using In-service Measurements and Big Data Analysis Methods
IMT-03-2022	Sangwoo Kim	Non-linear time domain analysis of deepwater riser vortex-induced vibrations
IMT-04-2022	Jarle Vinje Kramer	Hydrodynamic Aspects of Sail-Assisted Merchant Vessels
IMT-05-2022	Øyvind Rabliås	Numerical and Experimental Studies of Maneuvering in Regular and Irregular Waves

IMT-06-2022	Pramod Ghimire	Simulation-Based Ship Hybrid Power System Concept Studies and Performance Analyses
IMT-07-2022	Carlos Eduardo Silva de Souza	Structural modelling, coupled dynamics, and design of large floating wind turbines
IMT-08-2022	Lorenzo Balestra	Design of hybrid fuel cell & battery systems for maritime vessels
IMT-09-2022	Sharmin Sultana	Process safety and risk management using system perspectives – A contribution to the chemical process and petroleum industry
IMT-10-2022	Øystein Sture	Autonomous Exploration for Marine Minerals
IMT-11-2022	Tiantian Zhu	Information and Decision-making for Major Accident Prevention – A concept of information-based strategies for accident prevention
IMT-12-2022	Siamak Karimi	Shore-to-Ship Charging Systems for Battery-Electric Ships
IMT-01-2023	Huili Xu	Fish-inspired Propulsion Study: Numerical Hydrodynamics of Rigid/Flexible/Morphing Foils and Observations on Real Fish
IMT-02-2023	Chana Sinsabvarodom	Probabilistic Modelling of Ice-drift and Ice Loading on Fixed and Floating Offshore Structures
IMT-03-2023	Martin Skaldebø	Intelligent low-cost solutions for underwater intervention using computer vision and machine learning
IMT-04-2023	Hans Tobias Slette	Vessel operations in exposed aquaculture – Achieving safe and efficient operation of vessel fleets in fish farm systems experiencing challenging metocean conditions
IMT-05-2023	Ruochen Yang	Methods and models for analyzing and controlling the safety in operations of autonomous marine systems
IMT-06-2023	Tobias Rye Torben	Formal Approaches to Design and Verification of Safe Control Systems for Autonomous Vessels
IMT-07-2023	YoungRong Kim	Modeling Operational Performance for the Global Fleet & Application of an Energy Saving Measure
IMT-08-2023	Henrik Schmidt-Didlauskies	Modeling and Hybrid Feedback Control of Underwater Vehicles
IMT-09-2023	Ehsan Esmailian	Optimal Ship Design for Operating in Real Sea States
IMT-10-2023	Astrid Vamråk Solheim	Exploring the performance of conceptual offshore production systems for deep-sea mining
IMT-11-2023	Benjamin Lagemann	Conceptual design of low-emission ships

IMT-12-2023	Erling Neerland Lone	Fatigue reliability of offshore Mooring chains under influence of mean load and corrosion
IMT-13-2023	Kamyar Malekibagherabadi	Simulator Approach to Concept Analysis and Optimization of Marine Power Plants
IMT-14-2023	Håvard Sneffjellås Løvås	Optical Techniques for Hyperspectral Imaging of the Seafloor
IMT-15-2023	Stian Høegh Sørum	Uncertainties in the Design of Monopile Offshore Wind Turbines
IMT-16-2023	Nathalie Ramos	Mechanical and thermal simulations of 3D printed structures and the 3D printing process
IMT-17-2023	Daeseong Park	Model-Based Design of Marine Hybrid Power Systems
IMT-18-2023	Chuanqi Guo	Analysis and modeling of risk of an autonomous ferry for safer design and operation
IMT-01-2024	Dennis David Langer	Hyperspectral Push-broom Systems: Operations, Software Development, and Spatial Resolution
IMT-02-2024	Jens Einar Bremnes	Safe Autonomy in Marine Robotics
IMT-03-2024	George Katsikogiannis	Estimation of Long-Term Fatigue and Extreme Responses of Large-Diameter Monopiles for Offshore Wind Turbines
IMT-04-2024	Alexandre Cardaillac	Towards autonomous underwater navigation and perception for end-to-end ship hull inspection
IMT-05-2024	Tale Egeberg Aasland	Numerical studies of viscous flow around straight and curved tandem cylinders